Title
Reconstructing the timing and chemistry of aqueous processing of carbonaceous chondrite parent bodies: A coordinated, in-situ investigation

Author
McCain, Kaitlyn A

Publication Date
2022

Peer reviewed|Thesis/dissertation

UNIVERSITY OF CALIFORNIA

Los Angeles

Reconstructing the timing and chemistry of aqueous processing of carbonaceous chondrite parent bodies: A coordinated, in-situ investigation

A dissertation submitted in partial satisfaction of the requirements for the degree Doctor of Philosophy in Geochemistry

by

Kaitlyn A McCain

2022

ABSTRACT OF THE DISSERTATION

Reconstructing the timing and chemistry of aqueous processing of carbonaceous chondrite parent bodies: A coordinated, in-situ investigation

by

Kaitlyn A McCain

Doctor of Philosophy in Geochemistry

University of California, Los Angeles, 2022

Professor Kevin McKeegan, Chair

The CM and CI carbonaceous chondrites and C-type asteroids hosted abundant liquid water and organic compounds in the past. Studies of meteorites indicate that a diverse array of water-rich environments existed early in solar system history, and the chemistry of secondary minerals produced by this alteration record the physiochemical conditions and timescales under which fluid alteration occurred. In-situ studies of carbonate minerals found in these meteorites, which precipitate directly from the fluid and can be dated using the ^{53}Mn-^{53}Cr chronometer, can provide strong constraints on the timing and chemistry of aqueous activity. However, a lack of appropriate analytical standards may have affected the accuracy of in-situ measurements,

particularly measurements of carbonate formation ages. In this work, I developed standards designed to facilitate accurate measurements of the Mn-Cr age of carbonates and used them to measure the ages of carbonates from extensively altered meteorites, as well as samples returned from the Cb-type asteroid 162173 Ryugu by JAXA's Hayabusa2 mission. I combine measurements of the carbonate formation age with carbon and oxygen stable isotopic measurements on the same carbonates to connect the sequence and timing of alteration with the source of the fluids and the relevant carbon reservoirs present during alteration. Using the new standards, I found that the CI chondrites (and the CI-like material returned from Ryugu) formed earlier than previously inferred and attribute this difference to the use of the improved standards. I also identified signatures of impact resetting in measurements of CM carbonate.

The dissertation of Kaitlyn A McCain is approved.

Edward Donald Young

Timothy Mark Harrison

Craig E. Manning

Ming-Chang Liu

Kevin D. McKeegan, Committee Chair

University of California, Los Angeles

2022

Table of Contents

List of Figures, Equations, and Tables

Acknowledgments

Chapter 2 of this dissertation is a version of McCain, K.A., Liu, M.-C., McKeegan, K.D. 2020. Calibration of matrix-dependent biases in isotope and trace element analyses of carbonate minerals. Journal of Vacuum Science & Technology B **38**, 044005, doi: 10.1116/6.0000111. Reproduced with the permission of AIP Publishing.

Chapter 4 of this dissertation is a version of: McCain, K.A., Matsuda, N., Liu, M-C., McKeegan, K.D. et al. 2022. Early fluid activity on Ryugu: perspectives from oxygen, carbon, and ^{53}Mn-^{53}Cr isotopes, which has been submitted to Nature Astronomy and is under review at time of submission of this dissertation. Dr. Nozomi Matsuda is the co-first author.

I acknowledge the critical contributions made by the co-authors of the manuscripts that have become the chapters of this dissertation, including: Nozomi Matsuda (Co-first author of Chapter 4, sample handling), Akira Yamaguchi (EPMA analysis and data reduction, SEM-EDS analysis, sample handling), Makoto Kimura (SEM-EDS analysis, sample handling), Naotaka Tomioka (SEM-EDS analysis, sample handling), Motoo Ito (Phase 2 Curation Kochi PI, SEM-EDS analysis, sample handling), Naoya Imae (SEM-EDS analysis, sample handling), Masayuki Uesugi (sample handling), Naoki Shirai (sample handling), Takuji Ohigashi (sample handling), Richard C. Greenwood (data interpretation, manuscript revision), Kentaro Uesugi (sample handling), Aiko Nakato (JAXA Curation, sample handling), Kasumi Yogata (JAXA Curation, sample handling), Hayato Yuzawa (sample holder development), Yu Kodama (sample holder development), Kaori Hirahara (sample holder development), Ikuya Sakurai (sample holder development), Ikuo Okada (sample holder development), Yuzuru Karouji (sample holder development), Satoru Nakazawa (Hayabusa2 PI), Tatsuaki Okada (Hayabusa2 PI), Takanao

Saiki (Hayabusa2 PI), Satoshi Tanaka (Hayabusa2 PI), Fuyuto Terui (Hayabusa2 PI), Makoto Yoshikawa (Hayabusa2 PI), Akiko Miyazaki (JAXA Curation), Masahiro Nishimura (JAXA Curation), Toru Yada, Masanao Abe, Tomohiro Usui, Sei-ichiro Watanabe (Hayabusa2 PI), and Yuichi Tsuda (Hayabusa2 PI).

This work would not have been possible without meteorite samples on loan from Adrian Brearley at the University of New Mexico and the Field Museum of Natural History, nor without Paula Leek's valuable contributions to sample preparation. I also acknowledge the monumental efforts of the Hayabusa2 mission and curation teams to return and preserve samples from asteroid Ryugu.

To my friends and family, including: Bryce Mitsunaga, for his good humor and staunch support regardless of circumstances that came our way; Joseph, Janet, and Lauren McCain, for many years of grace and understanding as I pursued this dream; Dr. Heather Kirkpatrick, for being there every step of the way; Dr. Ellen Alexander, Daniel Fineman, and Erik Weidner for their friendship and support since I set foot on campus; and to the EPSS graduate students, including members of the board gaming and music groups—I am truly fortunate that there are too many who deserve recognition to list. To present and past UCLA isotope geochemists 'on the second floor', including Dr. Michelle Jordan, Dr. Haolan Tang, Dr. Nozomi Matsuda, Dr. Beth Ann Bell, and Dr. Junko Isa—without your advice, support, and camaraderie, this dissertation would not exist.

I am also grateful for the mentoring I have received during my time at UCLA. In particular: Prof. Edward Young, for years of advising and for affording me the opportunity to develop the knowledge and confidence to explore a wide range of geochemical fields using diverse tools; Dr. Ming-Chang Liu, for mentorship, invaluable expertise, hospitality, and for

keeping me ‘in the loop’; my additional committee members Prof. Timothy Mark Harrison and Prof. Craig Manning, whose perspectives broadened my own and improved the quality of my research and this manuscript.

Finally, I would like to sincerely thank my advisor and committee chair, Prof. Kevin McKeegan. His advocacy, support, and trust in me have been critical to any successes I can claim. This dissertation is built upon many years of work by Kevin and his collaborators, and it has been a great privilege to make my own contribution.

Funding for this work was provided by the NASA Earth and Space Science Fellowship (No. NESSF19R 19-PLANET19R-0001) to Kaitlyn McCain and NASA Emerging Worlds program grants to Ming-Chang Liu and Kevin McKeegan. The UCLA ion microprobe facility is partially supported by a grant from the NSF Instrumentation and Facilities program.

UCLA acknowledges the Gabrielino/Tongva peoples as the traditional land caretakers of Tovaangar (Los Angeles basin, So. Channel Islands) and is grateful to have the opportunity to work for the taraaxatom (indigenous peoples) in this place. As a land grant institution, we pay our respects to the Honuukvetam (Ancestors), 'Ahiihirom (Elders), and 'Eyoohiinkem (relations) past, present and emerging.

Vita / Biographical Sketch

EDUCATION

2015 B.S., Geophysical Sciences with Honors, University of Chicago, Chicago, IL
2017 M.S., Geochemistry, University of California at Los Angeles, Los Angeles, CA
2022 C.Ph., Geochemistry, University of California at Los Angeles, Los Angeles, CA

RESEARCH EXPERIENCE

2015-present	Graduate Student researcher, Dept. of Earth and Space Sciences, UCLA
2013-2015	Meteoritics Intern and Research Assistant, Field Museum of Natural History, Chicago, IL
Summer 2014	Lunar and Planetary Institute Summer Intern

AWARDS

Fall 2021	American Federation of Mineralogical Societies Scholarship
Summer 2021	Wiley-Blackwell Award for Outstanding Presentation
Summer 2021	NASA US Students Award
2018-2021	NASA NESSF Fellow
Fall 2019	Rowland Hill Award for Best Student Presentation
Summer 2019	Barringer Crater Company Award
Summer 2018	O. Richard Norton Award
Summer 2018	Planetary Studies Foundation Award
Spring 2018	EPSS Outreach Award
Sprint 2018	EPSS Extramural Funding Award

SELECTED PUBLICATIONS

Liu, M.-C., et al. (2022, accepted). Incorporation of ^{16}O-rich anhydrous silicates in the protolith of highly hydrated asteroid Ryugu. *Nature Astronomy*

Ito, M., et al. (2022, in press) A unique and pristine record of outer Solar System materials from C-type asteroid Ryugu. *Nature Astronomy*

Shollenberger, Q.R., et al. (2022) Titanium isotope systematics of refractory inclusions: Echoes of molecular cloud heterogeneity. *Geochimica et Cosmochimica Acta* **324**, 44-65

McCain K. A., Liu M.-C. and McKeegan K. D. (2020) Calibration of matrix-dependent biases in isotope and trace element analyses of carbonate minerals. *Journal of Vacuum Science & Technology B* **38**, 044005.

Simon, J.I., et al. (2018) Particle size distributions in chondritic meteorites: evidence for pre-planetesimal histories. *Earth and Planetary Science Letters* **494**, 69-82.

Young E.D., et al. (2017) The relative abundances of resolved $^{12}CH_2D_2$ and $^{13}CH_3D$ and mechanisms controlling isotopic bond ordering in abiotic and biotic methane gas. *Geochimica et Cosmochimica Acta* **203**, 235-264.

Chapter 1.

Introduction to

'Reconstructing the timing and chemistry of aqueous processing of carbonaceous chondrite parent bodies: A coordinated, in-situ investigation'

Kaitlyn A. McCain

Many of our efforts to explore and understand the formation and evolution of our Solar System have been guided by the astrobiological proverb of *"Follow the water"* in an attempt to address fundamental questions such as: How did the Earth get its water? What other water-rich environments exist or have existed over the course of the history of the Solar System? Were (or are) any of these environments capable of supporting life or facilitating prebiotic chemistry? To address these questions, solar system bodies such as Enceladus, Mars, Europa, and Ceres which show evidence of hosting liquid water in the present or recent past have been designated as prime targets for exploratory missions aimed at understanding the water's chemistry and history.

In addition to solar system bodies with extant evidence of liquid water, many other bodies show signs of having hosted abundant water and organic compounds in the past, even if this water is no longer present. The C and D-type asteroids make up over >75% of main-belt asteroids (DeMeo and Carry 2014; Fornasier et al. 2014), and reflected light spectroscopy of their surfaces reveals the presence of clay minerals and dark C-rich organic material despite the fact that liquid water and water ice are not stable on these bodies at their present-day locations and temperatures. Hydrated interplanetary dust particles (IDPs) are also common (Bradley 2014; Bradley and Brownlee 1991), providing further evidence that water-rock interactions in asteroidal settings was an important and widespread process in the Solar System. To investigate these aqueously-altered environments, asteroids such as the C-type asteroid 101955 Bennu (Lauretta et al. 2017) and Cb-type asteroid 162173 Ryugu (Watanabe et al. 2017) have become the targets of sample return missions with the goal of returning fragments of these formerly-wet asteroids to Earth, complementing remote sensing and astronomical observations with intensive laboratory studies.

Returned samples are not the only pieces of formerly water-rich environments which can be studied in the lab. Meteorites fall to Earth every day, conveniently delivering diverse samples from Mars, the Moon, and the asteroid belt. Some of these meteorites bear spectral similarities to the hydrated and organic-rich C-type asteroids (Gaffey et al. 1993), especially two meteorite classes designated as the CM (Mighei-type) and CI (Ivuna-type) chondrites. These meteorites contain abundant secondary minerals produced by interactions between anhydrous silicates and aqueous fluids, including phyllosilicates, carbonates, sulfides, phosphates, and more. By investigating these meteorites, we aim to determine the physiochemical conditions and timescales under which fluid alteration occurred in the parent bodies of asteroids.

The extent of aqueous alteration experienced by CM and CI chondrites varies widely, revealing a diverse array of fluid-rich environments in the early Solar System. The CM chondrites experienced a variety of alteration histories, continuously ranging from samples which experienced only minor fluid-rock interaction (e.g. Hewins et al. 2014; Rubin 2015; Vacher et al. 2017) to samples which are nearly completely hydrated (e.g. Zolensky et al. 1997). The CM chondrites accreted a mixture of water and nebular solids such as chondrules and CAIs, embedded in a matrix initially composed of FeNi metal, troilite (FeS), amorphous silicate, and anhydrous silicate (Hewins et al. 2014). As alteration began, metal, sulfide, and silicates in the matrix were converted into magnetite, sulfates, and phyllosilicates with the latter consisting mainly of cronstedtite - tochilinite intergrowths (TCIs) (e.g. Bunch and Chang 1980; Fuchs et al. 1973; Rubin et al. 2007; Suttle et al. 2021; Tomeoka and Buseck 1985; Trigo-Rodriguez et al. 2006). I note that the TCIs were previously designated as a “poorly characterized phase” (PCP). Calcium was leached from easily-altered silicate phases such as chondrule mesostasis, melilite, and Ca-pyroxene, precipitating from the fluid as calcite and aragonite in the matrix (Hewins et

al. 2014; Lee and Lindgren 2016) . As alteration proceeded, anhydrous silicates and oxides within chondrules and CAIs were progressively altered and replaced by phyllosilicates and carbonates, sometimes leaving easily-recognizable pseudomorphs of the primary nebular phases (e.g. Grady et al. 1987; Suttle et al. 2021; Zolensky et al. 1996, 1997). In the most highly altered CMs, the fluid had become sufficiently Mg-rich from interaction with anhydrous silicate to form Mg-rich serpentine in place of Fe-cronstedtite along with Mg-rich carbonates such as dolomite and breunnerite (Grady et al. 1987; King et al. 2017; Suttle et al. 2021; Zolensky et al. 1996, 1997).

In general, the CM2 designation is given to CM chondrites which retain anhydrous silicates and have not undergone complete replacement by phyllosilicates. The CM1 designation refers to samples which have undergone complete hydration, i.e, essentially no remaining primary silicates. The extent of aqueous alteration of the CM chondrites can be described by petrographic classification scale (Rubin et al. 2007) which is based on the abundances of index minerals such as olivine, phyllosilicates, tochilinite, Fe-Ni metal, and other primary and secondary phases to arrange chondrites from least (Type 2.9) to most (Type 2.0) altered (Rubin et al. 2007). According to the Rubin et al. 2007 scale, meteorites with a CM2.0 classification are fully hydrated, corresponding to the CM1 designation used by other workers. In this work, we refer to fully-hydrated CMs as CM1, and differentiate CM2 samples from 2.1 to 2.9 according to the Rubin petrologic scale when possible. Alternatively, the degree of alteration can also be characterized by the degree of hydration of the sample as determined using bulk analyses of the H (as H_2O/OH) and C content (Alexander et al. 2013).

The CI chondrites are a rare class of highly aqueously-altered meteorites, containing only 4 named members. They are composed nearly entirely of Mg-rich phyllosilicate matrix, with

minor occurrences of magnetites of various morphologies, sulfides (typically pyrrhotite), carbonates, and rare olivine and pyroxene fragments (Alfing et al. 2019; Endreß and Bischoff 1996). CI chondrites are genomict breccias which record relatively subtle mm-scale variability of various petrologic features, including the Fe content of the matrix, phosphate abundance, anhydrous silicate abundance, and calcite occurrence (Alfing et al. 2019). The CI chondrites are the most aqueously-altered meteorites discovered to date, but, paradoxically, have primitive non-volatile bulk elemental compositions similar to the composition of the solar photosphere (Lodders 2009; Palme et al. 2014).

Carbonate minerals such as calcite, aragonite, dolomite ($(Ca,Mg)(CO_3)_2$), and breunnerite ($(Mg,Fe,Mn,Ca)CO_3$) have emerged as useful tools to investigate the timing and chemistry of fluid activity on carbonaceous chondrite parent bodies. Carbonates precipitate directly from aqueous fluids, and as such record the chemistry of those fluids at the time of formation. Carbonates strongly fractionate Mn from Cr during formation, which allows them to be dated using the short-lived ^{53}Mn-^{53}Cr system (Brearley and Hutcheon 2002; Endress et al. 1996; Fujiya et al. 2012, 2019; Jilly et al. 2014; Jilly-Rehak et al. 2017; de Leuw et al. 2009; Petitat et al. 2009, 2011; Steele et al. 2017; Visser et al. 2020) to establish the timing of aqueous alteration and constrain the accretion time and size of the parent body. Studies of the oxygen and carbon isotopic compositions of carbonate minerals can provide insight into the sources of the fluid, the temperature of alteration, and the relative formation sequence of various secondary minerals. Measurements of carbonates can also be complemented by O isotopic studies of other secondary phases, such as magnetite. The combination of Mn-Cr dating and stable isotopic measurements has the potential to track the influence of various reservoirs and reactions in time.

Because carbonates in CI and CM meteorites are typically small, petrographically diverse, and challenging to separate from the bulk meteorite, measurements of their C, O, and Mn-Cr isotopic systematics are best performed in-situ at high spatial resolution. Typically, these analyses are performed using secondary ion mass spectrometry (SIMS, or ion microprobe), a technique which focuses a beam of ions (typically Cs^+ or O_x^-) to a small diameter, which is then used to sputter and ionize small volumes of material from the sample of interest. Using this method, only the desired region is sampled, preserving the complex petrographic context. The Cameca ims-1290 at UCLA is equipped with an Oregon Physics Hyperion-II oxygen plasma ion source (Liu et al. 2018), which allows high-precision measurements of the ^{53}Mn-^{53}Cr ages of carbonates to be performed on spot sizes <10 μm in diameter. In favorable circumstances, this high spatial resolution allows us to perform all three types of analysis on the same grains.

Review of previous studies of CM and CI carbonate

Oxygen isotopic systematics of carbonate and carbonaceous chondrites

Oxygen isotopic compositions are typically reported in delta notation as $\delta^{17}O$ and $\delta^{18}O$, which describes the $^{17}O/^{16}O$ and $^{18}O/^{16}O$ of the sample of interest relative to the O isotopic standard Standard Mean Ocean Water (SMOW) in parts per mil as:

$$\delta^{x}O = \left(\left(\frac{^{x}O}{^{16}O}_{sample} \Big/ \frac{^{x}O}{^{16}O}_{SMOW}\right) - 1\right) \times 1000 \qquad (1.1)$$

where ^{x}O represents either ^{17}O or ^{18}O, and the values for $^{x}O/^{16}O_{SMOW}$ are $^{17}O/^{16}O = 0.00038288$ and $^{18}O/^{16}O$ are 0.0020052. In a plot of $\delta^{17}O$ versus $\delta^{18}O$ (Figure 1.1), samples from a single O isotopic reservoir plot along a line with a slope of ~0.52, reflecting changes in $\delta^{18}O$ and $\delta^{17}O$ by mass-dependent fractionation of the reservoir. For the terrestrial reservoir, this line is known as the Terrestrial Fractionation Line (TFL) and is shown in Figures 1.1 and 1.2 for comparison with

extraterrestrial samples. Solar system materials often exhibit mass-independent variations relative to the TFL (Chaumard et al. 2021; Choi et al. 1998; Clayton and Mayeda 1984, 1999; Clayton et al. 1973; Kobayashi et al. 2003; MacPherson 2014; Rowe et al. 1994; Sakamoto et al. 2007; Scott and Krot 2014), and the vertical deviation (i.e., relative enrichment or depletion in ^{16}O relative to ^{17}O and ^{18}O) from the TFL can be described as $\Delta^{17}O = \delta^{17}O - 0.52 \times \delta^{18}O$.

The O isotopic compositions of carbonaceous chondrites and their components have been extensively investigated. As illustrated in Figure 1.1a, unaltered nebular solids such as chondrules and CAIs plot along a line with a slope ~1 (e.g. MacPherson 2014; Scott and Krot 2014), with a ^{16}O-rich (low $\Delta^{17}O$) end member inferred to be the solar composition by measurements of captured solar wind (McKeegan et al. 2011), and the $^{17,18}O$ rich (high $\Delta^{17}O$) end member inferred to be nebular water (Clayton and Mayeda 1984; Sakamoto et al. 2007). Variations in $\Delta^{17}O$ between these nebular components reflect the relative degree of mixing between ^{16}O-rich and $^{17,18}O$ rich reservoirs at the location and time of their formation.

Figure 1.1 Oxygen isotopic compositions of a.) solar system materials relative to SMOW (see text), (b) bulk CM and CI meteorites and and secondary minerals produced by aqueous alteration. The terrestrial fractionation line (TFL) and carbonaceous chondrite anhydrous material (CCAM) line are shown for reference.

a)

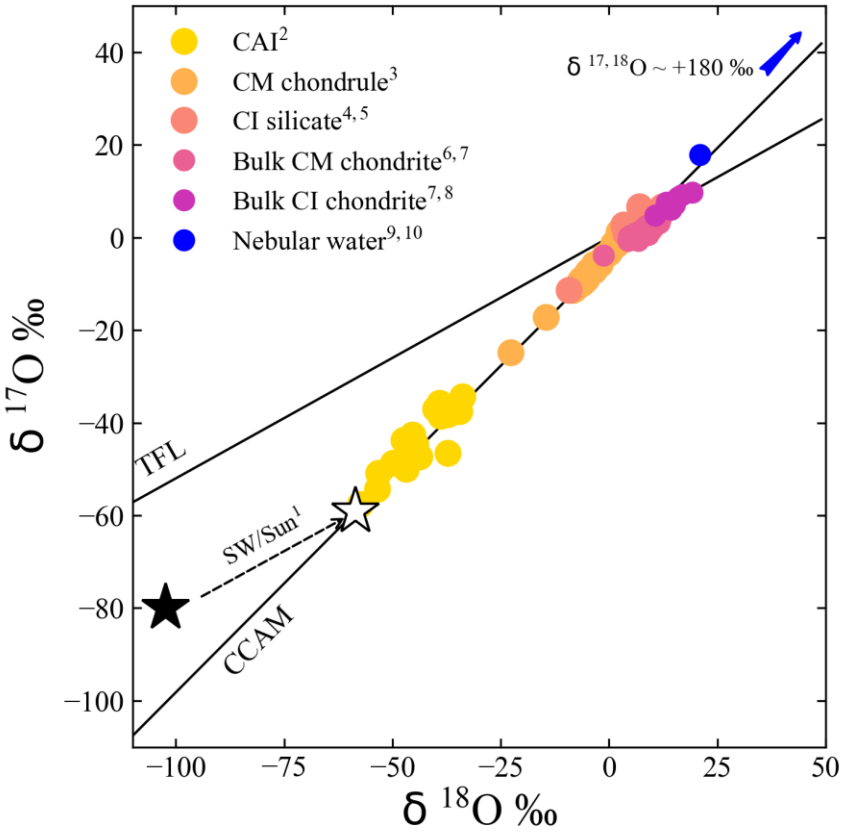

b)

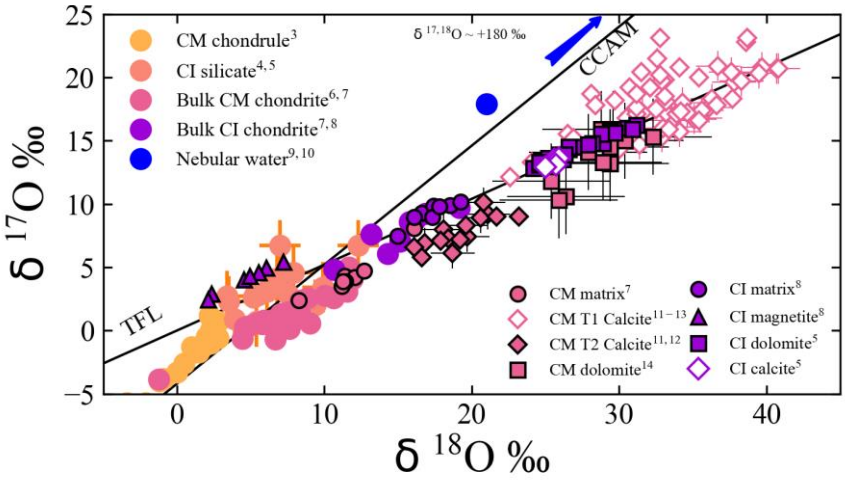

[1](McKeegan et al. 2011) [2](Liu et al. 2009) [3](Chaumard et al. 2021) [4](Leshin et al. 1997) [5](Piralla et al. 2020) [6](Clayton and Mayeda 1984) [7](Clayton and Mayeda 1999) [8](Rowe et al. 1994) [9](Choi et al. 1998) [10](Sakamoto et al. 2007) [11](Tyra et al. 2012) [12](Verdier-Paoletti et al. 2017) [13](Vacher et al. 2017) [14](Tyra et al. 2016)

The CM and CI parent bodies accreted mixtures of ^{16}O-rich anhydrous minerals and ^{17,18}O rich ices, therefore the Δ^{17}O of the secondary minerals produced during aqueous alteration reflects the degree of equilibration between water and silicate when the secondary mineral formed. The bulk compositions of CM and CI chondrites have higher Δ^{17}O than the anhydrous materials from which they accreted due to isotopic exchange between silicate and water during phyllosilicate formation (Figure 1.1). Secondary minerals with even higher Δ^{17}O, such as magnetite (Choi et al. 1998; Rowe et al. 1994) and CM calcite (Vacher et al. 2017; Verdier-Paoletti et al. 2017), precipitated from fluids that had exchanged relatively little of their oxygen with silicate. By measuring the Δ^{17}O of various secondary minerals in carbonaceous chondrites, it is possible to reconstruct the sequence of alteration and fluid evolution by arranging secondary phases into early-forming assemblages with high Δ^{17}O to progressively later-forming assemblages with lower Δ^{17}O.

The mass-dependent oxygen isotopic fractionation between a secondary mineral and the fluid from which it forms is temperature-dependent, so that if the compositions of the fluid and the secondary phase are known, the temperature of formation can be calculated directly (e.g. Hayles et al. 2018; Horita 2014; Kim and O'Neil 1997; Zheng 1995). If the fluid's composition is unknown, as is typically the case for carbonaceous chondrites, the formation temperature can still be constrained if two secondary phases (e.g. magnetite, phyllosilicate, carbonate) which formed in equilibrium with one another from fluid with the same Δ^{17}O can be identified. The difference in δ^{18}O between the two phases can then be used to calculate an equilibrium formation temperature under the assumption that both phases precipitated simultaneously from identical water compositions. Formation temperatures of matrix phyllosilicates, carbonates, and magnetite found to have identical Δ^{17}O have been calculated for both CM and CI chondrites. In the CI

chondrites, temperatures of aqueous alteration have been estimated to be ~50-150 °C based upon the bulk compositions of matrix phyllosilicate and carbonate (Clayton and Mayeda 1999; Leshin et al. 1997; Rowe et al. 1994), which have similar $\Delta^{17}O$. Equilibrium between magnetite and dolomite in a CM1 chondrite has been used to constrain alteration temperatures to 125 ± 60 °C (Telus et al. 2019).

The less-altered CM2 chondrites typically do not contain other minerals in equilibrium with Ca-carbonate, so estimates of their formation temperatures require assumptions to be made regarding the initial abundances and compositions of anhydrous materials and water so that mass-balance calculations can be performed to estimate the water composition at the time of carbonate formation. Studies of Ca-carbonate in CM2 chondrites have determined a variety of formation temperatures ranging from <25 °C (Clayton and Mayeda 1984, 1999) to >100 °C (Verdier-Paoletti et al. 2017).

In-situ studies of Ca-carbonate in the CM chondrites have identified several populations of calcite and aragonite which formed at different stages of fluid alteration. 'Type 1 Calcite' is found as small isolated Mn-poor grains in the matrix, and is high in $\Delta^{17}O$ (approx. −1 to + 2 ‰) and $\delta^{18}O$. By its petrography and relative enrichment in $^{17,18}O$, Type 1 calcite has been inferred to have formed by fill in pore spaces during the early stages of aqueous alteration (Lee et al. 2013, 2014, Tyra et al. 2012, 2016; Vacher et al. 2017). 'Type 2 Calcite' contains Mn, is found pseudomorphing chondrules and as large aggregates, and has lower $\Delta^{17}O$ (~ −2 ‰) and $\delta^{18}O$ (Lee et al. 2014; Tyra et al. 2012, 2016). Type 2 calcite is inferred to have formed in a later stage of aqueous alteration, after substantial equilibration of the fluid and rock had occurred and more anhydrous minerals were altered to phyllosilicates. Type 1 calcite is commonly found in the least-altered CMs, with the relative abundance of Type 2 calcite increasing as the degree of

alteration increases (Lee et al. 2014). These two populations with different $\Delta^{17}O$ are often found within the same meteorite, so that the O isotopic compositions of Ca-carbonate in a single sample plot along a line with a slope > 0.52, reflecting an evolution of the O isotopic reservoir during Ca-carbonate precipitation and suggesting closed-system behavior without substantial fluid flow (Fujiya et al. 2015; Telus et al. 2019; Vacher et al. 2017; Verdier-Paoletti et al. 2017). However, many of the features of the O isotopic compositions of CM and CI chondrites can also be formed during large-scale fluid flow (Young 2001; Young et al. 1999), and images of large veins of carbonate on asteroid Bennu provide petrographic evidence that some C-type asteroids experienced extensive fluid flow (Kaplan et al. 2020).

In-situ studies of dolomite and calcite in the CI chondrites show that they formed with homogeneous $\Delta^{17}O \sim 0$, within error of matrix phyllosilicates (Clayton and Mayeda 1999; Piralla et al. 2020; Rowe et al. 1994). CI magnetite has higher $\Delta^{17}O$ than carbonate or phyllosilicate (Rowe et al. 1994), indicating that it formed earlier when the fluid was less equilibrated with silicate.

Overall, the O isotopic systematics of carbonate in carbonaceous chondrites record complex alteration sequences and a variety of environments. Their O isotopic compositions are often related to the petrology of the carbonate, necessitating careful petrographic study prior to in-situ analysis.

Carbon isotopic systematics of meteoric carbonate

Carbon isotopic compositions of carbonates and other materials are reported in delta notation ($\delta^{13}C$), which describes the $^{13}C/^{12}C$ of the sample relative to the C isotopic standard Vienna Pee Dee Belemnite (VPDB) in parts per mil as:

$$\delta^{13}C = \left(\left(\frac{^{13}C}{^{12}C}_{sample} \Big/ \frac{^{13}C}{^{12}C}_{VPDB} \right) - 1 \right) \times 1000 \qquad (1.2)$$

where the value of $^{13}C/^{12}C_{VPDB}$ in Equation 1.2 is defined as 0.01118. The ranges of carbon isotopic compositions of a variety of solar system materials, including the Sun, the solar wind, organic matter in meteorites, carbonates from the CM chondrites, and cometary CO_2 ice are summarized in Figure 1.2.

As shown in Figure 1.2, the carbon isotopic compositions of carbonates (black and yellow lines) are highly variable and are enriched in ^{13}C compared to the Sun (dotted black lines) and the organic matter found in meteorites (pink lines and symbols). These compositions are diverse even within a single thin section of a meteorite, suggesting that they record the local contributions of various C sources to the fluids, including ^{13}C-rich CO_2 ice (Fujiya et al. 2019, 2020; Hässig et al. 2017), ^{13}C-poor organic matter (Alexander et al. 2007; Gilmour 2014; Sephton et al. 2000), and isotopically anomalous presolar graphites and SiC grains (Hynes and Gyngard 2009). Reactions within the fluid, such as progressive oxidation and incorporation of ^{13}C-poor organic matter (Fujiya et al. 2015; Vacher et al. 2017) and CO_2-CH_4 equilibrium in the fluid at various temperatures (Alexander et al. 2015; Telus et al. 2019) can also shift the C isotopic composition of the fluid and explain the broad range of carbonate $\delta^{13}C$ compositions.

In principle, the fluid's $\delta^{13}C$ composition can also be altered by methane release accompanying serpentinization. Petrographic observations show that as anhydrous silicates interact with water during serpentinization, they are converted to phyllosilicates and magnetite as:

$$6(Mg,Fe)_2SiO_4 + 7H_2O \rightarrow 3(Mg,Fe)_3Si_2O_5(OH)_4 + Fe_3O_4 + H_2 \qquad (1.3)$$

also releasing H_2 into the fluid (Andreani et al. 2007). The H_2 can react with dissolved carbonate in the fluid ((Horita and Berndt 1999):

$$HCO_3^- + 4H_2 \rightarrow CH_4 + OH^- + 2H_2O \quad (1.4)$$

to produce methane gas. This reaction produces ^{13}C-poor methane, driving the carbon isotopic composition of the fluid to heavier values. This process predicts that carbonate from more-altered samples, or carbonate forming in a later stage of aqueous alteration, should be isotopically heavier than carbonates whose parent fluids had not yet undergone methane release. This relationship has been observed in some studies of CM carbonate (Guo and Eiler 2007; Telus et al. 2019; Tyra et al. 2016; Vacher et al. 2018), but not in others (Alexander et al. 2015; Fujiya et al. 2015, 2019, 2020; Vacher et al. 2017), reflecting diversity in the processes occurring during the fluid evolution on the CM chondrite parent body.

Because the C isotopic compositions of carbonates are heterogenous and reflect contributions from diverse processes and reservoirs, it is important to determine their systematics (e.g., petrographic setting, temperature, formation sequence, or timing) for each meteorite sample to clarify which of these processes were most important during the phases of alteration recorded by each meteorite.

Figure 1.2. Carbon isotopic compositions of solar system materials relative to VPDB ($^{13}C/^{12}C$ = 0.011180). The local ISM refers to the local interstellar medium. SOM and IOM refers to soluble and insoluble organic matter found in meteorites. Carbon isotopic compositions of calcium carbonates (abbreviated CC, black solid lines) and dolomites (abbreviated Dol, yellow lines) are listed in increasing order of the extent of aqueous alteration of their host meteorite [1](Casassus et al. 2005), [2](Hässig et al. 2017), [3](Vacher et al. 2017), [4](Fujiya et al. 2020), [5](Fujiya et al. 2019), [6](Telus et al. 2019), [7](Tyra et al. 2016), [8](Sephton et al. 2000), [9](Alexander et al. 2007), [10](Deines 2002), [11](Coplen 1994), [12](Keeling et al. 2001), [13](Schidlowski et al. 1983) [14](Lyons et al. 2018), [15](Hashizume et al. 2004)

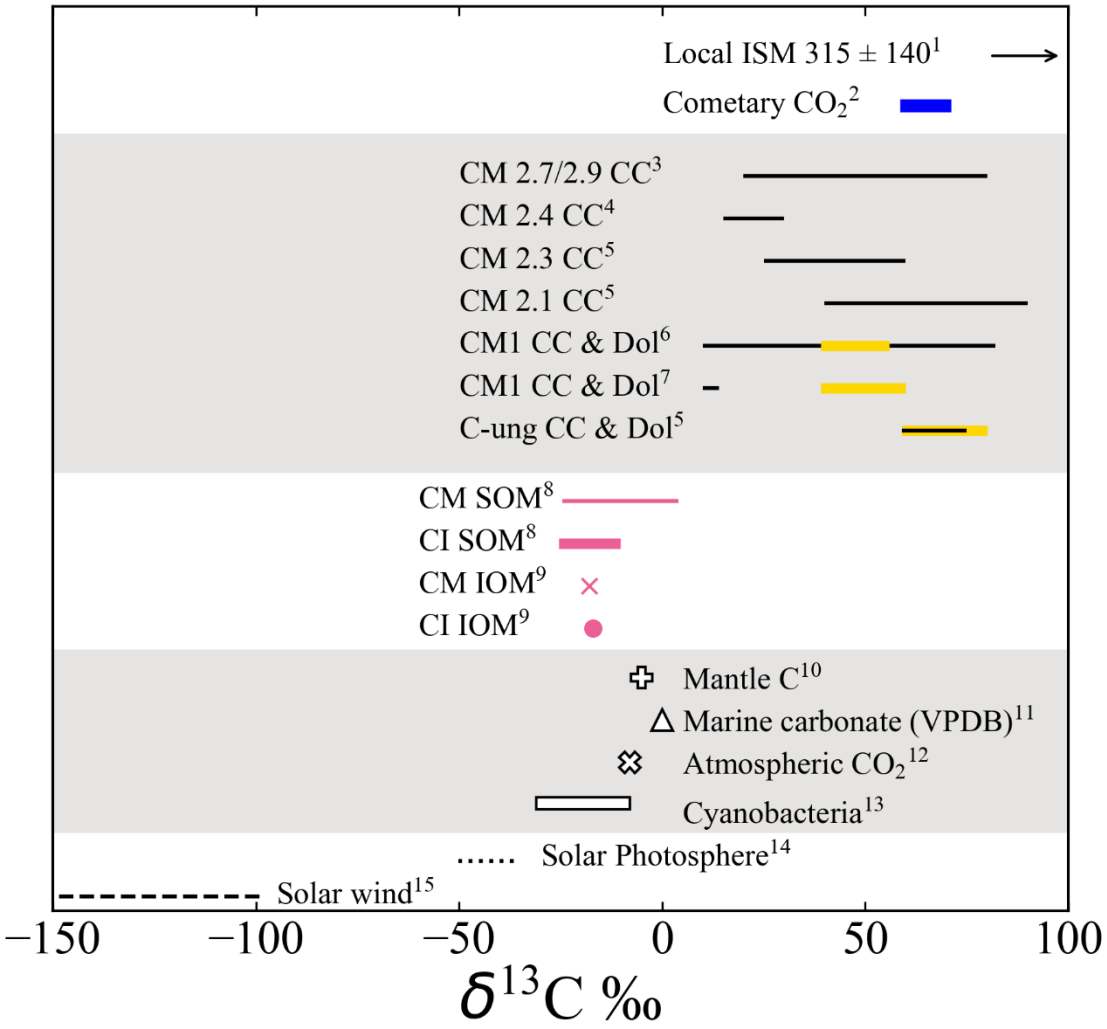

Dating carbonate using the ^{53}Mn-^{53}Cr system

In addition to their ability to track the isotopic composition of the fluid, carbonates are some of the only phases in highly aqueously altered meteorites that can be used for radiometric dating. Igneous materials frequently used to date nebular processes or establish the accretion timescales of chondrites, such as CAIs and chondrules, are partially or completely pseudomorphed to phyllosilicate in the CM chondrites and are practically absent in the CI chondrites, rendering them less useful for radiometric dating than in other meteorite classes. Rather than recording nebular events, carbonate records the time at which it precipitated from the fluid, directly constraining the timing and duration of hydrothermal activity on meteorite parent bodies.

Carbonate in meteorites can be dated using the short-lived ^{53}Mn-^{53}Cr chronometer. ^{53}Mn was present in the early solar system at an initial $^{53}Mn/^{55}Mn$ estimated at $6.71 \pm 0.56 \times 10^{-6}$ (Amelin et al. 2010; Brennecka and Wadhwa 2012; Connelly et al. 2012; Davis and McKeegan 2014; Glavin et al. 2004), and decays to ^{53}Cr with a half-life of 3.7 million years, making it suitable for dating events which took place within the first ~20 million years of Solar System history. Carbonates strongly fractionate Mn from Cr when they form, as the carbonate crystal structure accommodates 2+ ions including Mn^{2+} while strongly excluding 3+ ions such as Cr^{3+}. Carbonates forming when ^{53}Mn was present in the early solar system exhibit large excesses in the abundance of ^{53}Cr, which can be expressed either as the ratio of $^{53}Cr/^{52}Cr$ or as δ^{53}Cr, the parts per mil relative to the chondritic $^{53}Cr/^{52}Cr$ ratio of 0.113459 (Papanastassiou 1986):

$$\delta^{53}Cr = \left(\left(\frac{^{53}Cr}{^{52}Cr}_{sample} \Big/ \frac{^{53}Cr}{^{52}Cr}_{chondritic} \right) - 1 \right) \times 1000 \qquad (1.5)$$

where $^{53}Cr/^{52}Cr_{sample}$ represents the $^{53}Cr/^{52}Cr$ measured in the sample of interest.

Because ^{53}Mn has long since decayed to ^{53}Cr, the initial ^{53}Mn/^{55}Mn ratio present when the carbonate was formed can be inferred by measuring carbonate with various Mn contents and plotting the ^{53}Cr/^{52}Cr ratio against the ^{55}Mn/^{52}Cr ratio and determining the slope of the isochron. This inferred initial ^{53}Mn/^{55}Mn must then be 'anchored' to a sample which has a well-established initial ^{53}Mn/^{55}Mn and absolute age determined by Pb-Pb dating to calculate a relative age for the carbonate assuming a homogeneous distribution of ^{53}Mn in the early solar system (Davis and McKeegan 2014; Trinquier et al. 2008). For the ^{53}Mn-^{53}Cr system, the anchor sample is D'Orbigny, an angrite meteorite with an initial of ^{53}Mn/^{55}Mn 3.54×10^{-6} (McKibbin et al. 2015) and a Pb-Pb closure age of 4563.4 Ma (Amelin 2008; Brennecka and Wadhwa 2012). The age of a carbonate ($T_{carbonate}$) can be calculated using Equation 1.6 as:

$$T_{carbonate} = T_{anchor} + \frac{1}{\lambda} \times \ln\left[\left(^{53}Mn/^{55}Mn\right)_{carbonate} \Big/ \left(^{53}Mn/^{55}Mn\right)_{anchor}\right] \qquad (1.6)$$

where T_{anchor} is the Pb-Pb closure age of D'Orbigny, λ is the decay constant of ^{53}Mn, $(^{53}Mn/^{55}Mn)_{carbonate}$ is the slope of the isochron, and $(^{53}Mn/^{55}Mn)_{anchor}$ is the initial ^{53}Mn/^{55}Mn of D'Orbigny. These ages can also be expressed relative to the origin of the solar system as defined by the ^{207}Pb/^{206}Pb closure age for CAIs of 4567.3 Ma (Amelin et al. 2010) by subtracting the carbonate age from the CAI age.

The ^{53}Mn-^{53}Cr chronometer has been applied to calcite, dolomite, and breunnerite in CI and CM chondrites (Bischoff et al. 2021; Endress et al. 1996; Fujiya et al. 2012, 2013; Jilly et al. 2014; Petitat et al. 2009, 2011; Visser et al. 2020). Early studies of CI chondrite carbonate showed that carbonate formation began within the first 20 million years after CAI formation (Endress et al. 1996), and that dolomite formed ~3 million years after CAI formation, with breunnerite forming after a gap of ~7 million years, necessitating some method of sustaining or

restarting alteration long after internal heating from radioactive decay of ^{26}Al had ceased (Petitat et al. 2009, 2011). Other studies have found that calcite and dolomite in the CM and CI chondrites formed nearly contemporaneously, with most carbonate forming 4−6 million years after CAI formation (Fujiya et al. 2012, 2013; Jilly et al. 2014; Visser et al. 2020).

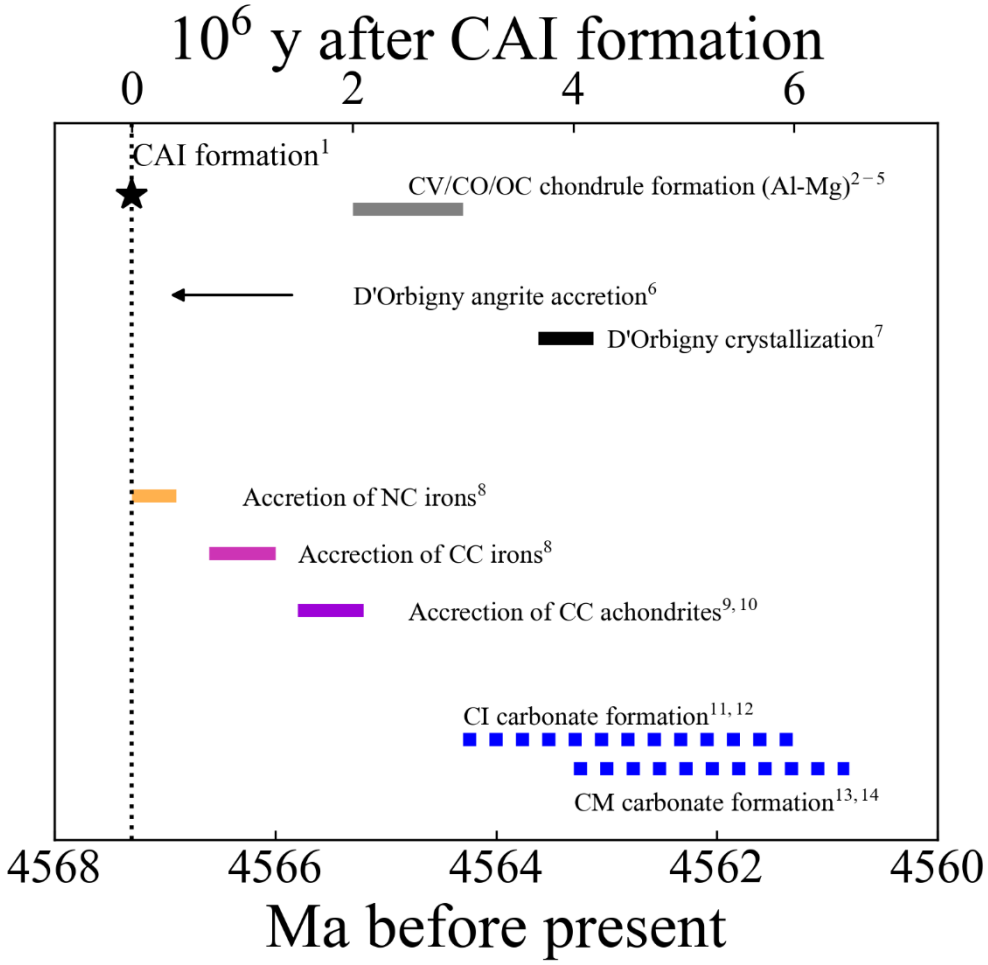

Figure 1.3. Summary of the formation timescales of CI and CM carbonate, compared with other solar system materials. [1](Amelin et al. 2010), [2](Kita and Ushikubo 2012), [3](Kunihiro et al. 2004), [4](Nagashima et al. 2017), [5](Pape et al. 2019), [6](Zhu et al. 2019), [7](Brennecka and Wadhwa 2012), [8](Kruijer et al. 2017), [9](Sanborn et al. 2019), [10](Sugiura and Fujiya 2014) [11](Fujiya et al. 2013), [12](Visser et al. 2020), [13](Fujiya et al. 2013), [14](Jilly et al. 2014).

Constraining parent body characteristics using Mn-Cr dating

Carbonate formation ages can be used to infer the size of the parent body and the time at which it accreted. Figure 1.4 illustrates a schematic view of the peak temperature reached by a parent body accreting at a given time and size. The parent body can be composed of various fractions of chondritic rock and water ice and is heated by the decay of ^{26}Al ($t_{1/2}$ = 0.73 million years) and ^{60}Fe ($t_{1/2}$ = 2.62 million years). ^{26}Al and ^{60}Fe have initial abundances of ^{26}Al/^{27}Al of 5.2×10^{-5} (Jacobsen et al. 2008; MacPherson et al. 2010, 2012; Wasserburg et al. 2012) and ^{60}Fe/^{56}Fe of 1.0×10^{-8} (Tang and Dauphas 2012). We assume chondritic concentrations of ^{27}Al and ^{56}Fe in the rock fraction of 11.8×10^{-3} g Al and 0.211 g Fe per g of rock (Kallemeyn and Wasson 1981; Zhou et al. 2013). The abundances of ^{26}Al and ^{60}Fe are reduced according to the time after CAI formation at which the parent body is accreted, according to their respective half-lives. The model accounts for heating or cooling due to the phase transitions of water and silicate. For parent bodies which reach temperatures high enough to melt silicates, the model accounts for increased heat flux due to convection of silicate melt by enhancing the thermal diffusivity (κ, m^2/s) of the silicate portions of the body by the Nusselt number $Nu_{silicate}$, where $Nu_{silicate}$ is the ratio of actual heat transfer to purely conductive heat transfer such that $\kappa_{actual} = Nu_{silicate}(\kappa)$, with $Nu_{silicate} = 100$ (Zhou et al. 2013).

This version of the thermal model does not incorporate the effect of enhanced heat transport to the surface caused by convection of liquid water, which may occur in large planetesimals (Bland and Travis 2017; Young et al. 2003). We tested the significance of convective heat transport upon the maximum temperature reached by a parent body by enhancing the thermal diffusivity for a large (100-km radius), water-rich planetesimal by the Nusselt number Nu_{water}, where Nu_{water} is the ratio of actual heat transfer to purely conductive heat

transfer such that $\kappa_{actual} = Nu_{water}(\kappa)$. We determine $Nu_{water} = 6$ following the prescription for convection in a fluid-saturated porous medium (Otero et al. 2004), with a critical Rayleigh number of 183.91 derived from a study of pore water convection in carbonaceous chondrite parent bodies (Young et al. 2003). While this sixfold enhancement in the thermal diffusivity affected the later cooling history of the body, the effect upon the maximum temperature reached by the parent body was very small. We therefore disregarded the effect of convection of liquid water for this application.

A suitable parent body for carbonate formation must be sufficiently warm to melt water ice (excluding parent bodies marked with the "Water Unmelted" label, and shaded grey) without becoming so warm as to vaporize the water, dehydrate phyllosilicates, or violate the temperatures of formation determined by O isotope thermometry at the time of carbonate formation ("Inconsistent with O isotopic thermometry" label with dark shading Figure 1.4). In addition, it must maintain these temperatures for the duration of carbonate formation. Parent bodies which satisfy these conditions are limited to the band which lacks dark shading in Figure 1.4 (McCain et al. 2017; Zhou et al. 2013).

Under these constraints, and assuming heating only by the decay of ^{26}Al and ^{60}Fe, the parent body of the CM chondrites was inferred to have accreted 3.5 million years after CAI, and been > 60 km in diameter to maintain liquid water at appropriate temperatures until carbonate formation ceased (Fujiya et al. 2012). Following a similar procedure, the CI chondrite parent body was inferred to have accreted 3−3.9 million years after CAI formation, and to have been >100 km in diameter to have sustained liquid water until breunnerite formation at >10 million years after CAI formation (Fujiya et al. 2013; Petitat et al. 2009).

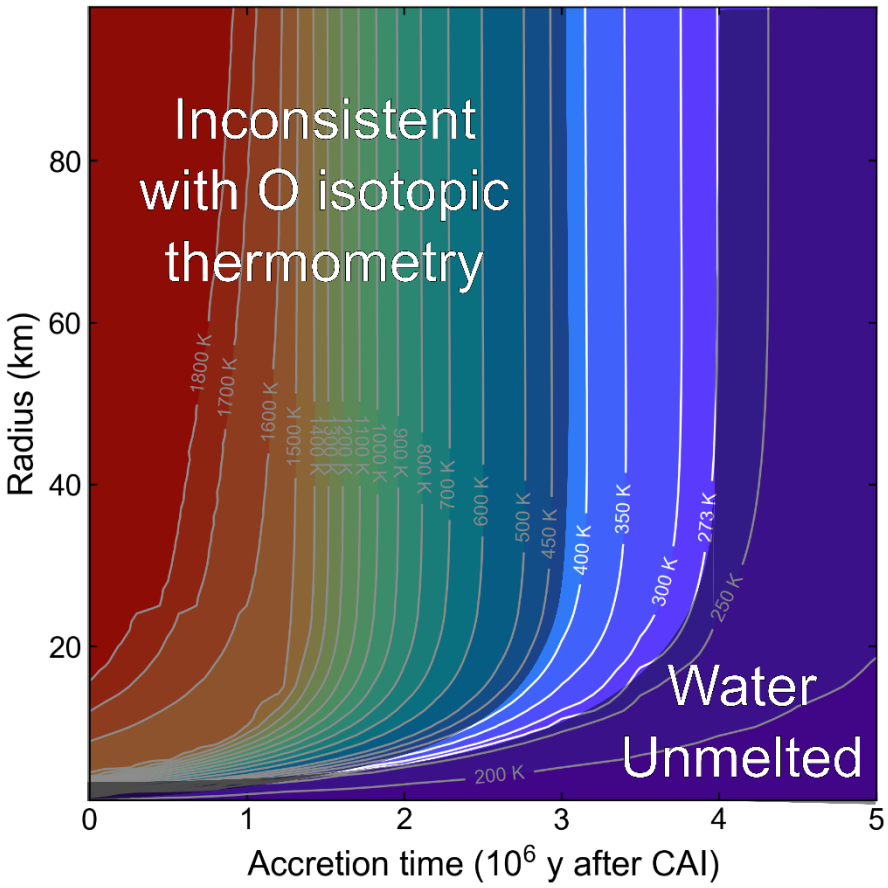

Figure 1.4. Maximum temperature (K) reached in a parent body accreting at a particular radius and time (in million years) after CAI formation. The parent body is composed of 25% water ice and 75% chondritic silicate. Suitable parent bodies for liquid water and carbonate formation should fall between the shaded bands to melt water ice and maintain consistency with oxygen isotopic thermometry.

Challenges associated with in-situ measurements: Matrix effects

In-situ measurements of carbonate are a powerful tool to understand the fluid systems present in the early solar system, but ion probe analyses pose challenges due to changes in instrumental discrimination factors that correlate with the chemical composition of the target carbonate in ways that are difficult to predict, a phenomenon generally known as "matrix effects". In practice, these effects are characterized empirically by analyzing standards with known chemical and isotopic compositions. Accurate stable isotopic analyses require quantification of the instrumental mass fractionation (IMF) on a reference material (or, 'standard') with similar Mg and Fe content to the target of interest (e.g. Rollion-Bard and Marin-Carbonne 2011; Śliwiński et al. 2016a, 2016b, 2017).

In addition to constraining the IMF to obtain accurate $^{53}Cr/^{52}Cr$ isotope ratios, Mn-Cr dating requires that the $^{55}Mn/^{52}Cr$ ratio be determined accurately. However, elemental ratios are challenging to measure by ion probe analysis, as the ion yields of different elements vary significantly based on the chemical composition of the target material—another 'matrix effect'. In practice, this effect is corrected empirically by connecting the true concentrations of the elements of interest (C_a and C_b) to the ratio of the intensities of the secondary ions produced by sputtering during the ion probe analysis (I_a and I_b) by using a relative sensitivity factor, or 'RSF'. The RSF may be defined as shown in Eq. 1.7.

$$RSF = \frac{C_a/C_b}{I_a/I_b} \qquad (1.7)$$

We note that some other studies define the RSF as the reciprocal of Eq. 1.7 (Donohue et al. 2018; Doyle et al. 2016; Sugiura and Ichimura 2010).

The RSF can be determined empirically by analyzing a standard material for which the concentrations of the target elements are known and homogeneous. In the case of the Mn/Cr ratio in carbonate minerals, such reference materials do not exist in nature as terrestrial carbonates contain too little Cr to be used as a suitable standard. Early SIMS studies used San Carlos Olivine as a proxy standard for determining the Mn/Cr RSF, since it is readily available and contains sufficient Mn and Cr for their abundances to be measured by electron probe microanalysis (EPMA) (de Leuw et al. 2009; Petitat et al. 2009, 2011). However, the accuracy of ages obtained using an olivine to quantify RSF in carbonate should be treated with caution due to matrix effects.

In an attempt to overcome this challenge, various workers have produced calcites doped with sufficient Mn and Cr so as to be suitable as standard for ^{53}Mn-^{53}Cr dating of calcite (Donohue et al. 2018, 2019; Sugiura and Ichimura 2010). However, EPMA analyses have shown that care must be taken as the concentrations of Mn and Cr in the doped synthetic calcites are spatially heterogeneous (Jilly et al. 2014). Compounding the problem of producing appropriate matrix-matched standards is the fact that dolomite is notoriously challenging to synthesize in a laboratory setting despite its ubiquitous presence in the terrestrial geologic record (e.g. Usdowski 2009), and attempts to synthesize Cr-enriched dolomite have not been successful (Donohue et al. 2018). As a result, many previous studies of meteoritic carbonate were performed using RSF values determined on materials which did not closely match the chemistry of the target carbonate minerals (e.g. calcite or olivine), leaving these analyses susceptible to inaccuracies due to matrix effects (Fujiya et al. 2012, 2013; Jilly et al. 2014; Visser et al. 2020). In fact, prior to this work, no matrix-matched measurements of the ^{53}Mn-^{53}Cr ages of dolomite or breunnerite had been performed.

As an alternative to synthetic or naturally occurring RSF reference materials, Cr can be implanted into natural minerals using ion accelerators with excellent lateral homogeneity (Burnett et al. 2015). Attempts to apply this technique to carbonate revealed that dolomite, breunnerite, and calcite have different RSF values for Mn/Cr (Steele et al. 2017), and that measurements of dolomite and breunnerite using calcite standards are likely to be systematically biased towards younger ages (that is, forming later in the solar system's history) due to the matrix mismatch. By referencing Figure 1.4, we can see that the >30 km radius parent bodies previously inferred for the CM and CI parent bodies become unsuitable for carbonate formation if they accrete before ~3 million years after CAI, as they reach higher temperatures than predicted by the matrix mineralogy and O isotopic systematics. Depending on the degree to which updated RSF values shift the timing of carbonate formation, the size of parent body required to produce this carbonate could also shift.

Because the RSF for the Mn-Cr analysis is sensitive to the analytical conditions used to perform the analysis, it is generally not possible to correct ages acquired using matrix mismatched standards *post hoc*. Rather, new measurements of the Mn-Cr ages of carbonates should be performed using appropriate matrix-matched standards. By leveraging recent improvements in the understanding of matrix effects in carbonate and the improved spatial resolution afforded by the Cameca ims-1290 ion probe at UCLA and its Oregon Physics Hyperion II source, I aim to perform the first fully matrix-matched analyses of a range of carbonate minerals in carbonaceous chondrites, combining petrographic, stable isotopic, and Mn-Cr dating to constrain the timing of aqueous alteration, the source(s) of the fluids, the role of fluid flow, and the important reactions occurring in the fluid.

The thesis is organized as follows. In Chapter 2, I describe how ion implantation of $^{52}Cr^{+}$ ions into terrestrial carbonate can be used to create and calibrate matrix-matched standards for analysis of Mn-Cr ages in meteoritic carbonate. This work has been published in the Journal of Vacuum Science and Technology B (McCain et al. 2020). In Chapter 3, I apply these standards to a study of CM and CI chondrites, combining petrographic observations with measurements of C and O isotopic compositions and Mn-Cr dating. In Chapter 4, working with colleagues as part of the Phase 2 Curation Kochi Team, I extend these methods to a study of Mn-Cr ages and stable isotopic compositions of carbonate in samples returned from asteroid Ryugu by the efforts of JAXA's Hayabusa2 mission. Finally, in Chapter 5, I present a discussion of the general implications of this work and consider future directions for further study.

References

Alexander C. M. O., Fogel M., Yabuta H., and Cody G. D. 2007. The origin and evolution of chondrites recorded in the elemental and isotopic compositions of their macromolecular organic matter. *Geochimica et Cosmochimica Acta* 71:4380–4403. https://www.sciencedirect.com/science/article/pii/S001670370700395X.

Alexander C. M. O., Howard K. T., Bowden R., and Fogel M. L. 2013. The classification of CM and CR chondrites using bulk H, C and N abundances and isotopic compositions. *Geochimica et Cosmochimica Acta* 123:244–260. http://www.sciencedirect.com/science/article/pii/S0016703713002986.

Alexander C. M. O., Bowden R., Fogel M. L., and Howard K. T. 2015. Carbonate abundances and isotopic compositions in chondrites. *Meteoritics & Planetary Science* 50:810–833. http://onlinelibrary.wiley.com/doi/10.1111/maps.12410/abstract (Accessed October 14, 2015).

Alfing J., Patzek M., and Bischoff A. 2019. Modal abundances of coarse-grained (>5 μm) components within CI-chondrites and their individual clasts – Mixing of various lithologies on the CI parent body(ies). *Geochemistry* 79:125532. https://www.sciencedirect.com/science/article/pii/S0009281919300248.

Amelin Y. 2008. U–Pb ages of angrites. *Geochimica et Cosmochimica Acta* 72:221–232. https://www.sciencedirect.com/science/article/pii/S0016703707005820.

Amelin Y., Kaltenbach A., Iizuka T., Stirling C. H., Ireland T. R., Petaev M., and Jacobsen S. B. 2010. U-Pb chronology of the Solar System's oldest solids with variable 238U/235U. *Earth and Planetary Science Letters* 300:343–350. https://ui.adsabs.harvard.edu/abs/2010E&PSL.300..343A/abstract (Accessed April 5, 2022).

Andreani M., Mével C., Boullier A.-M., and Escartín J. 2007. Dynamic control on serpentine crystallization in veins: Constraints on hydration processes in oceanic peridotites. *Geochemistry, Geophysics, Geosystems* 8. https://onlinelibrary.wiley.com/doi/abs/10.1029/2006GC001373.

Bischoff A. et al. 2021. The old, unique C1 chondrite Flensburg – Insight into the first processes of aqueous alteration, brecciation, and the diversity of water-bearing parent bodies and lithologies. *Geochimica et Cosmochimica Acta* 293:142–186. https://www.sciencedirect.com/science/article/pii/S0016703720306463.

Bland P. A., and Travis B. J. 2017. Giant convecting mud balls of the early solar system. *Science Advances* 3:e1602514. http://advances.sciencemag.org/content/3/7/e1602514 (Accessed July 21, 2017).

Bradley J. P., and Brownlee D. E. 1991. An Interplanetary Dust Particle Linked Directly to Type CM Meteorites and an Asteroidal Origin. *Science* 251:549–552. http://www.jstor.org/stable/2875086.

Bradley J. P. 2014. 1.8 - Early Solar Nebula Grains – Interplanetary Dust Particles. In *Treatise on Geochemistry (Second Edition)*, edited by Holland H. D., and Turekian K. K. Oxford: Elsevier. pp. 287–308 https://www.sciencedirect.com/science/article/pii/B9780080959757001145.

Brearley A. J., and Hutcheon I. D. 2002. Carbonates in the Y791198 CM2 Chondrite: Zoning and Mn-Cr Systematics. *Meteoritics and Planetary Science Supplement* 37:23. http://adsabs.harvard.edu/abs/2002M%26PSA..37Q..23B (Accessed October 2, 2015).

Brennecka G. A., and Wadhwa M. 2012. Uranium isotope compositions of the basaltic angrite meteorites and the chronological implications for the early Solar System. *Proceedings of the National Academy of Sciences* 109:9299–9303. https://www.pnas.org/content/109/24/9299 (Accessed April 8, 2020).

Bunch T. E., and Chang S. 1980. Carbonaceous chondrites—II. Carbonaceous chondrite phyllosilicates and light element geochemistry as indicators of parent body processes and surface conditions. *Geochimica et Cosmochimica Acta* 44:1543–1577. https://www.sciencedirect.com/science/article/pii/0016703780901180.

Burnett D. S. et al. 2015. Ion Implants as Matrix-Appropriate Calibrators for Geochemical Ion Probe Analyses. *Geostandards and Geoanalytical Research* 39:265–276. https://onlinelibrary.wiley.com/doi/abs/10.1111/j.1751-908X.2014.00318.x.

Casassus S., Stahl O., and Wilson T. L. 2005. Interstellar C/C ratios through CH3957,4232 absorption in local clouds: incomplete mixing in the ISM. *Astronomy & Astrophysics* 441:181–194. https://www.aanda.org/articles/aa/abs/2005/37/aa2149-04/aa2149-04.html (Accessed April 20, 2022).

Chaumard N., Defouilloy C., Hertwig A. T., and Kita N. T. 2021. Oxygen isotope systematics of chondrules in the Paris CM2 chondrite: Indication for a single large formation region across snow line. *Geochimica et Cosmochimica Acta* 299:199–218. https://www.sciencedirect.com/science/article/pii/S0016703721000983.

Choi B.-G., McKeegan K. D., Krot A. N., and Wasson J. T. 1998. Extreme oxygen-isotope compositions in magnetite from unequilibrated ordinary chondrites. *Nature* 392:577–579. https://www.nature.com/articles/33356 (Accessed July 12, 2021).

Clayton R. N., Grossman L., and Mayeda T. K. 1973. A Component of Primitive Nuclear Composition in Carbonaceous Meteorites. *Science*. https://www.science.org/doi/abs/10.1126/science.182.4111.485 (Accessed May 6, 2022).

Clayton R. N., and Mayeda T. K. 1984. The oxygen isotope record in Murchison and other carbonaceous chondrites. *Earth and Planetary Science Letters* 67:151–161. http://www.sciencedirect.com/science/article/pii/0012821X84901109 (Accessed December 21, 2016).

Clayton R. N., and Mayeda T. K. 1999. Oxygen isotope studies of carbonaceous chondrites. *Geochimica et Cosmochimica Acta* 63:2089–2104.

http://www.sciencedirect.com/science/article/pii/S0016703799000903 (Accessed December 21, 2016).

Connelly J. N., Bizzarro M., Krot A. N., Nordlund Å., Wielandt D., and Ivanova M. A. 2012. The Absolute Chronology and Thermal Processing of Solids in the Solar Protoplanetary Disk. *Science*. https://www.science.org/doi/full/10.1126/science.1226919 (Accessed May 6, 2022).

Coplen T. B. 1994. Reporting of stable hydrogen, carbon, and oxygen isotopic abundances (Technical Report). *Pure and Applied Chemistry* 66:273–276. https://www.degruyter.com/document/doi/10.1351/pac199466020273/html (Accessed May 10, 2022).

Davis A. M., and McKeegan K. D. 2014. 1.11 - Short-Lived Radionuclides and Early Solar System Chronology. In *Treatise on Geochemistry (Second Edition)*, edited by Holland H. D., and Turekian K. K. Oxford: Elsevier. pp. 361–395 http://www.sciencedirect.com/science/article/pii/B9780080959757001133.

Deines P. 2002. The carbon isotope geochemistry of mantle xenoliths. *Earth-Science Reviews* 58:247–278. https://www.sciencedirect.com/science/article/pii/S0012825202000648.

DeMeo F. E., and Carry B. 2014. Solar System evolution from compositional mapping of the asteroid belt. *Nature* 505:629–634. https://www.nature.com/articles/nature12908 (Accessed April 25, 2022).

Donohue P. H., Huss G. R., and Nagashima K. 2018. Synthesizing Calcite and Dolomite for Mn/Cr Relative Sensitivity Corrections: A Progress Report. *Lunar and Planetary Science Conference* 1569. https://ui.adsabs.harvard.edu/abs/2018LPI....49.1569D/abstract (Accessed October 26, 2020).

Donohue P. H., Huss G. R., and Nagashima K. 2019. New Synthetic Carbonates for Investigation of Manganese-Chromium Chronology by Secondary Ion Mass Spectrometry. *Lunar and Planetary Science Conference* 1959. https://ui.adsabs.harvard.edu/abs/2019LPI....50.1959D/abstract (Accessed October 26, 2020).

Doyle P. M., Jogo K., Nagashima K., Huss G. R., and Krot A. N. 2016. Mn–Cr relative sensitivity factor in ferromagnesian olivines defined for SIMS measurements with a Cameca ims-1280 ion microprobe: Implications for dating secondary fayalite. *Geochimica et Cosmochimica Acta* 174:102–121. http://www.sciencedirect.com/science/article/pii/S001670371500592X (Accessed January 3, 2017).

Endreß M., and Bischoff A. 1996. Carbonates in CI chondrites: Clues to parent body evolution. *Geochimica et Cosmochimica Acta* 60:489–507. https://www.sciencedirect.com/science/article/pii/0016703795003991.

Endress M., Zinner E., and Bischoff A. 1996. Early aqueous activity on primitive meteorite parent bodies. *Nature* 379:701–703. https://www.nature.com/nature/journal/v379/n6567/abs/379701a0.html (Accessed July 4, 2017).

Fornasier S., Lantz C., Barucci M. A., and Lazzarin M. 2014. Aqueous alteration on main belt primitive asteroids: Results from visible spectroscopy. *Icarus* 233:163–178. http://www.sciencedirect.com/science/article/pii/S0019103514000712 (Accessed November 4, 2016).

Fuchs L. H., Olsen E., and Jensen K. J. 1973. Mineralogy, Mineral-Chemistry, and Composition of the Murchison (C2) Meteorite. http://repository.si.edu/xmlui/handle/10088/804 (Accessed May 11, 2022).

Fujiya W., Sugiura N., Hotta H., Ichimura K., and Sano Y. 2012. Evidence for the late formation of hydrous asteroids from young meteoritic carbonates. *Nature Communications* 3:627. http://www.nature.com/ncomms/journal/v3/n1/full/ncomms1635.html (Accessed October 2, 2015).

Fujiya W., Sugiura N., Sano Y., and Hiyagon H. 2013. Mn–Cr ages of dolomites in CI chondrites and the Tagish Lake ungrouped carbonaceous chondrite. *Earth and Planetary Science Letters* 362:130–142. http://www.sciencedirect.com/science/article/pii/S0012821X12006838 (Accessed October 2, 2015).

Fujiya W., Sugiura N., Marrocchi Y., Takahata N., Hoppe P., Shirai K., Sano Y., and Hiyagon H. 2015. Comprehensive study of carbon and oxygen isotopic compositions, trace element abundances, and cathodoluminescence intensities of calcite in the Murchison CM chondrite. *Geochimica et Cosmochimica Acta* 161:101–117. http://www.sciencedirect.com/science/article/pii/S0016703715002033 (Accessed March 8, 2017).

Fujiya W., Hoppe P., Ushikubo T., Fukuda K., Lindgren P., Lee M. R., Koike M., Shirai K., and Sano Y. 2019. Migration of D-type asteroids from the outer Solar System inferred from carbonate in meteorites. *Nature Astronomy* 1. https://www.nature.com/articles/s41550-019-0801-4 (Accessed July 26, 2019).

Fujiya W., Aoki Y., Ushikubo T., Hashizume K., and Yamaguchi A. 2020. Carbon isotopic evolution of aqueous fluids in CM chondrites: Clues from in-situ isotope analyses within calcite grains in Yamato-791198. *Geochimica et Cosmochimica Acta* 274:246–260. http://www.sciencedirect.com/science/article/pii/S0016703720301046.

Gaffey M. J., Burbine T. H., and Binzel R. P. 1993. Asteroid Spectroscopy: Progress and Perspectives. *Meteoritics* 28:161. https://ui.adsabs.harvard.edu/abs/1993Metic..28..161G/abstract (Accessed May 1, 2022).

Gilmour I. 2014. 1.5 - Structural and Isotopic Analysis of Organic Matter in Carbonaceous Chondrites. In *Treatise on Geochemistry (Second Edition)*, edited by Holland H. D., and

Turekian K. K. Oxford: Elsevier. pp. 215–233 https://www.sciencedirect.com/science/article/pii/B9780080959757001078.

Glavin D. P., Kubny A., Jagoutz E., and Lugmair G. W. 2004. Mn-Cr isotope systematics of the D'Orbigny angrite. *Meteoritics & Planetary Science* 39:693–700. https://onlinelibrary.wiley.com/doi/abs/10.1111/j.1945-5100.2004.tb00112.x.

Grady M. M., Graham A. L., Barber D. J., Aylmer D., Kurat G., Ntaflos T., Ott U., Palme H., and Spettel B. 1987. Yamato-82042: An unusual carbonaceous chondrite with CM affinities. 46:162–178. https://nipr.repo.nii.ac.jp/index.php?active_action=repository_view_main_item_detail&page_id=13&block_id=104&item_id=2131&item_no=1 (Accessed May 11, 2022).

Guo W., and Eiler J. M. 2007. Temperatures of aqueous alteration and evidence for methane generation on the parent bodies of the CM chondrites. *Geochimica et Cosmochimica Acta* 71:5565–5575. http://www.sciencedirect.com/science/article/pii/S0016703707004383 (Accessed October 8, 2015).

Hashizume K., Chaussidon M., Marty B., and Terada K. 2004. Protosolar Carbon Isotopic Composition: Implications for the Origin of Meteoritic Organics. *The Astrophysical Journal* 600:480. https://iopscience.iop.org/article/10.1086/379637/meta (Accessed May 5, 2022).

Hässig M. et al. 2017. Isotopic composition of CO2 in the coma of 67P/Churyumov-Gerasimenko measured with ROSINA/DFMS. *Astronomy & Astrophysics* 605:A50. https://www.aanda.org/articles/aa/abs/2017/09/aa30140-16/aa30140-16.html (Accessed February 1, 2022).

Hayles J., Gao C., Cao X., Liu Y., and Bao H. 2018. Theoretical calibration of the triple oxygen isotope thermometer. *Geochimica et Cosmochimica Acta* 235:237–245. https://www.sciencedirect.com/science/article/pii/S0016703718303120.

Hewins R. H. et al. 2014. The Paris meteorite, the least altered CM chondrite so far. *Geochimica et Cosmochimica Acta* 124:190–222. https://www.sciencedirect.com/science/article/pii/S0016703713005139.

Horita J., and Berndt M. E. 1999. Abiogenic Methane Formation and Isotopic Fractionation Under Hydrothermal Conditions. *Science*. https://www.science.org/doi/full/10.1126/science.285.5430.1055 (Accessed May 6, 2022).

Horita J. 2014. Oxygen and carbon isotope fractionation in the system dolomite–water–CO2 to elevated temperatures. *Geochimica et Cosmochimica Acta* 129:111–124. https://www.sciencedirect.com/science/article/pii/S0016703713007230.

Hynes K. M., and Gyngard F. 2009. The Presolar Grain Database: http://presolar.wustl.edu/~pgd. *40th Annual Lunar and Planetary Science Conference*

1198. https://ui.adsabs.harvard.edu/abs/2009LPI....40.1198H/abstract (Accessed May 4, 2022).

Jacobsen B., Yin Q., Moynier F., Amelin Y., Krot A. N., Nagashima K., Hutcheon I. D., and Palme H. 2008. 26Al–26Mg and 207Pb–206Pb systematics of Allende CAIs: Canonical solar initial 26Al/27Al ratio reinstated. *Earth and Planetary Science Letters* 272:353–364. https://www.sciencedirect.com/science/article/pii/S0012821X0800318X.

Jilly C. E., Huss G. R., Krot A. N., Nagashima K., Yin Q.-Z., and Sugiura N. 2014. 53Mn-53Cr dating of aqueously formed carbonates in the CM2 lithology of the Sutter's Mill carbonaceous chondrite. *Meteoritics & Planetary Science* 49:2104–2117. http://onlinelibrary.wiley.com/doi/10.1111/maps.12305/abstract (Accessed December 7, 2015).

Jilly-Rehak C. E., Huss G. R., and Nagashima K. 2017. 53Mn–53Cr radiometric dating of secondary carbonates in CR chondrites: Timescales for parent body aqueous alteration. *Geochimica et Cosmochimica Acta* 201:224–244. http://www.sciencedirect.com/science/article/pii/S0016703716304938.

Kallemeyn G. W., and Wasson J. T. 1981. The compositional classification of chondrites—I. The carbonaceous chondrite groups. *Geochimica et Cosmochimica Acta* 45:1217–1230. https://www.sciencedirect.com/science/article/pii/0016703781901459.

Kaplan H. H. et al. 2020. Bright carbonate veins on asteroid (101955) Bennu: Implications for aqueous alteration history. *Science*. https://science.sciencemag.org/content/early/2020/10/07/science.abc3557 (Accessed October 16, 2020).

Keeling C. D., Piper S. C., Bacastow R. B., Wahlen M., Whorf T. P., Heimann M., and Meijer H. A. 2001. Exchanges of Atmospheric CO2 and 13CO2 with the Terrestrial Biosphere and Oceans from 1978 to 2000. I. Global Aspects. https://escholarship.org/uc/item/09v319r9 (Accessed May 10, 2022).

Kim S.-T., and O'Neil J. R. 1997. Equilibrium and nonequilibrium oxygen isotope effects in synthetic carbonates. *Geochimica et Cosmochimica Acta* 61:3461–3475. http://www.sciencedirect.com/science/article/pii/S0016703797001695.

King A. J., Schofield P. F., and Russell S. S. 2017. Type 1 aqueous alteration in CM carbonaceous chondrites: Implications for the evolution of water-rich asteroids. *Meteoritics & Planetary Science* 52:1197–1215. http://onlinelibrary.wiley.com/doi/10.1111/maps.12872/abstract.

Kita N. T., and Ushikubo T. 2012. Evolution of protoplanetary disk inferred from 26Al chronology of individual chondrules. *Meteoritics & Planetary Science* 47:1108–1119. https://onlinelibrary.wiley.com/doi/abs/10.1111/j.1945-5100.2011.01264.x.

Kobayashi S., Imai H., and Yurimoto H. 2003. New extreme 16O-rich reservoir in the early solar system. *GEOCHEMICAL JOURNAL* 37:663–669.

https://www.jstage.jst.go.jp/article/geochemj1966/37/6/37_6_663/_article (Accessed November 16, 2021).

Kruijer T. S., Burkhardt C., Budde G., and Kleine T. 2017. Age of Jupiter inferred from the distinct genetics and formation times of meteorites. *Proceedings of the National Academy of Sciences* 114:6712–6716.

Kunihiro T., Rubin A. E., McKeegan K. D., and Wasson J. T. 2004. Initial 26Al/27Al in carbonaceous-chondrite chondrules: too little 26Al to melt asteroids1 1Associate editor: A. N. Krot. *Geochimica et Cosmochimica Acta* 68:2947–2957. https://www.sciencedirect.com/science/article/pii/S0016703704001206.

Lauretta D. S. et al. 2017. OSIRIS-REx: Sample Return from Asteroid (101955) Bennu. *Space Science Reviews* 212:925–984. https://doi.org/10.1007/s11214-017-0405-1.

Lee M. R., Sofe M. R., Lindgren P., Starkey N. A., and Franchi I. A. 2013. The oxygen isotope evolution of parent body aqueous solutions as recorded by multiple carbonate generations in the Lonewolf Nunataks 94101 CM2 carbonaceous chondrite. *Geochimica et Cosmochimica Acta* 121:452–466. http://www.sciencedirect.com/science/article/pii/S001670371300389X.

Lee M. R., Lindgren P., and Sofe M. R. 2014. Aragonite, breunnerite, calcite and dolomite in the CM carbonaceous chondrites: High fidelity recorders of progressive parent body aqueous alteration. *Geochimica et Cosmochimica Acta* 144:126–156. http://www.sciencedirect.com/science/article/pii/S0016703714005146.

Lee M. R., and Lindgren P. 2016. Aqueous alteration of chondrules from the Murchison CM carbonaceous chondrite: Replacement, pore filling, and the genesis of polyhedral serpentine. *Meteoritics & Planetary Science* 51:1003–1021. https://onlinelibrary.wiley.com/doi/abs/10.1111/maps.12644.

Leshin L. A., Rubin A. E., and McKeegan K. D. 1997. The oxygen isotopic composition of olivine and pyroxene from CI chondrites. *Geochimica et Cosmochimica Acta* 61:835–845. http://adsabs.harvard.edu/abs/1997GeCoA..61..835L.

de Leuw S., Rubin A. E., Schmitt A. K., and Wasson J. T. 2009. 53Mn–53Cr systematics of carbonates in CM chondrites: Implications for the timing and duration of aqueous alteration. *Geochimica et Cosmochimica Acta* 73:7433–7442. http://www.sciencedirect.com/science/article/pii/S001670370900581X (Accessed October 2, 2015).

Liu M.-C., McKeegan K. D., Goswami J. N., Marhas K. K., Sahijpal S., Ireland T. R., and Davis A. M. 2009. Isotopic records in CM hibonites: Implications for timescales of mixing of isotope reservoirs in the solar nebula. *Geochimica et Cosmochimica Acta* 73:5051–5079. https://www.sciencedirect.com/science/article/pii/S0016703709003251.

Liu M.-C., McKeegan K. D., Harrison T. M., Jarzebinski G., and Vltava L. 2018. The Hyperion-II radio-frequency oxygen ion source on the UCLA ims1290 ion microprobe: Beam

characterization and applications in geochemistry and cosmochemistry. *International Journal of Mass Spectrometry* 424:1–9. http://www.sciencedirect.com/science/article/pii/S1387380617302907.

Lodders K. 2009. Abundances of the Elements in the Solar System. *Landolt Börnstein* 4B:712. https://ui.adsabs.harvard.edu/abs/2009LanB...4B..712L/abstract (Accessed March 19, 2021).

Lyons J. R., Gharib-Nezhad E., and Ayres T. R. 2018. A light carbon isotope composition for the Sun. *Nature Communications* 9:1–10. https://www.nature.com/articles/s41467-018-03093-3 (Accessed May 5, 2022).

MacPherson G. J., Bullock E. S., Janney P. E., Kita N. T., Ushikubo T., Davis A. M., Wadhwa M., and Krot A. N. 2010. EARLY SOLAR NEBULA CONDENSATES WITH CANONICAL, NOT SUPRACANONICAL, INITIAL 26Al/27Al RATIOS. *The Astrophysical Journal* 711:L117–L121. https://doi.org/10.1088/2041-8205/711/2/l117.

MacPherson G. J., Kita N. T., Ushikubo T., Bullock E. S., and Davis A. M. 2012. Well-resolved variations in the formation ages for Ca–Al-rich inclusions in the early Solar System. *Earth and Planetary Science Letters* 331–332:43–54. https://www.sciencedirect.com/science/article/pii/S0012821X12001240.

MacPherson G. J. 2014. Calcium–Aluminum-Rich Inclusions in Chondritic Meteorites. In *Treatise on Geochemistry*. Elsevier. pp. 139–179 https://linkinghub.elsevier.com/retrieve/pii/B9780080959757001054 (Accessed May 1, 2022).

McCain K. A., Young E. D., and Manning C. E. 2017. CM Carbonates Should Be Old: Insights from Parent Body Thermal Modeling. p. 2181 http://adsabs.harvard.edu/abs/2017LPI....48.2181M.

McCain K. A., Liu M.-C., and McKeegan K. D. 2020. Calibration of matrix-dependent biases in isotope and trace element analyses of carbonate minerals. *Journal of Vacuum Science & Technology B* 38:044005. https://avs.scitation.org/doi/10.1116/6.0000111.

McKeegan K. D. et al. 2011. The Oxygen Isotopic Composition of the Sun Inferred from Captured Solar Wind. *Science*. https://www.science.org/doi/full/10.1126/science.1204636 (Accessed May 6, 2022).

McKibbin S. J., Ireland T. R., Amelin Y., and Holden P. 2015. Mn–Cr dating of Fe- and Ca-rich olivine from “quenched” and “plutonic” angrite meteorites using Secondary Ion Mass Spectrometry. *Geochimica et Cosmochimica Acta* 157:13–27. https://www.sciencedirect.com/science/article/pii/S0016703715001027.

Nagashima K., Krot A. N., and Komatsu M. 2017. 26Al–26Mg systematics in chondrules from Kaba and Yamato 980145 CV3 carbonaceous chondrites. *Geochimica et Cosmochimica Acta* 201:303–319. https://www.sciencedirect.com/science/article/pii/S0016703716306081.

Otero J., Dontcheva L. A., Johnston H., Worthing R. A., Kurganov A., Petrova G., and Doering C. R. 2004. High-Rayleigh-number convection in a fluid-saturated porous layer. *Journal of Fluid Mechanics* 500:263–281. https://www.cambridge.org/core/journals/journal-of-fluid-mechanics/article/highrayleighnumber-convection-in-a-fluidsaturated-porous-layer/837C202E94EEEDB80CA2C766E4462858 (Accessed April 28, 2017).

Palme H., Lodders K., and Jones A. 2014. 2.2 - Solar System Abundances of the Elements. In *Treatise on Geochemistry (Second Edition)*, edited by Holland H. D., and Turekian K. K. Oxford: Elsevier. pp. 15–36 https://www.sciencedirect.com/science/article/pii/B9780080959757001182.

Papanastassiou D. A. 1986. Chromium isotopic anomalies in the Allende meteorite. *The Astrophysical Journal* 308:L27–L30.

Pape J., Mezger K., Bouvier A.-S., and Baumgartner L. P. 2019. Time and duration of chondrule formation: Constraints from 26Al-26Mg ages of individual chondrules. *Geochimica et Cosmochimica Acta* 244:416–436. https://www.sciencedirect.com/science/article/pii/S0016703718306033.

Petitat M., McKeegan K., Gounelle M., Mostefaoui S., Marrocchi Y., Meibom A., and Leshin L. A. 2009. Duration and Sequence of Carbonate Crystallization on the Orgueil Protolith: 53Mn-53Cr Systematics of their Evolution in O and C Isotopic Evolution. p. 1657 x` (Accessed May 17, 2017).

Petitat M., Marrocchi Y., McKEEGAN K. D., Mostefaoui S., Meibom A., Zolensky M. E., and Gounelle M. 2011. 53Mn-53Cr ages of Kaidun carbonates. *Meteoritics & Planetary Science* 46:275–283. http://onlinelibrary.wiley.com/doi/10.1111/j.1945-5100.2010.01150.x/abstract (Accessed September 28, 2015).

Piralla M., Marrocchi Y., Verdier-Paoletti M. J., Vacher L. G., Villeneuve J., Piani L., Bekaert D. V., and Gounelle M. 2020. Primordial water and dust of the Solar System: Insights from in situ oxygen measurements of CI chondrites. *Geochimica et Cosmochimica Acta* 269:451–464. https://www.sciencedirect.com/science/article/pii/S0016703719306957.

Rollion-Bard C., and Marin-Carbonne J. 2011. Determination of SIMS matrix effects on oxygen isotopic compositions in carbonates. *Journal of Analytical Atomic Spectrometry* 26:1285–1289. http://pubs.rsc.org/en/content/articlelanding/2011/ja/c0ja00213e (Accessed July 3, 2017).

Rowe M. W., Clayton R. N., and Mayeda T. K. 1994. Oxygen isotopes in separated components of CI and CM meteorites. *Geochimica et Cosmochimica Acta* 58:5341–5347. http://www.sciencedirect.com/science/article/pii/0016703794903174.

Rubin A. E., Trigo-Rodríguez J. M., Huber H., and Wasson J. T. 2007. Progressive aqueous alteration of CM carbonaceous chondrites. *Geochimica et Cosmochimica Acta* 71:2361–2382. http://www.sciencedirect.com/science/article/pii/S001670370700083X.

Rubin A. E. 2015. An American on Paris: Extent of aqueous alteration of a CM chondrite and the petrography of its refractory and amoeboid olivine inclusions. *Meteoritics & Planetary Science* 50:1595–1612. http://onlinelibrary.wiley.com/doi/10.1111/maps.12482/abstract (Accessed March 3, 2017).

Sakamoto N., Seto Y., Itoh S., Kuramoto K., Fujino K., Nagashima K., Krot A. N., and Yurimoto H. 2007. Remnants of the Early Solar System Water Enriched in Heavy Oxygen Isotopes. *Science*. https://www.science.org/doi/abs/10.1126/science.1142021 (Accessed October 27, 2021).

Sanborn M. E., Wimpenny J., Williams C. D., Yamakawa A., Amelin Y., Irving A. J., and Yin Q.-Z. 2019. Carbonaceous achondrites Northwest Africa 6704/6693: Milestones for early Solar System chronology and genealogy. *Geochimica et Cosmochimica Acta* 245:577–596. https://www.sciencedirect.com/science/article/pii/S0016703718305787.

Schidlowski M., Hayes J. M., and Kaplan I. R. 1983. Isotopic inferences of ancient biochemistries: carbon, sulfur, hydrogen, and nitrogen. In *Earth's Earliest biosphere: its origin and evolution*. Princeton: Princeton University Press. pp. 149–187.

Scott E. R. D., and Krot A. N. 2014. Chondrites and Their Components. In *Treatise on Geochemistry*. Elsevier. pp. 65–137 https://linkinghub.elsevier.com/retrieve/pii/B9780080959757001042 (Accessed May 1, 2022).

Sephton M. A., Pillinger C. T., and Gilmour I. 2000. Aromatic moieties in meteoritic macromolecular materials: analyses by hydrous pyrolysis and δ13C of individual compounds. *Geochimica et Cosmochimica Acta* 64:321–328. https://www.sciencedirect.com/science/article/pii/S0016703799002823.

Śliwiński M. G., Kitajima K., Kozdon R., Spicuzza M. J., Fournelle J. H., Denny A., and Valley J. W. 2016a. Secondary Ion Mass Spectrometry Bias on Isotope Ratios in Dolomite–Ankerite, Part I: δ18O Matrix Effects. *Geostandards and Geoanalytical Research* 40:157–172. http://onlinelibrary.wiley.com/doi/10.1111/j.1751-908X.2015.00364.x/abstract.

Śliwiński M. G., Kitajima K., Kozdon R., Spicuzza M. J., Fournelle J. H., Denny A., and Valley J. W. 2016b. Secondary Ion Mass Spectrometry Bias on Isotope Ratios in Dolomite–Ankerite, Part II: δ13C Matrix Effects. *Geostandards and Geoanalytical Research* 40:173–184. http://onlinelibrary.wiley.com/doi/10.1111/j.1751-908X.2015.00380.x/abstract.

Śliwiński M. G., Kitajima K., Spicuzza M. J., Orland I. J., Ishida A., Fournelle J. H., and Valley J. W. 2017. SIMS Bias on Isotope Ratios in Ca-Mg-Fe Carbonates (Part III): δ18O and δ13C Matrix Effects Along the Magnesite–Siderite Solid-Solution Series. *Geostandards and Geoanalytical Research* n/a-n/a. http://onlinelibrary.wiley.com/doi/10.1111/ggr.12194/abstract.

Steele R. C. J., Heber V. S., and McKeegan K. D. 2017. Matrix effects on the relative sensitivity factors for manganese and chromium during ion microprobe analysis of carbonate: Implications for early Solar System chronology. *Geochimica et Cosmochimica Acta* 201:245–259. http://www.sciencedirect.com/science/article/pii/S001670371630624X (Accessed March 13, 2017).

Sugiura N., and Ichimura K. 2010. Mn/Cr relative sensitivity factors for sythetic calcium carbonate measured with a NanoSIMS ion microprobe. *Geochemical Journal* 44:e11-316.

Sugiura N., and Fujiya W. 2014. Correlated accretion ages and ε54Cr of meteorite parent bodies and the evolution of the solar nebula. *Meteoritics & Planetary Science* 49:772–787. https://onlinelibrary.wiley.com/doi/abs/10.1111/maps.12292.

Suttle M. D., King A. J., Schofield P. F., Bates H., and Russell S. S. 2021. The aqueous alteration of CM chondrites, a review. *Geochimica et Cosmochimica Acta* 299:219–256. https://www.sciencedirect.com/science/article/pii/S0016703721000363.

Tang H., and Dauphas N. 2012. Abundance, distribution, and origin of 60Fe in the solar protoplanetary disk. *Earth and Planetary Science Letters* 359–360:248–263. https://www.sciencedirect.com/science/article/pii/S0012821X12005705.

Telus M., Alexander C. M. O., Hauri E. H., and Wang J. 2019. Calcite and dolomite formation in the CM parent body: Insight from in situ C and O isotope analyses. *Geochimica et Cosmochimica Acta* 260:275–291. http://www.sciencedirect.com/science/article/pii/S0016703719303515.

Tomeoka K., and Buseck P. R. 1985. Indicators of aqueous alteration in CM carbonaceous chondrites: Microtextures of a layered mineral containing Fe, S, O and Ni. *Geochimica et Cosmochimica Acta* 49:2149–2163. https://www.sciencedirect.com/science/article/pii/0016703785900730.

Trigo-Rodriguez J. M., Rubin A. E., and Wasson J. T. 2006. Non-nebular origin of dark mantles around chondrules and inclusions in CM chondrites. *Geochimica et Cosmochimica Acta* 70:1271–1290. https://www.sciencedirect.com/science/article/pii/S0016703705008872.

Trinquier A., Birck J.-L., Allègre C. J., Göpel C., and Ulfbeck D. 2008. 53Mn–53Cr systematics of the early Solar System revisited. *Geochimica et Cosmochimica Acta* 72:5146–5163. http://www.sciencedirect.com/science/article/pii/S0016703708001774.

Tyra M. A., Farquhar J., Guan Y., and Leshin L. A. 2012. An oxygen isotope dichotomy in CM2 chondritic carbonates—A SIMS approach. *Geochimica et Cosmochimica Acta* 77:383–395. http://www.sciencedirect.com/science/article/pii/S0016703711005904.

Tyra M., Brearley A., and Guan Y. 2016. Episodic carbonate precipitation in the CM chondrite ALH 84049: An ion microprobe analysis of O and C isotopes. *Geochimica et Cosmochimica Acta* 175:195–207.

http://www.sciencedirect.com/science/article/pii/S0016703715006596 (Accessed January 8, 2016).

Usdowski E. 2009. Synthesis of Dolomite and Geochemical Implications. In *Dolomites*. John Wiley & Sons, Ltd. pp. 345–360 https://onlinelibrary.wiley.com/doi/abs/10.1002/9781444304077.ch19.

Vacher L. G., Marrocchi Y., Villeneuve J., Verdier-Paoletti M. J., and Gounelle M. 2017. Petrographic and C & O isotopic characteristics of the earliest stages of aqueous alteration of CM chondrites. *Geochimica et Cosmochimica Acta* 213:271–290. http://www.sciencedirect.com/science/article/pii/S0016703717304088.

Vacher L. G., Marrocchi Y., Villeneuve J., Verdier-Paoletti M. J., and Gounelle M. 2018. Collisional and alteration history of the CM parent body. *Geochimica et Cosmochimica Acta* 239:213–234. https://www.sciencedirect.com/science/article/pii/S0016703718304344.

Verdier-Paoletti M. J., Marrocchi Y., Avice G., Roskosz M., Gurenko A., and Gounelle M. 2017. Oxygen isotope constraints on the alteration temperatures of CM chondrites. *Earth and Planetary Science Letters* 458:273–281. http://www.sciencedirect.com/science/article/pii/S0012821X16306203 (Accessed March 13, 2017).

Visser R., John T., Whitehouse M. J., Patzek M., and Bischoff A. 2020. A short-lived 26Al induced hydrothermal alteration event in the outer solar system: Constraints from Mn/Cr ages of carbonates. *Earth and Planetary Science Letters* 547:116440. http://www.sciencedirect.com/science/article/pii/S0012821X20303848.

Wasserburg G. J., Wimpenny J., and Yin Q.-Z. 2012. Mg isotopic heterogeneity, Al-Mg isochrons, and canonical 26Al/27Al in the early solar system. *Meteoritics & Planetary Science* 47:1980–1997. https://onlinelibrary.wiley.com/doi/abs/10.1111/maps.12014.

Watanabe S., Tsuda Y., Yoshikawa M., Tanaka S., Saiki T., and Nakazawa S. 2017. Hayabusa2 Mission Overview. *Space Science Reviews* 208:3–16. https://doi.org/10.1007/s11214-017-0377-1.

Young E. D., Ash R. D., England P., and Rumble D. 1999. Fluid Flow in Chondritic Parent Bodies: Deciphering the Compositions of Planetesimals. *Science* 286:1331–1335. http://science.sciencemag.org/content/286/5443/1331 (Accessed July 12, 2017).

Young E. D. 2001. The hydrology of carbonaceous chondrite parent bodies and the evolution of planet progenitors. *Philosophical Transactions of the Royal Society of London A: Mathematical, Physical and Engineering Sciences* 359:2095–2110. http://rsta.royalsocietypublishing.org/content/359/1787/2095 (Accessed July 12, 2017).

Young E. D., Zhang K. K., and Schubert G. 2003. Conditions for pore water convection within carbonaceous chondrite parent bodies – implications for planetesimal size and heat production. *Earth and Planetary Science Letters* 213:249–259.

http://www.sciencedirect.com/science/article/pii/S0012821X03003455 (Accessed April 28, 2017).

Zheng Y.-F. 1995. Oxygen isotope fractionation in magnetites: structural effect and oxygen inheritance. *Chemical Geology* 121:309–316. https://www.sciencedirect.com/science/article/pii/0009254194001493.

Zhou Q., Yin Q.-Z., Young E. D., Li X.-H., Wu F.-Y., Li Q.-L., Liu Y., and Tang G.-Q. 2013. SIMS Pb–Pb and U–Pb age determination of eucrite zircons at < 5 μm scale and the first 50 Ma of the thermal history of Vesta. *Geochimica et Cosmochimica Acta* 110:152–175. http://www.sciencedirect.com/science/article/pii/S0016703713001117 (Accessed April 10, 2017).

Zhu K., Moynier F., Wielandt D., Larsen K. K., Barrat J.-A., and Bizzarro M. 2019. Timing and Origin of the Angrite Parent Body Inferred from Cr Isotopes. *The Astrophysical Journal* 877:L13. https://doi.org/10.3847/2041-8213/ab2044.

Zolensky M. E., Ivanov A. V., Yang S. V., Mittlefehldt D. W., and Ohsumi K. 1996. The Kaidun meteorite: Mineralogy of an unusual CM1 lithology. *Meteoritics & Planetary Science* 31:484–493. https://onlinelibrary.wiley.com/doi/abs/10.1111/j.1945-5100.1996.tb02090.x.

Zolensky M. E., Mittlefehldt D. W., Lipschutz M. E., Wang M.-S., Clayton R. N., Mayeda T. K., Grady M. M., Pillinger C., and B D. 1997. CM chondrites exhibit the complete petrologic range from type 2 to 1. *Geochimica et Cosmochimica Acta* 61:5099–5115. http://www.sciencedirect.com/science/article/pii/S0016703797003578 (Accessed May 3, 2017).

Chapter 2

Calibration of matrix-dependent biases in isotope and trace element analyses of carbonate minerals

Kaitlyn A. McCain, Ming-Chang Liu, and Kevin McKeegan

Reproduced from McCain, K.A., Liu, M.-C., McKeegan, K.D., 2020. Calibration of matrix-dependent biases in isotope and trace element analyses of carbonate minerals. Journal of Vacuum Science & Technology B 38, 044005, with the permission of AIP Publishing

Abstract

The timing of important events in the early history of the solar system can be established by using the decay of the short-lived radionuclide ^{53}Mn to stable ^{53}Cr. Carbonate minerals found in meteorite samples can be dated using this system provided that an accurate and precise value for the Mn/Cr ratio can be established. However, the ion yields of Mn and Cr vary substantially based upon the elemental composition of the matrix and require calibration using standards of known Mn and Cr concentrations to relate the measured Mn/Cr ratio to the true ratio with a "relative sensitivity factor". We implant $^{52}Cr^{+}$ into a suite of terrestrial calcite and dolomite samples of varied elemental compositions to produce matrix-matched standards for ^{53}Mn-^{53}Cr analysis. Depth profiling of the implanted carbonates reveal variation in the relative sensitivity factors between carbonates low in Fe and Mn and dolomite rich in Fe and Mn. For carbonates with $FeCO_3$ > 8 mol%, the relative sensitivity factor is constant at 0.88 ±0.08 (2 SD). For carbonates with $FeCO_3$ < 2 mol%, the relative sensitivity factor is approximately 1.1. We also show that the use of an inappropriate relative sensitivity factor can lead to systematic error in the age determined for meteoritic carbonate.

Introduction

The determination of a chronology of key events in the chemical and mineralogical evolution of planetary materials is critical to developing a detailed understanding of processes associated with formation of the solar system. Such significant events include the accretion times of asteroids and the timing of important thermal processing events (e.g., circulation of hydrothermal fluids). Early solar system materials are found in primitive meteorites ("chondrites") and specific mineral phases can be dated with high precision using a variety of short-lived radiometric systems (Davis and McKeegan 2014). One such system is based on the radioactive decay of ^{53}Mn to ^{53}Cr with a half-life of 3.7 Myr. The relatively high abundance of ^{53}Mn in the early solar system and its short half-life allows a mineral which incorporated this nuclide within the first ~15 Myr of the birth of the solar system to have its relative age determined with good precision, in ideal circumstances at sub-million-year levels.

Solar system materials that have experienced alteration by aqueous fluids are of special interest to the planetary science community because liquid water makes possible complex organic and inorganic chemistries, even on small planetary bodies like asteroids. The secondary minerals formed by this alteration can be dated to determine the age and longevity of these water-rich environments. One useful group of minerals are carbonates, which form only in water-rich environments and preferentially incorporate 2+ ions (e.g., Ca, Mg, Fe, and Mn) and exclude 3+ ions (such as Cr) during crystallization. Carbonates forming early in the history of the Solar System had the potential to incorporate radioactive ^{53}Mn, which would have subsequently decayed to ^{53}Cr, leaving a "fossil" record of its former presence as an elevated ^{53}Cr/^{52}Cr ratio correlated to Mn abundance. The relative age of the carbonate can be estimated by comparing its inferred initial ^{53}Mn/^{55}Mn ratio with that of an "anchor" sample of known age,

assuming ^{53}Mn was homogeneously distributed in the early solar system(Davis and McKeegan 2014; Trinquier et al. 2008). This anchor sample is a differentiated meteorite whose ^{53}Mn/^{55}Mn has been determined to be 3.24×10^{-6} at 4563.4 Myr before present (Amelin 2008; Brennecka and Wadhwa 2012; Glavin et al. 2004). As shown in Equation 2.1, the formation age of the carbonate in millions of years before present ($T_{carbonate}$) may be calculated based on the inferred isotopic composition of Mn incorporated into the carbonate mineral, $(^{53}Mn/^{55}Mn)_{carbonate}$.

$$T_{carbonate} = 4563.4 + \frac{t_{1/2}}{\ln(2)} \times \ln\left[\left({}^{53}Mn/{}^{55}Mn \right)_{carbonate} \Big/ 3.24 \times 10^{-6} \right] \quad (2.1)$$

Because ^{53}Mn has undergone over one thousand half-lives since the formation of the carbonates, it can be considered to have decayed completely and the present day ^{53}Mn/^{55}Mn ratio cannot be directly measured in meteoritic carbonate. However, Cr was strongly excluded from the mineral during its formation, and so ^{53}Cr detected in meteoritic carbonates can be attributed to the decay of ^{53}Mn. Therefore, it is possible to infer the initial ^{53}Mn/^{55}Mn ratio in a carbonate by determining the amount of radiogenic ^{53}Cr present. This is done by observing the correlation of ^{53}Cr/^{52}Cr with the parent-element/daughter-element ratio, ^{55}Mn/^{52}Cr. Previous analyses of meteoritic carbonate using this system suggest that most carbonates formed 3-7 Myr after the birth of the solar system (Fujiya et al. 2012, 2013; Jilly et al. 2014; de Leuw et al. 2009; Steele et al. 2017).

Meteoritic carbonates are small, difficult to separate from the host meteorite, and texturally complex. Therefore, most meteoritic carbonate is dated in situ using secondary ion mass spectrometry (SIMS or ion probe), allowing both Mn and Cr species to be sampled from identical volumes in individual grains. To infer the correct formation age of a carbonate requires that the Mn/Cr ratio be determined accurately and precisely, but elemental ratios are difficult to

measure by ion probe, as the ion yields of different elements often vary substantially based upon the elemental composition of the matrix, a phenomenon known as the "matrix effect". The magnitude of this effect is difficult to model and must be corrected empirically by measuring standards of similar chemical composition and known Mn/Cr ratio (i.e., "matrix-matched"). Carbonates in particular exhibit strong matrix effects related to the abundance of Fe in the target carbonate (Steele et al. 2017).

In order to obtain accurate elemental ratios, it is necessary to relate the true concentrations of each element (C_a and C_b) to the intensities (I_a and I_b) measured by the ion probe via a relative sensitivity factor, or "RSF", shown in Equation (2.2).

$$RSF = \frac{C_a / C_b}{I_a / I_b} \qquad (2.2)$$

Reference materials (or "standards") can be analyzed to determine an RSF provided that the concentrations of the target elements are known and homogeneously distributed. In the case of carbonate minerals, however, such reference materials for the Mn/Cr ratio cannot be found in nature due to the strong exclusion of 3+ ions such as Cr from the carbonate crystal structure, and synthetic materials face challenges associated with growing homogeneous Cr-doped calcite (Jilly et al. 2014; Sugiura and Ichimura 2010) and synthesizing dolomite (Usdowski 2009). Because matrix-matched reference materials of known Mn/Cr ratio are not easily acquired or made, previous studies of meteoritic carbonate were restricted to using RSF values determined on materials of known Mn/Cr ratios which did not closely match the chemistry of the target carbonate minerals (and thus could be subject to matrix effects).

As an alternative to unaltered naturally-occurring or synthetic RSF reference materials, ion accelerators can be used to implant Cr into natural minerals with excellent lateral spatial homogeneity (Burnett et al. 2015). This technique allows any implanted material to become a standard of known Cr concentration so long as the total amount of implanted ions, or fluence, can be determined following correction for any initial Cr present. In a study where a variety of carbonate minerals were implanted with $^{52}Cr^{+}$, the RSF between Mn and Cr was shown to vary significantly as a function of the Fe and Mn contents of the mineral (Steele et al. 2017).

Previously implanted materials have been used to constrain the RSF for a large chemical range of carbonates (Steele et al. 2017). However, most carbonates appropriate for Mn-Cr dating in meteorites are dolomites containing up to ~20 mol% Fe. Only two carbonates implanted previously are within this range of natural meteoritic carbonate, dolomites with 25 and 9 mol% Fe (replacing Mg). The variation of the RSF in carbonate minerals relevant to studies of meteorite ages, i.e., the full range of matrix effects, is not yet determined. In this work, we measured the RSF of calcite and dolomite minerals with Fe contents ranging over 0-20 molar % to improve the accuracy of radiometric dating of carbonate in meteorites.

Experimental Methods

Sample Selection and Preparation

Natural carbonate minerals were selected from the UCLA mineral collection, including calcite ($CaCO_3$), Fe-poor dolomite ($CaMg(CO_3)_2$), and Fe-rich ferroan dolomite ($Ca(Mg,Fe)(CO_3)_2$). The minerals span the range of Fe contents observed in meteoritic carbonate, between 0 and 20 molar percent $FeCO_3$. A comparison of carbonate minerals in our study, meteoritic carbonate, and previously-implanted carbonates can be found in the

supplementary materials. A large crystal fragment of each mineral was embedded in Field's Metal and/or indium in the center of an aluminum disk, and polished to better than 0.25 μm using Beuhler MetaDi Supreme polycrystalline diamond compound. Samples of NIST 612 and NIST 614 soda lime glasses, which are certified concentration reference materials containing 36 ppm and 1 ppm Cr and 39 ppm and 1.3 ppm Mn, respectively (Jochum et al. 2011), were also mounted to be used to calibrate the implant fluence.

Electron Probe MicroAnalysis

The chemical composition and homogeneity of each mineral was determined using the JEOL Superprobe electron microprobe analyzer (EPMA) at UCLA using an accelerating voltage of 15 kV with a beam defocused to 10 μm to avoid damage to the carbonate minerals. Full details of the EPMA analytical conditions can be found in the Supplementary Methods section of the online supplementary material. In all cases, Cr concentrations in these natural carbonates were below the detection limit of the EPMA (~120 ppm). Carbonate minerals with homogeneous Fe content—that is, minerals for which repeated analyses remained within 2SD (internal error) of one another—were selected for depth profiling. The mounted fragment of the ferroan dolomite MS1312 was found to have two domains with distinct Fe and Mn concentrations, and these domains were treated separately. The composition of each selected carbonate mineral is summarized in Table 1, with the two domains of MS 1312 reported as MS 1312_D1 and MS1312_D2 referring to the high and low Mn domains respectively.

Table 2.1. Summary of elemental composition of carbonate minerals determined by electron probe microanalysis. Concentrations are reported in molar percent except when concentrations of Mn are reported in (ppm as µg Mn /g). Errors are reported as 2 SD molar % and incorporate the internal variation during analysis and the SD of repeated analyses. The detection limit of Fe and Mn is approximately 120 ppm, and elements below the detection limit are marked "b.d." Compositions marked with an asterisk denote material compositions determined by a higher current beam following depth profiling analysis (see supplementary material).

Name	Ca	±	Mg	±	Fe	±	Mn	±
Calcite	99.4	0.8	0.5	0.2	b.d.	-	b.d.	-
MS1317*	50.1	0.4	49.8	0.4	b.d.	-	(317)	(203)
MS1317J*	50.2	0.3	48.2	0.3	1.4	0.1	0.2	0.04
MS1318	48.0	0.5	42.7	0.3	8.2	0.2	1.1	0.2
MS1305*	49.5	0.3	49.4	0.4	0.9	0.1	(558)	(270)
MS1312_D1*	50.1	0.3	18.8	0.7	22.8	1.0	8.2	0.3
MS1312_D2*	49.6	0.4	21.8	0.7	21.9	0.9	6.6	0.2

Ion Implantation

The mount was coated with a 30 nm layer of gold to ensure conductivity and prevent charging during ion implantation and ion probe analysis. The mount was implanted with a 185 KeV $^{52}Cr^{+}$ ion beam at a nominal fluence of 4 x 10^{13} ions/cm^2, rastered over the entire surface. A mass filter was used to separate $^{52}Cr^{+}$ and $^{53}Cr^{+}$ after Cr ionization, ensuring that only $^{52}Cr^{+}$ was implanted. If some amount of $^{53}Cr^{+}$ was included during implantation, the $^{53}Cr^{+}$ abundance

observed during depth profiling would increase and then decay similarly (though at lower abundance) to $^{52}Cr^{+}$, which was not observed in any of our implanted materials. The implantation was carried out by Leonard Kroko, Inc.

Modeling of Backscatter Effects During Implantation

Variation in the chemistry of implanted targets can impact the total quantity and distribution of implanted ions within the target material. In particular, a target containing a higher proportion of high-Z elements such as Fe will backscatter the incident ion beam more efficiently than a target with fewer high-Z elements. If backscatter effects are sufficiently strong, dolomite samples with higher Fe contents could receive a lower dose of $^{52}Cr^{+}$ ions than targets with low Fe.

To constrain the magnitude of the backscatter effect in our implanted minerals, we used the SRIM (Stopping Range of Ions in Matter) program to simulate a dose of 2000 $^{52}Cr^{+}$ ions with energy of 185 KeV into soda lime glass, pure $CaCO_3$, $CaMgCO_3$, $Ca(Mg_{0.75},Fe_{0.25})(CO_3)_2$, and $Ca(Mg_{0.5},Fe_{0.5})(CO_3)_2$, all with a 30 nm Au coating (Ziegler et al. 2010). Four replicate simulations were performed for each target material. For all targets, including the NIST glasses, approximately 10±0.5% of incident $^{52}Cr^{+}$ ions were backscattered by the gold coat, with no correlation between the number of backscattered ions and Fe content. Because all targets showed identical backscattering behavior, we conclude that all targets received the same fluence, and therefore we do not apply separate backscatter corrections to our fluence calculations.

The distribution of the simulated implanted $^{52}Cr^{+}$ did not vary significantly between the dolomite targets, with the peak implanted Cr concentration occurring at approximately 92 nm for all simulated dolomites. The simulated peak concentration for the glass target occurred deeper

within the material at 108 nm. We suspect that this difference arises from the glass's lower density compared to dolomite minerals. Additional documentation of the SRIM simulations can be found in the supplementary material.

Depth Profiling

The implanted carbonate standards and NIST standard materials were analyzed on the Cameca ims-1290 ion microprobe at UCLA equipped with an Oregon Physics Hyperion oxygen plasma source. Two separate areas of each target material were analyzed by sputtering with a 2 nA O^{3-} primary ion beam focused into a ~3 µm spot rastered over ~50 µm by ~50 µm areas in each implanted material. A field aperture was inserted into an ion image plane to restrict the collected ions to the central 20 µm by 20 µm area of each raster square. A 75 µm entrance slit was used. Secondary ions of $^{44}Ca^{+}$, $^{52}Cr^{+}$, $^{53}Cr^{+}$, and $^{55}Mn^{+}$ were counted using an electron multiplier. The profile MS1317J #2 was acquired by sputtering for over twice as long to test whether the signal varied with increasing depth. For the ferroan dolomite MS1312, the two depth profiles were placed in the two different compositional regions: The profile 'MS1312 #1' was collected from the higher-Mn domain (MS1312_D1), and the profile 'MS1312 #2' from the lower-Mn domain (MS1312_D2).

Each material was sputtered until the $^{52}Cr^{+}$ and $^{53}Cr^{+}$ signals decayed to a stable background, which occurred in approximately 30 minutes. Representative profiles of the intensities as collected from NIST glass NBS 614 and the natural carbonate MS1317J are shown in Figures 1 and 2, respectively. The maximum implanted ^{52}Cr concentration depth is deeper in the NIST 614 glass, and the implant profile decays to background more slowly than in the MS1317J dolomite, which we attribute to the effect of mineral density identified during our

SRIM modeling. Additional profiles for all sputtered materials are included in the supplementary material.

To construct the implantation profile of ^{52}Cr, the measured $^{52}Cr^{+}$ signal was corrected for the natural abundance of ^{52}Cr in the mineral, which is calculated by multiplying the $^{53}Cr^{+}$ signal by the terrestrial $^{52}Cr/^{53}Cr$ ratio of 8.8190. The corrected $^{52}Cr^{+}$ signal was calculated at every block using the $^{53}Cr^{+}$ intensity recorded in the same block. This dynamic correction was necessary as the abundance of both Cr isotopes varied with depth over the time of the profile. Besides the variation in ^{52}Cr abundance attributed to the ion implantation procedure, background ^{52}Cr and ^{53}Cr are typically elevated at the beginning of the profile due to surface contamination.

Fig. 2.1. Intensities of $^{52}Cr^{+}$, $^{53}Cr^{+}$, and $^{55}Mn^{+}$ recorded during depth profiling of NIST 614 glass. The heavy black line represents the intensity of $^{52}Cr^{+}$ including the implanted Cr and the background Cr in the NIST glass. The dotted green line represents the intensity of the background $^{53}Cr^{+}$ during the profile. The dashed blue line represents the intensity of $^{55}Mn^{+}$ during the profile. The thin black line represents the intensity of $^{52}Cr^{+}$ attributed to ion implantation.

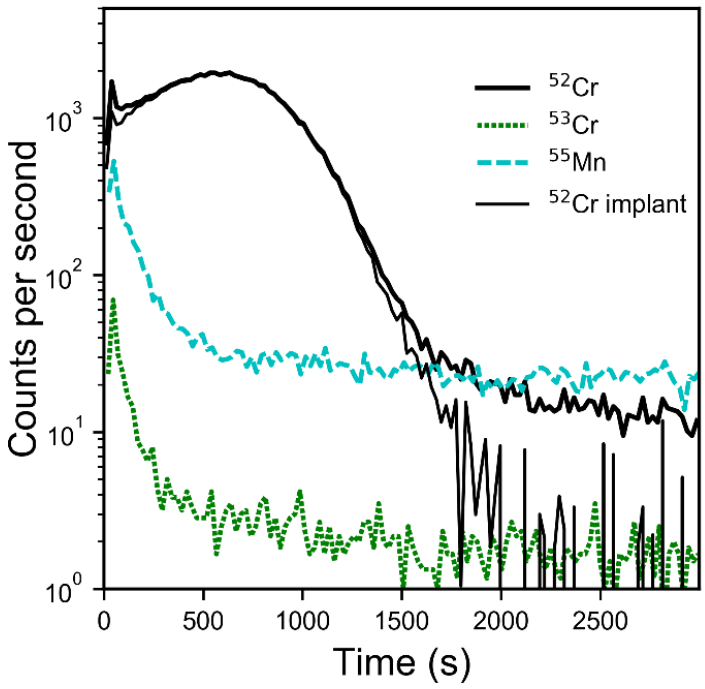

Fig. 2.2. Intensities of $^{52}Cr^{+}$, $^{53}Cr^{+}$, and $^{55}Mn^{+}$ recorded during depth profiling of the natural dolomite MS 1317J #2. The heavy black line represents the intensity of $^{52}Cr^{+}$ including the implanted $^{52}Cr^{+}$ and the background Cr in the dolomite. The dotted green line represents the intensity of the background $^{53}Cr^{+}$. The dashed blue line represents the intensity of $^{55}Mn^{+}$. The thin black line represents the intensity of ^{52}Cr attributed to ion implantation.

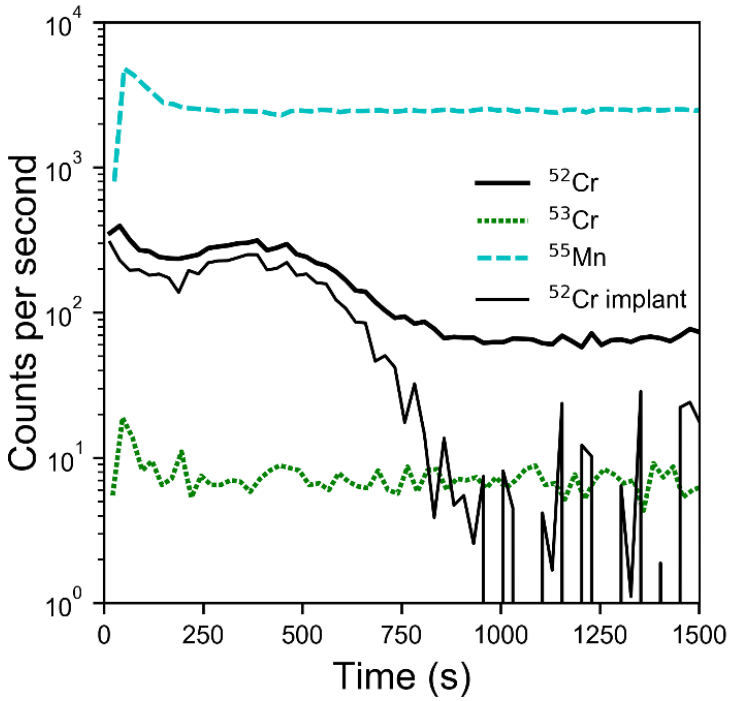

Surface Profilometry

The depth of each ion beam raster square was measured using the Dektak XT stylus profilometer at the Molecular Materials Research Center at the California Institute of Technology. Profiles were collected using a stylus tip diameter of 2 µm, a vertical range of 6 µm, and a vertical resolution of 0.1 nm. Each raster was profiled two times along perpendicular axes. The depth of each profile was determined using the Bruker Vision64 software, which determines the vertical distance between the flat region surrounding the rastered area and the flat bottom of the profile, which trims the edges of the rastered area from the depth. The rastered areas were flat

and did not show significant curvature at their bottoms. The average value of the depth of the two profiles was taken as the depth of the rastered area. The depth of each profile is summarized in Table 2, and additional information including SEM imagery of the rastered areas can be found in the supplementary materials.

Results

Calibration of implant fluence

While ion implantation guarantees a laterally homogeneous concentration of the implanted species, the accuracy of the fluence delivered can only be guaranteed to 10-20% of the nominal requested fluence. It is therefore necessary to independently calibrate the $^{52}Cr^{+}$ fluence received using materials with known (and homogeneous) Cr concentration. In this case, the two co-implanted NIST glasses described above were used to calibrate the implant fluence as previously described by Steele et al. in Equation 2.3, where F_{52Cr} refers to the actual fluence of the implanted ^{52}Cr, C_{52Cr} refers to the true concentration of ^{52}Cr as certified by NIST, and D refers to the depth of the analysis crater. A_{52Cr+} refers to the sum of all $^{52}Cr^{+}$ counts attributed to the implant, corrected for the background concentration of ^{52}Cr as described above, and can be represented as the area beneath the thin black line in Figure 2.1. I_{52Cr} refers to the intensity (cps) measured by the electron multiplier of the background $^{52}Cr^{+}$, as calculated from the intensity of $^{53}Cr^{+}$, the non-implanted Cr species of known concentration; and t is the total time of the profile in seconds.

$$F_{^{52}Cr} = \frac{C_{^{52}Cr} D A_{^{52}Cr^{+}}}{I_{^{52}Cr} t} \qquad (2.3)$$

Each NIST glass was profiled twice, and the fluence was calculated from each of the four profiles. There was no difference observed in the fluence calculated within a single NIST glass material or between the NIST 614 and 612 glasses. The implant fluence was determined to be $2.76 \pm 0.22 \times 10^{13}$ ions/cm^2, a significant deviation from the nominal fluence of 4×10^{13} ions/cm^2. Quoted uncertainties are 2 SD in the calculated fluence and incorporate uncertainties in the Cr concentrations of the NIST glass reference materials and the variability of the calculated fluence between the rastered areas; other sources of error (e.g., of crater depth determinations) contribute negligibly to the overall uncertainty.

Calculation of Relative Sensitivity Factors

The relative sensitivity factor of an implanted natural material can be calculated according to Equation 2.4, where C_{55Mn} represents the concentration of ^{55}Mn as determined by EPMA, D represents the depth of the rastered area, A_{52Cr+} represents the total number of counts of implanted $^{52}Cr^+$ (as defined above), I_{55Mn} represents the measured signal intensity of $^{55}Mn^+$ during the depth profile, F represents the fluence of ^{52}Cr implanted as calculated above, and t represents the total duration of the profile.

$$RSF = \frac{C_{^{55}Mn} D A_{^{52}Cr^+}}{I_{^{55}Mn} F t} \quad (2.4)$$

The RSF values for each implanted carbonate, along with the parameters from Equation 2.3 used to calculate the RSF, are summarized in Table 2.2. The relationship between the RSF value and the Fe content of the carbonate is shown in Figure 2.3. Uncertainties in the derived RSF value incorporate errors in the Mn concentration and the fluence. As the relative uncertainty for the fluence determination is 8% (= 2SD) (quantified empirically from depth profiling of the

implanted NIST glasses; see above), the error for the RSF for most carbonates is dominated by the error in the Mn concentration as determined by the EPMA. All repeated measurements of the RSF of carbonate materials are within error of one another. Because the calcite Mn concentration was below the detection limit of the EPMA (120 ppm), a Mn concentration of 100 ppm was used to perform the calculation. Therefore, the calcite RSF of 1.63 represents an upper bound and is associated with error of 100%.

Table 2.2. Results of RSF values derived from depth profiling of natural carbonate minerals. The error on the RSF value is 2SD. Refer to Table 2.1 for additional information about error in Fe and Mn concentrations. Fe and Mn concentrations are reported in mol % or (ppm as µg Mn /g).

Name	**RSF**	**±**	**Depth (nm)**	**SD (%)**	**^{55}Mn (cps)**	***A*($^{52}Cr^{+}$) (counts)**	***Time (s)***	**Fe**	**Mn**
Calcite #1	1.66	1.5	301	1.0	138	115472	1637	b.d.	b.d.
Calcite #2	1.60	1.5	297	1.7	163	131794	1612	b.d.	b.d.
MS1317 #1	1.03	0.67	302	2.0	462	118566	1767	b.d	(317)
MS1317 #2	1.32	0.86	285	4.0	915	158026	1761	b.d	(317)
MS1317J #1	1.16	0.25	327	1.3	3326	151971	1470	1.4	0.2
MS1317J #2	1.23	0.27	651	0.5	2506	143986	3470	1.4	0.2
MS1318 #1	0.867	0.16	293	0.6	28369	214744	1842	8.2	1.1
MS1305 #1	0.865	0.3	332	0.7	1976	152105	1859	0.9	(558)
MS1305 #2	0.825	0.29	329	0.8	1965	145875	1861	0.9	(558)
MS1312 #1	0.848	0.07	275	2.6	157260	181010	1915	22.8	8.2
MS1312 #2	0.927	0.08	315	5.7	105714	177507	2387	21.9	6.6

Fig. 2.3. Mn/Cr relative sensitivity factors of terrestrial carbonate minerals as a function of Fe content. Error bars on the RSF measurements represent 2 SD. The average value of all RSF values obtained from low-Fe dolomite is represented by the black star. The gray line represents the average value for high-Fe dolomite analyzed in this study and related errors (2SD). RSF values obtained by Steele et al. are plotted with open symbols for comparison. The exponential fit (black line) and related errors (dotted black lines, 2SD) were calculated using the curve_fit function from the SciPy Optimization module (Virtanen et al. 2020).

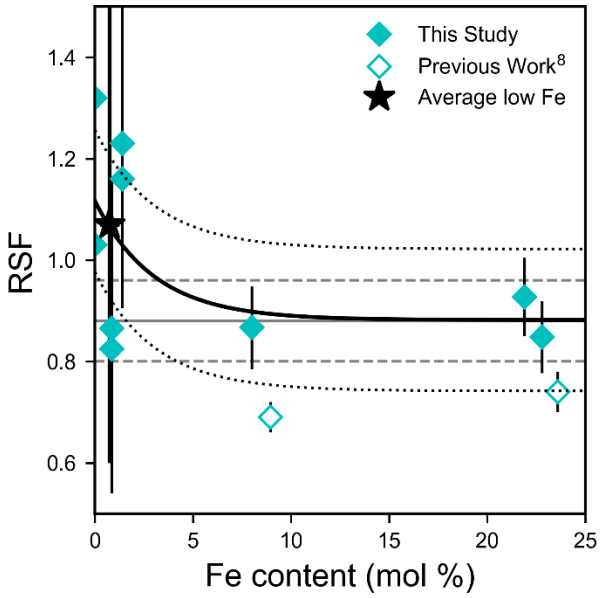

Nonlinear variation of Relative Sensitivity Factors

For dolomite samples with $FeCO_3$> 8%, the RSF remains constant at 0.88 ±0.08 (2 SD). At lower Fe content, the RSF value is higher, rising to around ~1.1 when $FeCO_3$ approaches zero. This trend is consistent with previous studies of matrix effects in instrumental fractionation for carbonate minerals, which also show that isotope fractionation effects change substantially as small amounts of Fe are added to the carbonate but then become nearly constant once some threshold Fe concentration is reached (Śliwiński et al. 2016a, 2016b).

Discussion

Comparison of RSFs with previous work

A previously quantified implanted ankerite (24 and 1.4 mol% Fe and Mn, respectively) is similar to our MS1312 material, though MS1312 contains significantly more Mn (Steele et al. 2017). Despite substantial differences in the analytical conditions between this work and the previous study, the RSF value of 0.888 obtained for MS 1312 is higher than, though similar to the value determined in the previous work for this similar mineral and is consistent with the overall trend of lower RSF with higher Fe content (Steele et al. 2017). Comparison of our MS1318 material (8.2 and 1.1 mol% Fe and Mn) with a similar ferroan dolomite (8.5 and 0.5 mol% Fe and Mn) show that the RSF value of 0.867 for MS 1318 is higher than that determined for the previously-quantified dolomite, though we note that Steele et al. report only the standard error for their study. For comparison with other determinations of the calcite RSF, a nearly pure $CaCO_3$ calcite was also implanted. However, only an upper limit of 120 ppm could be established for the Mn abundance for this material by EPMA. The calcite RSF we calculate assuming a Mn concentration of 100 ppm, though consistent within error with previous calcite RSF determinations of 1.16-1.41 (Fujiya et al. 2012, 2013; Jilly et al. 2014; Steele et al. 2017), is associated with large errors related to poor constraints on the Mn concentration.

Uncertainty in Mn Concentration

Large errors in the RSF when $FeCO_3$ < 2% are due to challenges in quantifying the Mn concentration by EPMA. In these low-Mn carbonates, Mn is heterogeneous on the order of a few 100 ppm at the spatial scale of our analyses. At low Mn concentration, this heterogeneity combined with a ~120 ppm detection limit of EPMA leads to substantial uncertainty in the calculated RSF. Although this might appear to be a significant problem in quantifying systematics of the matrix effect, in practice it is not very important. Meteoritic dolomite typically incorporates $MnCO_3$ > 2 mol% and $FeCO_3$ > 4 mol% (de Leuw et al. 2009; Tyra et al. 2016). Therefore, we do not expect large errors due to poor Mn (or Fe) quantification in natural meteoritic carbonate.

Change of RSF with depth

In a previous study by Doyle and others, the Mn/Cr RSF was shown to vary with depth during the analysis of olivine, a mineral that naturally incorporates trace amounts of Cr (Doyle et al. 2016). These analyses were performed in "spot mode", as is typical for ^{53}Mn-^{53}Cr geochemical analyses. The craters produced by Doyle et al. were 3 and 5 µm in diameter with a significantly greater depth/diameter ratio than were produced in our study, where the primary beam was rastered over a 50 µm x 50 µm area resulting in shallow (< 1µm deep) craters. Doyle et al. further found that the magnitude of the RSF variation changed depending upon the Fe content of the olivine: for an olivine of low Fe content (Fa_{10}), the value of the RSF increased by 10% over the course of the analysis, whereas for an olivine of higher Fe content (Fa_{34}) it increased only by only 4%. Because we have implanted Cr into the target, we cannot characterize any possible depth-dependent RSF variations for carbonates using the same method as has been applied to olivine.

Matrix effects are challenging to predict and model. As an example, in stable isotope analyses of $\delta^{18}O$ in carbonates of varying Fe content, increasing Fe content results in a bias towards higher values of $\delta^{18}O$ (Śliwiński et al. 2016a). In contrast, $\delta^{18}O$ in olivine would show the opposite relationship with the increasing Fe content (Isa et al. 2017). Therefore we do not make a quantitative attempt to use the variation in RSF during the sputtering of olivine to predict the behavior of the carbonate RSF.

In this work, we show that the RSF decreases from ~1.1 at 0 mol% Fe to 0.88 at 8-20 mol % Fe for an overall change of 19%. The magnitude of this effect is larger than the depth-induced RSF change observed in the olivine, although we do not know how carbonate would compare with olivine in terms of the degree of RSF variation with depth. As we continue to develop this method, we plan to conduct test analyses on implanted standards using smaller raster sizes (different crater aspect ratios) to assess the variability of the RSF in these different materials.

Effect of incorrect RSF usage

To illustrate the importance of selecting the appropriate RSF value on determination of initial $^{53}Mn/^{55}Mn$ in a carbonate, we consider a fictional dolomite with an inferred $^{53}Mn/^{55}Mn$ ratio of 4.00×10^{-6} before correction for matrix effects. Since the inferred $^{53}Mn/^{55}Mn$ ratio is inversely proportional to $^{55}Mn/^{52}Cr$, a smaller RSF value would result in a smaller true $^{55}Mn/^{52}Cr$ (Equation 2.2), and thus a higher $^{53}Mn/^{55}Mn$. If this hypothetical carbonate was corrected using an RSF value of 1.1 appropriate for a low-Fe dolomite, it would correspond to a $^{53}Mn/^{55}Mn$ ratio of 3.64×10^{-6} for an age, as calculated by Equation 2.1, of 3.9 Myr after the birth of the Solar System. On the other hand, if an RSF value of 0.88 is used as would be more appropriate for a high-Fe dolomite, the inferred $^{53}Mn/^{55}Mn$ ratio would be 4.55×10^{-6} corresponding to an age of 2.1 Myr after the birth of the solar system—a systematic difference of 1.8 Myr. Because the

^{53}Mn-^{53}Cr chronometer is used only within the first 15 Myr of the solar system's history, a systematic error of 1.8 Myr would represent a significant change to the interpretation of the chronology of hydrothermal alteration in the parent asteroid of a given meteorite.

Summary and Conclusions

We used ion implantation of a suite of terrestrial dolomite reference materials to show that the relative sensitivity factor for dolomite with 8-20% $FeCO_3$ is 0.88 ±0.04, consistent with previous estimates made for carbonates containing higher $FeCO_3$. At low Fe and Mn content, the RSF is ~1, although this value is associated with significant error due to uncertainties in the Mn concentration.

Acknowledgements

We thank Rosario Esposito for his assistance with the EPMA measurements, the Molecular Materials Research Centre at the Beckman Institute at Caltech and Bruce S. Brunschwig for the use of the Dektak XT stylus profilometer, and Kathrynn Haman for her assistance with the profilometer. We appreciate the detailed reviews provided by two anonymous reviewers—their attention and suggestions have improved this work. This work was supported by the NASA Earth and Space Science Fellowship NESSF19R 19-PLANET19R-0001 and the NASA Emerging Worlds program. The UCLA ion probe facility is partially supported by the NSF Instrumentation and Facilities Program.

Supplementary Materials

Supplementary Methods

Sample Selection

One large crystal fragment (~1 mm) of each carbonate composition was mounted into the Field's metal along with the NIST 612 and 614 glasses of similar size. The use of large crystal fragments was intended to allow space for multiple ~50×50 μm^2 rastered areas to be sputtered without approaching the contact between the mineral and the embedding material.

EPMA Methods

The goal of the EPMA analyses was to constrain the Fe and Mn concentrations of the rastered areas as closely as possible. Therefore we carried out two EPMA sessions: One session before ion implantation and depth profiling to assess the homogeneity of the mineral to determine its suitability for the analysis, and one session after the depth profiling to lower the detection limits and constrain the concentrations for heterogeneous materials.

Prior to ion implantation and depth profiling, each mounted carbonate was analyzed using the JEOL Superprobe EPMA. The beam was accelerated to 15 kV with a beam intensity of 10 nA. The beam was defocused to a diameter of 10 µm to limit heating, diffusion, and damage to the carbonate surface. The elements analyzed were Ca, Mg, Fe, and Mn, using the PETJ, TAPH, LIFH, and LIH crystals respectively. Each peak was counted for 20 seconds and each background was collected for 5 seconds. CaO was standardized using the NMNH calcite standard, MgO with the NMNH dolomite standard, FeO with the NMNH siderite standard, and MnO with the NMNH rhodochrosite standard. Each carbonate was analyzed multiple times to assess homogeneity of the sample. Under these conditions, the detection limit of Fe was

approximately 300 ppm, and the detection limit of Mn was approximately 450 ppm. The results of the first session are summarized in Table S1 below.

After depth profiling of the samples, the gold coating was carefully removed and each carbonate was re-analyzed by EPMA, focusing on regions adjacent to the rastered areas to determine the elemental compositions of the analyzed volumes more accurately. As the concentration of Mn and Fe is extremely low in the calcite, MS 1317, MS1317J, and MS 1305 material, we increased counting times and used higher beam current in order to lower the detection limit for Fe and Mn. The post-depth profiling EPMA conditions were similar to the conditions above except that the Fe and Mn peaks were collected for 80 seconds, the background was collected for 20 seconds, and the beam current was increased to 30 nA. The results of the second session are summarized in Table S2 below. Under these conditions, the detection limit of Fe and Mn was about 120 ppm. The calcite showed signs of beam damage during the analysis; however no Mn or Fe was detected. MS1318 was analyzed only one time to confirm that the new beam conditions gave Mn and Fe values consistent with the previous EPMA analysis.

The regions around the MS 1312 #1 and MS 1312 #2 regions were both analyzed with this stronger beam current to confirm that they were positioned within the intended high and low domains. We confirmed this as shown in Table S2, and use these Fe and Mn concentrations in the RSF calculations as they more closely reflect the composition of the mineral near the rastered area.

Mn Concentration calculation

To calculate the RSF using Equation 2.4, the concentration of Mn must be expressed as atoms/cm^3. To conform with usual practice in EPMA, we opted to present the Mn

concentrations in Tables 2.1 and 2.2 and Supplementary Tables 2.1 and 2.2 in the familiar units of mol % and ppm (μg Mn/ g). The conversion to atoms/cm^3 requires the known density of the material, which we present in Supplementary Table 2.3 below for the carbonates and NIST glasses used in our experiment. Uncertainties in the density for each material are of order 1% and thus are negligible relative to the other sources of uncertainty in calculating RSF values.

NIST Glass Density Calculation

As stated above, the density of the implanted material must be known to express the concentrations of Mn as atoms/cm^3. NIST does not certify the densities of its NIST 610 series glasses. To constrain the density of these glasses, we weighed unbroken discs of NIST 612, 614, and 616 glasses on a microbalance, then measured their dimensions using electronic calipers. As the discs were not perfectly circular, each disc's diameter was measured four times, and the average radius used to calculate the volume of the disc. Our measurement data is given in Supplementary Table 2.4. We do not claim that these densities are certified or representative of all NIST 610 series glass reference materials.

Supplementary Tables

Supplementary Table S2.1 Summary of elemental composition of carbonate minerals determined by electron probe microanalysis. Concentrations are reported in molar percent except when concentrations of Mn are reported in (ppm). Errors are reported as 2 SD molar % and incorporate the internal variation during analysis and the SD of repeated analyses. The detection limit of Fe and Mn is approximately 300 and 450 ppm respectively, and elements below the detection limit are marked "b.d." These analyses were performed using a 10 nA electron beam.

Session I	**Ca**	**2SD**	**Mg**	**2SD**	**Fe**	**2SD**	**Mn**	**2SD**
MS1305_1	50.6		48.3		0.9		(687)	
MS1305_2	51.5		47.3		1.0		(712)	
MS1305_3	50.7		48.0		1.1		(1217)	
	51.0	0.8	47.9	0.6	1.0	0.1	(872)	(698)
MS1312_1	49.9		24.1		20.8		5.1	
MS1312_2	49.9		26.3		18.2		5.5	
MS1312_3	49.1		29.8		15.6		5.4	
MS1312_4	50.5		28.2		12.9		8.4	
MS1312_5	50.5		23.6		19.8		6.2	
	50.0	0.7	26.4	2.4	17.5	3.0	6.1	1.3
MS1317J_1	50.1		48.4		1.4		834	
MS1317J_2	50.6		48.0		1.3		832	
MS1317J_3	51.0		47.5		1.4		920	
MS1317J_4	50.6		47.7		1.5		1039	
	50.6	0.6	47.9	0.6	1.4	0.1	906	725
MS1318_1	49.0		42.0		7.9		1.2	
MS1318_2	48.9		41.9		8.1		1.1	
MS1318_3	49.1		41.7		8.1		1.1	
MS1318_4	49.0		41.7		8.1		1.2	
MS1318_5	49.0		42.1		8.0		0.9	
	49.0	0.5	41.9	0.5	8.0	0.2	1.1	0.2
MS1317_1	50.9		49.0		b.d		623	
MS1317_2	51.2		48.7		b.d		b.d	
MS1317_3	51.8		48.0		b.d		831	
MS1317_4	52.2		47.8		b.d		b.d	
	51.5	0.8	48.4	0.8	-		-	
CAL_1	99.3		0.5		b.d		b.d	
CAL_2	99.5		0.5		b.d		b.d	
CAL_3	99.5		0.5		b.d		b.d	
CAL_4	99.5		0.4		b.d		b.d	
CAL_5	99.1		0.8		b.d		b.d	
	99.4	0.8	0.5	0.2	-		-	

Supplementary Table S2.2

Summary of elemental composition of carbonate minerals determined by electron probe microanalysis. Concentrations are reported in molar percent except when concentrations of Mn are reported in (ppm). Errors are reported as 2 SD molar % and incorporate the internal variation during analysis and the SD of repeated analyses. The detection limit of Fe and Mn is approximately 120 ppm, and elements below the detection limit are marked "b.d." These analyses were performed using a 30 nA electron beam.

Session II	**Ca**	**2SD**	**Mg**	**2SD**	**Fe**	**2SD**	**Mn**	**2SD**
MS1317_11	49.9		50.0		b.d		329	
MS1317_12	50.1		49.9		b.d		449	
MS1317_13	50.0		49.9		b.d		269	
MS1317_14	50.5		49.4		b.d		150	
MS1317_15	50.0		49.9		b.d		389	
	50.1	0.4	49.8	0.4	-		317	203
MS1318_1	48.0	0.5	42.7	0.3	8.2	0.2	1.1	0.2
calcite_1	99.4		0.6		b.d		b.d	
calcite_2	99.3		0.7		b.d		b.d	
calcite_3	99.2		0.7		b.d		b.d	
calcite_4	99.4		0.6		b.d		b.d	
calcite_5	99.3		0.7		b.d		b.d	
	99.3	0.4	0.7	0.1	-		-	
MS1305_1	49.5		49.7		0.7		510	
MS1305_2	49.5		49.7		0.8		570	
MS1305_3	49.3		49.9		0.7		390	
MS1305_4	49.7		49.1		1.0		749	
MS1305_5	49.8		49.1		1.0		569	
	49.5	0.3	49.5	0.4	0.9	0.1	557.5	270
MS1312_1_1	50.2		18.5		23.0		8.3	
MS1312_1_2	50.0		19.2		22.6		8.1	
	50.1	0.3	18.9	0.7	22.8	1.0	8.2	0.3
MS1312_2_1	49.5		22.2		21.6		6.8	
MS1312_2_2	49.6		22.3		21.8		6.3	
MS1312_2_3	49.9		20.9		22.5		6.8	
MS1312_2_4	49.8		21.8		21.7		6.7	
	49.7	0.4	21.8	0.7	21.9	0.9	6.6	0.2
MS1317J_1	50.3		48.0		1.5		0.2	
MS1317J_2	50.1		48.3		1.4		0.2	
MS1317J_3	50.3		48.1		1.4		0.1	
MS1317J_4	50.0		48.5		1.3		0.2	
MS1317J_5	50.4		48.1		1.3		0.2	
	50.2	0.3	48.2	0.3	1.4	0.1	0.2	0.04

Supplementary Table S2.3. Summary of material densities used to calculate the concentration of Mn as atoms/cm^3.

Material	Density (g/cm^3)	Reference
NIST 612	2.488	This work
NIST 614	2.486	This work
Calcite	2.71	Mindat.org
MS1317	2.8	Mindat.org
MS1317J	2.84	Mindat.org
MS1305	2.84	Mindat.org
MS1318	2.9	Mindat.org
MS1312 (both domains)	3.0	Mindat.org

Supplementary Table S2.4 Summary of dimension and mass measurements used in density calculations for NIST 610 series glasses.

	NIST 612	NIST 614	NIST 616
Diam. (cm)	1.262	1.405	1.313
	1.428	1.263	1.287
	1.263	1.404	1.291
	1.424	1.262	1.319
Mean Radius (cm)	0.672125	0.66675	0.65125
Width (cm)	0.308	0.324	0.156
Volume (cm^3)	0.43712	0.452502	0.20786
Mass (g)	1.08762	1.12471	0.50058
Density (g/cm^3)	2.488	2.486	2.408

Supplementary Figures S2.1-S2.5

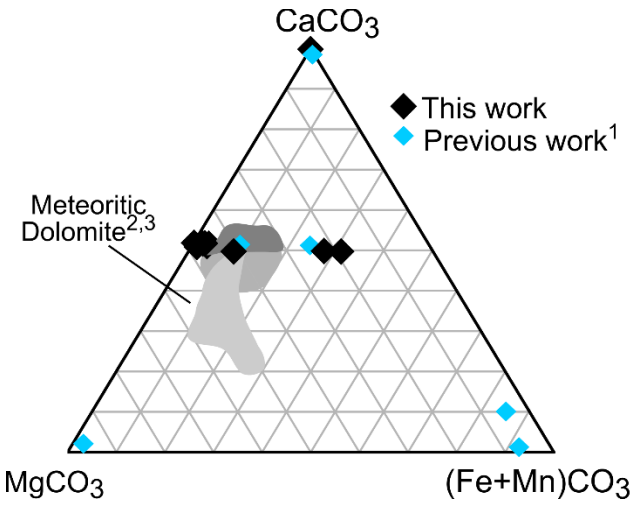

Supplementary Figure S2.1: Chemical composition of ion-implanted carbonate samples. Black diamonds represent dolomite analyzed in this study. Blue diamonds represent previously-implanted carbonates. Shaded regions represent dolomite in carbonaceous chondrite meteorites.[1](Steele et al., 2017) [2](Tyra et al. 2016) [3](De Leuw et al. 2010)

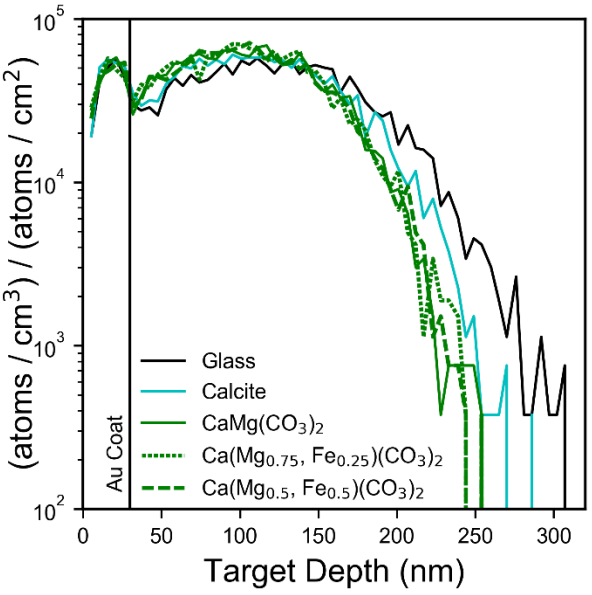

Supplementary Figure S2.2: Simulated implantation of $^{52}Cr+$ into glass, calcite, and various dolomite substrates. Simulated abundances of $^{52}Cr+$ ions implanted at 185 KeV into various targets. The $^{52}Cr+$ implantation peak occurs deeper in the glass substrate (black) than the calcite (blue) or dolomite (green, various dash types) due to the low density (2.33 g/cm^3) and amorphous structure of the glass. All dolomite substrates exhibit identical implantation profiles despite increasing Fe content (0-25 mol %) and mineral density (2.85-3.00 g/cm^3). The glass implantation profile also extends deeper into the target, which we again attribute to the material's lower density. The calcite peak occurs at approximately the same depth as the dolomites, but the full profile extends slightly deeper into the calcite target due to the lower density of calcite (2.71 g/cm^3) as compared to dolomite.

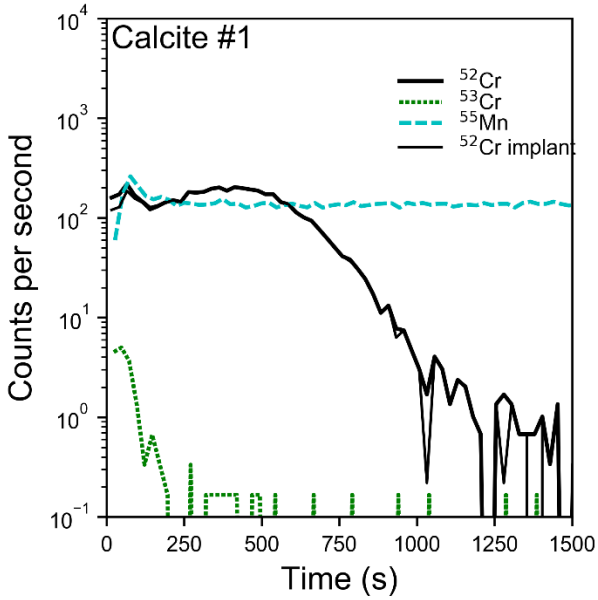
Calcite #1
^{52}Cr
^{53}Cr
^{55}Mn
^{52}Cr implant
Counts per second
Time (s)
10^{4}
10^{3}
10^{2}
10^{1}
10^{0}
10^{-1}
0
250
500
750
1000
1250
1500

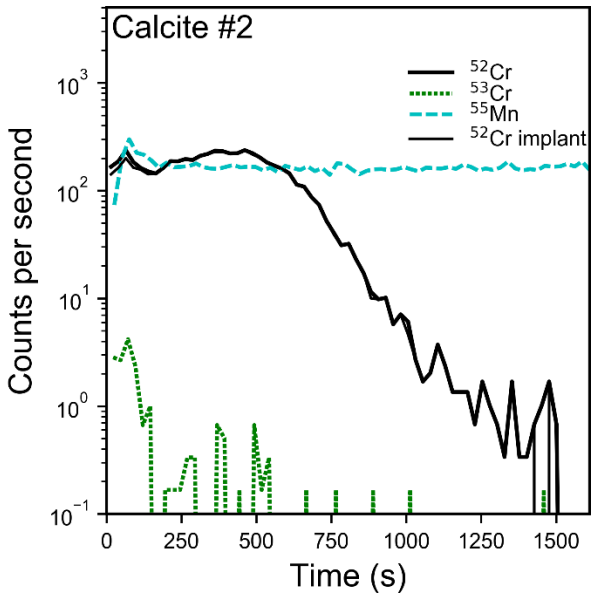
Calcite #2
^{52}Cr
^{53}Cr
^{55}Mn
^{52}Cr implant
Counts per second
Time (s)
10^{3}
10^{2}
10^{1}
10^{0}
10^{-1}
0
250
500
750
1000
1250
1500

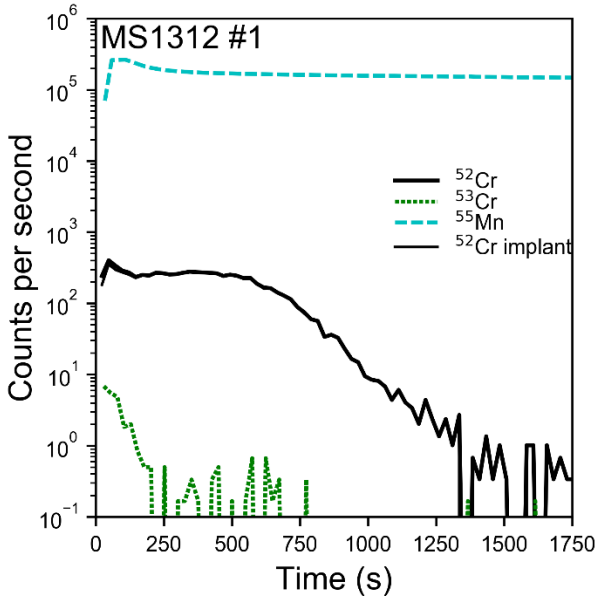
MS1312 #1
Counts per second
Time (s)
^{52}Cr
^{53}Cr
^{55}Mn
^{52}Cr implant

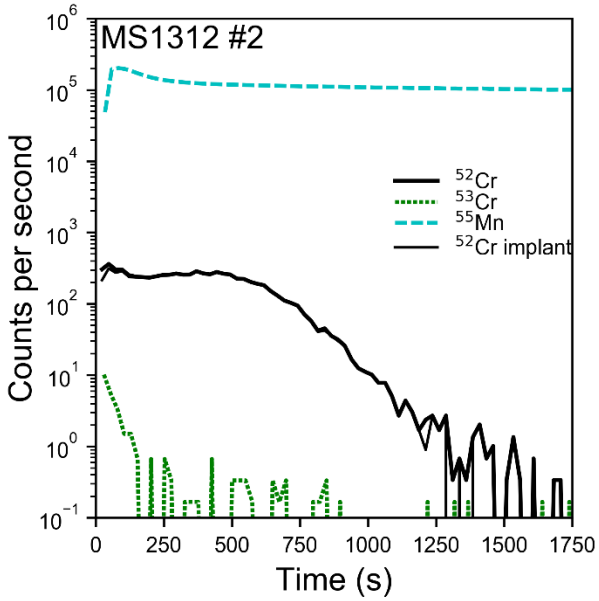
MS1312 #2
Counts per second
Time (s)
^{52}Cr
^{53}Cr
^{55}Mn
^{52}Cr implant

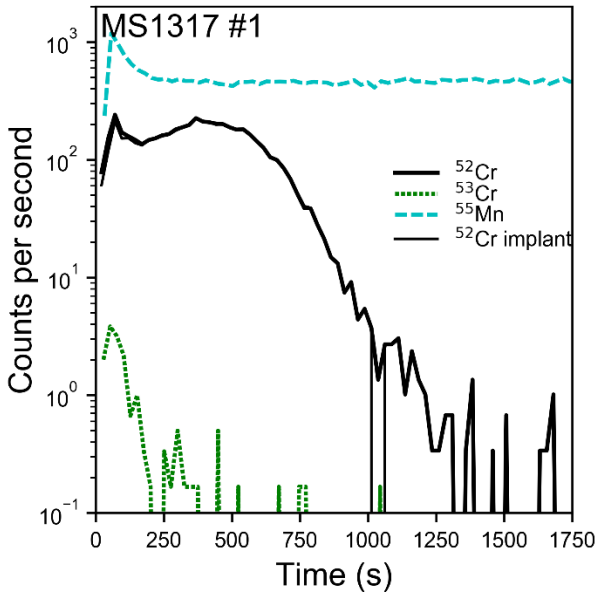
MS1317 #1
Counts per second
Time (s)
^{52}Cr
^{53}Cr
^{55}Mn
^{52}Cr implant

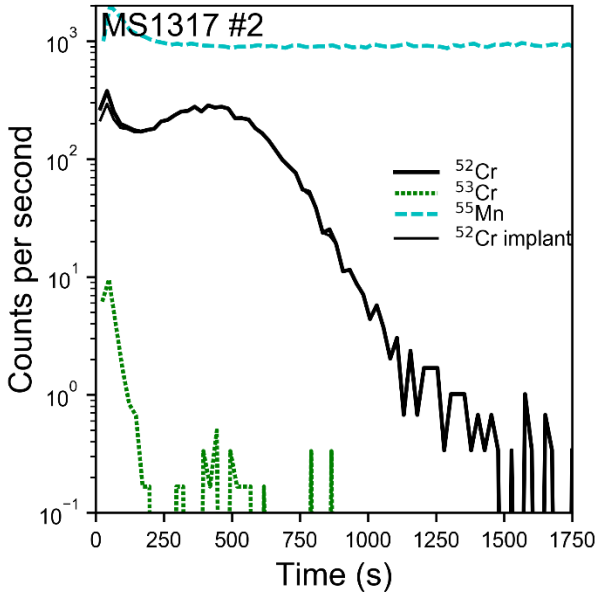
MS1317 #2
Counts per second
Time (s)
^{52}Cr
^{53}Cr
^{55}Mn
^{52}Cr implant

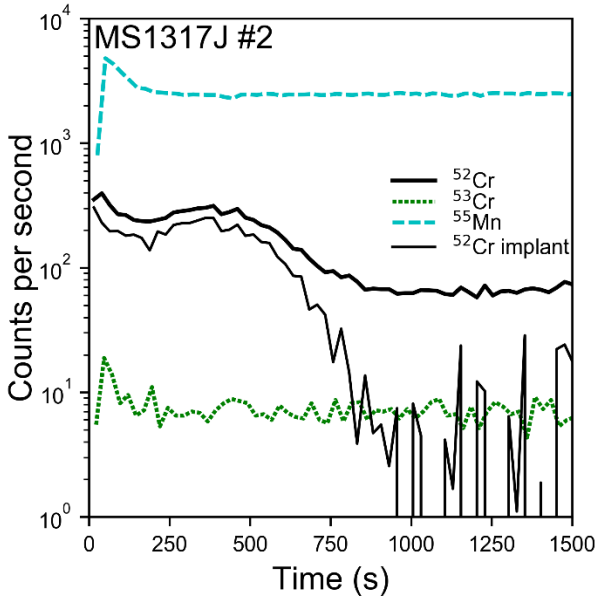
MS1317J #2
Counts per second
Time (s)
^{52}Cr
^{53}Cr
^{55}Mn
^{52}Cr implant

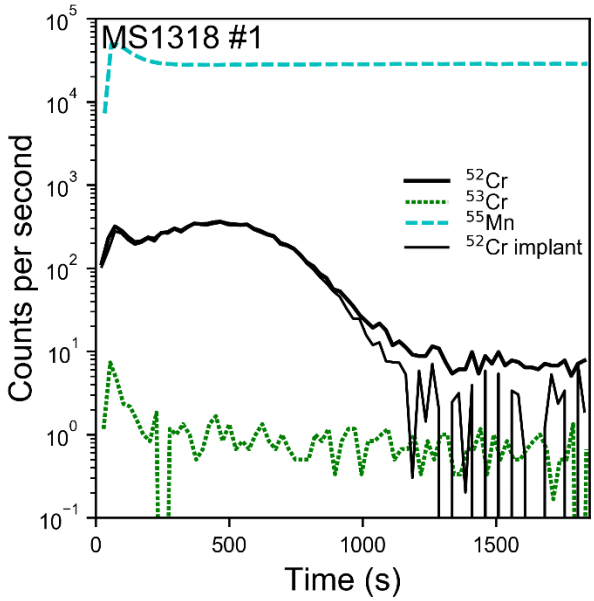
MS1318 #1
Counts per second
Time (s)
^{52}Cr
^{53}Cr
^{55}Mn
^{52}Cr implant

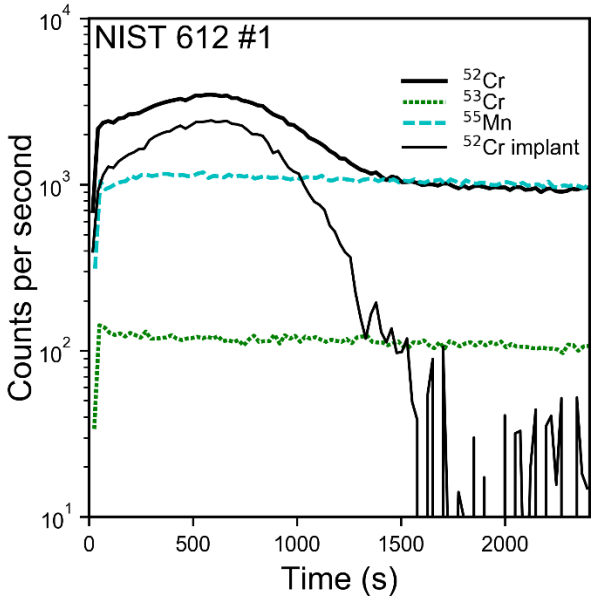
NIST 612 #1
^{52}Cr
^{53}Cr
^{55}Mn
^{52}Cr implant
Counts per second
Time (s)
10^4
10^3
10^2
10^1
0
500
1000
1500
2000

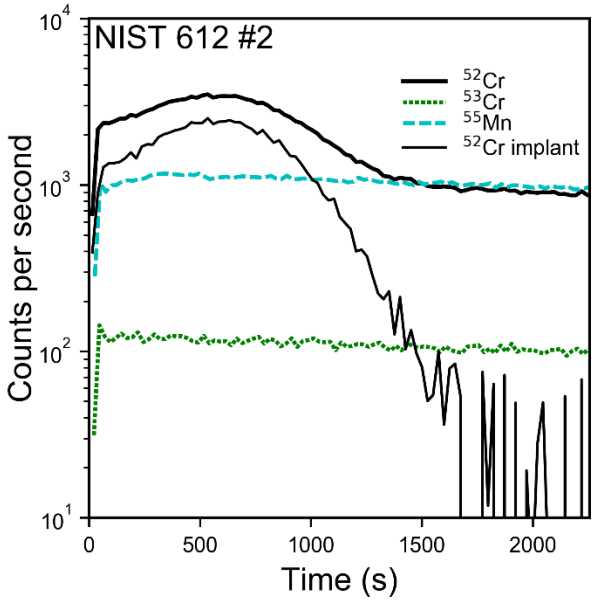
NIST 612 #2
^{52}Cr
^{53}Cr
^{55}Mn
^{52}Cr implant
Counts per second
Time (s)
10^4
10^3
10^2
10^1
0
500
1000
1500
2000

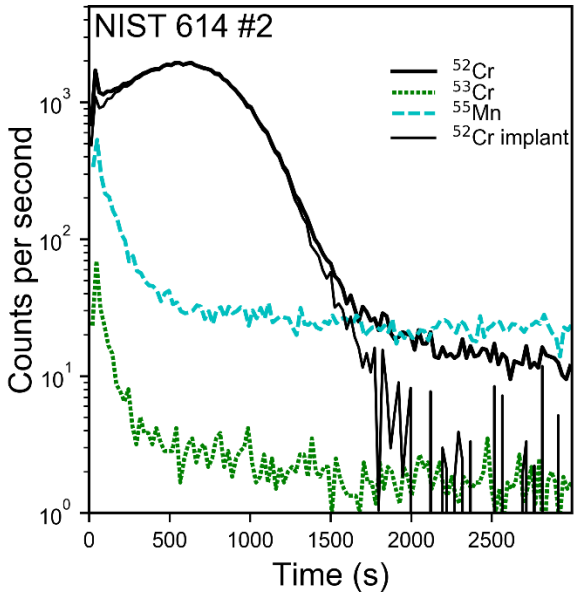
NIST 614 #2
^{52}Cr
^{53}Cr
^{55}Mn
^{52}Cr implant
Counts per second
Time (s)

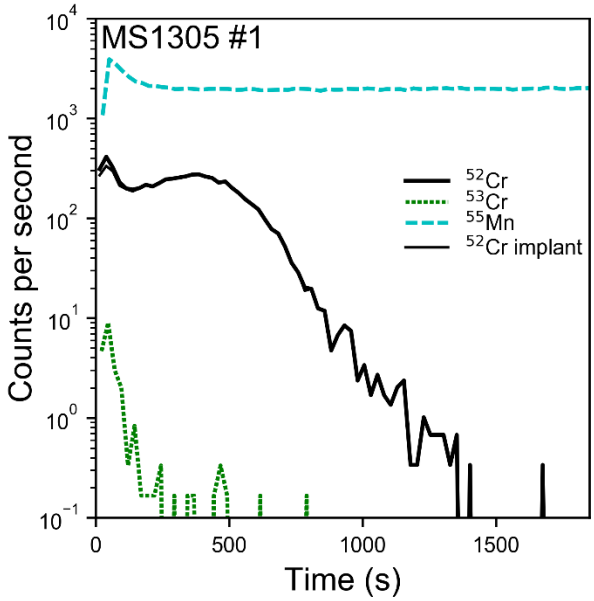
MS1305 #1
^{52}Cr
^{53}Cr
^{55}Mn
^{52}Cr implant
Counts per second
Time (s)

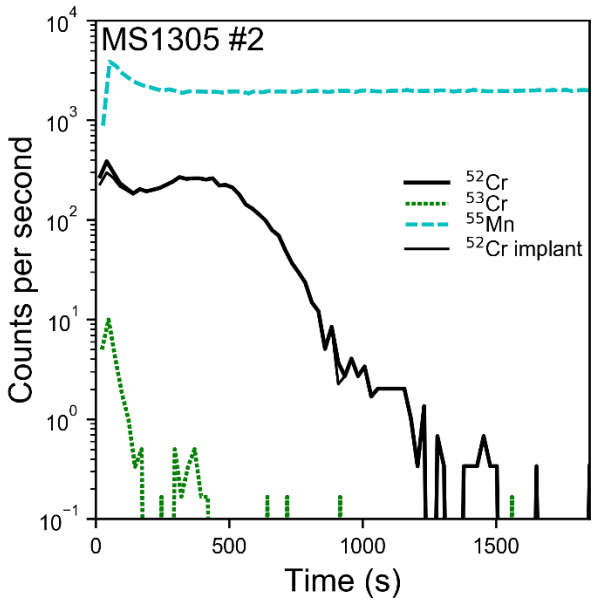

Supplementary Figures S2.3(A-M). Intensities of $^{52}Cr^{+}$, $^{53}Cr^{+}$, and $^{55}Mn^{+}$ recorded during depth profiling of standard NIST glasses, terrestrial calcite, and terrestrial dolomites. The heavy black line represents the intensity of $^{52}Cr^{+}$ including the implanted $^{52}Cr^{+}$ and the background Cr in the dolomite. The dotted green line represents the intensity of the background $^{53}Cr^{+}$. The dashed blue line represents the intensity of $^{55}Mn^{+}$. The thin black line represents the intensity of ^{52}Cr attributed to ion implantation.

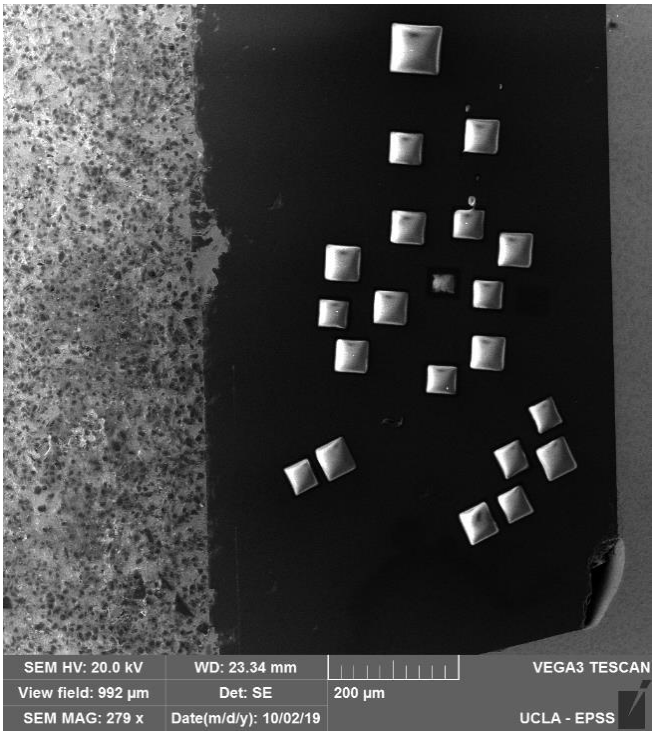

Supplementary Figure S2.4: Secondary Electron image of rastered areas in calcite.

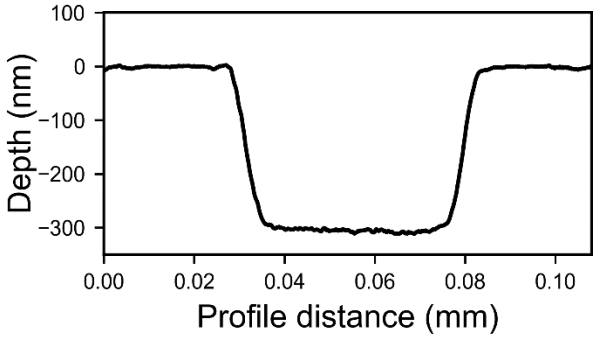

Supplementary Figure S2.5: Surface profile of the rastered area MS 1317 #1. Surface profile collected by the Dektak XT Stylus Profilometer. The depth of this profile was calculated to be 302 nm by the Bruker Vision64 software. The shape of the profile is typical.

Chapter 2 References

Amelin Y. 2008. U–Pb ages of angrites. *Geochimica et Cosmochimica Acta* 72:221–232. https://www.sciencedirect.com/science/article/pii/S0016703707005820.

Brennecka G. A., and Wadhwa M. 2012. Uranium isotope compositions of the basaltic angrite meteorites and the chronological implications for the early Solar System. *Proceedings of the National Academy of Sciences* 109:9299–9303. https://www.pnas.org/content/109/24/9299 (Accessed April 8, 2020).

Burnett D. S. et al. 2015. Ion Implants as Matrix-Appropriate Calibrators for Geochemical Ion Probe Analyses. *Geostandards and Geoanalytical Research* 39:265–276. https://onlinelibrary.wiley.com/doi/abs/10.1111/j.1751-908X.2014.00318.x.

Davis A. M., and McKeegan K. D. 2014. 1.11 - Short-Lived Radionuclides and Early Solar System Chronology. In *Treatise on Geochemistry (Second Edition)*, edited by Holland H. D., and Turekian K. K. Oxford: Elsevier. pp. 361–395 http://www.sciencedirect.com/science/article/pii/B9780080959757001133.

De LEUW S., Rubin A. E., and Wasson J. T. 2010. Carbonates in CM chondrites: Complex formational histories and comparison to carbonates in CI chondrites. *Meteoritics & Planetary Science* 45:513–530. http://onlinelibrary.wiley.com/doi/10.1111/j.1945-5100.2010.01037.x/abstract (Accessed December 1, 2015).

Doyle P. M., Jogo K., Nagashima K., Huss G. R., and Krot A. N. 2016. Mn–Cr relative sensitivity factor in ferromagnesian olivines defined for SIMS measurements with a Cameca ims-1280 ion microprobe: Implications for dating secondary fayalite. *Geochimica et Cosmochimica Acta* 174:102–121. http://www.sciencedirect.com/science/article/pii/S001670371500592X (Accessed January 3, 2017).

Fujiya W., Sugiura N., Hotta H., Ichimura K., and Sano Y. 2012. Evidence for the late formation of hydrous asteroids from young meteoritic carbonates. *Nature Communications* 3:627. http://www.nature.com/ncomms/journal/v3/n1/full/ncomms1635.html (Accessed October 2, 2015).

Fujiya W., Sugiura N., Sano Y., and Hiyagon H. 2013. Mn–Cr ages of dolomites in CI chondrites and the Tagish Lake ungrouped carbonaceous chondrite. *Earth and Planetary Science Letters* 362:130–142. http://www.sciencedirect.com/science/article/pii/S0012821X12006838 (Accessed October 2, 2015).

Glavin D. P., Kubny A., Jagoutz E., and Lugmair G. W. 2004. Mn-Cr isotope systematics of the D'Orbigny angrite. *Meteoritics & Planetary Science* 39:693–700. https://onlinelibrary.wiley.com/doi/abs/10.1111/j.1945-5100.2004.tb00112.x.

Isa J., Kohl I. E., Liu M.-C., Wasson J. T., Young E. D., and McKeegan K. D. 2017. Quantification of oxygen isotope SIMS matrix effects in olivine samples: Correlation with sputter rate. *Chemical Geology* 458:14–21. http://www.sciencedirect.com/science/article/pii/S0009254117301547.

Jilly C. E., Huss G. R., Krot A. N., Nagashima K., Yin Q.-Z., and Sugiura N. 2014. 53Mn-53Cr dating of aqueously formed carbonates in the CM2 lithology of the Sutter's Mill carbonaceous chondrite. *Meteoritics & Planetary Science* 49:2104–2117. http://onlinelibrary.wiley.com/doi/10.1111/maps.12305/abstract (Accessed December 7, 2015).

Jochum K. P. et al. 2011. Determination of Reference Values for NIST SRM 610–617 Glasses Following ISO Guidelines. *Geostandards and Geoanalytical Research* 35:397–429. https://onlinelibrary.wiley.com/doi/abs/10.1111/j.1751-908X.2011.00120.x.

de Leuw S., Rubin A. E., Schmitt A. K., and Wasson J. T. 2009. 53Mn–53Cr systematics of carbonates in CM chondrites: Implications for the timing and duration of aqueous alteration. *Geochimica et Cosmochimica Acta* 73:7433–7442. http://www.sciencedirect.com/science/article/pii/S001670370900581X (Accessed October 2, 2015).

Śliwiński M. G., Kitajima K., Kozdon R., Spicuzza M. J., Fournelle J. H., Denny A., and Valley J. W. 2016a. Secondary Ion Mass Spectrometry Bias on Isotope Ratios in Dolomite–Ankerite, Part I: δ18O Matrix Effects. *Geostandards and Geoanalytical Research* 40:157–172. http://onlinelibrary.wiley.com/doi/10.1111/j.1751-908X.2015.00364.x/abstract.

Śliwiński M. G., Kitajima K., Kozdon R., Spicuzza M. J., Fournelle J. H., Denny A., and Valley J. W. 2016b. Secondary Ion Mass Spectrometry Bias on Isotope Ratios in Dolomite–Ankerite, Part II: δ13C Matrix Effects. *Geostandards and Geoanalytical Research* 40:173–184. http://onlinelibrary.wiley.com/doi/10.1111/j.1751-908X.2015.00380.x/abstract.

Steele R. C. J., Heber V. S., and McKeegan K. D. 2017. Matrix effects on the relative sensitivity factors for manganese and chromium during ion microprobe analysis of carbonate: Implications for early Solar System chronology. *Geochimica et Cosmochimica Acta* 201:245–259. http://www.sciencedirect.com/science/article/pii/S001670371630624X (Accessed March 13, 2017).

Sugiura N., and Ichimura K. 2010. Mn/Cr relative sensitivity factors for sythetic calcium carbonate measured with a NanoSIMS ion microprobe. *Geochemical Journal* 44:e11-316.

Trinquier A., Birck J.-L., Allègre C. J., Göpel C., and Ulfbeck D. 2008. 53Mn–53Cr systematics of the early Solar System revisited. *Geochimica et Cosmochimica Acta* 72:5146–5163. http://www.sciencedirect.com/science/article/pii/S0016703708001774.

Tyra M., Brearley A., and Guan Y. 2016. Episodic carbonate precipitation in the CM chondrite ALH 84049: An ion microprobe analysis of O and C isotopes. *Geochimica et Cosmochimica Acta* 175:195–207. http://www.sciencedirect.com/science/article/pii/S0016703715006596 (Accessed January 8, 2016).

Usdowski E. 2009. Synthesis of Dolomite and Geochemical Implications. In *Dolomites*. John Wiley & Sons, Ltd. pp. 345–360 https://onlinelibrary.wiley.com/doi/abs/10.1002/9781444304077.ch19.

Virtanen P. et al. 2020. SciPy 1.0: fundamental algorithms for scientific computing in Python. *Nature Methods* 17:261–272. https://www.nature.com/articles/s41592-019-0686-2 (Accessed April 7, 2020).

Ziegler J. F., Ziegler M. D., and Biersack J. P. 2010. SRIM - The stopping and range of ions in matter (2010). *NIMPB* 268:1818–1823. https://ui.adsabs.harvard.edu/abs/2010NIMPB.268.1818Z/abstract (Accessed January 24, 2020).

Chapter 3.

Early aqueous alteration in the Outer Solar System recorded by Oxygen, Carbon, and Mn-Cr isotope systematics of CM and CI chondrites

McCain, K. A., Liu, M-C., Young, E. D., Brearley, A., McKeegan, K. D.

Abstract

The CM and CI carbonaceous chondrites record diverse conditions of aqueous alteration occurring on meteorite parent bodies. By measuring the carbon, oxygen, and ^{53}Mn-^{53}Cr isotopic systematics of secondary minerals such as carbonate and magnetite, the timing of aqueous alteration can be connected to details of the fluid's sources and evolution. Previous studies lacked suitable dolomite and breunnerite standards for ^{53}Mn-^{53}Cr dating, leading to outstanding questions about the timing of aqueous alteration. In this work, we present matrix-matched analyses of carbon, oxygen, and Mn-Cr isotopes of carbonates in the Alais, ALH 84034, and Boriskino carbonaceous chondrites. Alais dolomite formed less than 1 million years after CAI, suggesting formation on a small parent body or in a larger body which was later disrupted. Carbonate in ALH 84034 is frequently found replacing CAIs and chondrules and may inherit some oxygen and Mn-Cr isotopic characteristics of these inclusions. Boriskino carbonate recorded a complex sequence of fluid evolution, but brecciation has disturbed its Mn-Cr systematics.

Introduction

The CM (Mighei-type) and CI (Ivuna-type) carbonaceous chondrites contain abundant mineralogical evidence of organic-rich, aqueous fluid activity occurring on asteroids early in the history of the solar system. Although meteorites of these classes are relatively rare, hydrated and organic-rich bodies are thought to make up a majority of asteroids, as evidenced by the high abundance of hydrated interplanetary dust particles (Bradley and Brownlee 1991) and observations of numerous C- and D-type asteroids in the outer solar system (DeMeo and Carry 2014). The near-Earth asteroids Ryugu and Bennu, targets of JAXA and NASA sample-return missions, respectively, also bear similarities to the CM and CI carbonaceous chondrites (Lauretta et al. 2017; Watanabe et al. 2019; Yada et al. 2022).

The CM and CI chondrites record a diverse range of alteration conditions. The CM chondrites show a near-complete petrologic range from completely-hydrated CM1 material (Zolensky et al. 1997) to only slightly-altered CM 2.9 material (Hewins et al. 2014; Rubin 2015; Rubin et al. 2007; Vacher et al. 2017). The CM2 chondrites are composed of Fe-rich phyllosilicate matrix and anhydrous inclusions such as CAIs and chondrules that have experienced varying degrees of aqueous alteration and replacement by secondary minerals such as phyllosilicates, sulfides, and carbonates (Rubin et al. 2007). CM1 material, (alternatively, CM2.0 (Rubin et al. 2007)), has phyllosilicate fractions/total silicate ratios of ≥~0.90 (Russell et al. 2022), and typically contains less calcite and more magnetite and dolomite than CM2 material (King et al. 2017).

To better understand the nature and timing of the various styles of fluid-rock interaction that altered the primary minerals accreted by the parent asteroids of the carbonaceous chondrites, we investigated the mineralogy, chemistry, and isotopic compositions of the secondary minerals

produced by this alteration on the parent body. Because carbonate strongly fractionates Mn from Cr as it precipitates from an aqueous fluid, we can use the short-lived ^{53}Mn-^{53}Cr system ($t_{1/2}$=3.7 million years) to date secondary carbonate minerals, including Ca-carbonate ($CaCO_3$), dolomite ($CaMg(CO_3)$, and breunnerite ($(Mg,Fe,Mn)CO_3$). These dates constrain the timing of fluid activity, as carbonate requires liquid water to form. Measurements of the oxygen isotopic compositions of carbonate and magnetite and the carbon isotopic compositions of carbonate minerals can provide additional insight into the sources of the fluid, the temperature of alteration, and the relative formation sequence of various secondary minerals. As magnetite and carbonate are small and petrographically diverse, these analyses are best performed in-situ at high spatial resolution using Secondary Ion Mass Spectrometry (SIMS, or ion microprobe) to sputter materials from individual mineral grains while preserving their petrologic context.

The oxygen isotopic systematics of aqueous alteration products in CM and CI chondrites have been studied extensively (Clayton and Mayeda 1999; Fujiya et al. 2015; Lee et al. 2013, 2014; Piralla et al. 2020; Rowe et al. 1994; Telus et al. 2019; Tyra et al. 2012, 2016, Vacher et al. 2017, 2018; Verdier-Paoletti et al. 2017), revealing the sequence of alteration as ^{17,18}O-enriched water with positive Δ^{17}O (Sakamoto et al. 2007) reacts with ^{16}O-rich nebular silicates and oxides (e.g. CAIs, chondrules, and fine-grained matrix) with negative Δ^{17}O (Leshin et al. 1997; Liu et al. 2022; MacPherson 2014; Piralla et al. 2020; Scott and Krot 2014). Secondary minerals formed early in the process of aqueous alteration have higher Δ^{17}O than minerals formed later, as water and approach O isotopic equilibrium. Most in-situ studies have focused on Ca-carbonates (Fujiya et al. 2015, 2016, 2019; Tyra et al. 2012) as accurate measurements of the oxygen isotopic compositions of dolomite require standards which closely match the chemical composition of the target mineral (e.g. are ‘matrix-matched’) (Śliwiński et al. 2016a, 2017). This

has led to a relative paucity of matrix-matched O isotopic data for dolomite compared to Ca-carbonate.

The carbon isotopic compositions of carbonate capture the contributions of various C sources to the fluids, including ^{13}C-poor soluble and insoluble organic matter (Alexander et al. 2007; Gilmour 2014), ^{13}C-rich CO_2/CO ices (Fujiya et al. 2019; Hässig et al. 2017), and isotopically anomalous presolar graphite and SiC grains with $^{12}C/^{13}C$ ranging from ~2-7200 ((Hynes and Gyngard 2009). Reactions occurring within the fluid, such as oxidation of organic material (Fujiya et al. 2015; Vacher et al. 2017), CO_2-CH_4 equilibrium at various temperatures (Alexander et al. 2015; Telus et al. 2019), and methane formation during serpentinization (Guo and Eiler 2007; Telus et al. 2019; Tyra et al. 2016; Vacher et al. 2018) can also shift C isotopic compositions.

The Mn-Cr system can constrain the timing and duration of the alteration process, and these ages also place constraints on the accretion time of the meteorite's parent body. Carbonate minerals are an ideal target for this analysis, as they readily incorporate Mn while excluding Cr during their formation. This leads to large excesses in ^{53}Cr that can be used to infer the $^{53}Mn/^{55}Mn$ ratio in the fluid at the time of carbonate formation. Previous studies of ^{53}Mn-^{53}Cr ages of carbonates in CM and CI chondrites have suggested that most carbonate in these meteorites formed between 4-6 Ma after CAI formation, leading to an inference that they formed in large (>50 km radius) parent bodies (Fujiya et al. 2012, 2013; Jilly et al. 2014; Lee et al. 2012; de Leuw et al. 2009; Visser et al. 2020). However, inferring the $^{55}Mn/^{53}Mn$ ratios in carbonate using in-situ SIMS techniques requires matrix-matched standards to constrain the Mn/Cr ratio accurately, particularly with regards to the Fe content of the carbonate (McCain et al. 2020; Steele et al. 2017; Sugiura and Ichimura 2010). Previous studies measuring dolomite and

breunnerite were performed using calcite or olivine standards to determine the relative sensitivity factors (RSFs) needed to convert the measured ion ratio, Mn^+/Cr^+, to atomic Mn/Cr. Because the RSF depends on the target mineral's major element chemistry, use of standards which do not match the target mineral can affect the accuracy of the determination of the slope of an isochron, and therefore the inferred age of the carbonate (McCain et al. 2020; Steele et al. 2017). In this work, we used ion-implanted calcite, dolomite, and breunnerite standards to measure the Mn/Cr ratio in dolomite, Ca-carbonate, and breunnerite in CM and CI chondrites.

We selected the CI1 chondrite Alais, the CM2 chondrite Boriskino, and the CM1 chondrite ALH 84034 for this study because they all contain highly aqueously altered material, with abundant dolomite suitable for dating by SIMS. By specifically investigating dolomite-bearing meteorites, we aimed to use our advances in standard development to better understand the most fluid-rich environments in the early solar system.

Methods

Petrographic Characterization

Prior to ion microprobe analysis, polished sections of Alais, Boriskino, and ALH 84034 were coated with a ~20 nm carbon coating and mapped using the Vega3 scanning electron microscope (SEM) at UCLA equipped with an EDAX energy-dispersive (EDS) x-ray detector. Additional back-scattered electron (BSE), cathodoluminescence (CL), and electron probe microanalysis (EPMA) analyses of the ALH 84034 section were performed using the JEOL 8200 Electron Probe Microanalyzer at the University of New Mexico. Ca-carbonates were categorized as Mn-rich or Mn-poor based the presence of absence of a Mn peak during EDS spectroscopy (detection limit ~ 0.1 mol%) and the presence or absence of CL activity in order to determine

their suitability for Mn-Cr dating, as Mn-poor calcite typically does not have sufficient Mn to produce a notable ^{53}Cr excess.

In-situ oxygen, carbon, and Mn-Cr isotopic compositions of carbonates and magnetite were analyzed using the UCLA CAMECA ims-1290 ion microprobe. The Cs microbeam ion source was used for the O and C isotopic analyses, which preceded the Mn-Cr spot analyses which were sputtered by an $^{16}O_3^-$ primary ion beam generated by an Hyperion-II oxygen plasma source (Liu et al. 2018). After SIMS analysis, all sputtered pits were examined with the Tescan Vega3 SEM at UCLA. Analysis pits which overlapped inclusions, cracks, or voids were discarded. In all stable isotope analyses of carbonate, calcite and a suite of 4 dolomite standards of various Fe compositions were measured to quantify the instrumental mass fractionation (IMF) as a function of Fe content. For details of the standards used, see the Supplementary Materials. After ion microprobe analysis, the major element composition of each carbonate was measured using the JEOL Superprobe electron microprobe analyzer (EPMA) at UCLA at an accelerating voltage of 15 kV and the electron beam defocused to a 10 μm diameter to avoid damage to the carbonate minerals.

O isotope analyses of carbonate and magnetite

The oxygen isotopic compositions of carbonate and magnetite were measured using a Cs^+ ion beam with a 20 kV total accelerating voltage. Based on the size of the target mineral, we used one of two primary beam conditions: a ~800 pA beam with a ~10 μm spot and a ~60 pA beam with a ~3 μm spot. The oxygen isotopic compositions are reported as ‰ deviations relative to standard mean ocean water (SMOW). The deviation from the terrestrial fractionation line is expressed as $\Delta^{17}O = \delta^{17}O_{SMOW} - 0.52 \times \delta^{18}O_{SMOW}$. For the 800 pA condition, secondary ions were measured simultaneously using two Faraday cups (FCs, for $^{16}O^-$ and $^{18}O^-$) and an electron

multiplier (EM, for $^{17}O^-$). The mass resolution was set to ~5800 for $^{17}O^-$ in order to resolve $^{17}O^-$ from $^{16}OH^-$. For the 60 pA condition, secondary ions were collected simultaneously using one FC for the $^{16}O^-$ ions and two EMs for $^{17}O^-$ and $^{18}O^-$ under a mass resolution of ~ 5600 for $^{17}O^-$ and ~2500 for $^{16}O^-$ and $^{18}O^-$. Ion intensities were corrected for background (FC) or deadtime (EM) as appropriate for each detector type. A normal incidence electron gun was used for charge compensation.

Because the magnitude of the SIMS instrumental mass fractionation (IMF) of oxygen isotope analyses in dolomite varies with mineral chemistry (Śliwiński et al. 2016a), each dolomite analysis was corrected for IMF by comparison to a suite of four dolomite reference materials with $FeCO_3$ content ranging from 0-21 mol %. Prior to each set of analyses, all four dolomite reference materials were analyzed and an exponential fit for the instrumental mass fractionation as a function of Fe content was constructed using the curve_fit function from the SciPy Optimization Module (Virtanen et al. 2020). During data reduction, the IMF for $\delta^{18}O$ and $\delta^{17}O$ was corrected according to the daily IMF model according to the Fe content of each target dolomite similar to the procedure outlined by Śliwiński et al., 2016a. From day to day and session to session, the IMF model for $\delta^{18}O$ varied by less than 0.5 ‰ in the relevant range of dolomite compositions. No significant difference was found between the IMF model for $\delta^{17}O$ as derived from the measurements and an IMF model for $\delta^{17}O$ inferred from $\delta^{18}O$ based on an assumed mass-dependent fractionation. Each Ca-carbonate analysis was corrected using a calcite reference material. The isotopic and chemical compositions of our carbonate reference materials, along with typical $^{16}O^-$ count rates for each material under both primary beam conditions, can be found in the Supplementary Materials (Table S3.1).

Each magnetite analysis was corrected for instrumental mass fractionation by comparison to an Afrique Magnetite standard, with Burma spinel and San Carlos olivine reference materials serving as secondary reference materials. We did not constrain the effect of crystal orientation of magnetite on the instrumental mass fractionation, which has been previously estimated to be up to several permil depending upon the relative orientations of the magnetite crystal and the incoming primary beam (Huberty et al. 2010). We can estimate the crystal orientation of some of our analyses, as many were performed on the flat faces of magnetite plaquettes which correspond to the {100} crystal plane (Chan et al. 2016), but the orientation of our magnetite reference material is not known. Due to this potential confounding effects on the mass-dependent fractionation of $\delta^{18}O$, we do not interpret the range of $\delta^{18}O$ in magnetite and limit our discussion to the mass-independent $\Delta^{17}O$ value which is unaffected by crystal orientation.

C isotope analyses of calcite and dolomite

Prior to the C isotopic analysis, the carbon coating on the ALH 84034 section was removed and replaced by a 30 nm Au coating. In-situ analyses of carbon isotopes of calcite and dolomite were performed using a focused Cs^+ ion primary beam of ~1 nA. Secondary $^{12}C^-$ and $^{13}C^-$ ions were simultaneously detected using an FC and an EM respectively. A normal incidence electron gun was used for charge compensation. The instrumental bias was corrected by using the same suite of calcite and dolomite standards described for the O isotope analyses above following the IMF correction procedure outlined by (Śliwiński et al. 2016b) Errors represent 2σ analytical uncertainty, including the internal measurement precision and the external reproducibility for standard measurements summed in quadrature.

Mn-Cr analyses of calcite, dolomite, and magnesite

In-situ analyses of the $^{55}Mn/^{52}Cr$ and $^{53}Cr/^{52}Cr$ ratio were performed using focused O_3^- ion beams of ~150 pA, 300 pA, 500 pA, and 1 nA. For the 1 nA condition, secondary $^{52}Cr^+$, $^{53}Cr^+$, and $^{55}Mn^+$ ions were all collected simultaneously by using two EMs (for $^{52}Cr^+$ and $^{53}Cr^+$) and an FC (for $^{55}Mn^+$). The spectrometer was set to a mass-resolving power (MRP) of ~5500 to separate $^{52}Cr^+$ from $^{28}Si^{24}Mg^+$ and $^{53}Cr^+$ from $^{52}CrH^+$. For the 150, 300, and 500 pA conditions, secondary $^{52}Cr^+$ and $^{53}Cr^+$ were collected simultaneously for 20 seconds using two EMs, and then $^{55}Mn^+$ was collected for 2 seconds using an EM in peak-switching mode. Due to the long analysis times for the 150, 300, and 500 pA conditions, the energy distribution was periodically recentered. Analysis spots were presputtered using a 4-5 µm raster to remove surface contamination before focusing the beam to a 2 × 2 µm raster or point spot for the analysis. The dynamic transfer optic system (DTOS) was activated for analyses performed using the 2 × 2 µm raster analysis condition. The IMF for Cr isotopic ratios for each condition was corrected by repeated measurements of the 1317J dolomite, which contains 2.9 mol% Fe and trace amounts of terrestrial Cr ($^{53}Cr/^{52}Cr = 0.113459$) (Papanastassiou 1986).

Samples

Petrology of Alais

We acquired two small fragments of Alais totaling 26 mg from the Field Museum of Natural History, from which three polished sections were prepared at Leek Petrographics. The matrix of our Alais samples are dominated by Mg-rich phyllosilicates, though some clasts can be found with more Fe-rich phyllosilicate compositions indicating our sections (designated ALA-1, ALA-2, and ALA-3), similar to other Alais samples, are not completely homogeneous on the

mm-scale (Alfing et al. 2019). Anhydrous silicates in Alais are rare and limited to small (<30 μm) forsterite and Mg-rich pyroxene grains found isolated in the meteorite matrix. We find a variety of dolomite morphologies in Alais, as shown in Figure 3.1. A dolomite vein ~600 μm long and up to 75 μm wide (Figure 3.1a) was visible in two 100 μm-thick sections, leading us to infer that the vein is at least 100 μm thick. Magnetite can be found in three main morphologies, illustrated in Figure 3.1b-3.1d. The most abundant morphology is stacked plaquettes, which frequently appear to fill fractures and are also found in close association with dolomite (Figure 3.1b), including the dolomite vein (Fig 3.1a). Clumps of framboidal magnetite are also common and found in clusters up to 100 μm across, with individual magnetite crystals approximately 0.5 μm in diameter (Figure 3.1c). Spherulitic magnetite is also found with diameters between 10-25 μm (Figure 3.1d). A small magnetite-rich clast contains abundant rounded dolomites embedded within magnetite, as shown in Figure 3.1e. One dolomite in section ALA-3 contains a breunnerite inclusion (Figure 3.1f). Dolomite in Alais exhibits a narrow range of Fe content from 4 to 5 mol % $FeCO_3$ and a wider range of Mn content (1-5 Mol% $MnCO_3$), suggesting that the fluid's chemical composition varied during dolomite precipitation (Tables 3.3. and 3.5).

Figure 3.1. SEM images of dolomite (Dol) and magnetite (Mgt) in Alais. Dolomite found in a vein (a) and fracture-filling dolomite (b) are frequently associated with stacked placquette magnetite. Framboidal magnetite (c) and spherulitic magnetite (d) are also present. (e) A clast containing round dolomites embedded in magnetite. (f) Dolomite grain with breunnerite inclusion (black arrow). White arrows indicate ^{53}Mn-^{53}Cr analysis pits. Red arrows indicate O isotope analysis pits. Dolomites are outlined in yellow.

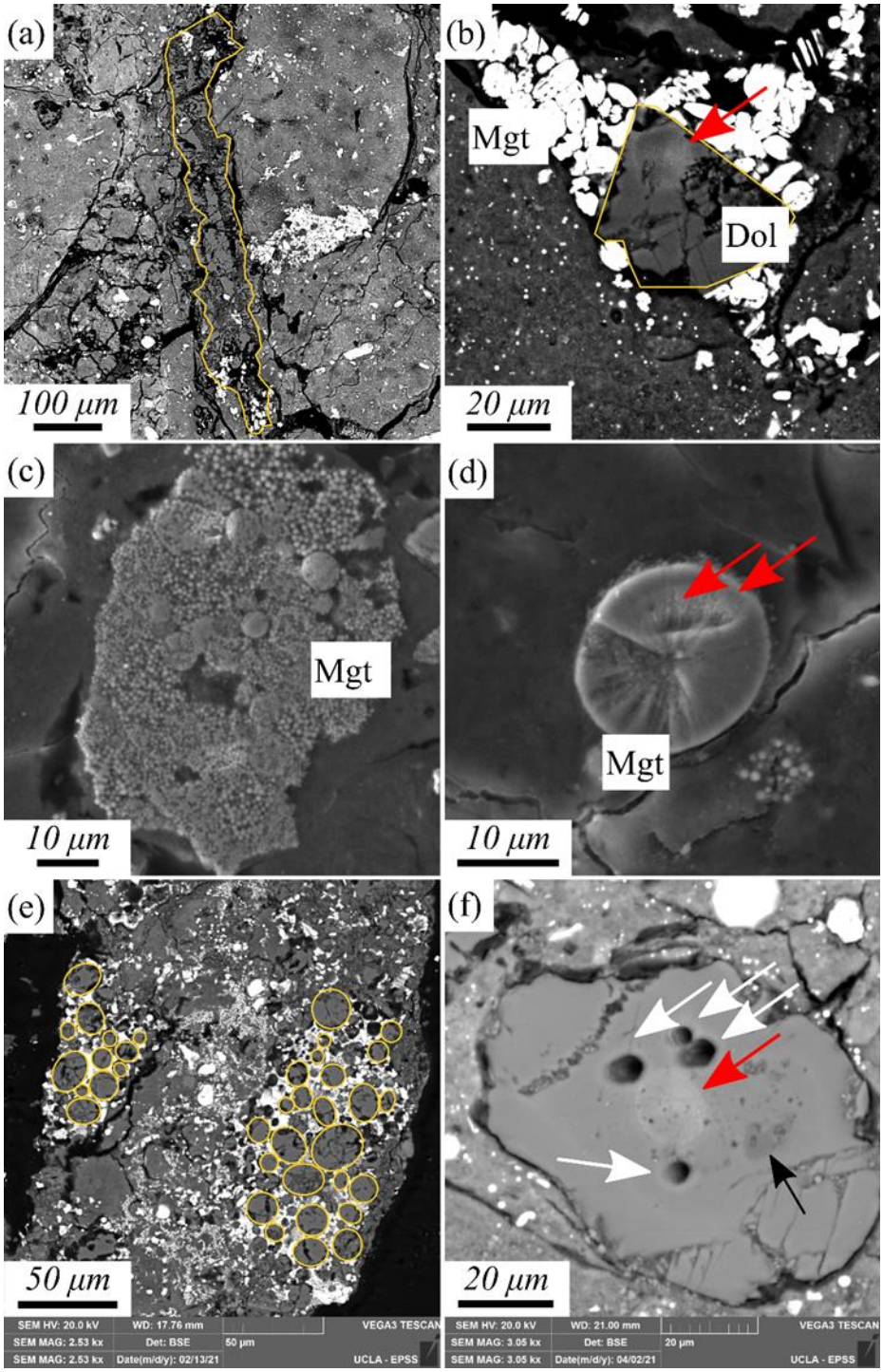

Petrology of ALH 84034

The detailed petrology of the ALH 84034 section and its carbonate mineralogy have been described previously as a completely-pseudomorphed CM breccia which contains a few clasts and fragments of less-altered material (Brearley and Hutcheon 2000; Llorca and Brearley 1992). Type 1 calcites (Figure 3.2a), which have been interpreted as having formed as cements in pore spaces during early stages of aqueous alteration (Lee et al. 2014; Tyra et al. 2012, 2016), can be found isolated in the matrix. Dolomite in ALH 84034 is often found as complex, fractured aggregates potentially crushed during brecciation (Figure 3.2b, 2f) that exhibit a wide range of Fe contents and contain phyllosilicate inclusions (Figure 3.2, red arrows). A pseudomorphed refractory inclusion (Brearley and Hutcheon 2000) contains calcite (RI calcite), dolomite, and Al-rich phyllosilicate (purple phase in Figure 3.2d). (Figure 3.2c-d). One large, round dolomite (Figure 3.2e) appears to pseudomorph a chondrule, containing phyllosilicates which resemble the morphology of mesostasis along with FeS inclusions.

Figure 3.2. SEM images of calcite and dolomite in ALH 84034. (a) Type 1 calcite. (b) Fe-poor dolomite aggregate with FeS and phyllosilicate inclusions. (c) BSE image of refractory inclusion pseudomorphed by phyllosilicate and carbonate. (d) X-ray map (Red = Mg, G = Ca, B = Al) of refractory inclusion pseudomorphed by phyllosilicate, calcite (Cal), and dolomite (Dol), with relict spinel (Sp). (e) Dolomite replacing large round object, with phyllosilicate interstices. (f) Fe-rich dolomite aggregate. Red arrows indicate phyllosilicate found in dolomite.

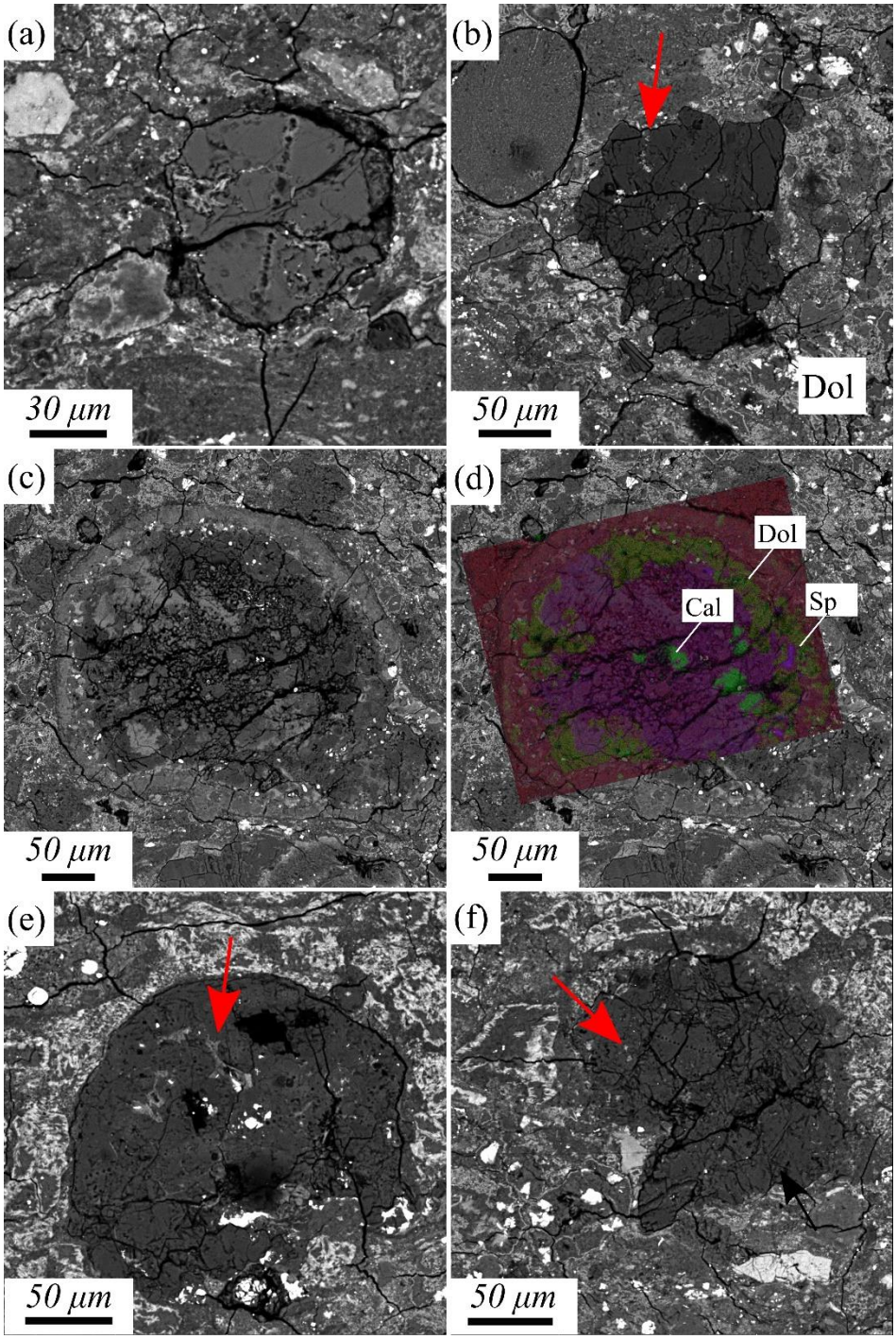

Petrology of Boriskino

Boriskino is a genomict breccia which has experienced shock pressures of 10-30 GPa and contains CM1 and CM2 clasts that experienced various degrees of aqueous alteration inferred to have taken place both prior to and after impact brecciation (Vacher et al. 2018; Verdier-Paoletti et al. 2019). We acquired a small, fully fusion-crusted fragment of Boriskino with a mass of 326 mg from the Field Museum of Natural History, from which 4 polished sections were prepared by Leek Petrographics. We selected the BOR-3 section for further study as it contained the greatest diversity of clast types and carbonates with varying compositions and morphologies. Carbonate and magnetite in Boriskino are shown in Figure 3.3. Type 1 calcite with diameters ranging from 50 to 60 μm in diameter is abundant in the main lithology (Figure 3.3a), a CM2 lithology containing partially pseudomorphed chondrules and refractory inclusions and characterized by a strong petrofabric. The main lithology, which we will refer to as CM2-1, is similar to Lithology A reported by (Verdier-Paoletti et al. 2019). The main lithology also contains an isolated dolomite grain (Figure 3.2b), an extremely large Ca-carbonate grain ('CC05', Figure 3.3c), and isolated round grains of magnetite (Figure 3.3d).

A CM1 lithology contains abundant Ca-carbonate resembling Type 2 calcites (Figure 3.3e, white dotted outline), which are calcite aggregates that contain FeS inclusions, often pseudomorph chondrule silicates, and represent a later stage of calcite formation than Type 1 calcite (Lee et al. 2014; Tyra et al. 2012). This lithology is characterized by the presence chondrules pseudomorphed to Type 2 calcite and Mg-rich phyllosilicate, an absence of FeS in the matrix, and a lack of petrofabric. We refer to this lithology as CM1-1. Dolomite (shown with yellow outline in Figure 3.3f) can also be found with calcite (white dotted outline in Figure 3.3f) pseudomorphing a round object in a CM1 lithology similar CM1-1, referred to as CM1-1a.

Fig. 3.3. Ca-carbonate, dolomite, and magnetite in Boriskino. Type 1 calcite (a), isolated dolomite (b), large Ca-carbonate (c), and magnetite (d) are all found in the main CM2 lithology. Type 2 calcite (e) and a round object (f) pseudomorphed by dolomite (yellow outline) and calcite (white outline) are found in CM1 lithologies (see text). White arrows indicate ^{53}Mn-^{53}Cr analysis pits. Red arrows indicate O isotope analysis pits.

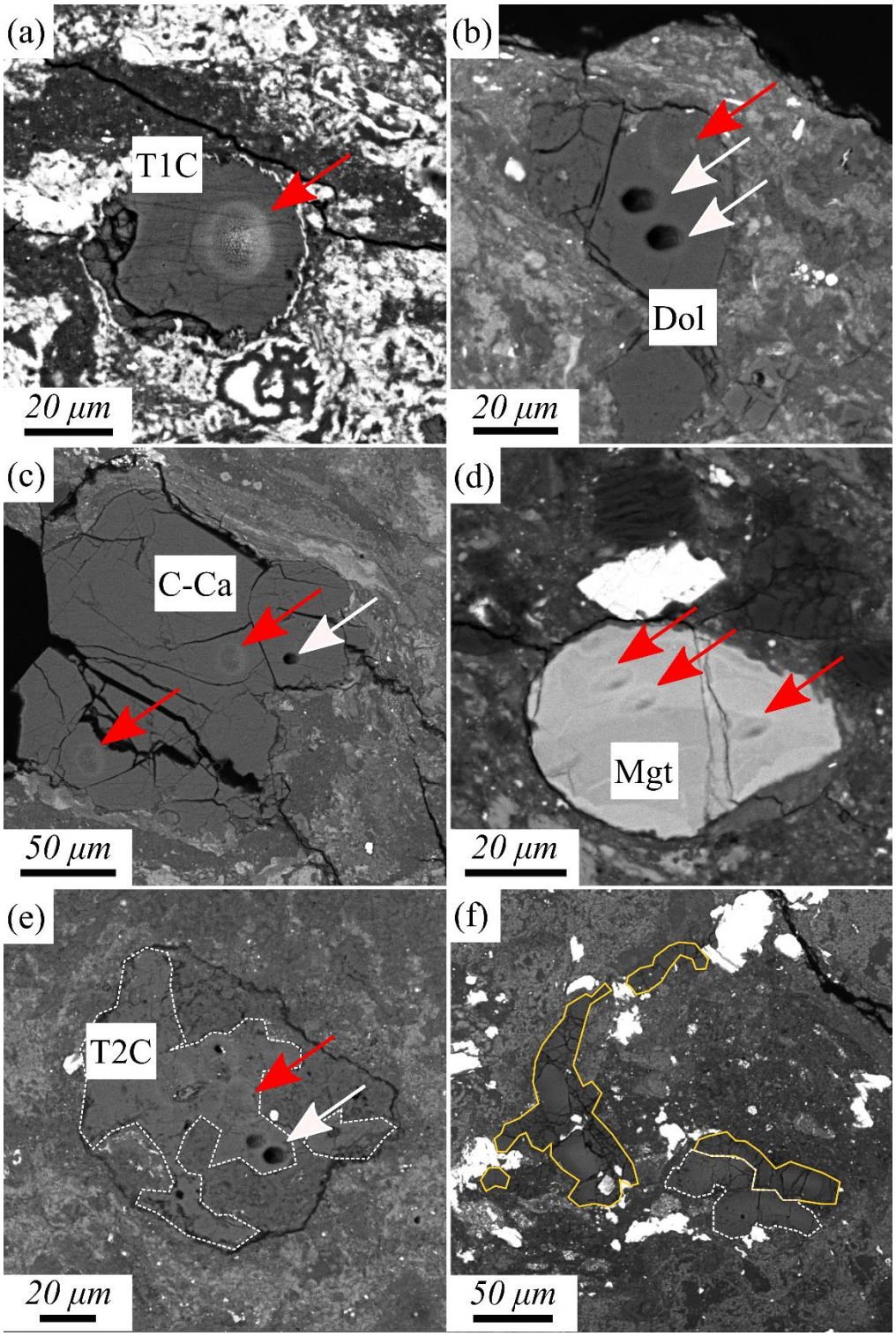

Results

Oxygen isotopes in Alais dolomite and magnetite

The O isotopic compositions of dolomite and magnetite in Alais are summarized in Tables 3.3 and 3.4 and illustrated in Figure 3.4a. Dolomite has an average $\Delta^{17}O$ of 0.25 ± 1.5 ‰ (2SD, MSWD = 1.4), with $\delta^{18}O$ varying from +23.2 ‰ to + 32 ‰. Our in situ measurements of $\delta^{18}O$ are consistent with the previous $\delta^{18}O$ measurements of bulk Alais dolomite measured by phosphoric acid digestion of the Alais whole-rock (Grady et al. 1988), suggesting that we measured a representative sample of the Alais dolomite population. The oxygen isotopic composition of Alais dolomites are consistent with other in situ measurements of CI dolomite in Orgueil and Ivuna (Piralla et al. 2020). Plaquette and spherulitic magnetite have identical $\Delta^{17}O$ within error (Figure 3.4a) and are resolved above the TFL with an average $\Delta^{17}O$ of + 2.2 ± 0.4 ‰ (2SD, MSWD = 1.6). This value is consistent with the bulk isotopic compositions of bulk CI magnetite (Rowe et al. 1994), as shown in Figure 3.4a. The $\delta^{18}O$ of Alais magnetite varies from −3.2 to + 2.5 ‰, though some of this range could be attributed to the effect of crystal orientation (Huberty et al. 2010). Framboidal magnetite could not be measured due to its small grain size and substantial void space within the framboid clumps (Figure 3.1c).

Oxygen isotopes in ALH 84034 carbonate

The oxygen isotopic compositions of calcite and dolomite in ALH 84034 are listed in Tables 3.2 and 3.3 and shown in Figure 3.4b. The $\Delta^{17}O$ of Type 1 calcite (white triangles, Fig. 3.4b) ranges from − 2.9 to + 2.6 ‰, with $\delta^{18}O$ varying from 26.3 to 33.5 ‰. The $\Delta^{17}O$ of dolomite (yellow squares) ranges from − 2.8 to − 6.9 ‰, with $\delta^{18}O$ varying from +13.8 to +25.2 ‰. Most dolomite falls near the average value of dolomite $\Delta^{17}O$ at – 5.5 ± 0.5 ‰ (2SD), though

some points are resolved above and below. The value of $\delta^{18}O$ of dolomite is anticorrelated with the Fe content of the dolomite so that Fe-poor dolomite has higher $\delta^{18}O$ than Fe-rich dolomite (Figure 3.5).

Carbon isotopes in ALH 84034 carbonate

The carbon isotopic compositions of calcite and dolomite in ALH 84034 are listed in Table 3.1 and shown in Figure 3.6 plotted against the Fe content of each carbonate. Calcite is plotted at $FeCO_3 = 0$. The $\delta^{13}C$ of Type 1 calcite (white triangles) in ALH 84034 ranges from 49 – 80 ‰. Calcite replacing a refractory inclusion (black triangle) has $\delta^{13}C$ of 20 ‰. The $\delta^{13}C$ of dolomite (yellow squares) ranges from 38 – 76 ‰ and is anticorrelated with the Fe content of the dolomite such that Fe-poor dolomite has higher $\delta^{13}C$ than Fe-rich dolomite. The range of $\delta^{13}C$ observed is consistent with previous studies of CM1 dolomite (Telus et al. 2019; Tyra et al. 2016), with the exception of the high $\delta^{13}C$ value of the Fe-poor dolomite.

Oxygen isotopes in Boriskino magnetite and carbonate

The O isotopic compositions of carbonate and magnetite in Boriskino are shown in Figure 3.4c and summarized in Tables 2, 3, and 4. Magnetite (blue circles) has $\Delta^{17}O$ ranging from +2.3 to +3.4 ‰, with $\delta^{18}O$ ranging from -2.3 to 7.0 ‰. Type 1 calcite (white triangles) has an oxygen isotopic composition of $\Delta^{17}O = 0 \pm 0.6$ ‰ (2SD) and $\delta^{18}O$ ranging from +29 to + 35 ‰, Type 2 calcite (black triangles) has an average oxygen isotopic composition of $\Delta^{17}O = -3.3$ ‰ and $\delta^{18}O$ of + 12.4 ‰. Dolomite (yellow squares) has $\Delta^{17}O$ ranging from −3.3 to −2.1 ‰ and $\delta^{18}O$ varying from +6.0 to +11.4 ‰. The O isotopic compositions of carbonates measured here are approximately in agreement with previous work (Verdier-Paoletti et al. 2019).

Figure 3.4. O isotopic compositions of alteration products in the (a) Alais, (b) ALH 84034, and (c) Boriskino meteorites. All values are reported relative to SMOW. Error bars for $\delta^{17}O$ and $\delta^{18}O$ ($\pm 2\sigma$) represent external and internal error summed in quadrature. Error bars for $\Delta^{17}O$ represent the external precision of repeated measurements of $\Delta^{17}O$ of terrestrial dolomite standards.

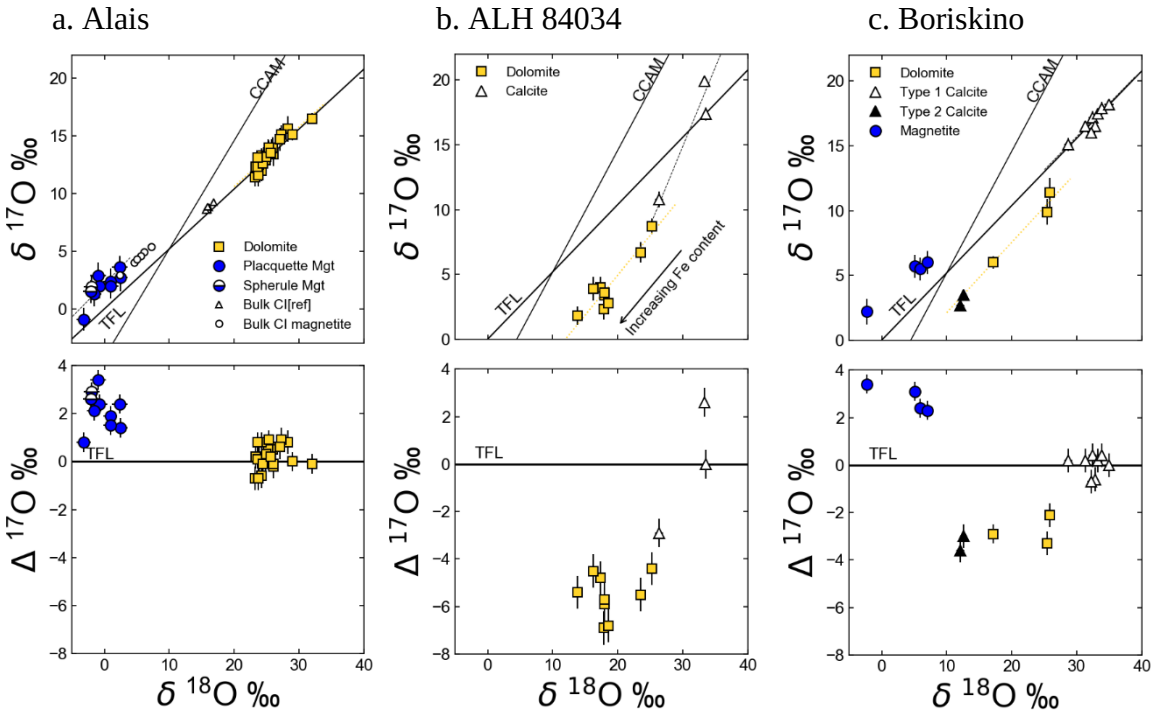

Figure 3.5. Fe contents and oxygen isotopic compositions of Type 1 calcite (white triangles) and dolomite (yellow squares) in ALH 84034. All values are reported relative to SMOW. Error bars (±2σ) represent external and internal error summed in quadrature.

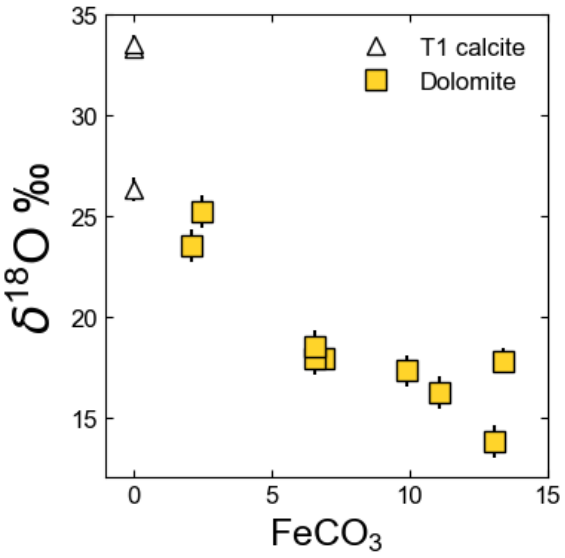

Figure 3.6. Carbon isotopic compositions of Type 1 calcite (white triangle), calcite replacing a refractory inclusion (black triangle), and dolomite (yellow square) in ALH 84034. Error bars are smaller than the size of the symbol. All values reported relative to Vienna Pee Dee Belemnite.

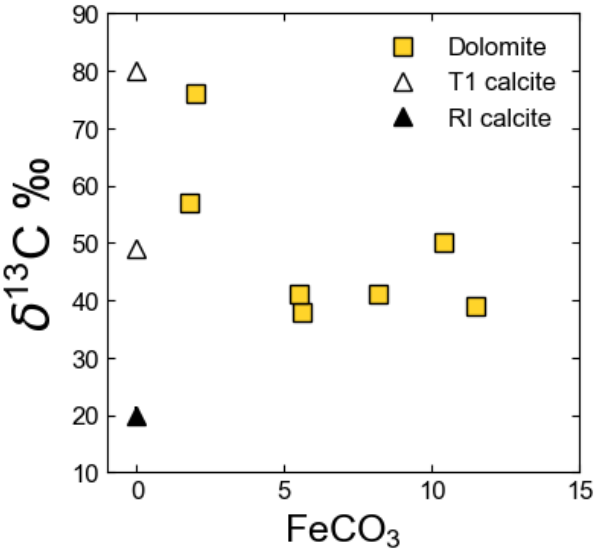

Mn-Cr ages of carbonate

Plots of the $^{53}Cr/^{52}Cr$ and $^{55}Mn/^{53}Cr$ ratios for CM and CI chondrites are shown in Figure 3.7. Dolomite and breunnerite in Alais show ^{53}Cr excesses that are well-correlated with the $^{55}Mn/^{52}Cr$ ratio (Figure 3.7a), suggesting an initial $^{53}Mn/^{55}Mn$ of $6.7 \pm 0.7 \times 10^{-6}$. The Alais $^{53}Mn/^{55}Mn$ ratio can be calibrated relative to the initial $^{53}Mn/^{55}Mn$ of the D'Orbigny angrite (McKibbin et al. 2015), which has a well-defined absolute crystallization age (Amelin 2008; Brennecka and Wadhwa 2012), to calculate that Alais dolomite formed 4566.8 ± 0.5 Ma. If the solar system origin is defined by the $^{207}Pb/^{206}Pb$ closure age for CAIs of 4567.3 Ma (Amelin et al. 2010), the carbonate in Alais formed within the first 1.0 million years of solar system formation.

Dolomite in ALH 84034 shows ^{53}Cr excesses that are well correlated (MSWD = 1.7) with the Mn/Cr ratio (Figure 3.7b) from which an initial $^{53}Mn/^{55}Mn$ of $13.3 \pm 2.4 \times 10^{-6}$ can be inferred. Calcite and dolomite in Boriskino show ^{53}Cr excesses which are only weakly correlated (MSWD = 8.2) with the $^{55}Mn/^{52}Cr$ ratio (Figure 3.7c), suggesting an initial $^{53}Mn/^{55}Mn$ of $10 \pm 1.7 \times 10^{-6}$.

Figure 3.7. Mn-Cr isochrons for carbonates in (a) Alais, (b) ALH 84034, and (c) Boriskino. Ages in Ma are reported relative to an absolute CAI age of 4567.3 Ma (Amelin et al. 2010) and anchored to the D'Orbigny angrite age and $(^{53}Mn/^{55}Mn)_0$ (see text). Error bars (±2σ) represent external and internal error summed in quadrature.

a.

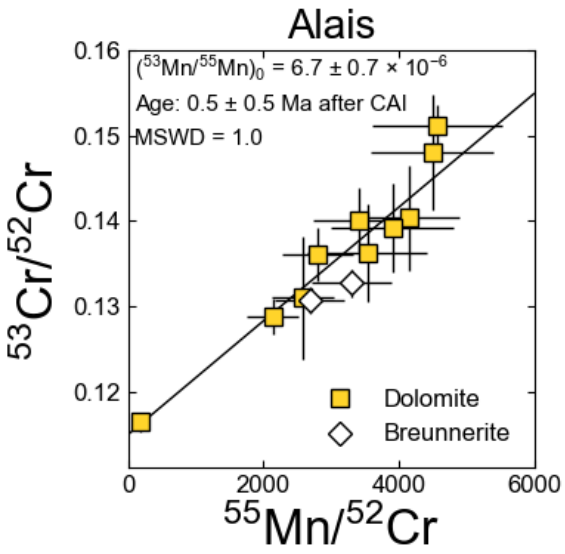

b.

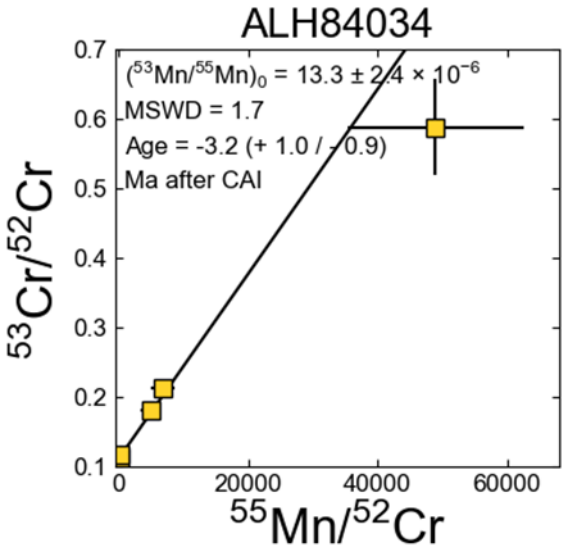

c.

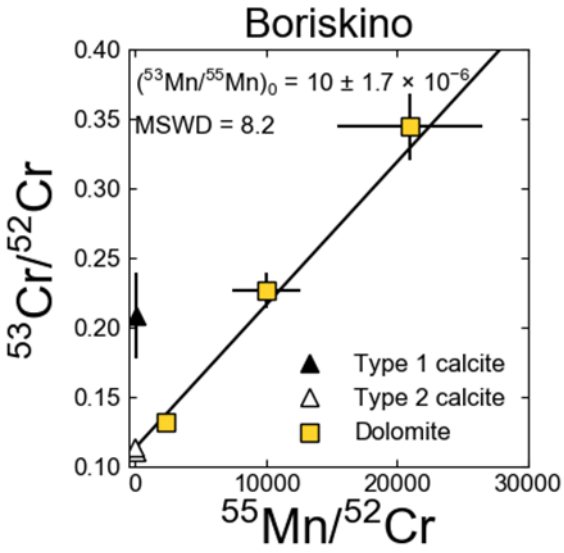

Discussion

Alais: Evidence of early multi-stage aqueous alteration

The average $\Delta^{17}O$ values for magnetite and dolomite are well-resolved from one another, indicating evolution of the fluid's oxygen isotopic composition between magnetite and dolomite formation. The high $\Delta^{17}O$ value of magnetite shows that initial CI water was enriched in ^{17}O and ^{18}O, suggesting an initial contribution from primordial solar system water, which has been inferred to be isotopically heavy (Clayton and Mayeda 1999; Rowe et al. 1994; Sakamoto et al. 2007). The dashed regression lines in Figure 3.4b indicate that dolomite and magnetite are arrayed along slopes of 0.52 ± 0.06 (2SD, MSWD 1.4) and 0.57 ± 0.22 (2SD, MSWD 1.6), suggesting that the fluid's O bulk isotopic composition did not evolve significantly during each phase of secondary mineral formation. As alteration proceeded, the water evolved towards $\Delta^{17}O \approx 0$ by interaction with more ^{16}O-rich material (Leshin et al. 1997) before dolomite formation began. The $\Delta^{17}O$ of dolomite is in approximate equilibrium with bulk Alais phyllosilicate (Rowe et al. 1994).

Our matrix-matched measurements of Alais dolomite indicate that substantial aqueous alteration including magnetite and dolomite formation occurred on the CI chondrite parent body within the first 1.0 million years after CAI. This result is substantially different from previous studies using calcite standards which found that most carbonate formed between 4-6 Ma after CAI (Fujiya et al. 2013; Visser et al. 2020). Had we corrected $^{55}Mn/^{52}Cr$ using the relative sensitivity factor derived from our implanted calcite standard (Chapter 4, Table S7), we would have obtained an age of 3.3 (+ 0.5 / − 0.4) million years after CAI for Alais, similar to the ages inferred by previous studies. We therefore attribute the difference between our carbonate

formation timescales and previous work to the use of matrix-matched dolomite and breunnerite standards.

Size and accretion time of the CI chondrite parent body

The early formation age determined for Alais carbonate in this study requires a significantly different parent body scenario for the CI chondrites than previously proposed. Young formation ages of 4-6 million years after CAI formation, as previously inferred, require that large parent bodies (>50 km diameter) accreted ~3-3.5 million years after CAI formation. Based upon our ^{53}Mn-^{53}Cr ages and assuming that ^{26}Al was homogeneously distributed throughout the disk, carbonate formation on the CI chondrite parent body occurred when ^{26}Al/^{27}Al was $\sim 2 \times 10^{-5}$: sufficiently abundant to not only melt accreted ice during aqueous alteration, but to also cause water loss or even silicate melting. Therefore, the CI chondrite parent body must have been sufficiently small as to effectively cool its interior by conduction of heat produced by ^{26}Al to the surface, where it could be lost to space. While large parent bodies produce regions in their interior which sustain liquid water under appropriate temperature conditions for CI chondrite formation, the high abundance of ^{26}Al at or before 1.0 million years after CAI formation means that such regions would be confined to thin 'shells' near the surface of the parent body. The volume of these shells is small compared to the volume of melted or dehydrated material towards the center of the body. Therefore, we do not consider parent bodies which create a thin shell of unheated, aqueously altered material to be good candidates for CI chondrite parent bodies.

To constrain the size of an early-accreting CI chondrite parent body, we use a spherically symmetric finite difference code that simulates the thermal evolution of planetesimals considering core formation, enthalpies of both water and rock phase transitions and convective

enhancement of heat flow upon rock melting (McCain et al. 2017; Zhou et al. 2013). The inferred presence of CO_2 ice in ALH 84034 and other CM chondrites suggests that the parent body must have accreted below the sublimation temperature of CO_2, which is 72 K (Mousis et al. 2010; Yamamoto 1985). Trapping CO_2 into water ice clathrates requires condensation to take place under higher pressures than typically inferred for the solar nebula (Dartois and Langlet 2021). Additionally, CO_2 ice condenses at a higher temperature than its associated clathrate (Mousis et al. 2010). We therefore do not consider CO_2 clathrate formation in our model. Further details of the thermal model are given in the Supplementary Materials.

Figure 3.8 shows the maximum temperature reached at the center of a parent body accreting at a given size and time after CAI formation, composed of 50% anhydrous chondritic material and 50% H_2O ice at an initial temperature of 78K. If we stipulate that a parent body should not exceed 400 K to avoid exceeding the temperatures inferred by bulk oxygen isotopic systematics of CI components (Clayton and Mayeda 1999; Leshin et al. 1997), a body forming within the first 1.0 Ma after CAI should not exceed a 13 km diameter. A representative time-temperature history of a parent body with a 12 km diameter accreting at 0.8 million years after CAI is shown in Figure 3.9a. Due to the high abundance of ^{26}Al, ice melts in less than 0.2 million years after accretion. Peak temperatures are achieved at approximately 700 kyr after accretion, and liquid water persists for up to 1 million years after accretion (1.8 million years after CAI formation). The exterior of the parent body does not reach sufficiently high temperatures to melt water ice until approximately 3 km below the surface. For comparison, Figure 3.9b shows a parent body with a 40 km diameter accreting at the same time. In the 40 km diameter body, only a small volumetric fraction of the parent body avoids melting.

Figure 3.8. Contour plot showing the maximum temperature reached at the center of a spherical parent body of a given size accreting at a given time. The body is composed of 50% water ice and 50% anhydrous chondritic material. Isotherms corresponding to the melting of water ice and silicate are also shown.

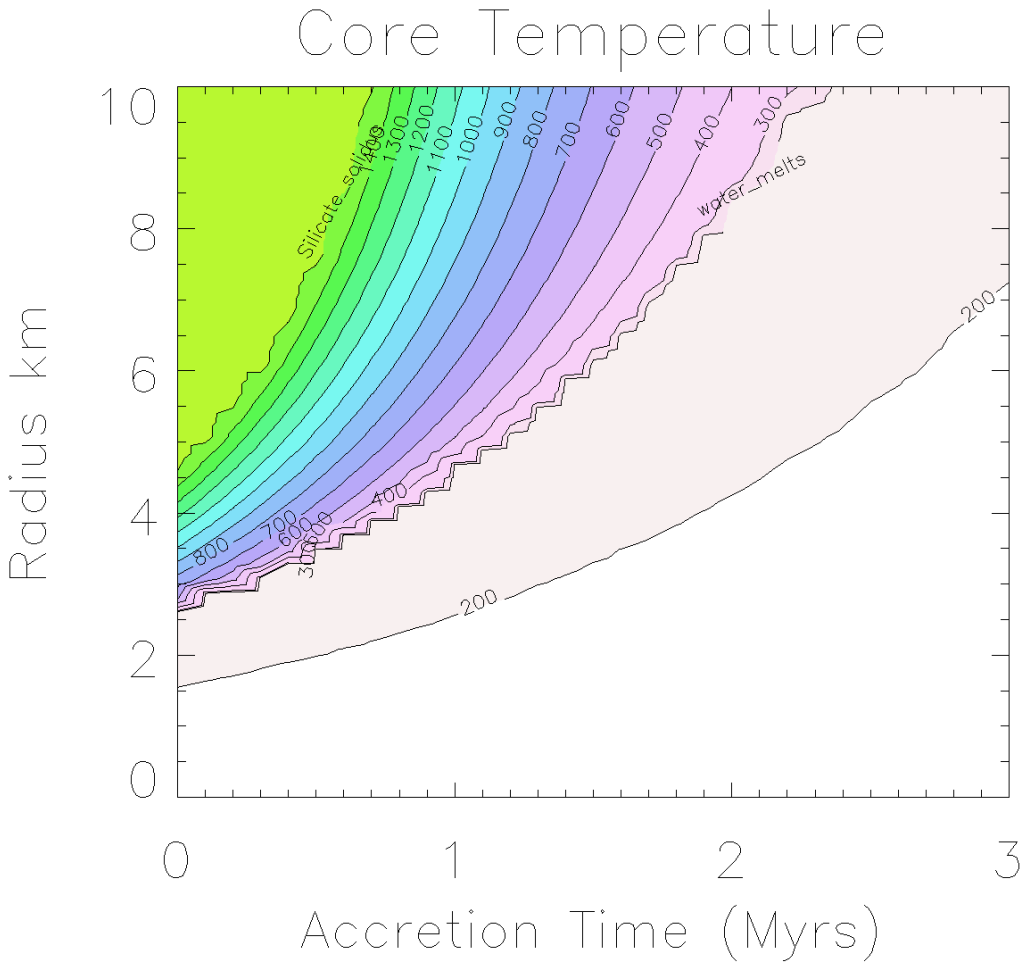

Figure 3.9. Thermal history of (a) a 12 km diameter and (b) a 40 km parent body composed of 50% ice and 50% silicate, accreting at 0.8 million years (Myr) after CAI. Contour lines represent the temperature in K achieved at a particular depth at a given time after accretion. The 'water_melts' contour represents the 273K isotherm, indicating the temperature at which water ice melts.

a.)

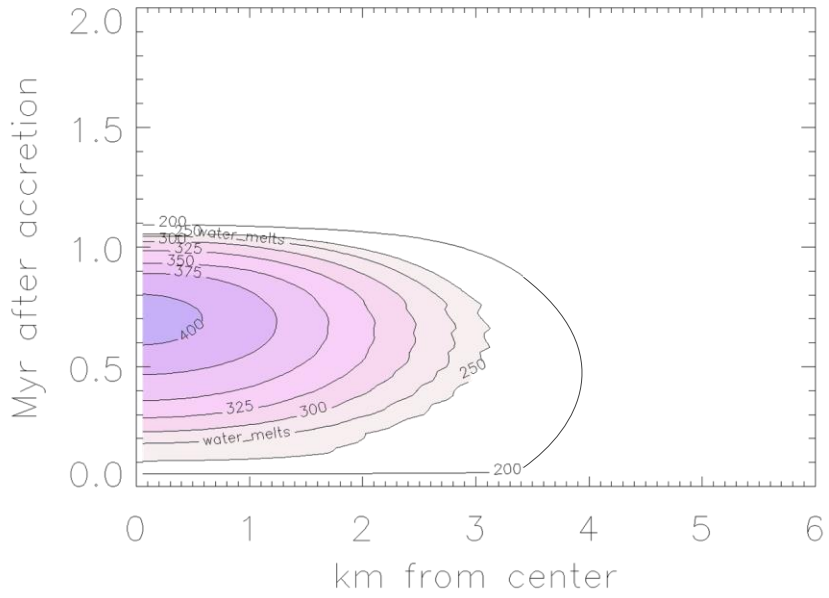

b.)

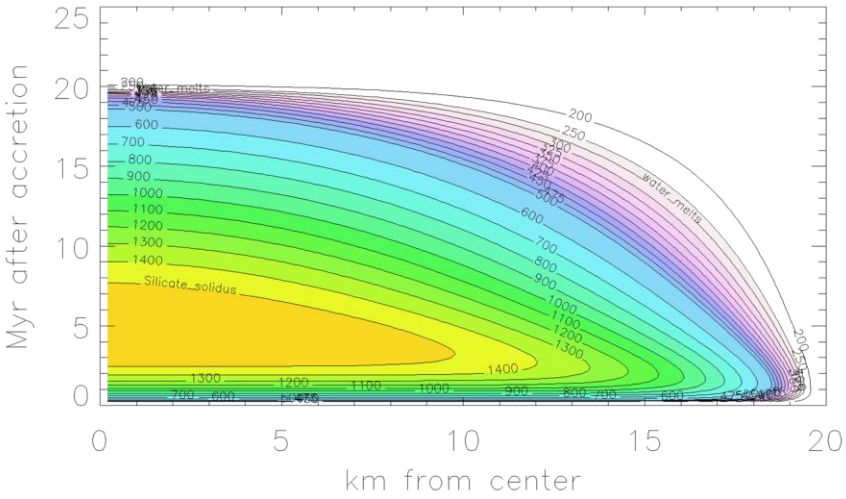

Alternatively, the CI chondrites could have formed in much larger parent bodies if these parent bodies were disrupted by impacts, cooling the interior by fragmenting the body (Ciesla et al. 2013). In this scenario, the body would have to be disrupted within the first 500 kyr of its accretion, before a substantial fraction of the body exceeded 400 K.

Boriskino: A record of evolution, brecciation, and disruption

The high $\Delta^{17}O$ in Boriskino magnetite of ~ 3 ‰, which appears in lithology CM2-1, suggests that the initial fluid was enriched in ^{17}O and ^{18}O, reflecting the incorporation of nebular water which has been inferred to be isotopically heavy (Clayton and Mayeda 1984, 1999; Rowe et al. 1994; Sakamoto et al. 2007). The O isotopic compositions of Boriskino T1 calcite in lithology CM2-1, with $\Delta^{17}O \sim 0$ ‰, are related along a mass-dependent fractionation line with a slope of 0.52 ± 0.12, indicating that the fluid's bulk O isotopic composition was static during T1 calcite formation and had evolved from the fluid that had originally produced magnetite in this lithology. The fluid altering CM 2-1 evolved further to produce dolomite with $\Delta^{17}O \sim -3$ ‰. In contrast, dolomite and Type 2 calcite in lithology CM1-1/CM1-1a have an identical $\Delta^{17}O$ of −3 ‰, suggesting that this system did not begin to form carbonate until the fluid had already interacted with sufficient anhydrous silicate to lower its $\Delta^{17}O$.

Mn-Cr systematics of carbonate in Boriskino

As shown in Figure 3.7c, Boriskino carbonate does not plot along an isochron, and several explanations informed by petrographic and stable isotopic observations of Boriskino are available. Boriskino is a shocked breccia, and many of its carbonates show microstructural damage (Dobrică et al. 2022). These impact-induced defects could facilitate loss of structural Mn in dolomite or Type 2 calcite. Damaged carbonates could also be infiltrated to various degrees by

younger fluids containing Cr. This would produce a mixing line between carbonates which are more or less affected by infiltration—therefore the slope defined by these carbonates, such as the slope defined by dolomite and Type 2 calcite in Figure 3.7c, would not represent a formation age. Additionally, as discussed above, carbonate formation in the CM1 lithology did not occur until after fluid had equilibrated with silicate, whereas carbonate formation in the CM2 lithologies occurred at various stages of fluid-rock equilibration as recorded by their diverse $\Delta^{17}O$ values. These different alteration conditions may have occurred at different locations or times on the parent body before impact and reassembly into the Boriskino breccia.

C and O isotopic systematics in ALH 84034

Type 1 calcite in ALH 84034, which has been inferred to form by filling pore spaces during the early phases of aqueous alteration (Tyra et al. 2012, 2016), is enriched in $\delta^{13}C$ (Figure 3.4), which may reflect the incorporation of ^{13}C-rich CO_2 ice into the parent body (Fujiya et al. 2019; Hässig et al. 2017). The $\Delta^{17}O$ of Type 1 calcite is highly variable (Figure 3.5a), suggesting that the fluid's O isotopic composition evolved rapidly during the early stages of aqueous alteration during pore space cementation. In dolomite, $\delta^{13}C$ is correlated with the Fe content of the mineral (Figure 3.4), indicating that the Fe^{2+} content of the fluid and the C isotopic reservoirs evolved together.

The majority of dolomite in ALH 84034 has $\Delta^{17}O$ near ~ −5.5 ‰ with large ranges in $\delta^{18}O$ correlated with Fe content (Figure 3.5). This suggests that the fluid reached O isotopic equilibrium with silicates by this phase of dolomite formation. Variations in $\delta^{18}O$ but not $\Delta^{17}O$ can be caused by variations in temperature, which would suggest that low-Fe dolomite with higher $\delta^{18}O$ precipitated at lower temperatures than high-Fe dolomite with lower $\delta^{18}O$. Low-Fe dolomite is similar in both $\delta^{18}O$ and $\delta^{13}C$ to Type 1 calcite, suggesting that it may have been the

first generation of dolomite to form. Alternately, the fluid's composition could have evolved along a mass-dependent line if alteration of silicates continued after O isotopic equilibrium between fluid and silicate was reached. In this case, the range of $\delta^{18}O$ of dolomite would record this evolution. The calcite replacing the refractory inclusion has a low $\delta^{13}C$, suggesting that it formed from a substantially different C isotopic reservoir than T1 calcite or dolomite. We therefore put forward the following formation sequence: Pore-filling Type 1 calcite formed with initially high $\delta^{13}C$ and $\Delta^{17}O$ from co-accreted water ice and CO_2 and continued to evolve towards lower $\delta^{13}C$ and $\Delta^{17}O$ as the fluid interacted with the ^{16}O-rich CAIs and chondrules seen pseudomorphed in the section. Fe-poor dolomite formation began after substantial fluid-silicate interaction had occurred, and increasingly Fe-rich dolomite precipitated as the temperature of the fluid increased, recording prograde heating of the parent body.

The presence of early-forming Type 1 calcites with high $\delta^{13}C$ and later-forming dolomites with lower $\delta^{13}C$ suggest that methane formation was not the dominant method of carbon isotopic evolution, as loss of CH_4 from the fluid as a gas would tend to cause the fluid to become enriched in ^{13}C as alteration proceeded (Guo and Eiler 2007). Instead, the opposite relationship is observed. Instead, we suggest that the prograde heating discussed above may have oxidized isotopically light organic matter, gradually decreasing the $\delta^{13}C$ of the fluid, a mechanism suggested for carbonate in other CM chondrites (Fujiya et al. 2015; Vacher et al. 2017)

Comparison of ALH 84034 C and O results to previous studies

Previous studies of C and O of calcite and dolomite in ALH 84034 found dolomite and calcite with wide and overlapping ranges of $\Delta^{17}O$ (Telus et al. 2019), in contrast to our results which show clear differences in $\Delta^{17}O$ between the two phases. We note that dolomite and calcite

in previous studies of ALH 84034 do not resemble dolomite and calcite in this section in their petrography—the fractured dolomite aggregates and refractory inclusion pseudomorphs present in our section were not reported in Telus et al. 2019, and the large Ca-carbonates previously described do not appear in our section. Previous work also does not completely account for matrix effects as a function of Fe content in dolomite, though this would not affect the value of $\Delta^{17}O$. Therefore, we attribute the differences in the stable isotopic compositions of carbonate reported for ALH 84034 carbonate to heterogeneity between the two sections.

Mn-Cr systematics of dolomite in ALH 84034: Nebular inheritance or shock resetting?

Dolomite in ALH 84034 plots along a well-resolved isochron, but the age inferred from the initial $^{53}Mn/^{53}Cr$ ratio of $13.3 \pm 2.4 \times 10^{-6}$ would suggest that dolomite formation occurred before CAI formation. We consider various explanations for this observation based upon petrologic and O isotopic characteristics of ALH 84034 dolomite. Many dolomites in ALH 84034 are found as fractured aggregates with complex Fe and Mn zoning, with small iron sulfide and phyllosilicate inclusions found in the interstices of the aggregates. The dolomite CC05 (Figure 3.2e) is rounded and of a similar size to pseudomorphed chondrules in the section, and the dolomite CC07 (Figure 3.2c-d) is found pseudomorphing a refractory inclusion. We also note that the ^{16}O-rich compositions of dolomite ($\Delta^{17}O \sim -5.5$ ‰) are similar to the compositions of forsterite in chondrules from the CM chondrite Paris (Chaumard et al. 2021) and other chondrite types (Scott and Krot 2014), which may suggest some degree of O isotope inheritance. Therefore, we consider whether Mn and Cr in ALH 84034 dolomite could have been inherited from the primary phases that the dolomite has replaced. CAIs have inferred initial $^{53}Mn/^{55}Mn$ compositions of $6.71 \pm 0.56 \times 10^{-6}$ (Davis and McKeegan 2014), which is lower than the inferred compositions of ALH 84034 dolomite. CAIs also do not contain high abundances of moderately

volatile elements such as Mn or Cr. Chondrules contain more Cr than CAIs, but are not enriched in ^{53}Cr (Kadlag et al. 2019). Therefore, we conclude that inheritance of CAI and chondrule material does not explain the observed high slopes.

Instead, we suggest that the fractured dolomite aggregates in ALH 84034 may record shock resetting of the Mn-Cr system and later infiltration of damaged carbonate by Cr-rich fluid, as discussed above for Boriskino. Regions of dolomite adjacent to fracture planes exhibit high cathodoluminescent (CL) brightness (Brearley and Hutcheon 2000), suggesting a second phase of dolomite formation after fracturing or damage to the crystal structure near these fractures. Though care was taken to avoid fractures during Mn-Cr analysis, damage could persist some distance away from the fracture. The steep slopes would then represent a mixing line between less-damaged, Cr-poor carbonate and more-damaged carbonate, and TEM studies of the analyzed carbonates could test this hypothesis. Relatively minor chondrule flattening and petrofabric development suggest that ALH 84034 is less affected by shock than Boriskino, which could place restrictions on how much shock a CM chondrite could experience before Mn-Cr dating of its secondary minerals becomes unreliable. In the future, we suggest that the petrology of each dolomite targeted for Mn-Cr dating should be carefully examined, and dolomite which has experienced shock metamorphism should be regarded with caution.

Overall, our study of the CM chondrites Boriskino and ALH 84034 underscore the necessity of contextualizing Mn-Cr ages and stable isotope measurements with petrographic information. Our study of Alais and its early formation scenario suggested by the matrix-matched analyses suggests that the Mn-Cr ages of the CM and CI chondrites be revisited in light of recent advancements in matrix-matched standard development.

Acknowledgements

We thank Philipp Heck and the Field Museum of Natural History for loaning the Alais and Boriskino samples, Rosario Esposito and Brian Damiata for their assistance with the EPMA measurements, the Molecular Materials Research Centre at the Beckman Institute at Caltech and Bruce S. Brunschwig for the use of the stylus profilometer, and Kathrynn Hamann for her assistance with the profilometer. This work was partially supported by the NASA Earth and Space Science Fellowship (No. NESSF19R 19-PLANET19R-0001) and the NASA Emerging Worlds program. The UCLA ion microprobe facility is partially supported by a grant from the NSF Instrumentation and Facilities program. Ion implantation of carbonate standards was performed by CuttingEdge Ions.

Chapter 3 Tables

Table 3.1. Carbon isotopic compositions of carbonate in ALH 84034. The value of $\delta^{13}C$ is reported relative to VPDB. Errors represent internal and external errors summed in quadrature.

Name	$FeCO_3$	$\delta^{13}C$	$\pm 2\sigma$
Calcite			
ALHA84034_CC01@2	-	80	1.0
ALHA84034_CC02@1	-	49	1.0
ALHA84034_CC07@2	-	20	1.4
Dolomite			
ALHA84034_CC04@2	10.4	50	1.4
ALHA84034_CC05@1	8.2	41	1.0
ALHA84034_CC05@2	5.6	38	2.0
ALHA84034_CC08@1	2	76	0.8
ALHA84034_CC08@2	1.8	57	1.8
ALHA84034_CC09@2	11.5	39	1.2
ALHA84034_CC10@1	5.5	41	1.6

Table 3.2. Oxygen isotopic compositions of calcite in Boriskino and ALH 84034. The values of $\delta^{17}O$ and $\delta^{18}O$ are reported relative to SMOW. Errors for $\delta^{17}O$ and $\delta^{18}O$ represent internal and external errors summed in quadrature. Errors on $\Delta^{17}O$ are the external precision determined by repeated measurements of the terrestrial carbonates. Each carbonate is designated as Type 1 (T1) or Type 2 (T2) calcite according to it petrology and O isotopic composition (Lee et al. 2014; Tyra et al. 2012, 2016). For Boriskino carbonate, the clast type is given as described in the text.

Name	Type	$\delta^{17}O$	±2σ	$\delta^{18}O$	±2σ	$\Delta^{17}O$	±2SE	Clast
Boriskino								
bor3_cc19	T1	17.2	0.5	32.4	0.6	0.4	0.3	CM2-1
bor3_cc21@60	T1	17.5	0.4	33.2	0.4	0.2	0.3	CM2-1
bor3_cc05@67	T1, L	17.9	0.5	33.8	0.5	0.4	0.3	CM2-1
bor3_cc05@68	T1, L	18.2	0.4	34.9	0.7	0.0	0.3	CM2-1
bor3_cc41@72	T2	3.5	0.4	12.6	0.5	-3.0	0.3	CM1-1
bor3_cc43@73	T2	2.7	0.4	12.1	0.6	-3.6	0.3	CM1-1
bor3_cc35@74	T1	16.5	0.4	32.8	0.5	-0.6	0.3	CM2-1
bor3_cc61@75	T1	16.5	0.4	31.3	0.4	0.2	0.3	CM2-1
bor3_cc75@92	T1	15.1	0.5	28.7	0.6	0.2	0.3	CM2-1
bor3_cc74@94	Pm	16.0	0.4	32.2	0.6	-0.7	0.2	CM1-a
ALH 84034								
ALH_CC01@1	T1	19.9	0.4	33.3	0.6	2.6	0.3	-
ALH_CC01@2	T1	17.4	0.5	33.5	0.9	0.3	0.3	-
ALH_CC02@1	T1	10.8	0.6	26.3	0.7	-2.9	0.3	-

Table 3.3. Oxygen isotopic composition of dolomite in Alais, ALH 84034, and Boriskino. The values of $\delta^{17}O$ and $\delta^{18}O$ are reported relative to SMOW. Errors for $\delta^{17}O$ and $\delta^{18}O$ represent internal and external errors summed in quadrature. Errors on $\Delta^{17}O$ are the external precision determined by repeated measurements of the terrestrial carbonates.

Name	$CaCO_3$	$MgCO_3$	FeCO3	$MnCO_3$	$\delta^{17}O$	±2σ	$\delta^{18}O$	±2σ	$\Delta^{17}O$	$\Delta^{17}O$ 2SE
Alais										
alais2_dolo7@47	49.3	42.2	4.8	2.9	12.9	1.0	24.8	0.7	0.0	0.5
alais2_dolo7@48	49.3	42.2	4.8	2.9	13.4	1.0	26.0	0.7	−0.2	0.5
alais2_dolo7@49	49.3	42.2	4.8	2.9	13.4	0.9	26.0	0.7	−0.1	0.5
alais2_dolo7@52	49.3	42.2	4.8	2.9	13.9	0.8	25.7	0.7	0.6	0.5
ALA2_dolo14@21	50.7	41.8	5.8	2.0	15.6	1.1	28.3	0.6	0.8	0.5
ALA2_dolo14@23	49.7	41.6	4.1	4.5	15.1	0.8	27.2	0.6	0.9	0.5
ALA2_dolo13@24	49.9	41.4	5.0	3.3	12.3	0.9	23.3	0.6	0.2	0.5
ALA2_dolo02@25	50.5	39.8	4.8	1.5	12.0	0.9	24.2	0.6	−0.6	0.5
ALA2_dolo02@26	50.5	39.8	4.8	1.5	14.0	0.9	25.9	0.6	0.5	0.5
ALA2_dolo02@28	50.5	39.8	4.8	1.5	13.6	1.1	25.2	0.6	0.5	0.5
ALA2_dolo07@29	49.3	42.2	4.8	2.9	14.7	1.0	27.0	0.6	0.6	0.5
alais3_dol3@56	47.6	42.5	4.9	3.9	12.5	0.9	23.8	0.6	0.1	0.5
alais3_dol3@57	47.6	42.5	4.9	3.9	11.4	0.8	23.2	0.6	−0.7	0.5
alais3_dol6@59	48.4	43.3	4.5	2.4	11.6	1.0	23.7	0.6	−0.7	0.5
alais2_dol06@22	48.8	42.6	5.1	5.0	12.3	0.3	23.6	0.4	0.1	0.4
alais2_dol01@23	49.9	41.4	5.0	3.3	12.6	0.4	24.4	0.5	−0.1	0.4
alais2_dolo14@10	50.7	41.8	5.8	2.0	13.3	0.6	24.2	0.5	0.8	0.4
alais2_dolo02@11	50.5	39.8	4.8	1.5	13.2	0.6	24.9	0.4	0.3	0.4
alais2_dolo02@12	50.5	39.8	4.8	1.5	13.1	0.5	23.6	0.5	0.8	0.4
alais2_dolo04@13	49.9	41.4	5.0	3.3	14.0	0.6	25.3	0.4	0.9	0.4
alais3_dolo1@18	48.7	45.3	4.3	1.1	15.1	0.5	29.0	0.3	0.0	0.4
alais3_dolo5@20	48.4	43.3	4.5	2.4	13.5	0.5	25.6	0.3	0.2	0.4
alais1_dolo1@21	49.3	42.2	4.8	2.9	16.5	0.5	32.0	0.3	-0.1	0.4
ALH 84034										
ALHA84034_CC04@2	46.4	38.1	13.1	1.2	1.8	0.7	13.8	0.8	-5.4	0.7
ALHA84034_CC05@1	51.7	38.3	6.9	2.7	3.4	1.0	17.9	0.6	-5.9	0.7

Table 3.3 continued

ALHA84034_CC05@2	46.8	38.9	9.9	2.8	4.0	0.8	17.3	0.8	-4.8	0.7
ALHA84034_CC06@1	36.2	42.4	11.1	2.0	3.9	0.9	16.2	0.8	-4.5	0.7
ALHA84034_CC08@1	50.0	44.5	2.5	1.1	8.7	0.6	25.2	0.8	-4.4	0.7
ALHA84034_CC08@2	50.6	42.0	2.1	1.5	6.7	0.8	23.5	0.8	-5.5	0.7
ALHA84034_CC09@1	41.5	35.2	13.4	6.4	2.3	0.8	17.8	0.6	-6.9	0.7
ALHA84034_CC10@1	50.5	37.3	6.6	3.4	3.6	0.7	17.9	0.8	-5.7	0.7
ALHA84034_CC10@2	47.2	34.2	6.6	5.1	2.8	0.8	18.5	0.8	-6.8	0.7
Boriskino										
bori3_dolo73@54	53.5	32.8	5.5	7.6	11.4	1.1	25.8	0.8	−2.1	0.5
bori3_dolo73@55	53.5	32.8	5.5	7.6	9.9	1.0	25.4	0.7	−3.3	0.5
bori3_cc22dol@21	55.1	37.0	5.8	1.9	6.0	0.5	17.1	4.0	−2.9	0.4

Table 3.4. Oxygen isotopic compositions of magnetite in Alais and Boriskino. The values of $\delta^{17}O$ and $\delta^{18}O$ are reported relative to SMOW. Errors for $\delta^{17}O$ and $\delta^{18}O$ represent internal and external errors summed in quadrature. Errors on $\Delta^{17}O$ are the external precision determined by repeated measurements of the magnetite standard.

Name	**$\delta^{17}O$**	**±2σ**	**$\delta^{18}O$**	**±2σ**	**$\Delta^{17}O$**	**±2 SE**	**Type**
Alais							
alais1_mgt1@10	-0.9	1.0	-3.2	1.1	0.8	0.3	Platelet
alais1_mgt4@16	1.9	1.0	-2.0	1.2	2.9	0.3	Spherule
alais1_mgt4@17	1.5	1.0	-2.1	1.2	2.6	0.3	Spherule
alais1_mgt5@22	3.6	1.0	2.4	1.2	2.4	0.3	Platelet
alais2_mgt7@23	2.7	1.2	2.5	1.1	1.4	0.3	'Froth'
alais3_mgt7@34	2.9	1.1	-1.0	1.2	3.4	0.3	Platelet
alais3_mgt7@35	2.0	1.1	-0.8	1.2	2.4	0.3	Platelet
alais3_mgt7@36	1.3	1.1	-1.6	1.1	2.1	0.3	Platelet
alais3_mgtnew@37	2.4	1.1	0.9	1.1	1.9	0.3	Platelet
alais3_mgtnew@38	2.0	1.1	1.0	1.2	1.5	0.3	Platelet
Boriskino							
bori3_mgt04@6	2.2	1.0	-2.3	0.8	3.4	0.3	I
bori3_mgt06@9	5.7	0.9	5.1	0.8	3.1	0.3	Frac
bori3_mgt06@10	5.5	0.9	5.9	0.8	2.4	0.3	Frac
bori3_mgt06@11	6.0	0.9	7.0	0.8	2.3	0.3	Frac

Table 3.5. Mn-Cr isotope data and chemical compositions of carbonates in Alais, Boriskino, and ALH 84034. Errors for Alais represent the internal error and external precision summed in quadrature. Errors for Boriskino and ALH 84034 represent the error predicted by counting statistics. b.d. Below detection limit, *Data obtained using SEM-EDS spectroscopy, †Data acquired at UNM.

Name	**$^{55}Mn/^{52}Cr$**	**±2σ**	**$^{53}Cr/^{52}Cr$**	**±2σ**	**$\delta^{53}Cr$**	**$CaCO_3$**	**$MgCO_3$**	**$FeCO_3$**	**$MnCO_3$**	**RSF**
Alais										
ALA@1	4158	737	0.1404	0.0061	237	48.7	45.3	4.3	1.1	0.76
ALA@10	4498	906	0.1481	0.0068	306	50.7	41.8	5.8	2.0	0.74
ALA@11	3299	596	0.1327	0.0017	170	3.9*	65.6*	26.7*	3.8*	0.8
ALA@12	2682	517	0.1307	0.0015	152	3.9*	65.6*	26.7*	3.8*	0.8
ALA@2	3532	877	0.1363	0.0057	201	48.7	45.3	4.3	1.1	0.76
ALA@3	3903	914	0.1393	0.0052	227	48.7	45.3	4.3	1.1	0.76
ALA@4	2587	459	0.1310	0.0071	154	48.7	45.3	4.3	1.1	0.76
ALA@5	179	32	0.1164	0.0011	26	49.7	43.5	5.0	1.6	0.75
ALA@6	3403	664	0.1401	0.0037	235	49.7	43.5	5.0	1.6	0.75
ALA@7	4569	963	0.1512	0.0024	333	49.7	43.5	5.0	1.6	0.75
ALA@8	2139	383	0.1288	0.0021	136	48.8	42.6	5.1	5.0	0.75
ALA@9	2799	527	0.1361	0.0032	200	49.9	41.4	5.0	3.3	0.75
Boriskino										
Boriskino3_cc22@1011	9970	1296	0.2269	0.0064	1000	55.1	37.0	5.8	1.9	0.74
Boriskino3_cc22@12	20975	2748	0.3447	0.0118	2038	55.1	37.0	5.8	1.9	0.74
Boriskino3_cc05@13	30	2	0.2090	0.0156	842	87.3*	b.d.	0.2*	b.d.	1.30
Boriskino3_cc73@14	2283	292	0.1320	0.0013	163	53.5	32.8	5.5	7.6	0.70
Boriskino3_cc41@16	25	1	0.1112	0.0038	-20	90.2*	b.d.	0.8*	0.2*	1.30
Boriskino3_cc43@17	14	1	0.1141	0.0009	5	90.7*	b.d.	0.5*	0.1*	1.30
ALH 84034										
ALH84034_cc08@4	238	20	0.1130	0.0009	-4	50.0	44.5	2.5	1.1	0.82
ALH84034_cc08@5	338	29	0.1176	0.0019	36	50.0	44.5	2.5	1.1	0.82
ALH84034_cc09@7	6983	694	0.1810	0.0050	595	41.5	35.2	13.4	6.4	0.71
ALH84034_cc07@15	66555	6771	0.5890	0.0349	4191	48.1†	34.3†	13.4†	6.4†	0.71
ALH84034_cc07@16	9550	925	0.2138	0.0049	884	48.1†	34.3†	13.4†	6.4†	0.71

Supplementary Materials for Chapter 3: Early aqueous alteration in the Outer Solar System recorded by Oxygen, Carbon, and Mn-Cr isotope systematics of CM and CI chondrites.

McCain, K.A., Liu, M-C., Young, E.D., Brearley, A., McKeegan, K.D.

Supplementary Materials containing:

Supplementary Methods

Supplementary Table S3.1

Supplementary Figures S3.1-4

Characterization of carbonate reference materials

A variety of carbonate minerals were requested from the UCLA mineral collection and the Field Museum of Natural History. The isotopic and major element compositions of each were characterized to assess whether they could be used as reference materials for carbon, oxygen, and Mn-Cr analysis.

Calcite and dolomite samples were crushed using an agate mortar and pestle and dissolved in anhydrous H_3PO_4 for 4 hours at 25° C for calcite and 75° for dolomite to produce CO_2 gas. The fractionation factors between carbonate and CO_2 gas evolved by phosphoric acid dissolution were $10^3 \ln\alpha = 10.25$ for calcite at 25 °C (Kim et al. 2007) and 9.54 – 9.78 for dolomite at 75 °C depending on the major element composition of the dolomite (Rosenbaum and Sheppard 1986). Each carbonate was measured at least in triplicate, alongside one of the reference materials NBS-19 and CARM-1 to monitor external error. The $\delta^{13}C$ and $\delta^{18}O$ of the gas evolved from phosphoric acid digestion was measured using the Thermo Fisher MAT 253 isotope ratio mass spectrometer. Carbonates which did not have consistent $\delta^{13}C$ and $\delta^{18}O$ values were excluded from consideration as reference materials. The oxygen and carbon isotopic compositions of each carbonate reference material are shown in Supplementary Table S3.1 below.

Each carbonate was mounted in Field's metal and indium and polished to 0.25 μm using Beuhler MetaDi™ Supreme polycrystalline diamond suspension. After polishing, the sections were coated with a thin (20 nm) carbon film. The major element composition of each carbonate was determined using the JEOL Superprobe electron microprobe (EPMA) at UCLA at an accelerating voltage of 15 kV and the electron beam defocused to 10 μm diameter to avoid damage to the carbonate minerals. Carbonates with substantial heterogeneity were excluded from

future use as reference materials unless homogenous domains could be identified. The chemical composition of each carbonate reference material is shown in Supplementary Table S3.1 below.

Table S3.1. Isotopic compositions, chemical compositions, and typical count rates of reference materials used for ion probe analyses. Isotopic compositions determined using conventional phosphoric acid digestion.

standard	$\delta^{17}O$	$\delta^{18}O$	$\delta^{13}C$	$CaCO_3$	$MgCO_3$	$FeCO_3$	$MnCO_3$	FCEMEM $^{16}O^-$ (cps)	FCEMFC $^{16}O^-$ (cps)	$^{12}C^-$ (cps)
OPTI calcite	5.76	11.10	1.42	99.4	0.5	0.0	0.0		7.0×10^8	8.0×10^6
MS1317*	11.80	22.82	-21.13	51.8	48.1	0.0	0.1	5.1×10^7	8.0×10^8	8.0×10^6
MS1305*	10.99	21.24	-1.10	50.8	48.0	1.1	0.1	5.2×10^7	8.3×10^8	8.4×10^6
MS1317J*	11.13	21.51	-1.20	51.1	45.8	2.9	0.2	5.3×10^7	8.4×10^8	8.6×10^6
MS1312*	11.63	22.48	0.00	51.1	21.6	21.1	6.2	5.6×10^7	8.6×10^8	1.1×10^7
Afrique Magnetite	0.74	1.42	-	-	-	-	-	4.5×10^7	-	-

*Dolomite from the UCLA mineral collection

Mn-Cr carbonate standard production and characterization

Natural carbonate minerals from the UCLA and Field Museum of Natural History (FMNH) mineral collection which span the range of Fe contents found in meteoritic carbonate (0–22 mol% $FeCO_3$ for dolomite and 0–40 mol % $FeCO_3$ for magnesite) were embedded in Field's Metal and/or indium in the center of aluminum disks. Fragments of San Carlos Olivine and the NIST 612 and 614 glasses were mounted in the same disks for use as concentration standards to calibrate the implant fluence. The mount was coated with 20 nm carbon to ensure conductivity and prevent charging during ion implantation. All mounts were implanted with a 185 KeV $^{52}Cr^+$ ion beam at a nominal fluence of 4×10^{13} ions/cm^2 rastered over the entire surface. A mass filter was used to separate $^{52}Cr^+$ and $^{53}Cr^+$ after Cr ionization, ensuring that only $^{52}Cr^+$ was implanted. No evidence of implanted $^{53}Cr^+$ (e.g. an increase and then decay in intensity similar in shape to the $^{52}Cr^+$ intensity) was observed in any of our implanted materials. Ion implantation was carried out by CuttingEdge Ions.

To determine the implanted $^{52}Cr^+$ fluence and RSF for each terrestrial carbonate, the NIST glasses, San Carlos Olivine, and terrestrial carbonates were sputtered using a 2nA O_3^- primary beam focused into a ~3 μm spot rastered over 50×50 μm^2 areas. A field aperture was inserted into an ion image plane to restrict the collected ions to the central 15×15 μm^2 area of each raster square. A 80 μm entrance slit width was used. Secondary ions of $^{44}Ca^+$, $^{52}Cr^+$, $^{53}Cr^+$, and $^{55}Mn^+$ were counted using an electron multiplier in monocollection mode. Prior to analysis, the C coating was removed without the use of polishing compound and replaced with a 30 nm layer of gold to prevent charging during the ion probe analysis.

The implanted fluence and RSF of each terrestrial carbonate were determined following methods previously described (McCain et al. 2020). The calibrated implanted fluence determined

using the NIST glasses was (4.57 ± 0.05) × 10^{13} ions/cm^2 (2SE). For depth profiles of calcite and dolomite, surface ^{52}Cr contamination was incompletely removed by measuring the background ^{53}Cr intensity due to the low background Cr abundance in these minerals and fast sputtering rates observed in depth profiles of these materials (shown in Figure S3.1). To correct the background due to this surface contamination, the expected position and width of the implantation peak in each mineral was estimated using the SRIM software (Ziegler et al. 2010) and found to be well-modeled by a Gaussian distribution (Figure S3.1, red line). As shown in the right panel of Figure S3.1, the modeled implantation peak (red line) fits the measured ^{53}Cr-corrected ^{52}Cr intensities (thin black line) well at depths below 50 nm after which contamination is no longer significant. Therefore, we used the ^{52}Cr intensity predicted by the Gaussian distribution as the corrected intensity for the upper 50 nm of the profile for profiles showing signs of surface contamination and used the measured intensities for the remainder of the profile. For calcite and dolomite, correction for surface contamination resulted in changes to the measured RSF by 20–30%. Analyses of magnesite, NIST glass, and olivine were not affected by surface contamination due to the higher natural Cr abundance of these standard materials.

Figure S3.1. Intensities of $^{52}Cr^{+}$, $^{53}Cr^{+}$, and $^{55}Mn^{+}$ recorded during depth profiling of terrestrial dolomite 1317J plotted against the time elapsed during the depth profile (left) and the depth below the sample surface (right). The left panel is shown with count rates on a logarithmic scale, and the right with count rates on a linear scale for comparison. The heavy black line represents the intensity of $^{52}Cr^{+}$ including the implanted Cr and the background Cr in the NIST glass. The dotted green line represents the intensity of the background $^{53}Cr^{+}$ during the profile. The dashed blue line represents the intensity of $^{55}Mn^{+}$ during the profile. The thin black line represents the intensity of $^{52}Cr^{+}$ when background-corrected only by the $^{53}Cr^{+}$ intensity. The red line represents the $^{52}Cr^{+}$ implantation peak as simulated by the SRIM software.

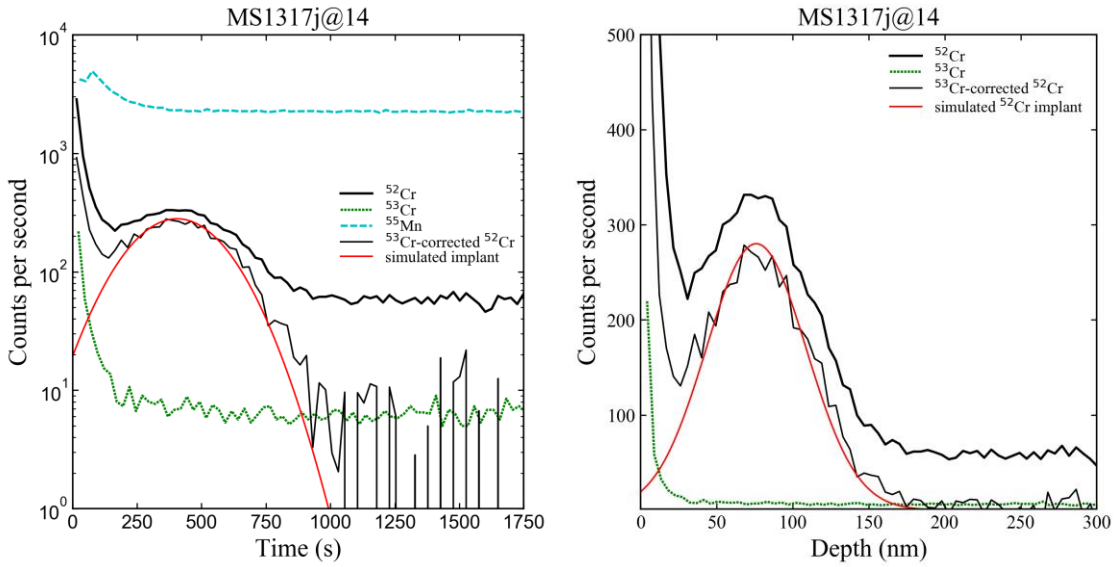

The RSF values obtained from depth profiling of natural materials are given in Supplementary Table 4.6, in Chapter 4 of this dissertation. The RSF is calculated as

$$RSF = \frac{C_{55_{Mn}} DA_{52_{Cr+}}}{I_{55_{Mn}} Ft} \qquad \text{(S3.1)}$$

where C_{55Mn} represents the concentration of ^{55}Mn as determined by EPMA (Shown in Table S2.1 in Chapter 2 of this dissertation), D represents the depth of the rastered area, A_{52Cr+} represents the total number of counts of implanted $^{52}Cr^{+}$ (as defined above), I_{55Mn} represents the measured signal intensity of $^{55}Mn^{+}$ during the depth profile, F represents the fluence of ^{52}Cr implanted as calculated

above, and *t* represents the total duration of the profile. The values used to calculate the RSF for each depth profile are given in Supplementary Table 4.7, in Chapter 4 of this dissertation.

The relationship of the RSF with the $FeCO_3$ content of dolomite is shown in Figure S3.2, and can be fit to an exponential using the curve_fit function from the SciPy Optimization module (Virtanen et al. 2020):

$$RSF = 0.235 * e^{0.345x} + 0.705 \qquad \text{(S3.2)}$$

where x refers to the Fe content of the dolomite in Mol %. Due to the large errors associated with MS1305 (yellow), this point was not included during calculation of the fit. The Fe content of each target dolomite was used to determine the RSF value used to correct the $^{55}Mn/^{52}Cr$ ratio.

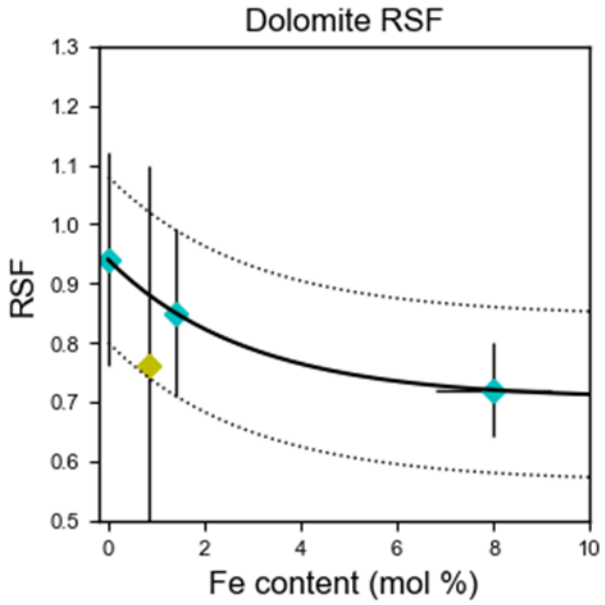

Figure S3.2. RSF values of dolomite versus the $FeCO_3$ content of dolomite. The black line is the exponential function given in Eqn. S3.2.

The relationship of the RSF with the FeCO3 content of magnesite is shown in Figure S3.3. The data was fit to a linear relationship using the 'fit_bivariate' python module, an implementation of the York et al. (2004) line fitting algorithm (York et al. 2004). For the breunnerite analysis in

Alais, the magnesite has an $FeCO_3$ content of approximately 27 mol % derived from EDS analyses. Using the equation derived from the line fitting algorithm printed on the plot, we obtain an RSF value of 0.8.

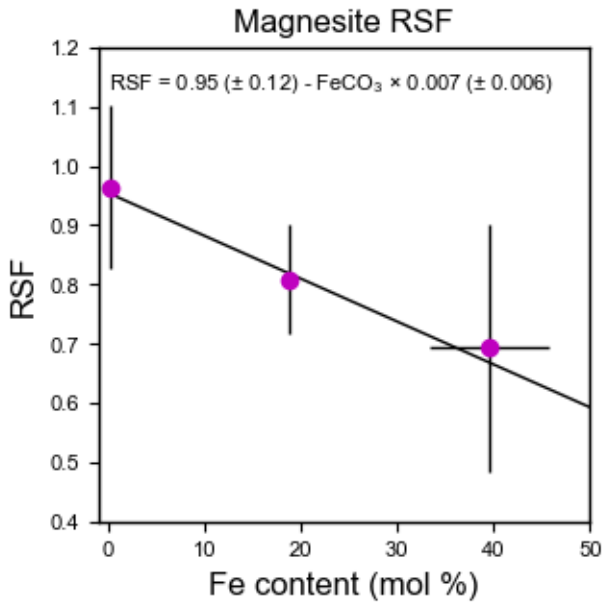

Figure S3.3. RSF values of magnesite versus the $FeCO_3$ composition of magnesite, errors 2SE. The black line is the best fit line printed on the plot.

Variation of RSF with ion probe spot geometry

Because the RSF of the $^{55}Mn/^{52}Cr$ ratio can be affected by the aspect ratio of the ion probe spot[7], we compared the RSF obtained for analyses of San Carlos olivine using the "spot mode" measurement conditions used for analyses of meteorite carbonate samples with the RSF obtained for San Carlos Olivine using the ion implantation and depth profiling method. The true $^{55}Mn/^{52}Cr$ ratio of our San Carlos Olivine standard was found to be 9.2 ± 0.7 by EPMA. We found that the values for the RSF acquired under the various conditions were identical within error (Figure S3.4),

and we therefore use the RSF values for dolomite and magnetite obtained in raster mode to correct the $^{55}Mn/^{52}Cr$ ratio of our spot analyses.

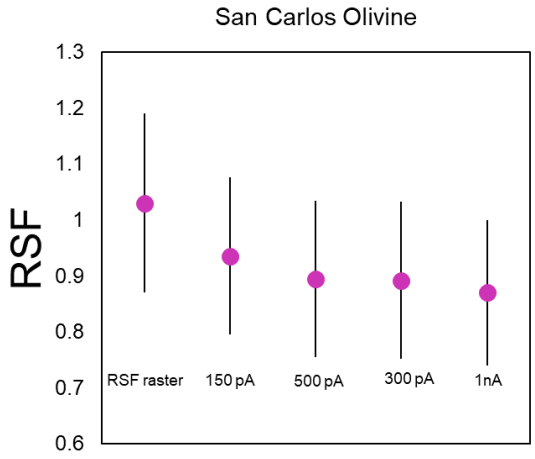

Figure S3.4. RSF values obtained by depth profiling (labeled 'RSF raster') and spot analyses of San Carlos Olivine under various analysis conditions (pink circles). Error bars represent 2 SE.

Thermal modeling of small parent bodies

We use the thermal model described in (Zhou et al. 2013) to simulate parent bodies containing significant fractions of liquid water early in the solar system's history. We solve the equation for conductive heat transfer in a sphere of radius r with internal heat production Q :

$$\frac{\partial T}{\partial t} = \kappa\left(\frac{\partial^2 T}{\partial r^2} + \frac{2}{r}\frac{\partial T}{\partial r}\right) + (1-\phi)\frac{Q}{c} \qquad \text{(S3.3)}$$

where κ is the thermal diffusivity, c is the effective heat capacity, φ is the volumetric fraction of the body initially composed of water ice, and T is temperature. Equation (S3.3) is solved using explicit finite difference in one dimension. The surface boundary condition is a fixed temperature of 78K to allow accretion of CO_2 ice. The initial condition is one of instantaneous accretion at an initial temperature of 78K. The heat production term Q is derived from the decay of ^{26}Al and ^{60}Fe. The chondritic concentrations of Al and Fe used are summarized in Zhou et al. 2013. This thermal

model accounts for the enthalpies of melting, crystallization, and vaporization phase changes of water ice and silicate rock, convection of melted silicate, and core formation. The thermal diffusivity of chondritic rock in m^2/s, is defined in Equation S3.4 as:

$$\kappa_{rock} = 1.59 \times 10^{-7} + 8.88 \times 10^{-5}/T \qquad \text{(S3.4)}$$

as reported from measurements of ordinary chondrites (Yomogida and Matsui 1983). Additional details of the thermal model are given in Zhou et al. 2013.

To produce Figure 3.8 in the main text of this chapter, the model was run multiple times for bodies of a given water fraction, at accretion times between 0 and 3 million years and with radii 1-20 km. The maximum temperature reached by each body was recorded. We categorize a body as being a good candidate for alteration if a significant portion of the object exists at temperature conditions favorable for liquid water (i.e., between 0-100° C) within times suggested by Mn-Cr dating. We further stipulate that these regions must not subsequently reach temperatures >120 °C (~400 K), as these temperatures are inconsistent with bulk O isotopic measurements of CI components which suggest CI phyllosilicate-dolomite equilibrium occurred at 50-150 °C (Clayton and Mayeda 1999; Leshin et al. 1997)

References

Alexander C. M. O., Fogel M., Yabuta H., and Cody G. D. 2007. The origin and evolution of chondrites recorded in the elemental and isotopic compositions of their macromolecular organic matter. *Geochimica et Cosmochimica Acta* 71:4380–4403. https://www.sciencedirect.com/science/article/pii/S001670370700395X.

Alexander C. M. O., Bowden R., Fogel M. L., and Howard K. T. 2015. Carbonate abundances and isotopic compositions in chondrites. *Meteoritics & Planetary Science* 50:810–833. http://onlinelibrary.wiley.com/doi/10.1111/maps.12410/abstract (Accessed October 14, 2015).

Alfing J., Patzek M., and Bischoff A. 2019. Modal abundances of coarse-grained (>5 μm) components within CI-chondrites and their individual clasts – Mixing of various lithologies on the CI parent body(ies). *Geochemistry* 79:125532. https://www.sciencedirect.com/science/article/pii/S0009281919300248.

Amelin Y. 2008. U–Pb ages of angrites. *Geochimica et Cosmochimica Acta* 72:221–232. https://www.sciencedirect.com/science/article/pii/S0016703707005820.

Amelin Y., Kaltenbach A., Iizuka T., Stirling C. H., Ireland T. R., Petaev M., and Jacobsen S. B. 2010. U-Pb chronology of the Solar System's oldest solids with variable 238U/235U. *Earth and Planetary Science Letters* 300:343–350. https://ui.adsabs.harvard.edu/abs/2010E&PSL.300..343A/abstract (Accessed April 5, 2022).

Bradley J. P., and Brownlee D. E. 1991. An Interplanetary Dust Particle Linked Directly to Type CM Meteorites and an Asteroidal Origin. *Science* 251:549–552. http://www.jstor.org/stable/2875086.

Brearley A. J., and Hutcheon I. D. 2000. Carbonates in the CM1 Chondrite ALH84034: Mineral Chemistry, Zoning and Mn-Cr Systematics. *Lunar and Planetary Science Conference* 1407. https://ui.adsabs.harvard.edu/abs/2000LPI....31.1407B/abstract (Accessed April 17, 2022).

Brennecka G. A., and Wadhwa M. 2012. Uranium isotope compositions of the basaltic angrite meteorites and the chronological implications for the early Solar System. *Proceedings of the National Academy of Sciences* 109:9299–9303. https://www.pnas.org/content/109/24/9299 (Accessed April 8, 2020).

Chan Q. H. S., Zolensky M. E., Martinez J. E., Tsuchiyama A., and Miyake A. 2016. Magnetite plaquettes are naturally asymmetric materials in meteorites. *American Mineralogist* 101:2041–2050. https://www.degruyter.com/document/doi/10.2138/am-2016-5604/html (Accessed June 20, 2021).

Chaumard N., Defouilloy C., Hertwig A. T., and Kita N. T. 2021. Oxygen isotope systematics of chondrules in the Paris CM2 chondrite: Indication for a single large formation region

across snow line. *Geochimica et Cosmochimica Acta* 299:199–218. https://www.sciencedirect.com/science/article/pii/S0016703721000983.

Ciesla F. J., Davison T. M., Collins G. S., and O'Brien D. P. 2013. Thermal consequences of impacts in the early solar system. *Meteoritics & Planetary Science* 48:2559–2576. http://onlinelibrary.wiley.com/doi/10.1111/maps.12236/abstract (Accessed June 6, 2016).

Clayton R. N., and Mayeda T. K. 1984. The oxygen isotope record in Murchison and other carbonaceous chondrites. *Earth and Planetary Science Letters* 67:151–161. http://www.sciencedirect.com/science/article/pii/0012821X84901109 (Accessed December 21, 2016).

Clayton R. N., and Mayeda T. K. 1999. Oxygen isotope studies of carbonaceous chondrites. *Geochimica et Cosmochimica Acta* 63:2089–2104. http://www.sciencedirect.com/science/article/pii/S0016703799000903 (Accessed December 21, 2016).

Dartois E., and Langlet F. 2021. Carbon dioxide clathrate hydrate formation at low temperature - Diffusion-limited kinetics growth as monitored by FTIR. *Astronomy & Astrophysics* 652:A74. https://www.aanda.org/articles/aa/abs/2021/08/aa40858-21/aa40858-21.html (Accessed May 2, 2022).

Davis A. M., and McKeegan K. D. 2014. 1.11 - Short-Lived Radionuclides and Early Solar System Chronology. In *Treatise on Geochemistry (Second Edition)*, edited by Holland H. D., and Turekian K. K. Oxford: Elsevier. pp. 361–395 http://www.sciencedirect.com/science/article/pii/B9780080959757001133.

DeMeo F. E., and Carry B. 2014. Solar System evolution from compositional mapping of the asteroid belt. *Nature* 505:nature12908. https://www.nature.com/articles/nature12908 (Accessed November 20, 2017).

Dobrică E., McCain K. A., McKeegan K. D., and Brearley A. J. 2022. Carbonates, New Tools to Investigate Shock Metamorphic Effects in Chondrites. *LPI Contributions* 2678:2313. https://ui.adsabs.harvard.edu/abs/2022LPICo2678.2313D/abstract (Accessed April 27, 2022).

Fujiya W., Sugiura N., Hotta H., Ichimura K., and Sano Y. 2012. Evidence for the late formation of hydrous asteroids from young meteoritic carbonates. *Nature Communications* 3:627. http://www.nature.com/ncomms/journal/v3/n1/full/ncomms1635.html (Accessed October 2, 2015).

Fujiya W., Sugiura N., Sano Y., and Hiyagon H. 2013. Mn–Cr ages of dolomites in CI chondrites and the Tagish Lake ungrouped carbonaceous chondrite. *Earth and Planetary Science Letters* 362:130–142. http://www.sciencedirect.com/science/article/pii/S0012821X12006838 (Accessed October 2, 2015).

Fujiya W., Sugiura N., Marrocchi Y., Takahata N., Hoppe P., Shirai K., Sano Y., and Hiyagon H. 2015. Comprehensive study of carbon and oxygen isotopic compositions, trace element abundances, and cathodoluminescence intensities of calcite in the Murchison CM chondrite. *Geochimica et Cosmochimica Acta* 161:101–117. http://www.sciencedirect.com/science/article/pii/S0016703715002033 (Accessed March 8, 2017).

Fujiya W., Fukuda K., Koike M., Ishida A., and Sano Y. 2016. Oxygen and Carbon Isotopic Ratios of Carbonates in the Nogoya CM Chondrite. p. 1712 http://adsabs.harvard.edu/abs/2016LPI....47.1712F.

Fujiya W., Hoppe P., Ushikubo T., Fukuda K., Lindgren P., Lee M. R., Koike M., Shirai K., and Sano Y. 2019. Migration of D-type asteroids from the outer Solar System inferred from carbonate in meteorites. *Nature Astronomy* 1. https://www.nature.com/articles/s41550-019-0801-4 (Accessed July 26, 2019).

Gilmour I. 2014. 1.5 - Structural and Isotopic Analysis of Organic Matter in Carbonaceous Chondrites. In *Treatise on Geochemistry (Second Edition)*, edited by Holland H. D., and Turekian K. K. Oxford: Elsevier. pp. 215–233 https://www.sciencedirect.com/science/article/pii/B9780080959757001078.

Grady M. M., Wright I. P., Swart P. K., and Pillinger C. T. 1988. The carbon and oxygen isotopic composition of meteoritic carbonates. *Geochimica et Cosmochimica Acta* 52:2855–2866. https://www.sciencedirect.com/science/article/pii/0016703788901524.

Guo W., and Eiler J. M. 2007. Temperatures of aqueous alteration and evidence for methane generation on the parent bodies of the CM chondrites. *Geochimica et Cosmochimica Acta* 71:5565–5575. http://www.sciencedirect.com/science/article/pii/S0016703707004383 (Accessed October 8, 2015).

Hässig M. et al. 2017. Isotopic composition of CO2 in the coma of 67P/Churyumov-Gerasimenko measured with ROSINA/DFMS. *Astronomy & Astrophysics* 605:A50. https://www.aanda.org/articles/aa/abs/2017/09/aa30140-16/aa30140-16.html (Accessed February 1, 2022).

Hewins R. H. et al. 2014. The Paris meteorite, the least altered CM chondrite so far. *Geochimica et Cosmochimica Acta* 124:190–222. https://www.sciencedirect.com/science/article/pii/S0016703713005139.

Huberty J. M., Kita N. T., Kozdon R., Heck P. R., Fournelle J. H., Spicuzza M. J., Xu H., and Valley J. W. 2010. Crystal orientation effects in δ18O for magnetite and hematite by SIMS. *Chemical Geology* 276:269–283. http://www.sciencedirect.com/science/article/pii/S0009254110002238.

Hynes K. M., and Gyngard F. 2009. The Presolar Grain Database: http://presolar.wustl.edu/~pgd. *40th Annual Lunar and Planetary Science Conference* 1198. https://ui.adsabs.harvard.edu/abs/2009LPI....40.1198H/abstract (Accessed May 4, 2022).

Jilly C. E., Huss G. R., Krot A. N., Nagashima K., Yin Q.-Z., and Sugiura N. 2014. 53Mn-53Cr dating of aqueously formed carbonates in the CM2 lithology of the Sutter's Mill carbonaceous chondrite. *Meteoritics & Planetary Science* 49:2104–2117. http://onlinelibrary.wiley.com/doi/10.1111/maps.12305/abstract (Accessed December 7, 2015).

Kadlag Y., Becker H., and Harbott A. 2019. Cr isotopes in physically separated components of the Allende CV3 and Murchison CM2 chondrites: Implications for isotopic heterogeneity in the solar nebula and parent body processes. *Meteoritics & Planetary Science* 54:2116–2131. https://onlinelibrary.wiley.com/doi/abs/10.1111/maps.13375.

Kim S.-T., Mucci A., and Taylor B. E. 2007. Phosphoric acid fractionation factors for calcite and aragonite between 25 and 75 °C: Revisited. *Chemical Geology* 246:135–146. http://www.sciencedirect.com/science/article/pii/S0009254107003658.

King A. J., Schofield P. F., and Russell S. S. 2017. Type 1 aqueous alteration in CM carbonaceous chondrites: Implications for the evolution of water-rich asteroids. *Meteoritics & Planetary Science* 52:1197–1215. http://onlinelibrary.wiley.com/doi/10.1111/maps.12872/abstract.

Lauretta D. S. et al. 2017. OSIRIS-REx: Sample Return from Asteroid (101955) Bennu. *Space Science Reviews* 212:925–984. https://doi.org/10.1007/s11214-017-0405-1.

Lee M. R., Lindgren P., Sofe M. R., O'D Alexander C. M., and Wang J. 2012. Extended chronologies of aqueous alteration in the CM2 carbonaceous chondrites: Evidence from carbonates in Queen Alexandra Range 93005. *Geochimica et Cosmochimica Acta* 92:148–169. http://www.sciencedirect.com/science/article/pii/S0016703712003572.

Lee M. R., Sofe M. R., Lindgren P., Starkey N. A., and Franchi I. A. 2013. The oxygen isotope evolution of parent body aqueous solutions as recorded by multiple carbonate generations in the Lonewolf Nunataks 94101 CM2 carbonaceous chondrite. *Geochimica et Cosmochimica Acta* 121:452–466. http://www.sciencedirect.com/science/article/pii/S001670371300389X.

Lee M. R., Lindgren P., and Sofe M. R. 2014. Aragonite, breunnerite, calcite and dolomite in the CM carbonaceous chondrites: High fidelity recorders of progressive parent body aqueous alteration. *Geochimica et Cosmochimica Acta* 144:126–156. http://www.sciencedirect.com/science/article/pii/S0016703714005146.

Leshin L. A., Rubin A. E., and McKeegan K. D. 1997. The oxygen isotopic composition of olivine and pyroxene from CI chondrites. *Geochimica et Cosmochimica Acta* 61:835–845. http://adsabs.harvard.edu/abs/1997GeCoA..61..835L.

de Leuw S., Rubin A. E., Schmitt A. K., and Wasson J. T. 2009. 53Mn–53Cr systematics of carbonates in CM chondrites: Implications for the timing and duration of aqueous alteration. *Geochimica et Cosmochimica Acta* 73:7433–7442. http://www.sciencedirect.com/science/article/pii/S001670370900581X (Accessed October 2, 2015).

Liu M.-C., McKeegan K. D., Harrison T. M., Jarzebinski G., and Vltava L. 2018. The Hyperion-II radio-frequency oxygen ion source on the UCLA ims1290 ion microprobe: Beam characterization and applications in geochemistry and cosmochemistry. *International Journal of Mass Spectrometry* 424:1–9. http://www.sciencedirect.com/science/article/pii/S1387380617302907.

Liu M.-C., McCain K. A., Matsuda N., Yamaguchi A., Kimura M., and Tomioka N. 2022. Incorporation of 16O-rich anhydrous silicates in the protolith of highly hydrated asteroid Ryugu. https://www.researchsquare.com (Accessed April 8, 2022).

Llorca J., and Brearley A. J. 1992. Alteration of Chondrules in ALH 84034, an Unusual CM2 Carbonaceous Chondrite. *Lunar and Planetary Science Conference* 23:793. https://ui.adsabs.harvard.edu/abs/1992LPI....23..793L/abstract (Accessed April 17, 2022).

MacPherson G. J. 2014. Calcium–Aluminum-Rich Inclusions in Chondritic Meteorites. In *Treatise on Geochemistry*. Elsevier. pp. 139–179 https://linkinghub.elsevier.com/retrieve/pii/B9780080959757001054 (Accessed May 1, 2022).

McCain K. A., Young E. D., and Manning C. E. 2017. CM Carbonates Should Be Old: Insights from Parent Body Thermal Modeling. p. 2181 http://adsabs.harvard.edu/abs/2017LPI....48.2181M.

McCain K. A., Liu M.-C., and McKeegan K. D. 2020. Calibration of matrix-dependent biases in isotope and trace element analyses of carbonate minerals. *Journal of Vacuum Science & Technology B* 38:044005. https://avs.scitation.org/doi/10.1116/6.0000111.

McKibbin S. J., Ireland T. R., Amelin Y., and Holden P. 2015. Mn–Cr dating of Fe- and Ca-rich olivine from “quenched” and “plutonic” angrite meteorites using Secondary Ion Mass Spectrometry. *Geochimica et Cosmochimica Acta* 157:13–27. https://www.sciencedirect.com/science/article/pii/S0016703715001027.

Mousis O., Lunine J. I., Picaud S., and Cordier D. 2010. Volatile inventories in clathrate hydrates formed in the primordial nebula. *Faraday Discussions* 147:509–525. https://pubs.rsc.org/en/content/articlelanding/2010/fd/c003658g (Accessed May 2, 2022).

Papanastassiou D. A. 1986. Chromium isotopic anomalies in the Allende meteorite. *The Astrophysical Journal* 308:L27–L30.

Piralla M., Marrocchi Y., Verdier-Paoletti M. J., Vacher L. G., Villeneuve J., Piani L., Bekaert D. V., and Gounelle M. 2020. Primordial water and dust of the Solar System: Insights from in situ oxygen measurements of CI chondrites. *Geochimica et Cosmochimica Acta* 269:451–464. https://www.sciencedirect.com/science/article/pii/S0016703719306957.

Rosenbaum J., and Sheppard S. M. F. 1986. An isotopic study of siderites, dolomites and ankerites at high temperatures. *Geochimica et Cosmochimica Acta* 50:1147–1150. http://www.sciencedirect.com/science/article/pii/0016703786903960.

Rowe M. W., Clayton R. N., and Mayeda T. K. 1994. Oxygen isotopes in separated components of CI and CM meteorites. *Geochimica et Cosmochimica Acta* 58:5341–5347. http://www.sciencedirect.com/science/article/pii/0016703794903174.

Rubin A. E., Trigo-Rodríguez J. M., Huber H., and Wasson J. T. 2007. Progressive aqueous alteration of CM carbonaceous chondrites. *Geochimica et Cosmochimica Acta* 71:2361–2382. http://www.sciencedirect.com/science/article/pii/S001670370700083X.

Rubin A. E. 2015. An American on Paris: Extent of aqueous alteration of a CM chondrite and the petrography of its refractory and amoeboid olivine inclusions. *Meteoritics & Planetary Science* 50:1595–1612. http://onlinelibrary.wiley.com/doi/10.1111/maps.12482/abstract (Accessed March 3, 2017).

Russell S. S., Suttle M. D., and King A. J. 2022. Abundance and importance of petrological type 1 chondritic material. *Meteoritics & Planetary Science* 57:277–301. https://onlinelibrary.wiley.com/doi/abs/10.1111/maps.13753.

Sakamoto N., Seto Y., Itoh S., Kuramoto K., Fujino K., Nagashima K., Krot A. N., and Yurimoto H. 2007. Remnants of the Early Solar System Water Enriched in Heavy Oxygen Isotopes. *Science*. https://www.science.org/doi/abs/10.1126/science.1142021 (Accessed October 27, 2021).

Scott E. R. D., and Krot A. N. 2014. Chondrites and Their Components. In *Treatise on Geochemistry*. Elsevier. pp. 65–137 https://linkinghub.elsevier.com/retrieve/pii/B9780080959757001042 (Accessed May 1, 2022).

Śliwiński M. G., Kitajima K., Kozdon R., Spicuzza M. J., Fournelle J. H., Denny A., and Valley J. W. 2016a. Secondary Ion Mass Spectrometry Bias on Isotope Ratios in Dolomite–Ankerite, Part I: δ18O Matrix Effects. *Geostandards and Geoanalytical Research* 40:157–172. http://onlinelibrary.wiley.com/doi/10.1111/j.1751-908X.2015.00364.x/abstract.

Śliwiński M. G., Kitajima K., Kozdon R., Spicuzza M. J., Fournelle J. H., Denny A., and Valley J. W. 2016b. Secondary Ion Mass Spectrometry Bias on Isotope Ratios in Dolomite–Ankerite, Part II: δ13C Matrix Effects. *Geostandards and Geoanalytical Research* 40:173–184. http://onlinelibrary.wiley.com/doi/10.1111/j.1751-908X.2015.00380.x/abstract.

Śliwiński M. G., Kitajima K., Spicuzza M. J., Orland I. J., Ishida A., Fournelle J. H., and Valley J. W. 2017. SIMS Bias on Isotope Ratios in Ca-Mg-Fe Carbonates (Part III): δ18O and δ13C Matrix Effects Along the Magnesite–Siderite Solid-Solution Series. *Geostandards and Geoanalytical Research* n/a-n/a. http://onlinelibrary.wiley.com/doi/10.1111/ggr.12194/abstract.

Steele R. C. J., Heber V. S., and McKeegan K. D. 2017. Matrix effects on the relative sensitivity factors for manganese and chromium during ion microprobe analysis of carbonate: Implications for early Solar System chronology. *Geochimica et Cosmochimica Acta*

201:245–259. http://www.sciencedirect.com/science/article/pii/S001670371630624X (Accessed March 13, 2017).

Sugiura N., and Ichimura K. 2010. Mn/Cr relative sensitivity factors for synthetic calcium carbonate measured with a NanoSIMS ion microprobe. *Geochemical Journal* 44:e11-316.

Telus M., Alexander C. M. O., Hauri E. H., and Wang J. 2019. Calcite and dolomite formation in the CM parent body: Insight from in situ C and O isotope analyses. *Geochimica et Cosmochimica Acta* 260:275–291. http://www.sciencedirect.com/science/article/pii/S0016703719303515.

Tyra M. A., Farquhar J., Guan Y., and Leshin L. A. 2012. An oxygen isotope dichotomy in CM2 chondritic carbonates—A SIMS approach. *Geochimica et Cosmochimica Acta* 77:383–395. http://www.sciencedirect.com/science/article/pii/S0016703711005904.

Tyra M., Brearley A., and Guan Y. 2016. Episodic carbonate precipitation in the CM chondrite ALH 84049: An ion microprobe analysis of O and C isotopes. *Geochimica et Cosmochimica Acta* 175:195–207. http://www.sciencedirect.com/science/article/pii/S0016703715006596 (Accessed January 8, 2016).

Vacher L. G., Marrocchi Y., Villeneuve J., Verdier-Paoletti M. J., and Gounelle M. 2017. Petrographic and C & O isotopic characteristics of the earliest stages of aqueous alteration of CM chondrites. *Geochimica et Cosmochimica Acta* 213:271–290. http://www.sciencedirect.com/science/article/pii/S0016703717304088.

Vacher L. G., Marrocchi Y., Villeneuve J., Verdier-Paoletti M. J., and Gounelle M. 2018. Collisional and alteration history of the CM parent body. *Geochimica et Cosmochimica Acta* 239:213–234. https://www.sciencedirect.com/science/article/pii/S0016703718304344.

Verdier-Paoletti M. J., Marrocchi Y., Avice G., Roskosz M., Gurenko A., and Gounelle M. 2017. Oxygen isotope constraints on the alteration temperatures of CM chondrites. *Earth and Planetary Science Letters* 458:273–281. http://www.sciencedirect.com/science/article/pii/S0012821X16306203 (Accessed March 13, 2017).

Verdier-Paoletti M. J., Marrocchi Y., Vacher L. G., Gattacceca J., Gurenko A., Sonzogni C., and Gounelle M. 2019. Testing the genetic relationship between fluid alteration and brecciation in CM chondrites. *Meteoritics & Planetary Science, Volume 54, Issue 8, pp. 1692-1709.* 54:1692. https://ui.adsabs.harvard.edu/abs/2019M%26PS...54.1692V/abstract (Accessed August 14, 2021).

Virtanen P. et al. 2020. SciPy 1.0: fundamental algorithms for scientific computing in Python. *Nature Methods* 17:261–272. https://www.nature.com/articles/s41592-019-0686-2 (Accessed April 7, 2020).

Visser R., John T., Whitehouse M. J., Patzek M., and Bischoff A. 2020. A short-lived 26Al induced hydrothermal alteration event in the outer solar system: Constraints from Mn/Cr ages of carbonates. *Earth and Planetary Science Letters* 547:116440. http://www.sciencedirect.com/science/article/pii/S0012821X20303848.

Watanabe S. et al. 2019. Hayabusa2 arrives at the carbonaceous asteroid 162173 Ryugu—A spinning top–shaped rubble pile. *Science*. https://www.science.org/doi/full/10.1126/science.aav8032 (Accessed April 13, 2022).

Yada T. et al. 2022. Preliminary analysis of the Hayabusa2 samples returned from C-type asteroid Ryugu. *Nature Astronomy* 6:214–220. https://www.nature.com/articles/s41550-021-01550-6 (Accessed April 7, 2022).

Yamamoto T. 1985. Formation environment of cometary nuclei in the primordial solar nebula. *Astronomy and Astrophysics* 142:31–36. https://ui.adsabs.harvard.edu/abs/1985A&A...142...31Y/abstract (Accessed May 2, 2022).

Yomogida K., and Matsui T. 1983. Physical properties of ordinary chondrites. *Journal of Geophysical Research: Solid Earth (1978–2012)* 88:9513–9533. http://onlinelibrary.wiley.com/doi/10.1029/JB088iB11p09513/full (Accessed September 25, 2015).

York D., Evensen N. M., Martínez M. L., and De Basabe Delgado J. 2004. Unified equations for the slope, intercept, and standard errors of the best straight line. *American Journal of Physics* 72:367–375. https://aapt.scitation.org/doi/10.1119/1.1632486.

Zhou Q., Yin Q.-Z., Young E. D., Li X.-H., Wu F.-Y., Li Q.-L., Liu Y., and Tang G.-Q. 2013. SIMS Pb–Pb and U–Pb age determination of eucrite zircons at < 5 μm scale and the first 50 Ma of the thermal history of Vesta. *Geochimica et Cosmochimica Acta* 110:152–175. http://www.sciencedirect.com/science/article/pii/S0016703713001117 (Accessed April 10, 2017).

Ziegler J. F., Ziegler M. D., and Biersack J. P. 2010. SRIM - The stopping and range of ions in matter (2010). *NIMPB* 268:1818–1823. https://ui.adsabs.harvard.edu/abs/2010NIMPB.268.1818Z/abstract (Accessed January 24, 2020).

Zolensky M. E., Mittlefehldt D. W., Lipschutz M. E., Wang M.-S., Clayton R. N., Mayeda T. K., Grady M. M., Pillinger C., and B D. 1997. CM chondrites exhibit the complete petrologic range from type 2 to 1. *Geochimica et Cosmochimica Acta* 61:5099–5115. http://www.sciencedirect.com/science/article/pii/S0016703797003578 (Accessed May 3, 2017).

Chapter 4.

Early fluid activity on Ryugu: perspectives from oxygen, carbon, and ^{53}Mn-^{53}Cr isotopes

Kaitlyn A. McCain*, Nozomi Matsuda*, Ming-Chang Liu, Kevin D. McKeegan, Akira Yamaguchi, Makoto Kimura, Naotaka Tomioka, Motoo Ito, Naoya Imae, Masayuki Uesugi, Naoki Shirai, Takuji Ohigashi, Richard C. Greenwood, Kentaro Uesugi, Aiko Nakato, Kasumi Yogata, Hayato Yuzawa, Yu Kodama, Kaori Hirahara, Ikuya Sakurai, Ikuo Okada, Yuzuru Karouji, Satoru Nakazawa, Tatsuaki Okada, Takanao Saiki, Satoshi Tanaka, Fuyuto Terui, Makoto Yoshikawa, Akiko Miyazaki, Masahiro Nishimura, Toru Yada, Masanao Abe, Tomohiro Usui, Sei-ichiro Watanabe, and Yuichi Tsuda.

This work has been submitted to Nature Astronomy under the same name and has been modified slightly to fit the dissertation format. Kaitlyn McCain and Nozomi Matsuda contributed equally.

Abstract

Samples from asteroid Ryugu returned by the Hayabusa2 mission contain evidence of extensive alteration by aqueous fluids and appear related to the CI chondrites. To understand the sources of the fluid and the timing of chemical reactions occurring during the alteration processes, we investigated the oxygen, carbon, and ^{53}Mn-^{53}Cr systematics of carbonate and magnetite in two Ryugu particles. We find that the fluid was initially between 0−20 °C and enriched in ^{13}C, and ^{17}O and ^{18}O, and subsequently evolved towards lighter carbon and oxygen isotopic compositions as alteration proceeded. Carbonate ages show that this fluid-rock interaction took place within the first ~1.4 million years of solar system history requiring early accretion and preservation of carbonaceous material, either in a planetesimal less than ~17 km in diameter or a larger body which was disrupted and reassembled.

Introduction

The Hayabusa2 mission returned approximately 5.4 g of material from the C-type asteroid Ryugu. This material is highly aqueously altered and resembles the rare CI (Ivuna-type) chondrite meteorites, with abundant Mg-phyllosilicate, pyrrhotite, magnetite, and carbonate recording extensive fluid evolution on Ryugu's parent body (Ito et al., 2022; Pilorget et al., 2022; Yada et al., 2022). Because aqueous alteration products such as magnetite and carbonate record information about the fluid from which they form, isotopic measurements of these components can be used to constrain the timing and characteristics of aqueous alteration of Ryugu materials.

In addition to their mineralogical similarities, the bulk oxygen isotopic compositions of the Ryugu particles and CI chondrites are also similar in $\Delta^{17}O$ (Greenwood et al., 2022). These values are primarily defined by the phyllosilicate matrix, the most abundant component in both Ryugu and the CI chondrites. Oxygen isotopic compositions of CI components such as carbonate, anhydrous silicate, phyllosilicate, and magnetite have been used to estimate the temperatures of final equilibration between carbonate and phyllosilicate to ~50–150 °C (Clayton and Mayeda, 1999; Leshin et al., 1997), and radiometric dating of secondary minerals has constrained the timing of fluid alteration to ~4–6 Myr after CAI formation (Fujiya et al., 2013; Visser et al., 2020). However, the CI chondrites have been exposed to various degrees of terrestrial alteration, which appear to have affected the bulk oxygen isotopic compositions (Greenwood et al., 2022). Ryugu particles therefore represent a unique opportunity to study pristine samples of hydrated asteroidal material.

Of the various alteration products found in hydrated extraterrestrial materials like returned Ryugu particles and CI chondrites, carbonate minerals are of particular interest because they can be dated using the short-lived ^{53}Mn-^{53}Cr chronometer ($t_{1/2}$ = 3.7 Myr), thereby tracking when liquid

water was present and establishing a timescale for the accretion and alteration of carbonaceous planetesimals. Stable isotope studies of the major elements O and C can also provide insight into the sources of the fluids present as well as the temperatures and reactions occurring in the asteroid or its progenitor. To preserve the petrologic context and minimize consumption of precious Ryugu material, these analyses can be performed in-situ with high spatial resolution using Secondary Ion Mass Spectrometry (SIMS) to sputter material from individual mineral grains with a spot size of ~3–15 μm (see Supplementary Methods). This technique has also been applied to analyses of carbonate and other secondary minerals in CM and CI carbonaceous chondrites, which facilitates comparison between the returned Ryugu particles and previously-studied meteorite samples.

The oxygen isotopic systematics of aqueous alteration products in carbonaceous chondrite meteorites have been extensively studied (Clayton and Mayeda, 1999, 1984; Fujiya et al., 2015; Lee et al., 2014, 2013; Piralla et al., 2020; Rowe et al., 1994; Telus et al., 2019; Tyra et al., 2016, 2012, Vacher et al., 2018, 2017; Verdier-Paoletti et al., 2017) and used to infer the extent of equilibration between co-accreted water ice, inferred to be ^{17,18}O-enriched (Clayton and Mayeda, 1984; Sakamoto et al., 2007) with positive Δ^{17}O, and primary, anhydrous silicates (Leshin et al., 1997; Liu et al., 2022; Piralla et al., 2020) with negative Δ^{17}O on the parent body, thereby tracking the sequence of alteration. In addition, if two secondary phases with the same Δ^{17}O are identified, the difference in δ^{18}O between the two phases can be used to calculate an equilibrium formation temperature, based on the assumption that they precipitated from the same water composition (Clayton and Mayeda, 1984; Leshin et al., 1997; Rowe et al., 1994; Telus et al., 2019). For the CI chondrites, temperatures of aqueous alteration have been estimated to be ~50−150 °C based upon the phyllosilicate-carbonate pair (Clayton and Mayeda, 1999; Leshin et al., 1997). The oxygen

isotopic compositions of magnetite, if found to be in equilibrium with other secondary phases, can be used in a similar fashion (Telus et al., 2019).

The carbon isotopic compositions of carbonate have been used to infer the contributions of various C sources, such as insoluble and soluble organic matter (Alexander et al., 2007; Sephton et al., 2000) and isotopically heavy CO_2–CO ices (Fujiya et al., 2020; Hässig et al., 2017), to the fluids in the carbonaceous chondrite parent bodies. In addition, carbon isotope compositions can track reactions occurring within the fluid such as methane formation and loss (Guo and Eiler, 2007; Telus et al., 2019; Tyra et al., 2016; Vacher et al., 2018), oxidation of organic material (Fujiya et al., 2015; Vacher et al., 2017), and CH_4–CO equilibration (Alexander et al., 2015; Telus et al., 2019). However, such studies have thus far been limited to carbonate from CM (Mighei-type) chondrites; no in-situ C isotopic measurements have been conducted on CI carbonate.

The timing and duration of these chemical changes can be constrained using Mn-Cr dating, and these ages can also be used to constrain the accretion time of the parent bodies from which samples originate. Carbonate minerals are an ideal target for this analysis as they strongly fractionate Mn from Cr during their formation, leading to large excesses in ^{53}Cr through which a $^{53}Mn/^{55}Mn$ ratio at the time of carbonate formation can be inferred. Previous in-situ studies of highly-altered carbonaceous chondrites have found that most carbonate in these meteorite classes formed between 4–6 Myr after CAI formation in large (> 50 km radius) parent bodies which accreted 3–4 Myr after CAI formation (Fujiya et al., 2013, 2012; Visser et al., 2020). However, deriving initial $^{53}Mn/^{55}Mn$ ratios of carbonate based on in-situ SIMS analyses requires standards that closely match the chemical composition of the target mineral to constrain the Mn/Cr ratio accurately (e.g., are ‘matrix-matched’), particularly with regard to the Fe content of the carbonate (McCain et al., 2020; Steele et al., 2017; Sugiura and Ichimura, 2010). Previous studies which

targeted dolomite were performed using non-matrix-matched standards (primarily calcite) for the Mn/Cr ratio, which can affect the accuracy of the results (McCain et al., 2020; Steele et al., 2017). In this work, we use matrix-matched calcite, dolomite, and magnesite standards obtain the Mn/Cr ratios of respective mineral phases in Ryugu.

Sample description

Ryugu particles A0037 and C0009, which were acquired from the 1st and 2nd touchdown sites respectively (Ito et al., 2022), are dominated by minerals produced via aqueous alteration (Ito et al., 2022; Yada et al., 2022). A0037 contains a much higher abundance of carbonate (21.2 vol%) than C0009 (1.8 vol%) (Ito et al., 2022). Carbonates found in these two particles are primarily dolomite ($CaMg(CO_3)_2$, Figure 4.1a; see also Figure 2 in Yamaguchi et al., 2022) with minor occurrence of Ca-carbonate ($CaCO_3$, Figure 4.1b; see also Supplementary Figure 6 in Yamaguchi et al., 2022) and breunnerite ($(Mg,Fe,Mn)CO_3$, see Supplementary Figure 6 in Yamaguchi et al., 2022) in C0009. Both particles contain magnetite (3.6 vol%) (Ito et al., 2022) with a variety of morphologies, often enclosed within dolomite (Figure 4.1a, see also Supplementary Figure 6 in Yamaguchi et al., 2022). Detailed petrological and mineralogical descriptions of both particles are given by Ito et al. 2022 and Yamaguchi et al. 2022.

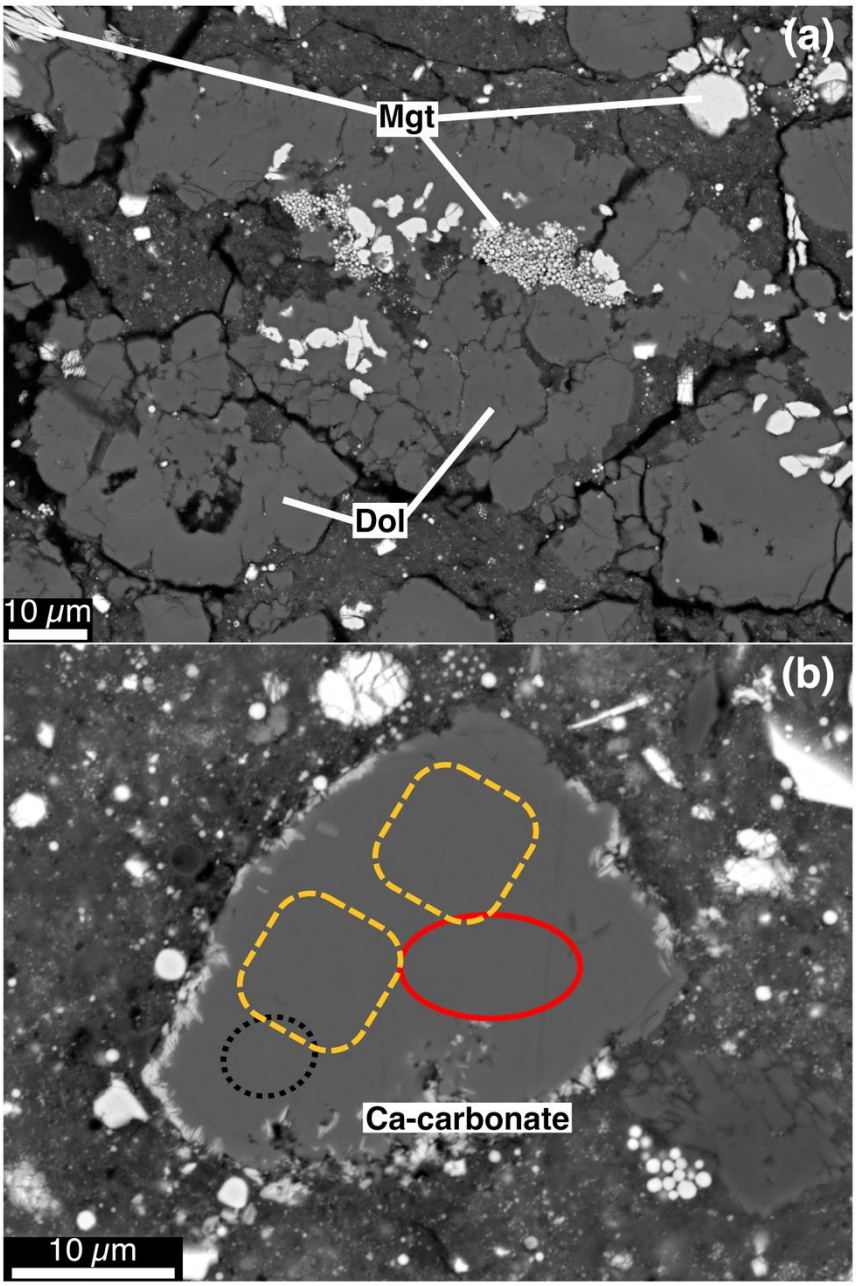

Figure 4.1. Backscattered electron (BSE) images of Ryugu particles (a) A0037 and (b) C0009 (Yamaguchi et al., 2022). Dol: dolomite, Mgt: magnetite. The dotted black oval, red oval, and dashed yellow squares in (b) represent the size and location of the oxygen, carbon, and Mn-Cr analysis pits, respectively.

Methods

Petrographic characterization

The detailed SEM and EPMA methods are reported by Yamaguchi et al. (2022).

Secondary ion mass spectrometry

In-situ oxygen, carbon, and Mn-Cr isotopes analyses of Ryugu carbonates and magnetite were performed using the UCLA CAMECA ims-1290 ion microprobe. The Ryugu A0037 and C0009 particles were mounted in epoxy and polished under dry conditions and coated with a thin layer of Au for SIMS analyses after petrographic characterization. After SIMS analysis, all pits were observed by scanning electron microscopy (SEM, Tescan Vega) at UCLA. Analyses found to overlap inclusions, cracks, or voids were discarded. In all stable isotope analyses, calcite, magnetite, and a suite of 4 dolomite standards of various Fe compositions were measured to quantify the instrumental mass fractionation (IMF) as a function of Fe content (Śliwiński et al., 2016a, 2016b). The chemical and isotopic compositions of these reference materials are listed in Supplementary Table 5.

Oxygen isotope analysis

Oxygen isotope analyses were performed with a focused Cs^+ primary ion beam with 20 kV total accelerating voltage. Based on the size of the grains analyzed, we used three different primary beam conditions: 3O-I (~3 nA) with ~15 µm spot for dolomite, 3O-II (~700 pA) with ~10 µm spot for dolomite, and 3O-III (~60 pA) with ~ 3µm spot for dolomite, Ca-carbonate, and magnetite. A normal incident electron gun was used for charge compensation. The oxygen isotopic compositions are reported as per mil deviations relative to standard mean ocean water (SMOW), which can be calculated by using $\delta\,{}^{x}O = \left[\frac{\left({}^{x}O/{}^{16}O\right)_m}{\left({}^{x}O/{}^{16}O\right)_t} - 1\right] \times 1000$, where x = 17 or 18, and "m"

and “t” stand for “measured” and “true”. The deviation from the terrestrial fractionation line is expressed as $\Delta^{17}O_{SMOW} = \delta^{17}O_{SMOW} - 0.52 \times \delta^{18}O_{SMOW}$.

In session 3O-I, secondary $^{16}O^-$, $^{17}O^-$, and $^{18}O^-$ ions were collected simultaneously using three Faraday cups (FCs) to achieve the highest possible precision. Typical $^{16}O^-$ current was equivalent to ~3×10^9 counts/sec for the MS1317J dolomite standard. The mass resolution power (MRP) was set to ~5500 for $^{17}O^-$. In the second session (3O-II), the secondary ions were measured simultaneously using two FCs (for $^{16}O^-$ and $^{18}O^-$) and the axial electron multiplier (EM; for $^{17}O^-$) under the mass resolution of ~5800 for $^{17}O^-$ with a typical count rate of for $^{16}O^-$ ~ 7.8×10^8 cps (for MS1317J standard). In the third session (3O-III), we used a FC (for $^{16}O^-$) and two EMs (for $^{17}O^-$ and$^{18}O^-$) in multicollection mode. The secondary ion count rates of $^{16}O^-$ were ~ 6.1×10^7 cps, ~ 5.8×10^7 cps, and ~ 6.4×10^7 cps for MS1317J, calcite, and dolomite, respectively. The MRP was ~ 5600. Ion intensities were corrected for background and yield (FC) or deadtime (EM) as appropriate for each detector.

The contribution of $^{16}OH^-$ tail to the $^{17}O^-$ signal was determined by using the ratio of the ion signal measured at the tail of the $^{16}OH^-$ peak on the high mass end (mass unit = 17.00274 + 0.00361) to that measured at the center of the $^{16}OH^-$ peak and assuming a symmetric peak. This ratio was then multiplied by the $^{16}OH^-$ count rate on the unknown samples recorded at the end of each spot analysis. All reported $\delta^{17}O$ values have been corrected for the $^{16}OH^-$ tail.

The compositional dependence of instrumental bias (i.e., the “matrix effect” on instrumental mass fractionation) was calibrated using the equation similar to that suggested in Śliwiński et al. (2016a). Errors represent 2σ analytical uncertainty including both the internal measurement precision and the external reproducibility for standard measurements.

Carbon isotope analysis

Carbon isotope analysis of carbonate was carried out using a focused Cs^+ ion primary beam of ~600 to 700 pA. Secondary $^{12}C^-$ and $^{13}C^-$ ions were simultaneously detected using a FC and EM, respectively. A normal incidence electron gun was used for charge compensation. The typical count rate of $^{12}C^-$ was ~ 5.5 – 6 $\times 10^6$ cps for MS1317J. The instrumental bias was corrected using MS1317J with a $\delta^{13}C_{VPDB}$ value of –1.20 ‰ ($^{13}C/^{12}C$ = 0.011167) and optical calcite with a $\delta^{13}C_{VPDB}$ value of 1.42 ‰ ($^{13}C/^{12}C$ = 0.011196) for dolomite and Ca-carbonate, respectively.

We defined the bias as

$$\text{bias} = \frac{\left(^{13}C/^{12}C\right)_m}{\left(^{13}C/^{12}C\right)_t} \qquad (4.1)$$

where "m" and "t" stand for "measured" and "true" isotope ratios, respectively. Errors represent 2σ analytical uncertainty including both the internal measurement precision and the external reproducibility for standard measurements.

Mn-Cr isotope analysis

Mn-Cr analyses of carbonates were carried out using a 1nA $^{16}O_3^-$ primary ion beam generated by a Hyperion-II plasma ion source. For dolomite and magnesite with sufficient Mn content, secondary $^{52}Cr^+$, $^{53}Cr^+$, and $^{55}Mn^+$ ions were collected simultaneously using two EMs (for $^{52}Cr^+$ and $^{53}Cr^+$) and an FC (for $^{55}Mn^+$). An MRP of ~5500 was used to separate $^{52}Cr^+$ from $^{28}Si^{24}Mg^+$ and $^{53}Cr^+$ from $^{52}CrH^+$. For dolomite and calcite with low Mn concentrations, $^{55}Mn^+$ was collected using an EM in peak-switching mode. Analysis spots were presputtered using an 8 × 8 or a 5 × 5 μm raster to remove any surface Cr contamination before focusing the beam to a tighter raster (5 × 5 or 2 × 2 μm) for the analysis, resulting in an effective spot size of ~ 8 × 10 μm^2. The instrumental mass fractionation for Cr was corrected by comparison to repeated measurements of

the 1317J dolomite, which contains trace amounts of terrestrial Cr ($^{53}Cr/^{52}Cr$ = 0.113459) (Papanastassiou, 1986). The relative sensitivity factor between ^{55}Mn and ^{52}Cr is defined as

$$RSF = \frac{(55Mn/52Cr)_{True}}{(55Mn/52Cr)_{SIMS}} \qquad (4.2)$$

and was determined using a combination of San Carlos Olivine and ion-implanted carbonate standards (see next section). Prior to the Mn-Cr analysis, the local distribution of ^{52}Cr was assessed using scanning ion imaging to avoid regions with high ^{52}Cr background, which can indicate contamination from Cr-rich phases.

Calculation of the isochron slope was performed using the 'fit_bivariate' python module, an implementation of the York et al., (2004) line fitting algorithm.

Mn-Cr carbonate standard production and characterization

Natural carbonate minerals from the UCLA and Field Museum of Natural History (FMNH) mineral collection which span the range of Fe contents found in Ryugu carbonate (0–8 mol% $FeCO_3$ for dolomite and 0–40 mol % $FeCO_3$ for magnesite) were embedded in Field's Metal and/or indium in the center of aluminum disks. Fragments of San Carlos Olivine and the NIST 612 and 614 glasses were mounted in the same disks for use as concentration standards to calibrate the implant fluence. The mount was coated with 20 nm carbon to ensure conductivity and prevent charging during ion implantation. All mounts were implanted with a 185 KeV $^{52}Cr^+$ ion beam at a nominal fluence of 4×10^{13} ions/cm^2 rastered over the entire surface. A mass filter was used to separate $^{52}Cr^+$ and $^{53}Cr^+$ after Cr ionization, ensuring that only $^{52}Cr^+$ was implanted. No evidence of implanted $^{53}Cr^+$ (e.g. an increase and then decay in intensity similar in shape to the $^{52}Cr^+$ intensity) was observed in any of our implanted materials. Ion implantation was carried out by CuttingEdge Ions.

To determine the implanted $^{52}Cr^{+}$ fluence and RSF for each terrestrial carbonate, the NIST glasses, San Carlos Olivine, and terrestrial carbonates were sputtered using a 2nA O_3^- primary beam focused into a ~3 μm spot rastered over 50 × 50 μm^2 areas. A field aperture was inserted into an ion image plane to restrict the collected ions to the central 15 × 15 μm^2 area of each raster square. An 80 μm entrance slit width was used. Secondary ions of $^{44}Ca^{+}$, $^{52}Cr^{+}$, $^{53}Cr^{+}$, and $^{55}Mn^{+}$ were counted using an electron multiplier in monocollection mode. Prior to analysis, the C coating was removed without the use of polishing compound and replaced with a 30 nm layer of gold to prevent charging during the ion probe analysis.

The implanted fluence and RSF of each terrestrial carbonate were determined following methods previously described(McCain et al., 2020). The calibrated implanted fluence determined using the NIST glasses was (4.57 ± 0.05) × 10^{13} ions/cm^2 (2SE). For depth profiles of calcite and dolomite, surface ^{52}Cr contamination cannot be completely accounted for by simply measuring the background ^{53}Cr intensity, due to the low background Cr abundance in these minerals and fast sputtering rates observed in depth profiles of these materials (shown in Supplementary Figure S4.1). Instead, the ^{52}Cr background was corrected for by estimating the expected position and width of the implantation peak, which can be well-modeled by a Gaussian distribution, in each mineral with the SRIM software (Ziegler et al., 2010) (Supplementary Figure S4.1, red line). As shown in the right panel of Supplementary Figure S4.1, the modeled implantation peak (red line) fits the measured ^{53}Cr-corrected ^{52}Cr intensities (thin black line) well at depths below 50 nm after which contamination is no longer significant. Therefore, we used the ^{52}Cr intensity predicted by the Gaussian distribution as the corrected intensity for the upper 50 nm of the profile for profiles showing signs of surface contamination and used the measured intensities for the remainder of the profile. For calcite and dolomite, correction for surface contamination resulted in changes to the

measured RSF by 20–30%. Analyses of magnesite, NIST glass, and olivine were not affected by surface contamination due to the higher natural Cr abundance of these standard materials.

Variation of RSF with ion probe spot geometry

To ascertain that the RSF of the $^{55}Mn/^{52}Cr$ ratio obtained by depth profiling can be applied to the Ryugu data acquired with a static spot (Doyle et al., 2016), we compared the RSF results on non-implanted and implanted San Carlos olivine measured in spot and depth profiling modes, respectively. The true $^{55}Mn/^{52}Cr$ ratio of our San Carlos Olivine standard was found to be 9.2 ± 0.7 by EPMA. We found that the RSF values acquired under the two conditions were identical within error (Supplementary Figure S4.2), and we can therefore use the RSF values for dolomite and magnetite obtained in raster mode to correct the $^{55}Mn/^{52}Cr$ ratio of our spot analyses.

The RSF values obtained from depth profiling of natural materials are given in Supplementary Table S4.6. The RSF is calculated as

$$RSF = \frac{C_{55_{Mn}} D A_{52_{Cr+}}}{I_{55_{Mn}} Ft} \qquad (4.3)$$

where C_{55Mn} represents the concentration of ^{55}Mn as determined by EPMA (Shown in Supplementary Table 1), D represents the depth of the rastered area, A_{52Cr+} represents the total number of counts of implanted $^{52}Cr^+$ (as defined above), I_{55Mn} represents the measured signal intensity of $^{55}Mn^+$ during the depth profile, F represents the fluence of ^{52}Cr implanted as calculated above, and t represents the total duration of the profile. The values used to calculate the RSF for each depth profile are given in Supplementary Table 7.

RSF of dolomite and magnesite

The relationship of the RSF with the $FeCO_3$ content of dolomite is shown in supplementary Figure S4.3, and can be fit to an exponential using the curve_fit function from the SciPy Optimization module(Virtanen et al., 2020):

$$RSF = 0.235 * e^{0.345x} + 0.705 \qquad (4.4)$$

where x refers to the Fe content of the dolomite in Mol %. Due to the large errors associated with MS1305, this point was not included during calculation of the fit. As shown in Supplementary Table 1 of the main text, dolomite in Ryugu has a restricted range of Fe content, with an average of 3.5 mol% $FeCO_3$. This value corresponds to an RSF value of 0.8. The Fe content of Ryugu dolomites show only small departures from the average Fe abundance, which would lead to RSF variations well within our errors. Therefore, we use the value of 0.8 obtained for the average Ryugu dolomite composition for all analyses of Ryugu dolomite.

The relationship of the RSF with the $FeCO_3$ content of magnesite is shown in Supplementary Figure S4.4. The data was fit to a linear relationship using the 'fit_bivariate' python module, an implementation of the York et al. (2004) line fitting algorithm(York et al., 2004). For the single magnesite analysis in C0009, the magnesite has an $FeCO_3$ content of approximately 14 mol% derived from EDS analyses. Using the equation derived from the line fitting algorithm, we obtain an RSF value of 0.86.

Results

Oxygen isotopic composition of carbonate and magnetite

The oxygen isotopic compositions of dolomite in particles A0037 and C0009, magnetite in particle A0037, and Ca-carbonate in C0009 are shown in Figure 4.2 and are summarized in Supplementary Tables 1–3. The oxygen isotopic compositions of dolomites mostly plot near the terrestrial mass fractionation (TF) line; however several dolomite grains have positive $\Delta^{17}O$ well resolved from 0‰, ranging up to a maximum of +1.6 ± 0.3‰ (2σ) for an A0037 dolomite grain. The $\delta^{18}O$ values of dolomite grains are also somewhat variable, ranging from +25‰ to +34‰. The range of oxygen isotopic compositions of Ryugu dolomite is in good agreement with prior in-situ analyses of CI-chondrite dolomite (Piralla et al., 2020) (see Figure 4.2). The $\Delta^{17}O$ values of magnetite in A0037 show a limited range from +2.1‰ to +3.9‰ which nevertheless exceeds analytical uncertainty (MSWD = 5.2). The variation of $\delta^{18}O$ values among 4 grains measured are likewise small, ranging from +1‰ to +3‰. These $\delta^{18}O$ and $\Delta^{17}O$ values are similar to those observed in bulk analyses of CI chondrite magnetite (Rowe et al., 1994, see Figure 4.2). In contrast, the Ca-carbonate found in particle C0009 ranges in composition from $\Delta^{17}O$ ~0 to +2.2‰ and $\delta^{18}O$ ~+34‰ to +39‰, which differs significantly from $\Delta^{17}O$ ~0‰ and $\delta^{18}O$ = +25.5‰ found in calcite separated from Orgueil (Piralla et al., 2020).

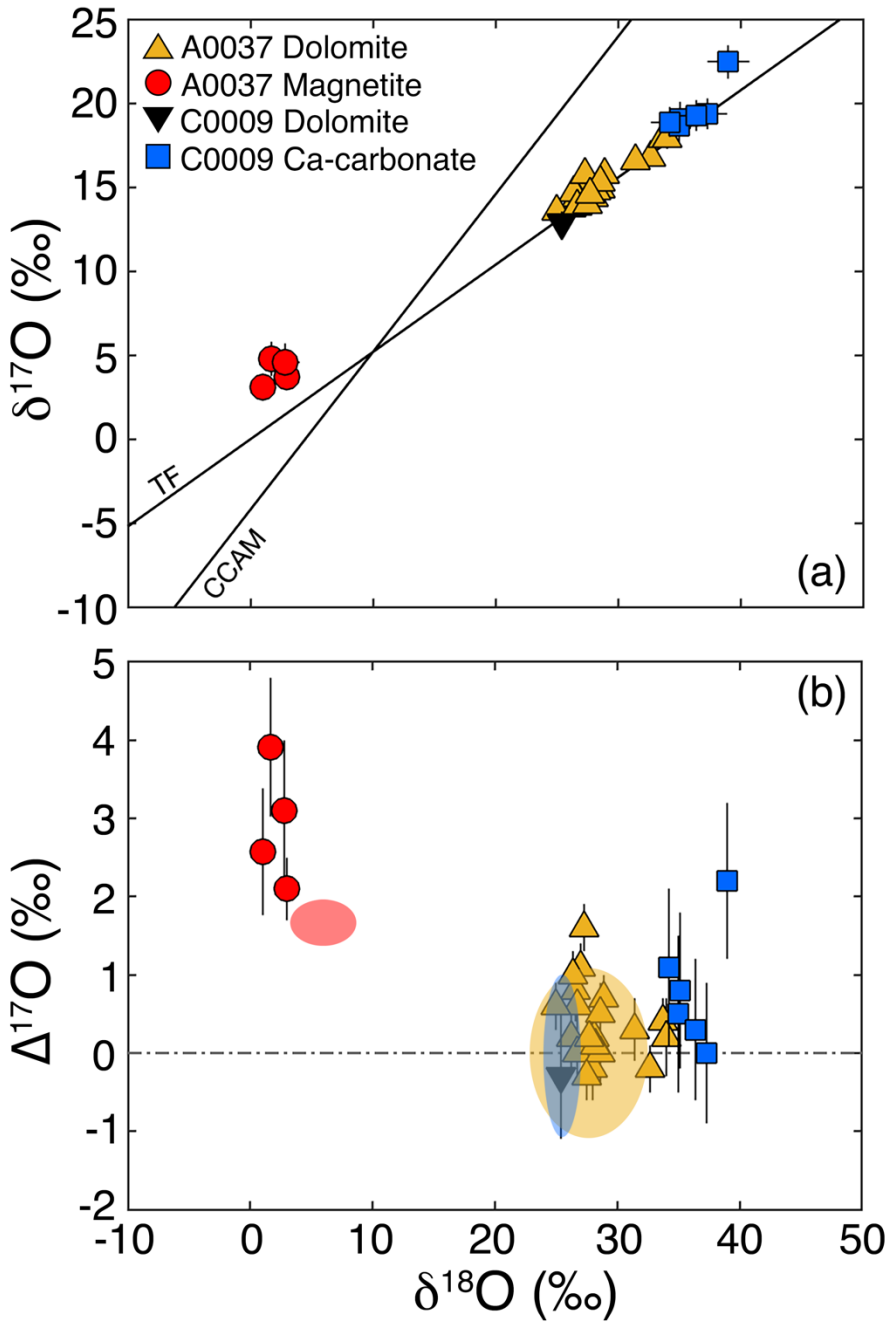

Figure 4.2. (a) A three-oxygen isotope diagram of carbonate and magnetite in Ryugu particles A00037 and C0009 relative to SMOW. The blue, yellow, and red shaded regions represent previous studies of in situ calcite, in-situ dolomite, and bulk magnetite, respectively(Piralla et al., 2020; Rowe et al., 1994). Errors are 2σ standard errors. TF: terrestrial fractionation line, CCAM: carbonaceous chondrite anhydrous minerals line. (b) $\Delta^{17}O$ vs. $\delta^{18}O$ values of Ryugu carbonate and magnetite.

Carbon isotopic compositions of carbonate

Dolomite in both Ryugu particles show a range of $\delta^{13}C$ values from 55.4‰ to 74.5‰ (Figure 4.3 and Supplementary Table 4.4). Dolomite in A0037 appears to follow a bimodal distribution with $\delta^{13}C$ peaks at ~55 and ~70‰. Dolomite (and some Ca-carbonate) in C0009 show a range of 64‰ to 75‰, with one Ca-carbonate enriched in $\delta^{13}C$ at 97‰ (Figure 4.3 and Supplementary Table 4.4). These $\delta^{13}C$ values are consistent with bulk measurements of Orgueil carbonates (Grady et al., 1988).

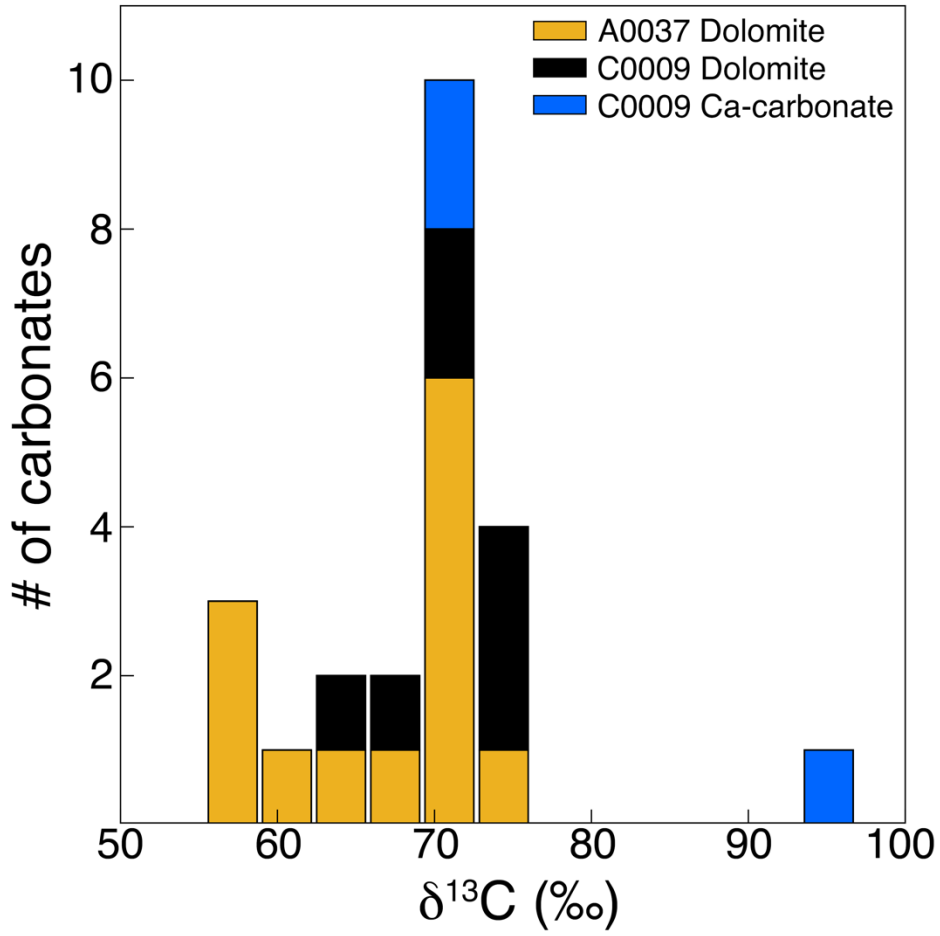

Figure 4.3. Stacked histogram of C isotopic compositions of carbonate in Ryugu particles A0037 and C0009 relative to VPDB. The Ca-carbonate outlier at $\delta^{13}C$ = 96 ‰ is 'Ca2' (see text).

Mn-Cr dating of carbonate

We measured $^{55}Mn/^{52}Cr$ and $^{53}Cr/^{52}Cr$ ratios for 20 spots on dolomite in A0037 and 16 spots on dolomite, breunnerite, and calcite in C0009. The data show ^{53}Cr excesses that are well-correlated with $^{55}Mn/^{52}Cr$ (Figure 4.4) implying initial $^{53}Mn/^{55}Mn$ of $6.8 \pm 0.5 \times 10^{-6}$ (MSWD = 0.7) for A0037 dolomite and $6.1 \pm 0.9 \times 10^{-6}$ (MSWD = 0.3) for C0009 (all errors 2SE). By calibrating these initial ratios relative to the initial $^{53}Mn/^{55}Mn$ ratio (McKibbin et al., 2015) of the D'Orbigny angrite, which has a well-defined absolute crystallization age (Amelin, 2008; Brennecka and Wadhwa, 2012), we calculate that A0037 and C0009 carbonates formed at 4566.9 ± 0.4 Ma and 4566.3 ± 0.8 Ma, respectively. Assuming 'time-zero' defined by a $^{207}Pb/^{206}Pb$ closure age (Amelin et al., 2010) for CAIs of 4567.3 Ma, the carbonates in Ryugu formed within the first 1.4 Myr of solar system origin—earlier than inferred from previous studies (Fujiya et al., 2013, 2012; Visser et al., 2020).

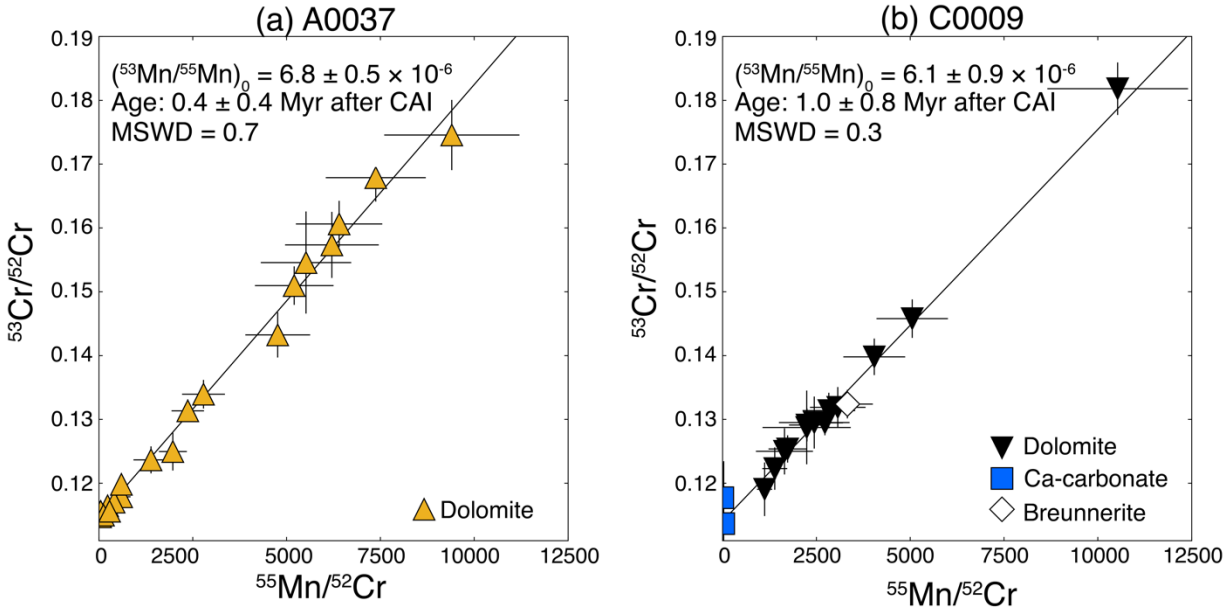

Figure 4.4. Mn-Cr isochrons for carbonates in Ryugu particles (a) A0037 and (b) C0009. Ages in Myr are reported relative to an absolute CAI age of 4567.3 Ma (Amelin et al., 2010) and anchored to the D'Orbigny angrite age and $(^{53}Mn/^{55}Mn)_0$ (see text). Error bars (±2σ) represent external and internal error summed in quadrature.

Discussion

A Ca-carbonate grain designated 'Ca 2' has $\Delta^{17}O = +2.2‰$, the highest value of $\Delta^{17}O$ we have measured in Ryugu carbonate, which suggests that it recorded an early phase of fluid evolution when relatively ^{17}O- and ^{18}O-enriched fluid (Sakamoto et al., 2007) was less equilibrated with ^{16}O-rich nebular solids.(Liu et al., 2022) The petrology of 'Ca 2' is distinct from the other Ca-carbonates, further supporting that its formation conditions were distinct from the other Ca-carbonates (Yamaguchi et al., 2022). Figure 4.3 shows that 'Ca 2' is also enriched in ^{13}C at $\delta^{13}C = +96.9‰$, suggesting that carbon in the fluid was initially isotopically heavy and derived from outer solar system CO_2 ices, similar to what has been inferred for some carbonaceous chondrites (Fujiya et al., 2020, 2019; Hässig et al., 2017). Therefore, we conclude that Ryugu accreted in the outer solar system beyond the CO_2 ice line, consistent with previous observations of bulk H and N isotopes that are consistent with an outer solar system origin (Ito et al., 2022).

The population of Ca-carbonate in particle C0009 shows a range in $\Delta^{17}O$ of ~0 to +2.2‰, following a mass-independent trend which requires that the O isotopic composition of the fluid evolved over the course of Ca-carbonate precipitation. This is in contrast to calcite grains found in Orgueil (Piralla et al., 2020), which follow a mass-dependent trend with constant $\Delta^{17}O$ with a restricted range in $\delta^{18}O$. We suggest that this difference reflects variation in alteration processes between Ryugu and Orgueil: The Ca-carbonate in Ryugu recorded the progress of equilibration between fluid and ^{16}O-poor anhydrous silicate (Liu et al., 2022), while calcite in Orgueil precipitated after this equilibration had occurred.

Magnetite in A0037 and the "Ca 2" Ca-carbonate grain (Figure 4.1b; see also Figure 4b in Yamaguchi et al., 2022) in C0009 share the same $\Delta^{17}O$ values (within uncertainty) that is higher than the $\Delta^{17}O$ of dolomite and other Ca-carbonates, reflecting a less-equilibrated fluid

composition. We conclude that magnetite and Ca-carbonate like 'Ca 2' were among the earliest minerals to precipitate during the alteration of the Ryugu protolith, predating most carbonate formation. Though magnetite in A0037 and 'Ca 2' in C0009 are from different particles, if we assume that alteration was sufficiently widespread on the Ryugu parent body so that 'Ca 2' and A0037 magnetite formed in equilibrium (Yamaguchi et al., 2022), we estimate the formation temperature at this early stage of alteration using equilibrium thermometry of calcite and magnetite to be 0−20 °C (Hayles et al., 2018). Further discussion of magnetite-H_2O and calcite-H_2O fractionation can be found in the Supplementary Information.

Dolomite in this study and bulk Ryugu particles share a value of $\Delta^{17}O$ within our uncertainties (Greenwood et al., 2022). The bulk oxygen isotopic composition is dominated by phyllosilicates, with variable contributions from carbonates which can increase the $\delta^{18}O$ of the bulk analysis. If we suppose that the weighted average of bulk Ryugu $\delta^{18}O$ from Greenwood et al., 2022 of 15.88 ± 4.85‰ (2SD) represents the composition of phyllosilicate, we may calculate an equilibrium formation temperature using this phyllosilicate-dominated bulk analysis and our observed range of dolomite $\delta^{18}O$ values (+25–34‰). Using experimentally-determined fractionation factors for dolomite (Horita, 2014) and brucite (Saccocia et al., 2015), we constrain the equilibration temperature of dolomite and phyllosilicate to 88–240 °C. Further discussion of phyllosilicate-H_2O and dolomite-H_2O fractionation can be found in the Supplementary Methods of this chapter.

We suggest the following order for the sequence of aqueous alteration on Ryugu: first, magnetite and Ca-carbonates like 'Ca 2' precipitated from aqueous fluids with high $\Delta^{17}O$ at T <20 °C with C composition dominated by CO_2 ice. As the fluid continued to exchange oxygen with ^{16}O-rich anhydrous silicates (Liu et al., 2022), additional Ca-carbonate precipitated as $\Delta^{17}O$ fell

from ~+1.1 to 0 ‰. Finally, most dolomite formed at about $\Delta^{17}O$ = +0.4 ‰ after Mg had been added to the fluid by alteration of Mg-rich silicates to form phyllosilicates with similar $\Delta^{17}O$ to dolomite. The relatively homogeneous $\Delta^{17}O$ composition of dolomite indicates that the pace of evolution of the fluid's oxygen isotopic composition had slowed by the time of dolomite formation. Petrographic observations of magnetite inclusions enclosed in dolomite but not in calcite support this sequence of events (Yamaguchi et al., 2022).

Carbon and oxygen isotopic analyses performed on the same grains were used to explore correlations between the two isotopic systems. Figure 4.5 illustrates that $\delta^{13}C$ is correlated with $\delta^{18}O$ (upper panel) and $\Delta^{17}O$ (lower panel), similar to trends observed for some CM chondrites (Alexander et al., 2015). This observation suggests that methane formation via serpentinization of the protolith followed by loss to space did not strongly affect the $\delta^{13}C$ of Ryugu carbonate, as methane release would enrich ^{13}C in the fluid over time (Guo and Eiler, 2007; Vacher et al., 2017). In contrast, we observe that carbonate formed from less-equilibrated water (e.g., with higher $\delta^{18}O$ and $\Delta^{17}O$) is also the most enriched in $\delta^{13}C$. One possible scenario could be that the initial unequilibrated fluid composition, presumably similar to the fluid recorded by 'Ca 2', evolved towards lower $\delta^{13}C$ as the fluid interacted with and oxidized Ryugu's relatively ^{13}C-depleted organic matter (Ito et al., 2022).

Figure 4.5. Carbon isotopic composition (relative to VPDB) of Ryugu dolomite (yellow triangles) and Ca-carbonate (blue squares) versus (a) $\delta^{18}O$ and (b) $\Delta^{17}O$ from the same carbonate grains.

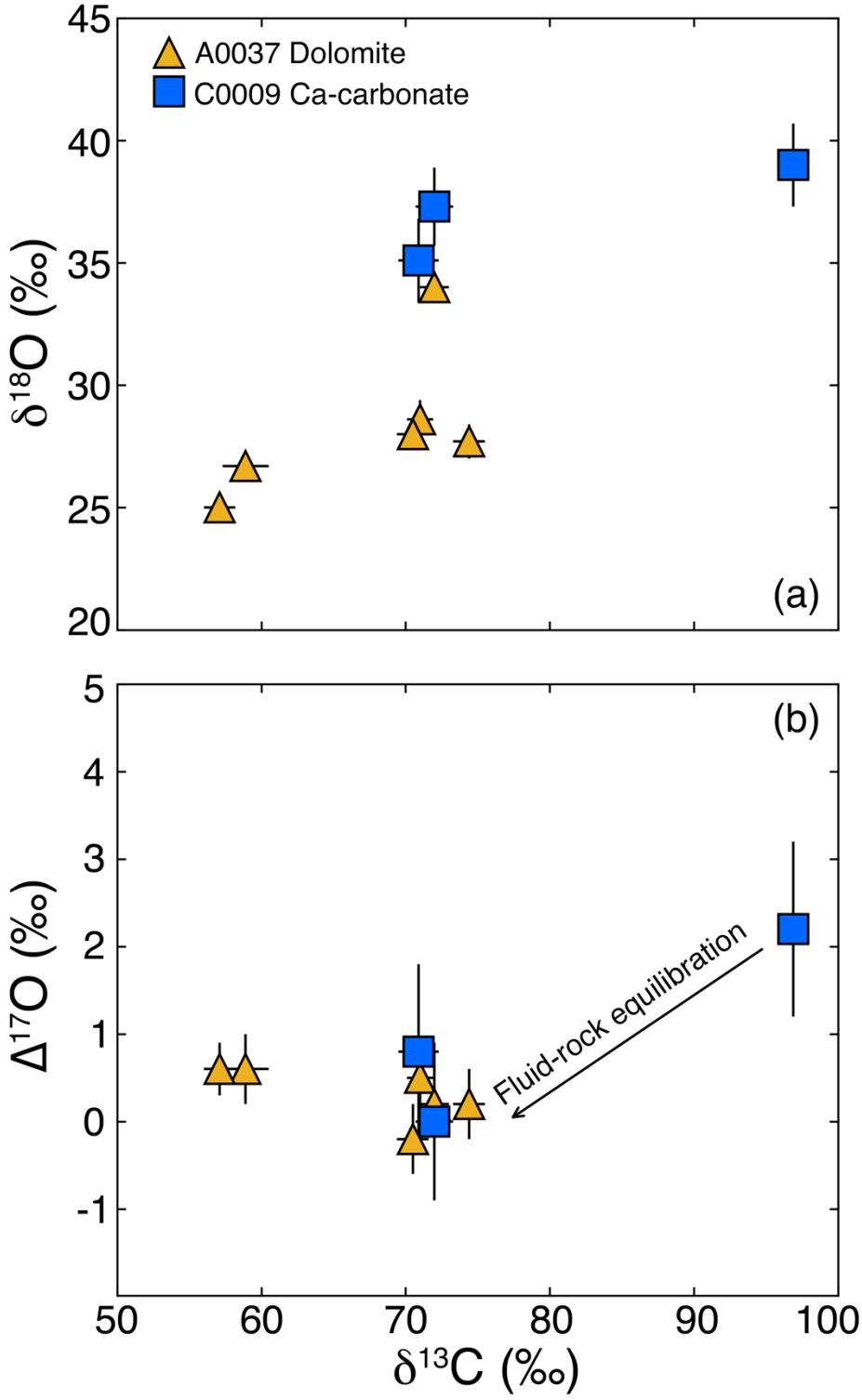

The old ages measured in Ryugu carbonate stand in contrast to ages obtained from carbonate in carbonaceous chondrites, most of which were thought to have formed 4–6 Myr after CAIs (Fujiya et al., 2013, 2012; Visser et al., 2020). This difference arises from our use of matrix-matched standards, as opposed to calcite standards used exclusively in previous studies, to determine the Mn/Cr of the carbonates. Had we corrected measured Mn^+/Cr^+ using a relative sensitivity factor derived only from analyses of calcite, we would have obtained ages of 3.0 Myr and 3.5 Myr after CAI formation for A0037 and C0009 carbonate respectively, approaching the range of ages previously determined for carbonates in carbonaceous chondrites (Fujiya et al., 2013, 2012; Visser et al., 2020).

These old carbonate formation ages suggest a significantly different formation scenario for Ryugu than those previously proposed for the asteroid parent bodies of carbonaceous chondrites. Our data clearly show that aqueous fluids responsible for carbonate formation were active on Ryugu (or its progenitor asteroid) early in Solar System history, within the first ~1.4 Myr after CAI formation. At that time, ^{26}Al in chondritic material was still at the level of $^{26}Al/^{27}Al \sim 10^{-5}$, abundant enough to melt accreted ices and drive aqueous alteration. However, for ^{26}Al heating to not be so intensive as to cause water loss or even silicate melting and chemical differentiation, Ryugu must have accreted as a small asteroid which could effectively conduct heat away from its interior to cool itself by radiation. The inferred presence of co-accreted CO_2 ice constrains the initial temperature of the parent body to below the sublimation temperature of CO_2. By modeling parent bodies accreting as mixtures of 50% chondritic material and 50% water ice (Clayton and Mayeda, 1999; Zolensky et al., 1993) at an initial temperature of 78 K, we find that parent bodies accreting before 1.4 Myr must be smaller than 17 km in diameter for the internal temperature to remain below 400 K (McCain et al., 2017; Zhou et al., 2013). In these bodies, the interior 4 km

reaches the melting point of water within 0.2 Myr after accretion, and remains warm enough to support liquid water for an additional 1.5 Myr.

Alternatively, it could be possible to form Ryugu components in a progenitor body larger than 17 km in diameter which was later disrupted by impact before reaching peak temperatures. Ryugu is a ~1 km diameter asteroid inferred, like many asteroids, to be a 'rubble pile' characterized by large internal void spaces and a low bulk density (1,190 ± 20 kg m^{-3}) (Watanabe et al., 2019). A multi-stage scenario of brecciation and reassembly is also supported by petrographic and shock characteristics observed in Ryugu particles (Ito et al., 2022; Tomioka et al., 2022; Yamaguchi et al., 2022). This view is very different from prior estimates of parent body size and accretion times based upon younger carbonate ages, which suggested that CM and CI parent bodies were >50 km in diameter and accreted ~3–3.5 Myr after CAI formation (Fujiya et al., 2013, 2012; Visser et al., 2020).

An early formation scenario for C-type asteroids has implications for models seeking to understand the origins of the so-called 'isotopic dichotomy' within the solar nebula. In this framework, the early solar system was divided into two reservoirs, one characterized by isotopic compositions similar to those of the volatile-rich carbonaceous chondrites (CC), and the other being isotopically similar to the compositions of volatile-depleted ordinary-chondrite, enstatite-chondrite, and terrestrial (collectively known as the non-carbonaceous (NC) isotopic reservoir) materials (Kleine et al., 2020). Whereas the NC group accreted from materials formed in the inner solar system, the CC group is thought to have accreted in the outer solar system, beyond the snow line. Based on ^{182}Hf-^{182}W ages of iron meteorites with CC affinities, it has been suggested that some planetesimals in the outer solar system accreted within ~1 Myr of CAI formation (Kruijer et al., 2017). This timescale is consistent with such objects having melted and chemically

differentiated into core-mantle structures due to ^{26}Al heating, and is also consistent with the accretion time of NWA 011, a basaltic achondrite with CC affinities that accreted within 1.6 Myr of CAI formation (Sugiura and Fujiya, 2014). Based on previous Mn-Cr dating of carbonates it was thought that CM and CI chondrites escaped such heating by virtue of having accreted at later times, after most ^{26}Al had decayed. However, early formation for undifferentiated CC material, such as that from Ryugu, requires an explanation (e.g., formation in a small body or early disruption by impact) for the simultaneous existence of differentiated and unmelted CC materials. Similarly, models of accretion and transport in the disk which invoke a late formation time for carbonaceous chondrite parent bodies (Desch et al., 2018) should consider the implications of early formation of these objects.

Data availability

Correspondence and requests for materials should be addressed to K.A.M and N.M. All analytical data related to this manuscript will be put on the JAXA Data ARchives and Transmission System (DARTS) after a one-year proprietary period.

Acknowledgements

We thank all scientists and engineers of the Hayabusa2 project whose dedication and skill brought these precious particles back to Earth. This research was supported in part by the JSPS KAKENHI (JP18K18795 and JP18H04468 to M.I., NESSF19R 19-PLANET19R-0001 to K.A.M., JP20H01965 to N.T., JP18H05479 [Innovative Areas "MFS Materials Science"] to M.U., JP19H01959 to A.Y., JP18K03729 to M.K., JP21K03652 to N.I., JP17H06459 to T.U., JP19K03958 to M.A., JP17H06459 to T.O., JP18K03830 to T.Y., JP19K23473, JP20K14548 to T.H., JP19K23474, JP21K13986 to D.Y., JP20K14535 to R.F., JP17H06459 and JP19H01951 to S.W.), and by the NIPR Research Project (KP307 to A.Y.). We thank Edward Young for discussions of the implications of the data and for the parent body modeling code. The UCLA ion microprobe facility is partially supported by a grant from the NSF Instrumentation and Facilities program. Ion implantation of carbonate standards was performed by CuttingEdge Ions.

Author contributions

K.A.M. and N.M led the project and wrote the initial draft. K.A.M., N.M., M-C.L., A.Y., N.T., M.I., M.U., N.I., N.S., T. Ohigashi., M.K., K.U., A.N., KY., H.Y., and Y.K. conducted sample handling, preparation, and mounting processes of Ryugu grains. M.I., N.T., T. Ohigashi., M.U., K.U., H.Y., Y.K., K.H., I.S., I.O., and K.U. developed universal sample holders for multiple

instruments. A.Y., M.K., N.I., M.I., and N.T. performed SEM-EDS analysis. A.Y. conducted EPMA analysis and data reduction. K.A.M., N.M., and M.-C.L. carried out oxygen, carbon, and Mn-Cr isotopes measurements of anhydrous carbonate and magnetite with SIMS. A.N., K.Y., A.M., M.N., T.Y., T. Okada., M.A., and T.U lead the JAXA curation activities for initial characterization of allocated Ryugu particles. S.N., T. Okada., T.S., S.T., F.T., M.Y., S.W., and Y.T. administered the project and acted as principal investigators. All authors contributed to the data interpretation, commented on the earlier versions of the manuscript, and approved the final version of the manuscript for submission.

Chapter 4 Supplementary Materials

Supplementary Methods

Magnetite-calcite equilibrium calculation

The formation temperature is calculated under the assumption that Ca-carbonate 'Ca 2' and magnetite were in equilibrium with water of identical oxygen isotopic composition. Ryugu magnetite has an average $\delta^{18}O$ value of 2.1 ± 1.9‰ (2SD) and 'Ca 2' has a value of 39 ± 1.7‰ (2SE). With these uncertainties, the 1000 ln $\alpha_{Cal\text{-}Mgt}$ inferred by these values ranges from 40.4−33.4‰. Calcite fractionation factors for 'Ca 2' were adopted due to the strong resemblance of this target to Type 1b calcite in CM chondrites.

We assume no significant effect of crystallographic orientation on the mass fractionation of oxygen isotopic measurements of magnetite (Huberty et al., 2010). In principle, this could affect the accuracy of our measured $\delta^{18}O$ values of magnetite by up to 3‰, but would not affect measurements of $\Delta^{17}O$. Any shift in the $\delta^{18}O$ value of magnetite would affect the $\alpha_{Cal\text{-}Mgt}$ inferred using the magnetite and calcite pair, thereby affecting the temperature calculation. However, we note that magnetite-water fractionation has a weak temperature dependence relative to calcite-water fractionation. Therefore, a crystallographic orientation effect for $\delta^{18}O$ of would not strongly affect the inferred temperature range.

We estimated the formation temperature of calcite and magnetite to be 0–20 °C based on fractionation factors for the calcite-water and magnetite-water systems derived from theoretical calculations performed by Hayles et al., 2018. Some previous studies of magnetite-carbonate equilibrium in carbonaceous chondrites have used other fractionation factors for the magnetite-water equilibrium (Telus et al., 2019; Zheng, 1995). If we use the magnetite-water fractionation factors calculated in Zheng et al. 1995, along with experimentally-derived calcite-water

fractionation factors (Kim and O'Neil, 1997), we obtain a formation temperature of 23–47 °C. Experimental data for the magnetite-water equilibrium fractionation are available only at temperatures above 300 °C (Cole et al., 2004). Therefore, we have elected to use the most recent theoretical predictions of the equilibrium fractionation between magnetite and water at low temperature to perform our calculations.

Dolomite-phyllosilicate equilibrium calculation

We estimated the formation temperature of phyllosilicate and dolomite to be 88–240 °C using dolomite-H_2O (Horita, 2014) and brucite-H_2O (Saccocia et al., 2015) fractionation factors which have been experimentally determined at the relevant low temperatures. Relatively few hydrated Mg-rich minerals have reliable fractionation factors measured at low temperature. While other minerals (e.g. serpentine) would be better fits to the mineralogy observed in the Ryugu matrix, their mineral-H_2O fractionations are not well constrained at the relevant temperatures. Therefore, we elect to use the brucite-H_2O fractionation factor. The range of temperatures inferred by this calculation is extremely wide due to the uncertainty in the bulk phyllosilicate $\delta^{18}O$ composition, so variation in the phyllosilicate-water fractionation factors is likely within this range of inferred temperatures.

Supplementary Figures

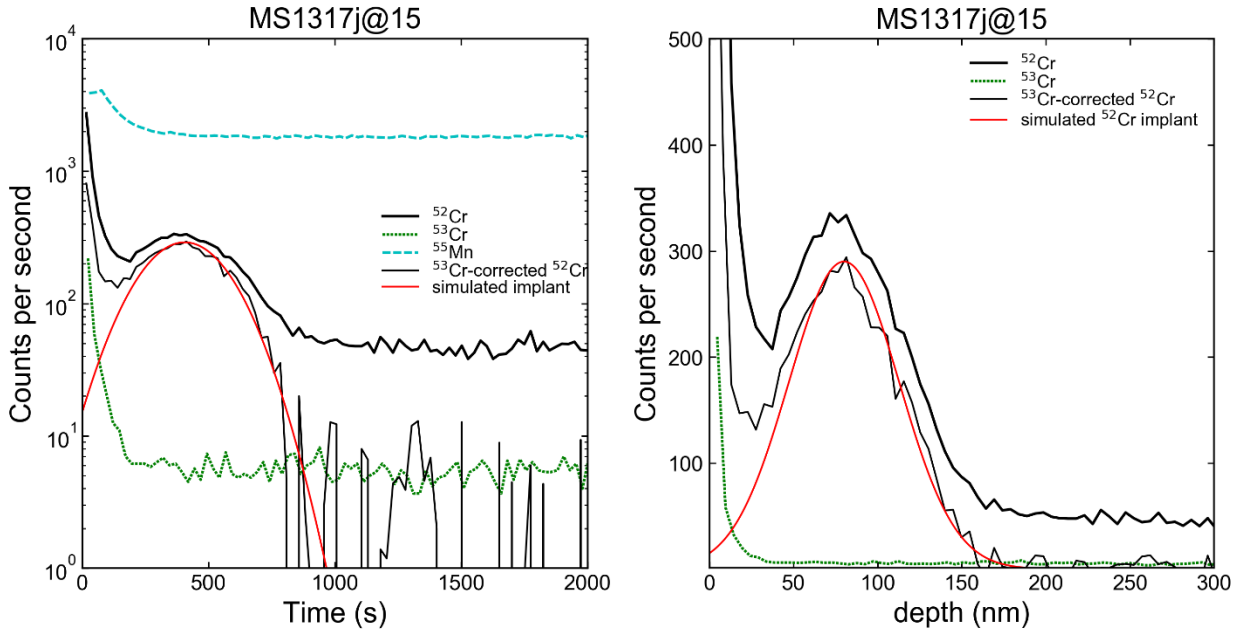

Supplementary Figure S4.1. Intensities of $^{52}Cr^{+}$, $^{53}Cr^{+}$, and $^{55}Mn^{+}$ recorded during depth profiling of terrestrial dolomite 1317J plotted against the time elapsed during the depth profile (left) and the depth below the sample surface (right). The left panel is shown with count rates on a logarithmic scale, and the right with count rates on a linear scale for comparison. The heavy black line represents the intensity of $^{52}Cr^{+}$ including the implanted Cr and the background Cr in the NIST glass. The dotted green line represents the intensity of the background $^{53}Cr^{+}$ during the profile. The dashed blue line represents the intensity of $^{55}Mn^{+}$ during the profile. The thin black line represents the intensity of $^{52}Cr^{+}$ when background-corrected only by the $^{53}Cr^{+}$ intensity. The red line represents the $^{52}Cr^{+}$ implantation peak as simulated by the SRIM software.

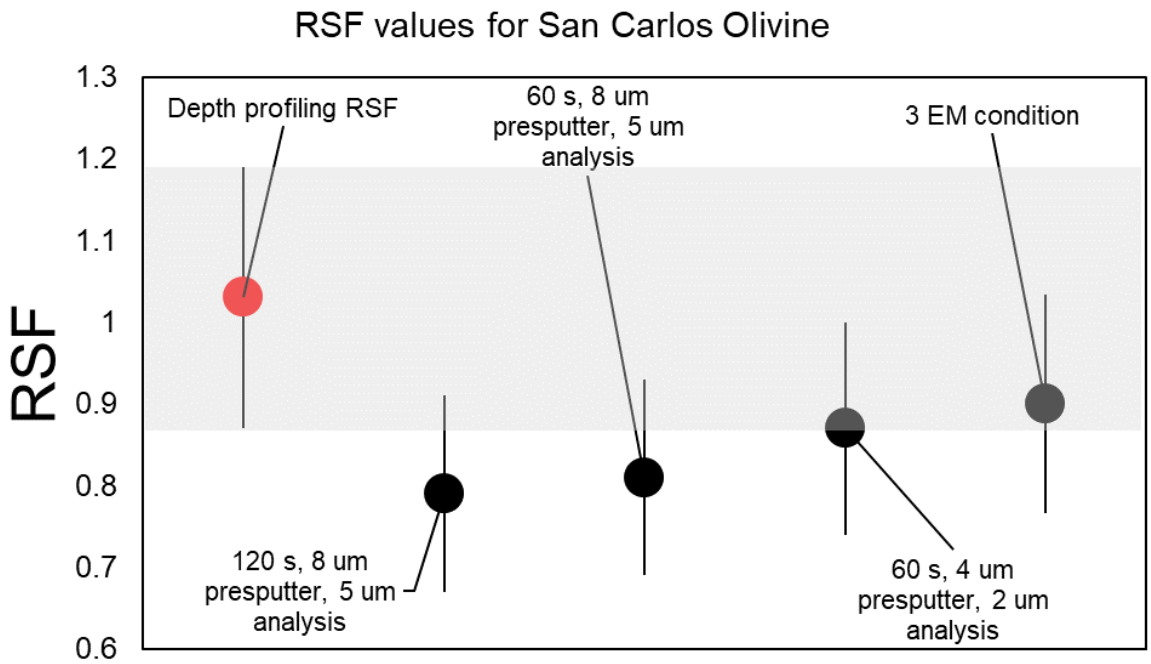

Supplementary Figure S4.2. RSF values of San Carlos Olivine obtained by depth profiling (red point, shaded area) and spot analyses under various presputtering and analysis conditions (black circles). Error bars represent 2 SE.

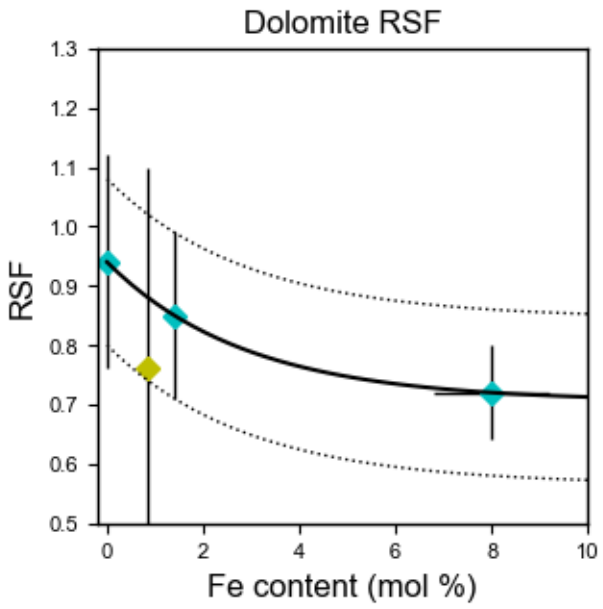

Supplementary Figure S4.3. RSF values of dolomite versus the $FeCO_3$ composition of dolomite. The black line is the exponential function given in Eq. 4.4.

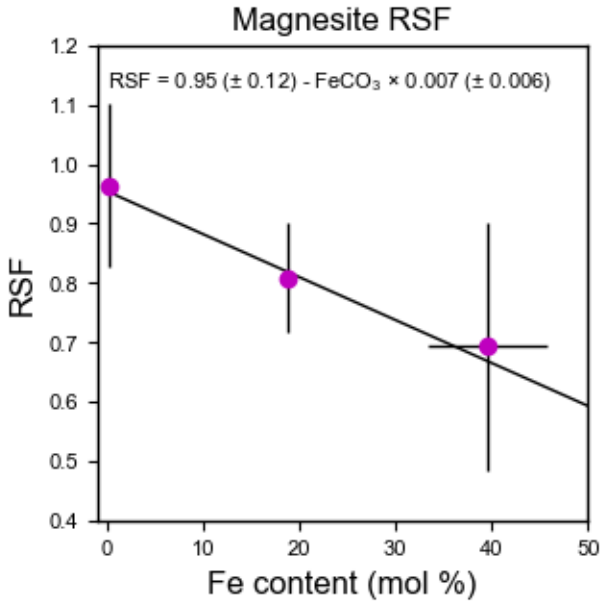

Supplementary Figure S4.4. RSF values of magnesite versus the $FeCO_3$ composition of magnesite, errors 2SE. The black line is the best fit line printed on the plot.

Supplementary Table 4.1. Oxygen-isotope compositions of carbonates in A0037 and C0009.

Particles	Mineral	Spot	$\delta^{17}O$	2σ	$\delta^{18}O$	2σ	$\Delta^{17}O$	2σ	$FeCO_3$*	$MnCO_3$*
A0037	Dolomite	A37_3oxy3FCs@1	14.8	0.4	28.1	0.4	0.2	0.4	4.1	4.4
		A37_3oxy3FCs@2	13.8	0.4	26.2	0.4	0.2	0.4	3.8	2.7
		A37_3oxy3FCs@3	14.7	0.4	26.6	0.4	0.8	0.4	4.1	2.3
		A37_3oxy3FCs@4	15.1	0.4	27.0	0.4	1.1	0.3	3.9	4.0
		A37_3oxy3FCs@6	14.4	0.5	26.7	0.4	0.6	0.4	4.6	4.7
		A37_3oxy3FCs@7	14.7	0.4	26.4	0.4	1.0	0.3	4.3	5.8
		A37_3oxy3FCs@8	16.8	0.3	32.7	0.4	–0.2	0.3	3.2	5.3
		A37_3oxy3FCs@9	16.6	0.5	31.4	0.4	0.3	0.4	4.1	3.7
		A37_3oxy3FCs@10	14.4	0.4	28.0	0.4	–0.2	0.4	3.8	4.1
		A37_3oxy3FCs@11	17.9	0.3	33.7	0.4	0.4	0.3	3.2	5.3
		A37_3oxy3FCs@13	13.6	0.4	25.0	0.4	0.6	0.3	4.0	6.8
		A37_3oxy3FCs@14	15.8	0.4	28.9	0.4	0.7	0.3	4.0	3.9
		A37_3oxyFCEMFC@1	13.9	0.4	26.7	0.6	0.0	0.3	3.0	5.7
		A37_3oxyFCEMFC@2	15.8	0.5	27.3	0.7	1.6	0.3	4.3	5.8
		A37_3oxyFCEMFC@4	14.9	0.3	28.6	0.6	0.0	0.4	3.8	5.7
		A37_3oxyFCEMFC@5	17.9	0.6	34.0	0.6	0.2	0.5	4.0	3.9
		A37_3oxyFCEMFC@6	14.8	0.5	28.2	0.6	0.1	0.4	4.0	3.9
		A37_3oxyFCEMFC@7	14.0	0.4	27.5	0.7	–0.3	0.3	4.0	2.4
		A37_3oxyFCEMFC@8	15.3	0.5	28.6	0.8	0.5	0.4	3.4	6.9
		A37_3oxyFCEMFC@9	14.6	0.4	27.7	0.7	0.2	0.4	3.8	6.1
C0009	Dolomite	C009_dolo@3	12.9	0.7	25.4	0.7	–0.3	0.8	2.9	4.7
	Ca-carbonate	C009_calcite@1	19.1	1.0	35.1	1.7	0.8	1.0	1.3	n.d.
		C009_calcite@2	19.4	0.9	37.3	1.6	0.0	0.9	1.3	n.d.

Supplementary Table 4.1 (continued).

Particles	Mineral	Spot	$\delta^{17}O$	2σ	$\delta^{18}O$	2σ	$\Delta^{17}O$	2σ	$FeCO_3$*	$MnCO_3$*
C0009	Ca-carbonate	C009_calcite@3	22.5	1.0	39.0	1.7	2.2	1.0	1.1	n.d.
		C009_calcite@5	18.7	1.0	35.0	1.6	0.5	1.0	1.5	n.d
		C009_calcite@6	18.9	0.9	34.2	1.5	1.1	1.0	1.5	n.d.
		C009_calcite@7	19.3	0.9	36.4	1.7	0.3	0.9	1.5	n.d

* Data from Yamaguchi et al. (2022).
$FeCO_3$ and $MnCO_3$ are mol%.
n.d.: not detected.

Supplementary Table 4.2. Oxygen-isotope compositions of magnetite in A00037.

Particles	Mineral	Spot	$\delta^{17}O$	2σ	$\delta^{18}O$	2σ	$\Delta^{17}O$	2σ	FeO*
A0037	Magnetite	A37_3oxyFCEMFC@10	3.7	0.5	3.0	0.9	2.1	0.4	93.0
		A37_3oxyFCEMEM@1	4.8	1.0	1.7	1.0	3.9	0.9	92.8
		A37_3oxyFCEMEM@5	3.1	0.8	1.0	0.7	2.6	0.8	93.0
		A37_3oxyFCEMEM@10	4.6	1.1	2.8	1.2	3.1	0.9	92.0

Data from Yamaguchi et al. (2022).
FeO is wt%.

Supplementary Table 4.3. Carbon-isotope compositions of carbonates in A0037 and C0009.

Particles	Mineral	Spot	$\delta^{13}C$	2σ
A0037	Dolomite	A37_C_dolo@1.asc	55.4	1.6
		A37_C_dolo@2.asc	62.3	1.3
		A37_C_dolo@3.asc	58.9	1.6
		A37_C_dolo@5.asc	58.2	1.2
		A37_C_dolo@6.asc	72.1	1.0
		A37_C_dolo@7.asc	70.5	1.1
		A37_C_dolo@8.asc	72.0	1.0
		A37_C_dolo@9.asc	69.7	1.0
		A37_C_dolo@10.asc	57.1	1.2
		A37_C_dolo@11.asc	68.1	1.0
		A37_C_dolo@12.asc	74.4	1.1
		A37_C_dolo@13.asc	71.0	0.9
		A37_C_dolo@14.asc	72.6	1.1
C0009	Dolomite	C0009_C_dolo@1.asc	74.5	1.0
		C0009_C_dolo@2.asc	73.3	0.9
		C0009_C_dolo@3.asc	69.7	0.8
		C0009_C_dolo@4.asc	74.3	0.8
		C0009_C_dolo@5.asc	64.0	0.8
		C0009_C_dolo@6.asc	66.4	1.0
		C0009_C_dolo@7.asc	69.3	1.1
C0009	Ca-carbonate	C0009_ca2@1.asc	96.9	1.1
		C0009_ca1@3.asc	72.0	1.3
		C0009_ca1@4.asc	70.9	1.4

Supplementary Table S4.4. Mn-Cr isotope data of carbonates in A0037 and C0009.

Particle	Mineral	Spot	$^{55}Mn/^{52}Cr$	2σ	$^{53}Cr/^{52}Cr$	2σ	$\delta^{53}Cr$	2σ	# cycles	RSF used
A0037	Dolomite	A37@1	232	47	0.11646	0.00116	26	10	30	0.8
		A37@2	23	5	0.11535	0.00108	17	10	30	0.8
		A37@3	44	14	0.11473	0.00108	11	10	30	0.8
		A37@4	51	13	0.11557	0.00110	19	10	30	0.8
		A37@5	122	40	0.11498	0.00114	13	10	14	0.8
		A37_Feb15@6	601	110	0.11982	0.00134	56	12	26	0.8
		A37_Feb15@7	7377	1333	0.16786	0.00374	480	33	30	0.8
		A37_Feb15@8	2787	572	0.13394	0.00224	181	20	30	0.8
		A37_Feb15@9	283	63	0.11560	0.00118	19	10	30	0.8
		A37_Feb15@10	1972	371	0.12495	0.00296	101	26	11	0.8
		A37_Feb15@12	606	239	0.11786	0.00138	39	12	7	0.8
		A37_Feb15@13	404	129	0.11702	0.00160	31	14	10	0.8
		A37_Feb15@14	4765	865	0.14324	0.00354	262	31	30	0.8
		A37_Feb15@15	6209	1247	0.15734	0.00518	387	46	27	0.8
		A37_Feb15@17	1387	466	0.12365	0.00212	90	19	14	0.8
		A37_Feb15@18	9404	1801	0.17455	0.00550	538	48	30	0.8
		A37_Feb15@19	5204	1047	0.15095	0.00302	330	27	15	0.8
		A37_Feb15@21	5518	1204	0.15457	0.00800	362	71	14	0.8
		A37_Feb15@23	2368	433	0.13134	0.00178	158	16	30	0.8
		A37_Feb15@24	6401	1151	0.16061	0.00362	416	32	30	0.8
C0009	Dolomite	C9@2	1393	332	0.12229	0.00332	78	29	9	0.8
		C9@3	4044	822	0.13980	0.00286	232	25	9	0.8
		C9@4	2252	478	0.12912	0.00258	138	23	12	0.8
		C9@5	2445	942	0.12950	0.00408	141	36	30	0.8
		C9@6	2833	700	0.13138	0.00278	158	25	30	0.8
		C9@7	3070	741	0.13189	0.00318	162	28	20	0.8
		C9@8	2729	479	0.12945	0.00194	141	17	11	0.8
		C9@9	1121	202	0.11905	0.00420	49	37	30	0.8

Supplementary Table S4.4 (continued).

Particle	Mineral	Spot	$^{55}Mn/^{52}Cr$	2σ	$^{53}Cr/^{52}Cr$	2σ	$\delta^{53}Cr$	2σ	# Cycles	RSF used
C0009	Dolomite	C9@11	10529	1874	0.18181	0.00412	602	36	12	0.8
		C9@12	5055	951	0.14578	0.00302	285	27	30	0.8
		C9@14	1735	509	0.12537	0.00214	105	19	26	0.8
		C9@16	1650	761	0.12499	0.00362	102	32	10	0.8
		C9_3EM@3	2243	1175	0.12873	0.00578	135	51	13	0.8
C0009	Breunnerite	C9@10	3326	680	0.13239	0.00224	167	20	30	0.86
C0009	Ca-carbonate	C9_3EM@1	32	14	0.11367	0.00978	2	86	10	1.3
		C9_3EM@2	8	3	0.11772	0.00546	38	48	10	1.3

Supplementary Table S4.5. Chemical and isotopic compositions of reference materials used to constrain instrumental mass fractionation during carbon and oxygen stable isotopic analysis of carbonates. Carbon and oxygen isotopic compositions were determined by phosphoric acid digestion and IRMS of CO_2 at UCLA. Elemental compositions were determined using EPMA analysis.

Material name	Mineral	$\delta^{17}O$ SMOW	$\delta^{18}O$ SMOW	$\delta^{13}C$ VPDB	$CaCO_3$	$MgCO_3$	$FeCO_3$	$MnCO_3$
OPTI calcite	Calcite	5.76	11.10	1.42	99.4	0.5	n.d.	n.d.
MS1317	Dolomite	11.80	22.82	–21.13	51.8	48.1	n.d.	0.1
MS1305	Dolomite	10.99	21.24	–1.10	50.8	48.0	1.1	0.1
MS1317J	Dolomite	11.13	21.51	–1.20	51.1	45.8	2.9	0.2
MS1312	Dolomite	11.63	22.48	0.00	51.1	21.6	21.1	6.2

$CaCO_3$, $MgCO_3$, $FeCO_3$, and $MnCO_3$ are mol%.
n.d.: not detected.

Supplementary Table S4.6. RSF values obtained using depth profiling of ion-implanted materials, where n represents the number of repeat depth profiles. The Mn concentration in each mineral is derived from EPMA data and reported as µg Mn/g.

Mineral	$FeCO_3$ mol%	weighted mean RSF	2SE	n	Mn concentration (ppm)
Calcite	n.d.	1.3	0.84	2	100
Dolomite					
MS1317 (D)	n.d.	0.94	0.18	6	411
MS1305 (D)	0.85	0.76	0.34	2	558
MS1317J (D)	1.4	0.85	0.14	2	1011
MS1318 (D)	8.0	0.72	0.088	6	6244
Magnesite					
MS1223D	0.2	0.96	0.14	2	761
M1952	18.8	0.81	0.10	2	6402
M2035	39.5	0.69	0.21	1	2969
San Carlos Olivine	–	1.03	0.17	2	1029

n.d.: not detected.

Supplementary Table S4.7. Values used to calculate the RSF from individual depth profiles of carbonate, glass, and San Carlos olivine. A_{52Cr+}_R refers to the total number of counts of implanted $^{52}Cr^{+}$ detected before using the SRIM simulation to correct for surface contamination (see supplemental text above). A_{52Cr+}_C refers to the total number of counts of $^{52}Cr^{+}$ detected after surface contamination correction, and is the value used to calculate the RSF. ΔA_{52Cr} represents the fractional difference between A_{52Cr+}_C and A_{52Cr+}_R, and is defined as

$$\Delta A_{52Cr+} = {(A_{52Cr+}\_R - A_{52Cr+}\_C)}/{A_{52Cr+}\_R}$$

The position and shape of the gaussian derived from SRIM modeling and used to correct for surface contamination are reported as Mean of Gaussian and 1SD.

Name	RSF	2SD	A_{52Cr+}_R (counts)	A_{52Cr+}_C (counts)	ΔA_{52Cr+}	I_{55Mn} (cps)	2SD	D (μm)	t (s)	Gaussian mean (nm)	1SD
Calcite@16	1.32	1.20	152159	102185	0.33	100	10	0.4649	2331	72	37
Calcite@17	1.33	1.20	154536	100183	0.35	97	12	0.4176	2089	72	37
Dolomite											
MS1305@21	0.68	0.38	172564	126476	0.27	1303	44	0.6017	3257	85	33
MS1305@22	0.95	0.52	168933	127681	0.24	916	32	0.4101	2284	85	33
MS1317j@14	0.74	0.10	175584	130843	0.25	2261	56	0.3448	1837	76	33
MS1317j@15	0.95	0.26	168575	127908	0.24	1825	58	0.5383	2730	80	33
MS1317@19	0.75	0.32	165357	128631	0.22	895	38	0.4992	2608	88	32
MS1317@20	1.72	0.71	148793	120931	0.19	372	20	0.5167	2679	88	32
MS1317_@23	0.78	0.32	153109	121795	0.20	858	36	0.9917	4963	92	32
MS1317_@24	1.56	0.66	150681	120610	0.20	426	30	0.9972	4961	95	32
MS1317_@25	1.02	0.42	150376	122448	0.19	673	34	1.015	4962	96	32
MS1317_@26	0.74	0.30	156392	127232	0.19	940	34	0.9951	4962	93	32
MS1318_fa2500_max80@43	0.70	0.16	404863	288031	0.29	30411	546	0.3228	1895	78	33
MS1318@12	0.74	0.18	199599	139926	0.30	14920	194	0.6268	3451	75	33
MS1318@13	0.73	0.18	191658	134540	0.30	14761	200	0.5582	3003	78	33
MS1318_@28	0.74	0.18	186121	132740	0.29	13642	244	0.4727	2678	80	33

Supplementary Table S4.7 (continued).

Name	RSF	2SD	A_{52Cr+}_R (counts)	A_{52Cr+}_C (counts)	ΔA_{52Cr+}	I_{55Mn} (cps)	2SD	D (μm)	t (s)	Gaussian mean (nm)	1SD
Magnesite											
MAGN_M2035@42	0.69	0.22	766726	769886	0.00	46956	1020	0.7215	3600	99	38
MAGN_MS1223D@33	0.88	0.18	443427	438043	0.01	5601	162	0.6594	3173	96	36
MAGN_MS1223D@34	1.09	0.22	450860	448074	0.01	4279	110	0.5084	2632	94	36
MAGN_MS1952@35	0.80	0.12	469061	466691	0.01	53761	3594	0.4671	2386	94	36
MAGN_MS1952@36	0.82	0.14	426366	423043	0.01	48211	3873	0.5067	2579	91	36
NIST Glass											
MAGN_NIST612@32	1.04	0.14	2089105	2075818	0.01	617	52	0.667	4962	115	40
MAGN_NIST614@30	1.06	0.32	2052221	2047233	0.00	23	8	0.661	4668	120	40
San Carlos Olivine											
SCOL@10	1.02	0.22	1474422	1455160	0.01	9837	1910	0.3971	4713	90	38
SCOL@11	1.05	0.28	1347762	1324634	0.02	9059	2274	0.3922	4485	95	38

References

Alexander, C.M.O., Bowden, R., Fogel, M.L., Howard, K.T., 2015. Carbonate abundances and isotopic compositions in chondrites. Meteorit Planet Sci 50, 810–833. https://doi.org/10.1111/maps.12410

Alexander, C.M.O., Fogel, M., Yabuta, H., Cody, G.D., 2007. The origin and evolution of chondrites recorded in the elemental and isotopic compositions of their macromolecular organic matter. Geochimica et Cosmochimica Acta 71, 4380–4403. https://doi.org/10.1016/j.gca.2007.06.052

Amelin, Y., 2008. U–Pb ages of angrites. Geochimica et Cosmochimica Acta 72, 221–232. https://doi.org/10.1016/j.gca.2007.09.034

Amelin, Y., Kaltenbach, A., Iizuka, T., Stirling, C.H., Ireland, T.R., Petaev, M., Jacobsen, S.B., 2010. U-Pb chronology of the Solar System's oldest solids with variable 238U/235U. Earth and Planetary Science Letters 300, 343–350. https://doi.org/10.1016/j.epsl.2010.10.015

Brennecka, G.A., Wadhwa, M., 2012. Uranium isotope compositions of the basaltic angrite meteorites and the chronological implications for the early Solar System. PNAS 109, 9299–9303. https://doi.org/10.1073/pnas.1114043109

Clayton, R.N., Mayeda, T.K., 1999. Oxygen isotope studies of carbonaceous chondrites. Geochimica et Cosmochimica Acta 63, 2089–2104. https://doi.org/10.1016/S0016-7037(99)00090-3

Clayton, R.N., Mayeda, T.K., 1984. The oxygen isotope record in Murchison and other carbonaceous chondrites. Earth and Planetary Science Letters 67, 151–161. https://doi.org/10.1016/0012-821X(84)90110-9

Cole, D.R., Horita, J., Polyakov, V.B., Valley, J.W., Spicuzza, M.J., Coffey, D.W., 2004. An experimental and theoretical determination of oxygen isotope fractionation in the system magnetite-H2O from 300 to 800°C 1 1Associate editor: E. M. Ripley. Geochimica et Cosmochimica Acta 68, 3569–3585. https://doi.org/10.1016/j.gca.2004.02.017

Desch, S.J., Kalyaan, A., Alexander, C.M.O., 2018. The Effect of Jupiter's Formation on the Distribution of Refractory Elements and Inclusions in Meteorites. ApJS 238, 11. https://doi.org/10.3847/1538-4365/aad95f

Doyle, P.M., Jogo, K., Nagashima, K., Huss, G.R., Krot, A.N., 2016. Mn–Cr relative sensitivity factor in ferromagnesian olivines defined for SIMS measurements with a Cameca ims-

1280 ion microprobe: Implications for dating secondary fayalite. Geochimica et Cosmochimica Acta 174, 102–121. https://doi.org/10.1016/j.gca.2015.10.010

Fujiya, W., Aoki, Y., Ushikubo, T., Hashizume, K., Yamaguchi, A., 2020. Carbon isotopic evolution of aqueous fluids in CM chondrites: Clues from in-situ isotope analyses within calcite grains in Yamato-791198. Geochimica et Cosmochimica Acta 274, 246–260. https://doi.org/10.1016/j.gca.2020.02.003

Fujiya, W., Hoppe, P., Ushikubo, T., Fukuda, K., Lindgren, P., Lee, M.R., Koike, M., Shirai, K., Sano, Y., 2019. Migration of D-type asteroids from the outer Solar System inferred from carbonate in meteorites. Nature Astronomy 1. https://doi.org/10.1038/s41550-019-0801-4

Fujiya, W., Sugiura, N., Hotta, H., Ichimura, K., Sano, Y., 2012. Evidence for the late formation of hydrous asteroids from young meteoritic carbonates. Nat Commun 3, 627. https://doi.org/10.1038/ncomms1635

Fujiya, W., Sugiura, N., Marrocchi, Y., Takahata, N., Hoppe, P., Shirai, K., Sano, Y., Hiyagon, H., 2015. Comprehensive study of carbon and oxygen isotopic compositions, trace element abundances, and cathodoluminescence intensities of calcite in the Murchison CM chondrite. Geochimica et Cosmochimica Acta 161, 101–117. https://doi.org/10.1016/j.gca.2015.04.010

Fujiya, W., Sugiura, N., Sano, Y., Hiyagon, H., 2013. Mn–Cr ages of dolomites in CI chondrites and the Tagish Lake ungrouped carbonaceous chondrite. Earth and Planetary Science Letters 362, 130–142. https://doi.org/10.1016/j.epsl.2012.11.057

Grady, M.M., Wright, I.P., Swart, P.K., Pillinger, C.T., 1988. The carbon and oxygen isotopic composition of meteoritic carbonates. Geochimica et Cosmochimica Acta 52, 2855–2866. https://doi.org/10.1016/0016-7037(88)90152-4

Greenwood, R.C., Franchi, I.A., Findlay, R., Malley, J.A., Ito, M., Yamaguchi, A., 2022. Oxygen isotope analysis of Ryugu particles: Fresh evidence for hydration of Earth by CI chondrites. Nature Astronomy.

Guo, W., Eiler, J.M., 2007. Temperatures of aqueous alteration and evidence for methane generation on the parent bodies of the CM chondrites. Geochimica et Cosmochimica Acta 71, 5565–5575. https://doi.org/10.1016/j.gca.2007.07.029

Hässig, M., Altwegg, K., Balsiger, H., Berthelier, J.J., Bieler, A., Calmonte, U., Dhooghe, F., Fiethe, B., Fuselier, S.A., Gasc, S., Gombosi, T.I., Roy, L.L., Luspay-Kuti, A., Mandt, K., Rubin, M., Tzou, C.-Y., Wampfler, S.F., Wurz, P., 2017. Isotopic composition of CO2 in the coma of 67P/Churyumov-Gerasimenko measured with ROSINA/DFMS. A&A 605, A50. https://doi.org/10.1051/0004-6361/201630140

Hayles, J., Gao, C., Cao, X., Liu, Y., Bao, H., 2018. Theoretical calibration of the triple oxygen isotope thermometer. Geochimica et Cosmochimica Acta 235, 237–245. https://doi.org/10.1016/j.gca.2018.05.032

Horita, J., 2014. Oxygen and carbon isotope fractionation in the system dolomite–water–CO2 to elevated temperatures. Geochimica et Cosmochimica Acta 129, 111–124. https://doi.org/10.1016/j.gca.2013.12.027

Huberty, J.M., Kita, N.T., Kozdon, R., Heck, P.R., Fournelle, J.H., Spicuzza, M.J., Xu, H., Valley, J.W., 2010. Crystal orientation effects in δ18O for magnetite and hematite by SIMS. Chemical Geology 276, 269–283. https://doi.org/10.1016/j.chemgeo.2010.06.012

Ito, M., Tomioka, N., Uesugi, M., Yamaguchi, A., Shirai, N., 2022. Hayabusa2 returned samples: A unique and pristine record of outer Solar System materials from asteroid Ryugu. Nature Astronomy.

Kim, S.-T., O'Neil, J.R., 1997. Equilibrium and nonequilibrium oxygen isotope effects in synthetic carbonates. Geochimica et Cosmochimica Acta 61, 3461–3475. https://doi.org/10.1016/S0016-7037(97)00169-5

Kleine, T., Budde, G., Burkhardt, C., Kruijer, T.S., Worsham, E.A., Morbidelli, A., Nimmo, F., 2020. The Non-carbonaceous–Carbonaceous Meteorite Dichotomy. Space Sci Rev 216, 55. https://doi.org/10.1007/s11214-020-00675-w

Kruijer, T.S., Burkhardt, C., Budde, G., Kleine, T., 2017. Age of Jupiter inferred from the distinct genetics and formation times of meteorites. Proceedings of the National Academy of Sciences 114, 6712–6716.

Lee, M.R., Lindgren, P., Sofe, M.R., 2014. Aragonite, breunnerite, calcite and dolomite in the CM carbonaceous chondrites: High fidelity recorders of progressive parent body aqueous alteration. Geochimica et Cosmochimica Acta 144, 126–156. https://doi.org/10.1016/j.gca.2014.08.019

Lee, M.R., Sofe, M.R., Lindgren, P., Starkey, N.A., Franchi, I.A., 2013. The oxygen isotope evolution of parent body aqueous solutions as recorded by multiple carbonate generations in the Lonewolf Nunataks 94101 CM2 carbonaceous chondrite. Geochimica et Cosmochimica Acta 121, 452–466. https://doi.org/10.1016/j.gca.2013.07.010

Leshin, L.A., Rubin, A.E., McKeegan, K.D., 1997. The oxygen isotopic composition of olivine and pyroxene from CI chondrites. Geochimica et Cosmochimica Acta 61, 835–845. https://doi.org/10.1016/S0016-7037(96)00374-2

Liu, M.-C., McCain, K.A., Matsuda, N., Yamaguchi, A., Kimura, M., Tomioka, N., 2022. Incorporation of 16O-rich anhydrous silicates in the protolith of hihgly hydrated asteroid Ryugu. Nature Astronomy.

McCain, K.A., Liu, M.-C., McKeegan, K.D., 2020. Calibration of matrix-dependent biases in isotope and trace element analyses of carbonate minerals. Journal of Vacuum Science & Technology B 38, 044005. https://doi.org/10.1116/6.0000111

McCain, K.A., Young, E.D., Manning, C.E., 2017. CM Carbonates Should Be Old: Insights from Parent Body Thermal Modeling. Presented at the Lunar and Planetary Science Conference, p. 2181.

McKibbin, S.J., Ireland, T.R., Amelin, Y., Holden, P., 2015. Mn–Cr dating of Fe- and Ca-rich olivine from "quenched" and "plutonic" angrite meteorites using Secondary Ion Mass Spectrometry. Geochimica et Cosmochimica Acta 157, 13–27. https://doi.org/10.1016/j.gca.2015.02.019

Papanastassiou, D.A., 1986. Chromium isotopic anomalies in the Allende meteorite. The Astrophysical Journal 308, L27–L30.

Pilorget, C., Okada, T., Hamm, V., Brunetto, R., Yada, T., Loizeau, D., Riu, L., Usui, T., Moussi-Soffys, A., Hatakeda, K., Nakato, A., Yogata, K., Abe, M., Aléon-Toppani, A., Carter, J., Chaigneau, M., Crane, B., Gondet, B., Kumagai, K., Langevin, Y., Lantz, C., Le Pivert-Jolivet, T., Lequertier, G., Lourit, L., Miyazaki, A., Nishimura, M., Poulet, F., Arakawa, M., Hirata, N., Kitazato, K., Nakazawa, S., Namiki, N., Saiki, T., Sugita, S., Tachibana, S., Tanaka, S., Yoshikawa, M., Tsuda, Y., Watanabe, S., Bibring, J.-P., 2022. First compositional analysis of Ryugu samples by the MicrOmega hyperspectral microscope. Nature Astronomy 6, 221–225. https://doi.org/10.1038/s41550-021-01549-z

Piralla, M., Marrocchi, Y., Verdier-Paoletti, M.J., Vacher, L.G., Villeneuve, J., Piani, L., Bekaert, D.V., Gounelle, M., 2020. Primordial water and dust of the Solar System: Insights from in situ oxygen measurements of CI chondrites. Geochimica et Cosmochimica Acta 269, 451–464. https://doi.org/10.1016/j.gca.2019.10.041

Rowe, M.W., Clayton, R.N., Mayeda, T.K., 1994. Oxygen isotopes in separated components of CI and CM meteorites. Geochimica et Cosmochimica Acta 58, 5341–5347. https://doi.org/10.1016/0016-7037(94)90317-4

Saccocia, P.J., Seewald, J.S., Shanks, W.C., 2015. Oxygen isotope fractionation in the portlandite–water and brucite–water systems from 125 to 450°C, 50MPa. Geochimica et Cosmochimica Acta 169, 137–151. https://doi.org/10.1016/j.gca.2015.07.017

Sakamoto, N., Seto, Y., Itoh, S., Kuramoto, K., Fujino, K., Nagashima, K., Krot, A.N., Yurimoto, H., 2007. Remnants of the Early Solar System Water Enriched in Heavy Oxygen Isotopes. Science. https://doi.org/10.1126/science.1142021

Sephton, M.A., Pillinger, C.T., Gilmour, I., 2000. Aromatic moieties in meteoritic macromolecular materials: analyses by hydrous pyrolysis and δ13C of individual compounds. Geochimica et Cosmochimica Acta 64, 321–328. https://doi.org/10.1016/S0016-7037(99)00282-3

Śliwiński, M.G., Kitajima, K., Kozdon, R., Spicuzza, M.J., Fournelle, J.H., Denny, A., Valley, J.W., 2016a. Secondary Ion Mass Spectrometry Bias on Isotope Ratios in Dolomite–Ankerite, Part I: δ18O Matrix Effects. Geostand Geoanal Res 40, 157–172. https://doi.org/10.1111/j.1751-908X.2015.00364.x

Śliwiński, M.G., Kitajima, K., Kozdon, R., Spicuzza, M.J., Fournelle, J.H., Denny, A., Valley, J.W., 2016b. Secondary Ion Mass Spectrometry Bias on Isotope Ratios in Dolomite–Ankerite, Part II: δ13C Matrix Effects. Geostand Geoanal Res 40, 173–184. https://doi.org/10.1111/j.1751-908X.2015.00380.x

Steele, R.C.J., Heber, V.S., McKeegan, K.D., 2017. Matrix effects on the relative sensitivity factors for manganese and chromium during ion microprobe analysis of carbonate: Implications for early Solar System chronology. Geochimica et Cosmochimica Acta, Isotopic studies of planetary and nuclear materials: A scientific tribute to Ian Douglass Hutcheon (1947-2015) 201, 245–259. https://doi.org/10.1016/j.gca.2016.10.046

Sugiura, N., Fujiya, W., 2014. Correlated accretion ages and ε54Cr of meteorite parent bodies and the evolution of the solar nebula. Meteoritics & Planetary Science 49, 772–787. https://doi.org/https://doi.org/10.1111/maps.12292

Sugiura, N., Ichimura, K., 2010. Mn/Cr relative sensitivity factors for sythetic calcium carbonate measured with a NanoSIMS ion microprobe. Geochemical Journal 44, e11-316. https://doi.org/10.2343/geochemj.1.0089

Telus, M., Alexander, C.M.O., Hauri, E.H., Wang, J., 2019. Calcite and dolomite formation in the CM parent body: Insight from in situ C and O isotope analyses. Geochimica et Cosmochimica Acta 260, 275–291. https://doi.org/10.1016/j.gca.2019.06.012

Tomioka, N., Yamaguchi, A., Ito, M., Uesugi, M., Imae, N., Shirai, N., 2022. Calibrating the shock regime experienced by hydrated asteroid Ryugu. Nature Astronomy.

Tyra, M., Brearley, A., Guan, Y., 2016. Episodic carbonate precipitation in the CM chondrite ALH 84049: An ion microprobe analysis of O and C isotopes. Geochimica et Cosmochimica Acta 175, 195–207. https://doi.org/10.1016/j.gca.2015.10.034

Tyra, M.A., Farquhar, J., Guan, Y., Leshin, L.A., 2012. An oxygen isotope dichotomy in CM2 chondritic carbonates—A SIMS approach. Geochimica et Cosmochimica Acta 77, 383–395. https://doi.org/10.1016/j.gca.2011.10.003

Vacher, L.G., Marrocchi, Y., Villeneuve, J., Verdier-Paoletti, M.J., Gounelle, M., 2018. Collisional and alteration history of the CM parent body. Geochimica et Cosmochimica Acta 239, 213–234. https://doi.org/10.1016/j.gca.2018.08.006

Vacher, L.G., Marrocchi, Y., Villeneuve, J., Verdier-Paoletti, M.J., Gounelle, M., 2017. Petrographic and C & O isotopic characteristics of the earliest stages of aqueous alteration of CM chondrites. Geochimica et Cosmochimica Acta 213, 271–290. https://doi.org/10.1016/j.gca.2017.06.049

Verdier-Paoletti, M.J., Marrocchi, Y., Avice, G., Roskosz, M., Gurenko, A., Gounelle, M., 2017. Oxygen isotope constraints on the alteration temperatures of CM chondrites. Earth and Planetary Science Letters 458, 273–281. https://doi.org/10.1016/j.epsl.2016.10.055

Virtanen, P., Gommers, R., Oliphant, T.E., Haberland, M., Reddy, T., Cournapeau, D., Burovski, E., Peterson, P., Weckesser, W., Bright, J., van der Walt, S.J., Brett, M., Wilson, J., Millman, K.J., Mayorov, N., Nelson, A.R.J., Jones, E., Kern, R., Larson, E., Carey, C.J., Polat, İ., Feng, Y., Moore, E.W., VanderPlas, J., Laxalde, D., Perktold, J., Cimrman, R., Henriksen, I., Quintero, E.A., Harris, C.R., Archibald, A.M., Ribeiro, A.H., Pedregosa, F., van Mulbregt, P., 2020. SciPy 1.0: fundamental algorithms for scientific computing in Python. Nature Methods 17, 261–272. https://doi.org/10.1038/s41592-019-0686-2

Visser, R., John, T., Whitehouse, M.J., Patzek, M., Bischoff, A., 2020. A short-lived 26Al induced hydrothermal alteration event in the outer solar system: Constraints from Mn/Cr ages of carbonates. Earth and Planetary Science Letters 547, 116440. https://doi.org/10.1016/j.epsl.2020.116440

Watanabe, S., Hirabayashi, M., Hirata, N., Hirata, Na, Noguchi, R., Shimaki, Y., Ikeda, H., Tatsumi, E., Yoshikawa, M., Kikuchi, S., Yabuta, H., Nakamura, T., Tachibana, S., Ishihara, Y., Morota, T., Kitazato, K., Sakatani, N., Matsumoto, K., Wada, K., Senshu, H., Honda, C., Michikami, T., Takeuchi, H., Kouyama, T., Honda, R., Kameda, S., Fuse, T., Miyamoto, H., Komatsu, G., Sugita, S., Okada, T., Namiki, N., Arakawa, M., Ishiguro, M., Abe, M., Gaskell, R., Palmer, E., Barnouin, O.S., Michel, P., French, A.S., McMahon, J.W., Scheeres, D.J., Abell, P.A., Yamamoto, Y., Tanaka, S., Shirai, K., Matsuoka, M., Yamada, M., Yokota, Y., Suzuki, H., Yoshioka, K., Cho, Y., Tanaka, S., Nishikawa, N., Sugiyama, T., Kikuchi, H., Hemmi, R., Yamaguchi, T., Ogawa, N., Ono, G., Mimasu, Y., Yoshikawa, K., Takahashi, T., Takei, Y., Fujii, A., Hirose, C., Iwata, T., Hayakawa, M., Hosoda, S., Mori, O., Sawada, H., Shimada, T., Soldini, S., Yano, H., Tsukizaki, R., Ozaki, M., Iijima, Y., Ogawa, K., Fujimoto, M., Ho, T.-M., Moussi, A.,

Jaumann, R., Bibring, J.-P., Krause, C., Terui, F., Saiki, T., Nakazawa, S., Tsuda, Y., 2019. Hayabusa2 arrives at the carbonaceous asteroid 162173 Ryugu—A spinning top–shaped rubble pile. Science. https://doi.org/10.1126/science.aav8032

Yada, T., Abe, M., Okada, T., Nakato, A., Yogata, K., Miyazaki, A., Hatakeda, K., Kumagai, K., Nishimura, M., Hitomi, Y., Soejima, H., Yoshitake, M., Iwamae, A., Furuya, S., Uesugi, M., Karouji, Y., Usui, T., Hayashi, T., Yamamoto, D., Fukai, R., Sugita, S., Cho, Y., Yumoto, K., Yabe, Y., Bibring, J.-P., Pilorget, C., Hamm, V., Brunetto, R., Riu, L., Lourit, L., Loizeau, D., Lequertier, G., Moussi-Soffys, A., Tachibana, S., Sawada, H., Okazaki, R., Takano, Y., Sakamoto, K., Miura, Y.N., Yano, H., Ireland, T.R., Yamada, T., Fujimoto, M., Kitazato, K., Namiki, N., Arakawa, M., Hirata, Naru, Yurimoto, H., Nakamura, T., Noguchi, T., Yabuta, H., Naraoka, H., Ito, M., Nakamura, E., Uesugi, K., Kobayashi, K., Michikami, T., Kikuchi, H., Hirata, Naoyuki, Ishihara, Y., Matsumoto, K., Noda, H., Noguchi, R., Shimaki, Y., Shirai, K., Ogawa, K., Wada, K., Senshu, H., Yamamoto, Y., Morota, T., Honda, R., Honda, C., Yokota, Y., Matsuoka, M., Sakatani, N., Tatsumi, E., Miura, A., Yamada, M., Fujii, A., Hirose, C., Hosoda, S., Ikeda, H., Iwata, T., Kikuchi, S., Mimasu, Y., Mori, O., Ogawa, N., Ono, G., Shimada, T., Soldini, S., Takahashi, T., Takei, Y., Takeuchi, H., Tsukizaki, R., Yoshikawa, K., Terui, F., Nakazawa, S., Tanaka, S., Saiki, T., Yoshikawa, M., Watanabe, S., Tsuda, Y., 2022. Preliminary analysis of the Hayabusa2 samples returned from C-type asteroid Ryugu. Nature Astronomy 6, 214–220. https://doi.org/10.1038/s41550-021-01550-6

Yamaguchi, A., Tomioka, N., Ito, M., Shirai, N., Kimura, M., Greenwood, R.C., 2022. Complex geologic history of C-type asteroids: Fresh insights from the analysis of Ryugu particles. Nature Astronomy.

York, D., Evensen, N.M., Martínez, M.L., De Basabe Delgado, J., 2004. Unified equations for the slope, intercept, and standard errors of the best straight line. American Journal of Physics 72, 367–375. https://doi.org/10.1119/1.1632486

Zheng, Y.-F., 1995. Oxygen isotope fractionation in magnetites: structural effect and oxygen inheritance. Chemical Geology 121, 309–316. https://doi.org/10.1016/0009-2541(94)00149-3

Zhou, Q., Yin, Q.-Z., Young, E.D., Li, X.-H., Wu, F.-Y., Li, Q.-L., Liu, Y., Tang, G.-Q., 2013. SIMS Pb–Pb and U–Pb age determination of eucrite zircons at < 5 μm scale and the first 50 Ma of the thermal history of Vesta. Geochimica et Cosmochimica Acta 110, 152–175. https://doi.org/10.1016/j.gca.2013.02.016

Ziegler, J.F., Ziegler, M.D., Biersack, J.P., 2010. SRIM - The stopping and range of ions in matter (2010). NIMPB 268, 1818–1823. https://doi.org/10.1016/j.nimb.2010.02.091

Zolensky, M., Barrett, R., Browning, L., 1993. Mineralogy and composition of matrix and chondrule rims in carbonaceous chondrites. Geochimica et Cosmochimica Acta 57, 3123–3148. https://doi.org/10.1016/0016-7037(93)90298-B

Chapter 5.

Summary of key results and future directions for studies of aqueous alteration

Kaitlyn A. McCain

Summary of major results of this work

To constrain the timing and chemistry of carbonate formation and aqueous alteration occurring on carbonaceous asteroids, I performed carbon, oxygen, and ^{53}Mn-^{53}Cr isotope analyses on carbonate minerals in carbonaceous chondrites. To ensure that the Mn-Cr ages were accurate, I used ion implantation to create matrix-matched calcite, dolomite, and breunnerite standards, the results of which are described in Chapter 2 and the Supplementary Methods of Chapter 4. Measurements of the age of dolomite in the CI chondrite Alais (Chapter 3) and dolomite, calcite, and breunnerite in CI-like particles (Chapter 4) returned from the Ryugu asteroid indicated that fluid activity and carbonate formation took place before 1.4 Myr after the beginning of the solar system as defined by Calcium-Aluminum-rich Inclusion (CAI) formation. Ages of calcite and dolomite in the CM chondrites ALH 84034 and Boriskino could not be calculated, which I argue is due to shock alteration.

Implications of the early formation of CI chondrites

The old ages inferred for CI and Ryugu carbonates suggest that aqueous alteration occurred when ^{26}Al was abundant at the level of $^{26}Al/^{27}Al = 1 - 2 \times 10^{-5}$. The high concentration of ^{26}Al requires that the parent body cool its interior to allow fluid activity to occur without water loss or silicate melting. I proposed that this could have occurred either on small bodies (inferred to be < 17 km in diameter for Ryugu) which could efficiently cool their interiors by conduction, or on larger parent bodies which were disrupted by impacts before the body reached its peak temperature. The petrography of Ryugu and the CI chondrites show evidence of brecciation and reassembly (Alfing et al., 2019; Endreß and Bischoff, 1996; Tomioka et al., 2022), which could favor the second scenario.

Regardless of the size of the CI chondrite parent body, its early formation has implications for models of solar system formation and evolution. One important isotopic feature of solar system materials is the so-called 'isotopic dichotomy', a framework which divides the early solar system into two reservoirs: one characterized by isotopic compositions similar to the volatile-rich carbonaceous chondrites (CC), and one with isotopic similarities to volatile-depleted classes such as the ordinary chondrites, the enstatite chondrites, and the Earth (collectively described as the non-carbonaceous (NC) isotopic reservoir) (Kleine et al., 2020; Warren, 2011). The NC group has been inferred to have accreted from materials formed in the inner solar system, and the CC group from materials in the outer solar system, beyond the water ice snow line, which were separated from one another within ~1 Myr after the beginning of the solar system, as defined as the timing of CAI formation (Kruijer et al., 2017).

Based on the ^{182}Hf-^{182}W ages of iron meteorites with CC affinities, it has been suggested that planetesimals in the outer solar system accreted within ~1 Myr of CAI formation and differentiated at 2.2−2.8 Myr after CAI, slightly later than NC iron meteorites, which were found to have accreted <0.4 Myr after CAI formation and differentiated 0.3 – 1.8 Myr after CAI formation (Kruijer et al., 2017). This timescale is consistent with heating due to the decay of ^{26}Al as the heat source driving melting and chemical differentiation of these planetesimals, and is also consistent with the inferred accretion times of NWA 011, Tafassasset, and NWA 6704/6693, achondrites with CC affinities that accreted within 2.1 Myr of CAI formation (Sanborn et al., 2019; Sugiura and Fujiya, 2014). Based on the late formation of CM and CI chondrites as inferred from the formation ages of carbonate (Fujiya et al., 2012, 2013; Visser et al., 2020), these meteorite groups were thought to have escaped similar heating by accreting much later than melted CC material. The early formation of undifferentiated material as inferred from our

measurements of CI dolomite requires an explanation for the simultaneous existence of differentiated and unmelted CC material. CI material could have formed in a smaller parent body than differentiated CC material, or the CI parent body happened to be disrupted early by impact while other CC material remained more intact.

Models of accretion and transport in the disk which attempt to explain the NC/CC dichotomy used the apparently late accretion times of CI chondrite material inferred from carbonate formation ages (Fujiya et al., 2013; Sugiura and Fujiya, 2014) to constrain models of disk transport (Desch et al., 2018). These models propose that dust in the inner solar system became depleted in the refractory lithophile elements due to incorporation of these elements into CAIs, and that this depleted material spread to the outer portions of the disk over time. These models found that CI chondrites could maintain their solar compositions of refractory lithophile elements if they formed early and far out in the disk, where mixing with the material depleted by CAI formation had not yet occurred. It was difficult, though possible, to form the CIs after 3.0 Myr while maintaining refractory lithophile depletion to within the error of the observed solar photospheric and CI chondrite abundances. Our Mn-Cr data for Ryugu samples and Alais suggest that the CI chondrites did in fact form early, and the $\delta^{13}C$ compositions of carbonate in Ryugu suggest that the formation region was far enough out in the disk for the parent body to accrete CO_2 ice. I conclude that the change in the inferred accretion time of the CI chondrites is compatible with current models of disk evolution and the CC/NC dichotomy.

Complementarity of petrographic and stable isotopic data

Another important conclusion of this work is the necessity of petrographic characterization of the targets of Mn-Cr dating and the utility of stable isotopic data. The petrographic observations of the shock state and petrologic type of Boriskino clasts informed our

interpretation of our observation of uncorrelated $^{53}Cr/^{52}Cr$ and $^{55}Mn/^{52}Cr$. From this, I conclude that the impact shock experienced by Boriskino was sufficient to affect the Mn-Cr systematics of carbonate. However, the O isotopic compositions of Boriskino calcite (both Type 1 and Type 2) and dolomite are similar to calcite and dolomite in other CM chondrites (Telus et al., 2019; Tyra et al., 2016, 2012), suggesting that impact processes may not have affected O isotopic systematics.

Our measurements of the C isotopic compositions of ALH 84034 and Ryugu carbonate have led to the inference that the CM and CI chondrite parent bodies accreted with CO_2 ice, which I used in Chapters 3 and 4 to specify the initial temperature of the accreted water and rock in our models of parent body evolution. This has been previously observed in CM material (Fujiya et al., 2019, 2020), but is novel for CI-like material. For both ALH 84034 and Ryugu particles, I observed a correlation between the $\delta^{13}C$ and the $\Delta^{17}O$ of the carbonate, recording an evolution of the fluid towards lighter C isotopic compositions as alteration proceeded. This suggests that in these samples, serpentinization and methane production (which would produce an inverse correlation between $\delta^{13}C$ and $\Delta^{17}O$ (Guo and Eiler, 2007; Telus et al., 2019; Tyra et al., 2016; Vacher et al., 2018)) did not drive the evolution of the fluid's C isotopic composition. Rather, in both samples I favor an initially heavy C isotopic composition derived from co-accreted CO_2 ice which progressively equilibrates with light organic matter. The heterogeneity observed in the correlation between C and O isotopes, and the inferred heterogeneity in formation conditions this entails, underscores the importance of measuring both isotopic systems.

In the future, I suggest that attempts to apply the Mn-Cr dating system to CM carbonates should be accompanied by careful petrographic surveys to identify any targets affected by shock.

In cases where an age cannot be calculated, petrographic and stable isotopic measurements can help constrain any parent body processes which may have affected the ^{53}Mn-^{53}Cr systematics of the target carbonate.

Alternative explanations for old ^{53}Mn-^{53}Cr ages of CI and CM chondrites

In the main text of this dissertation, I describe older carbonate formation ages for CI chondrites than have been previously reported (Fujiya et al., 2013; Nagashima et al., 2022; Petitat et al., 2009; Visser et al., 2020) and favor formation scenarios in which carbonates form on small parent bodies or just prior to the disruption of a large parent body as aqueous activity is occurring. The CM chondrites Boriskino and ALH 84034 also have unrealistically high inferred initial ^{53}Mn/^{55}Mn higher than the assumed initial solar system ratio based upon the D'Orbigny anchor. In the case of ALH 84034 and Boriskino, I cite evidence of shock, brecciation, and microstructural damage to carbonate (Brearley and Hutcheon, 2000; Dobrică et al., 2022; Vacher et al., 2018) to explain similarly high inferred initial ^{53}Mn/^{55}Mn and the poor correlation of ^{53}Cr/^{52}Cr with ^{55}Mn/^{52}Cr. Below, I discuss an alternate hypothesis for these high initial ^{53}Mn/^{55}Mn ratios and their corresponding inferred old carbonate ages.

Carbonate dating using the ^{53}Mn-^{53}Cr system relies upon the assumption that ^{53}Mn was homogeneously distributed throughout the solar nebula so that the anchor sample D'Orbigny formed from the same Mn isotopic reservoirs as the CM and CI chondrites so that any variation in the ^{53}Mn/^{55}Mn ratio can be attributed solely to differences in their formation times. I note that the D'Orbigny angrite is used as an anchor for the Mn-Cr system because its formation age and initial ^{53}Mn/^{55}Mn are well-known (Amelin, 2008; Brennecka and Wadhwa, 2012; McKibbin et al., 2015). The initial ^{53}Mn/^{55}Mn of the solar system cannot be directly determined using CAIs, as these refractory materials do not contain sufficient concentrations of moderately volatile

elements such as Mn. Rather, the initial $^{53}Mn/^{55}Mn$ ratio for the solar system is inferred from the age of the CAIs and the known age and $^{53}Mn/^{55}Mn$ ratio of the anchor, D'Orbigny. However, if the angrites and the CM and CI chondrites did not form from materials with a homogeneous ^{53}Mn abundance, the relative age would be invalid. There is good agreement between the ^{206}Pb-^{207}Pb and ^{53}Mn-^{53}Cr ages of Allende CV chondrules (Connelly et al., 2012; Yin et al., 2009), angrites (Kleine et al., 2012; Sugiura et al., 2005), Gujba CB chondrules (Bollard et al., 2015; Yamashita et al., 2010), and a carbonaceous achondrite (Sanborn et al., 2019), suggesting that that the initial $^{53}Mn/^{55}Mn$ was homogeneously distributed where these meteorites formed. These studies include meteorites from both the NC and CC reservoirs. However, no Pb-Pb ages have been determined for the CM and CI chondrites or their components, as they do not contain unaltered igneous materials. It is not currently possible to determine whether CM and CI chondrites formed with the same initial ^{53}Mn abundance as the other NC and CC meteorites. Instead, measurements of Mn-Cr ages of carbonate must rely on the assumption that the initial $^{53}Mn/^{55}Mn$ compositions of other CC material is representative of the CM and CI chondrites.

Accuracy of the Mn-Cr RSF value measured from implanted standards

Because the calculated age of a carbonate is directly affected by the value of the RSF used to determine its $^{55}Mn/^{52}Cr$, it is of paramount importance that this RSF be accurate. The relative sensitivity factor (RSF) of the Mn/Cr ratio can be affected by the geometry of the crater produced by sputtering during the ion probe analysis (Doyle et al., 2016). Our measurements of the carbonate RSF were performed using a 2nA beam rastered over a 50 × 50 μm area. This produces a much flatter (i.e., shallower) crater geometry than the "spot-mode" condition used for analyses of meteoritic and Ryugu dolomite, which was performed using a 0.15 -1nA beam rastered over much smaller areas (Chapters 3,4). Therefore, in principle a systematic error could

arise when applying an RSF determined from a large raster to a small spot-mode analysis. To estimate the potential magnitude of this error, we measured an ion-implanted sample of San Carlos Olivine and compared the RSF determined using the depth profiling method to RSF values of San Carlos Olivine measured using the spot-mode conditions applied to meteoritic carbonate samples. For all spot-mode beam conditions, the RSF for San Carlos Olivine did not vary between the large-raster (RSF = 1.03 ± 0.16 2SE) and the various spot-mode conditions , which have RSF values ranging from 0.87 to 0.94 with typical 2SE errors of 0.14 ‰ (See Supplementary Materials, Chapter 3 and 4). The major source of uncertainty for the San Carlos Olivine RSF analyses is the true $^{55}Mn/^{52}Cr$ ratio of San Carlos Olivine, which was determined to be 9.2 ± 0.7 (2SE) by electron probe microanalysis (EPMA). I note that the behavior of San Carlos Olivine and carbonate during sputtering are not identical, as evidenced by their sputtering rates during depth profiling—San Carlos Olivine sputters at a rate of 0.3 μm/hr, and carbonates sputter at rates from 0.62 – 0.75 μm/hr. However, this exercise suggested that the RSF values derived from depth profiling of implanted materials could be applied to spot-mode analyses without significantly compromising the accuracy of the Mn-Cr age.

Avenues for future study

Determining Mn-Cr ages of Ca-carbonate and CM chondrite dating

In this dissertation, I focused my attention on standards for dating dolomite and breunnerite, as matrix-matched standards for these minerals did not yet exist. I implanted $^{52}Cr^{+}$ into terrestrial calcite as well, but this calcite (OPTI-Cal) had a $MnCO_3$ content just above the detection limit of the EPMA (Chapter 2), leading to large uncertainties in its Mn concentration. The RSF value derived by depth profiling (Chapter 4, Supplementary Table 4.7) of this calcite was ~1.3, which is similar to RSF values of obtained from measurements of synthetic calcites

doped with Mn and Cr (Sugiura and Ichimura, 2010). However, there are extremely large errors of ±1.2 (2σ) associated with this calcite RSF due to the low Mn concentration. Therefore, future analyses of meteoritic calcite require further development of ion-implanted calcite standards. This development would be particularly important for studies of less-altered CM2 chondrites, which typically do not contain dolomite or breunnerite. A variety of Ca-carbonates, including aragonite, calcite containing Fe, and calcite containing Mn could be characterized and implanted according to the procedure described in Chapter 2 to expand our study of carbonate formation timescales. It may also be possible to determine the Mn concentration of Mn-poor calcites using methods that are more sensitive than the EPMA analyses used in this work, such as synchrotron X-ray fluorescence (XRF) or inductively-coupled plasma mass spectrometry (ICPMS), though we note that the latter method would not be able to quantify whether the Mn concentration of the carbonate is laterally homogeneous. Though synthetic calcites can also be used to date Ca-carbonates, these calcites exhibit substantial lateral heterogeneity in both Mn and Cr concentrations (Jilly et al., 2014; Visser et al., 2020) which can lead to complications when determining the RSF.

Modeling of CI chondrite parent bodies

In this dissertation, I modeled the timing and formation of the CI chondrite parent body using the 'Astemp' spherically symmetric 1D explicit finite difference code (See Chapter 3 and its supplementary materials, (McCain et al., 2017; Zhou et al., 2013)). While this code accounts for relevant parent body processes such as core formation and heat production or loss due to the enthalpies of freezing and melting for water and rock, it does not model fluid chemistry or the effect of fluid flow. While the extent to which large-scale fluid flow affected carbonaceous chondrites remains a topic of debate (Bland et al., 2009; Bland and Travis, 2017; Young et al., 1999; Young, 2001; Young et al., 2003), images of bright veins on asteroid Bennu suggest the presence of fluid flow on the scale of 40-90 km on Bennu's progenitor (Kaplan et al., 2020). Therefore, the possibility of fluid flow should be considered.

We tested the possible significance of enhanced heat transport to the surface caused by fluid flow by enhancing the thermal diffusivity (κ, m^2/s) for a large (100-km radius), water-rich planetesimal by the Nusselt number Nu_{water}, where Nu_{water} is the ratio of actual heat transfer to purely conductive heat transfer such that $\kappa_{actual} = Nu_{water}(\kappa)$. We determine $Nu_{water} = 6$ following the prescription for convection in a fluid-saturated porous medium (Otero et al., 2004), with a critical Rayleigh number of 183.91 derived from a study of pore water convection in carbonaceous chondrite parent bodies (Young et al., 2003). While this sixfold enhancement in the thermal diffusivity causes this parent body to cool more quickly after reaching its peak temperature, the peak temperature and the time required for the parent body to reach this peak temperature do not change significantly. The effect upon the temperature profiles in the time interval before 1 Myr, or in smaller parent bodies, requires future investigation.

The effects of impacts into and fragmentation of water-rich bodies were also not considered in this dissertation, beyond noting that disruption of a parent body is an effective mechanism for cooling the interior of a planetesimal which might otherwise lose water or differentiate (Ciesla et al., 2013). Hydrocode simulations of parent bodies composed of serpentine and laboratory studies of volatile loss during hypervelocity impact into CI simulant suggest that catastrophic disruption of a CI-like body would result in devolatilization for only a small volume of the disrupted body (Kurosawa et al., 2021). While this study shows that phyllosilicate is not dehydrated during such an impact, the simulated parent bodies did not contain liquid water. Further study of the effect of impacts into water-rich objects will be needed to verify whether impact disruption is indeed a viable mechanism for producing CI-like material <1.4 Myr after CAI.

Additional insight into fluid evolution could also be gained by using programs such as Geochemist's Workbench (GWB, Bethke, 1996) to determine the secondary mineral assemblages produced by the equilibration of static or flowing water with various primary mineral assemblages. For both CM and CI material in Chapters 3 and 4, we use measurements of $\Delta^{17}O$ to constrain the formation sequence of magnetite, calcite, and dolomite, and observe an evolution towards more Fe-rich dolomite as alteration proceeded in ALH 84034. Using GWB, various combinations of starting minerals, W/R ratios, and presence or absence of fluid flow can be explored. Though calibrating the starting materials, temperatures, and pH to produce the minerals actually observed in chondrites requires some trial and error, noting which sets of initial conditions produce the correct sequences of mineral formation could provide insight into the W/R ratio and fluid flow regime experienced by each sample.

Uncertainties related to equilibrium mineral-water fractionations

In Chapter 4, I discussed temperatures derived from the oxygen isotopic compositions of the calcite-magnetite and dolomite-phyllosilicate pairs. In the supplementary portion of the same chapter, I discuss some of the challenges faced when attempting to perform oxygen isotopic thermometry at low temperature. Here, I extend this discussion.

Because the equilibrium oxygen isotopic fractionation between carbonate and water is a fundamental tool of terrestrial carbonate sedimentology and paleoclimate studies, the mineral-water fractionations of calcite and dolomite have been experimentally determined at the low temperatures relevant to terrestrial surface processes (Horita, 2014; Kim and O'Neil, 1997). The mineral-water fractionations for other components of carbonaceous chondrites, such as Mg- and Fe-rich phyllosilicates and magnetite, have been experimentally determined at the higher temperatures and pressures (e.g., >250 °C and 50 MPa) typically reached during terrestrial serpentinization and hydrothermal processes (Cole et al., 2004; Saccocia et al., 2009). However, the authors of these studies caution that their calibrations should not be extended to lower temperatures, and so I do not apply the fractionation factors derived from these experiments to our study. Though brucite ($Mg(OH)_2$) is not a phase found in carbonaceous chondrites, it is a hydrated Mg-rich material for which the mineral-water fractionation at low temperatures has been determined (Saccocia et al., 2015). For this reason, I use the brucite-water fractionation factor as a stand-in for phyllosilicate-water fractionation in Chapter 4. For magnetite, a variety of theoretical estimates of the mineral-water oxygen isotope fractionation at low temperatures have been proposed, and I adopt a recent estimate for the equilibrium magnetite-water fractionation (Hayles et al., 2018). Previous applications of the carbonate-magnetite thermometer in meteorite

samples have used other theoretical calibrations (Telus et al., 2019; Zheng, 1995), which would shift our estimates of the temperature from 0-20 °C to 23-47 °C.

Improvements to these mineral-water thermometers would require further experiments to constrain the equilibrium mineral-water oxygen isotopic fractionation factors at low temperatures and pressures. However, these experiments are challenging to conduct because isotopic equilibrium is difficult to achieve under such conditions within reasonable experimental timescales. Measurements of the O isotopic compositions of extremely slow-growing (<1 μm/year) natural calcites from Devil's Hole, which formed from well-known water compositions and at known temperatures (Coplen, 2007; Devriendt et al., 2017; Gabitov et al., 2012), resulted in the calculation of calcite-water fractionation factors which are different from the fractionation factors inferred from marine calcite or the products of calcite-water fractionation experiments (Kim and O'Neil, 1997). Marine calcite and experimental products precipitated at much faster rates than the calcite, so this discrepancy is likely due to kinetic effects. Though difficult to conduct, experiments placing better constraints on equilibrium mineral-water fractionations would greatly improve estimates of alteration temperatures on carbonaceous chondrite parent bodies.

Conclusion

By producing a suite of matrix-matched carbonate standards and applying them to a variety of carbonaceous materials, I found that the fluid activity on the CI chondrite parent body, as recorded by carbonate formation timescales in the CI chondrite Alais and in returned samples of asteroid Ryugu, occurred much earlier than previously inferred. These data require a reappraisal of parent body conditions capable of producing CI material. My measurements of CM chondrite carbonate ages reflected complex inheritance and parent body histories, which

were partially detangled using petrographic observations and measurements of C and O stable isotopes. In the future, careful evaluation of the petrology of CM chondrite carbonate should be applied to dolomite-rich CM chondrites to determine reliable formation ages using matrix-matched standards.

References

Alfing, J., Patzek, M., Bischoff, A., 2019. Modal abundances of coarse-grained (>5 μm) components within CI-chondrites and their individual clasts – Mixing of various lithologies on the CI parent body(ies). Geochemistry, In Honor to Prof. Keil 79, 125532. https://doi.org/10.1016/j.chemer.2019.08.004

Amelin, Y., 2008. U–Pb ages of angrites. Geochimica et Cosmochimica Acta 72, 221–232. https://doi.org/10.1016/j.gca.2007.09.034

Bethke, C.M., 1996. Geochemical Reaction Modeling, 1st ed. Oxford University Press.

Bland, P.A., Jackson, M.D., Coker, R.F., Cohen, B.A., Webber, J.B.W., Lee, M.R., Duffy, C.M., Chater, R.J., Ardakani, M.G., McPhail, D.S., McComb, D.W., Benedix, G.K., 2009. Why aqueous alteration in asteroids was isochemical: High porosity ≠ high permeability. Earth and Planetary Science Letters 287, 559–568. https://doi.org/10.1016/j.epsl.2009.09.004

Bland, P.A., Travis, B.J., 2017. Giant convecting mud balls of the early solar system. Science Advances 3, e1602514. https://doi.org/10.1126/sciadv.1602514

Bollard, J., Connelly, J.N., Bizzarro, M., 2015. Pb-Pb dating of individual chondrules from the CBa chondrite Gujba: Assessment of the impact plume formation model. Meteoritics & Planetary Science 50, 1197–1216. https://doi.org/https://doi.org/10.1111/maps.12461

Brearley, A.J., Hutcheon, I.D., 2000. Carbonates in the CM1 Chondrite ALH84034: Mineral Chemistry, Zoning and Mn-Cr Systematics. Lunar and Planetary Science Conference 1407.

Brennecka, G.A., Wadhwa, M., 2012. Uranium isotope compositions of the basaltic angrite meteorites and the chronological implications for the early Solar System. PNAS 109, 9299–9303. https://doi.org/10.1073/pnas.1114043109

Ciesla, F.J., Davison, T.M., Collins, G.S., O'Brien, D.P., 2013. Thermal consequences of impacts in the early solar system. Meteorit Planet Sci 48, 2559–2576. https://doi.org/10.1111/maps.12236

Cole, D.R., Horita, J., Polyakov, V.B., Valley, J.W., Spicuzza, M.J., Coffey, D.W., 2004. An experimental and theoretical determination of oxygen isotope fractionation in the system magnetite-H2O from 300 to 800°C 1 1Associate editor: E. M. Ripley. Geochimica et Cosmochimica Acta 68, 3569–3585. https://doi.org/10.1016/j.gca.2004.02.017

Connelly, J.N., Bizzarro, M., Krot, A.N., Nordlund, Å., Wielandt, D., Ivanova, M.A., 2012. The Absolute Chronology and Thermal Processing of Solids in the Solar Protoplanetary Disk. Science. https://doi.org/10.1126/science.1226919

Coplen, T.B., 2007. Calibration of the calcite–water oxygen-isotope geothermometer at Devils Hole, Nevada, a natural laboratory. Geochimica et Cosmochimica Acta 71, 3948–3957. https://doi.org/10.1016/j.gca.2007.05.028

Desch, S.J., Kalyaan, A., Alexander, C.M.O., 2018. The Effect of Jupiter's Formation on the Distribution of Refractory Elements and Inclusions in Meteorites. ApJS 238, 11. https://doi.org/10.3847/1538-4365/aad95f

Devriendt, L.S., Watkins, J.M., McGregor, H.V., 2017. Oxygen isotope fractionation in the CaCO3-DIC-H2O system. Geochimica et Cosmochimica Acta 214, 115–142. https://doi.org/10.1016/j.gca.2017.06.022

Dobrică, E., McCain, K.A., McKeegan, K.D., Brearley, A.J., 2022. Carbonates, New Tools to Investigate Shock Metamorphic Effects in Chondrites. LPI Contributions 2678, 2313.

Donohue, P.H., Huss, G.R., Nagashima, K., 2018. Synthesizing Calcite and Dolomite for Mn/Cr Relative Sensitivity Corrections: A Progress Report. Lunar and Planetary Science Conference 1569.

Doyle, P.M., Jogo, K., Nagashima, K., Huss, G.R., Krot, A.N., 2016. Mn–Cr relative sensitivity factor in ferromagnesian olivines defined for SIMS measurements with a Cameca ims-1280 ion microprobe: Implications for dating secondary fayalite. Geochimica et Cosmochimica Acta 174, 102–121. https://doi.org/10.1016/j.gca.2015.10.010

Endreß, M., Bischoff, A., 1996. Carbonates in CI chondrites: Clues to parent body evolution. Geochimica et Cosmochimica Acta 60, 489–507. https://doi.org/10.1016/0016-7037(95)00399-1

Fujiya, W., Aoki, Y., Ushikubo, T., Hashizume, K., Yamaguchi, A., 2020. Carbon isotopic evolution of aqueous fluids in CM chondrites: Clues from in-situ isotope analyses within calcite grains in Yamato-791198. Geochimica et Cosmochimica Acta 274, 246–260. https://doi.org/10.1016/j.gca.2020.02.003

Fujiya, W., Hoppe, P., Ushikubo, T., Fukuda, K., Lindgren, P., Lee, M.R., Koike, M., Shirai, K., Sano, Y., 2019. Migration of D-type asteroids from the outer Solar System inferred from carbonate in meteorites. Nature Astronomy 1. https://doi.org/10.1038/s41550-019-0801-4

Fujiya, W., Sugiura, N., Hotta, H., Ichimura, K., Sano, Y., 2012. Evidence for the late formation of hydrous asteroids from young meteoritic carbonates. Nat Commun 3, 627. https://doi.org/10.1038/ncomms1635

Fujiya, W., Sugiura, N., Sano, Y., Hiyagon, H., 2013. Mn–Cr ages of dolomites in CI chondrites and the Tagish Lake ungrouped carbonaceous chondrite. Earth and Planetary Science Letters 362, 130–142. https://doi.org/10.1016/j.epsl.2012.11.057

Gabitov, R.I., Watson, E.B., Sadekov, A., 2012. Oxygen isotope fractionation between calcite and fluid as a function of growth rate and temperature: An in situ study. Chemical Geology 306–307, 92–102. https://doi.org/10.1016/j.chemgeo.2012.02.021

Guo, W., Eiler, J.M., 2007. Temperatures of aqueous alteration and evidence for methane generation on the parent bodies of the CM chondrites. Geochimica et Cosmochimica Acta 71, 5565–5575. https://doi.org/10.1016/j.gca.2007.07.029

Hayles, J., Gao, C., Cao, X., Liu, Y., Bao, H., 2018. Theoretical calibration of the triple oxygen isotope thermometer. Geochimica et Cosmochimica Acta 235, 237–245. https://doi.org/10.1016/j.gca.2018.05.032

Horita, J., 2014. Oxygen and carbon isotope fractionation in the system dolomite–water–CO2 to elevated temperatures. Geochimica et Cosmochimica Acta 129, 111–124. https://doi.org/10.1016/j.gca.2013.12.027

Jilly, C.E., Huss, G.R., Krot, A.N., Nagashima, K., Yin, Q.-Z., Sugiura, N., 2014. 53Mn-53Cr dating of aqueously formed carbonates in the CM2 lithology of the Sutter's Mill carbonaceous chondrite. Meteorit Planet Sci 49, 2104–2117. https://doi.org/10.1111/maps.12305

Kaplan, H.H., Lauretta, D.S., Simon, A.A., Hamilton, V.E., DellaGiustina, D.N., Golish, D.R., Reuter, D.C., Bennett, C.A., Burke, K.N., Campins, H., Connolly, H.C., Dworkin, J.P., Emery, J.P., Glavin, D.P., Glotch, T.D., Hanna, R., Ishimaru, K., Jawin, E.R., McCoy, T.J., Porter, N., Sandford, S.A., Ferrone, S., Clark, B.E., Li, J.-Y., Zou, X.-D., Daly, M.G., Barnouin, O.S., Seabrook, J.A., Enos, H.L., 2020. Bright carbonate veins on asteroid (101955) Bennu: Implications for aqueous alteration history. Science. https://doi.org/10.1126/science.abc3557

Kim, S.-T., O'Neil, J.R., 1997. Equilibrium and nonequilibrium oxygen isotope effects in synthetic carbonates. Geochimica et Cosmochimica Acta 61, 3461–3475. https://doi.org/10.1016/S0016-7037(97)00169-5

Kleine, T., Budde, G., Burkhardt, C., Kruijer, T.S., Worsham, E.A., Morbidelli, A., Nimmo, F., 2020. The Non-carbonaceous–Carbonaceous Meteorite Dichotomy. Space Sci Rev 216, 55. https://doi.org/10.1007/s11214-020-00675-w

Kleine, T., Hans, U., Irving, A.J., Bourdon, B., 2012. Chronology of the angrite parent body and implications for core formation in protoplanets. Geochimica et Cosmochimica Acta 84, 186–203. https://doi.org/10.1016/j.gca.2012.01.032

Kruijer, T.S., Burkhardt, C., Budde, G., Kleine, T., 2017. Age of Jupiter inferred from the distinct genetics and formation times of meteorites. Proceedings of the National Academy of Sciences 114, 6712–6716.

Kurosawa, K., Moriwaki, R., Yabuta, H., Ishibashi, K., Komatsu, G., Matsui, T., 2021. Ryugu's observed volatile loss did not arise from impact heating alone. Commun Earth Environ 2, 1–6. https://doi.org/10.1038/s43247-021-00218-3

McCain, K.A., Young, E.D., Manning, C.E., 2017. CM Carbonates Should Be Old: Insights from Parent Body Thermal Modeling. Presented at the Lunar and Planetary Science Conference, p. 2181.

McKibbin, S.J., Ireland, T.R., Amelin, Y., Holden, P., 2015. Mn–Cr dating of Fe- and Ca-rich olivine from "quenched" and "plutonic" angrite meteorites using Secondary Ion Mass

Spectrometry. Geochimica et Cosmochimica Acta 157, 13–27. https://doi.org/10.1016/j.gca.2015.02.019

Nagashima, K., Kawasaki, N., Sakamoto, N., Yurimoto, H., Chemistry, H.-I.-A., Core, H.-I.-A., 2022. In-Situ Oxygen and Manganese-Chromium Isotope Studies of Ryugu: Implications to Temperature and Timing of Aqueous Activity. LPI Contributions 2678, 1689.

Otero, J., Dontcheva, L.A., Johnston, H., Worthing, R.A., Kurganov, A., Petrova, G., Doering, C.R., 2004. High-Rayleigh-number convection in a fluid-saturated porous layer. Journal of Fluid Mechanics 500, 263–281. https://doi.org/10.1017/S0022112003007298

Petitat, M., McKeegan, K., Gounelle, M., Mostefaoui, S., Marrocchi, Y., Meibom, A., Leshin, L.A., 2009. Duration and Sequence of Carbonate Crystallization on the Orgueil Protolith: 53Mn-53Cr Systematics of their Evolution in O and C Isotopic Evolution. Presented at the Lunar and Planetary Science Conference, p. 1657.

Saccocia, P.J., Seewald, J.S., Shanks III, W.C., 2009. Oxygen and hydrogen isotope fractionation in serpentine-water and talc-water systems from 250 to 450 °C, 50 MPa. Geochimica et Cosmochimica Acta 73, 67896804. https://doi.org/10.1016/j.gca.2009.07.036

Saccocia, P.J., Seewald, J.S., Shanks, W.C., 2015. Oxygen isotope fractionation in the portlandite–water and brucite–water systems from 125 to 450°C, 50MPa. Geochimica et Cosmochimica Acta 169, 137–151. https://doi.org/10.1016/j.gca.2015.07.017

Sanborn, M.E., Wimpenny, J., Williams, C.D., Yamakawa, A., Amelin, Y., Irving, A.J., Yin, Q.-Z., 2019. Carbonaceous achondrites Northwest Africa 6704/6693: Milestones for early Solar System chronology and genealogy. Geochimica et Cosmochimica Acta 245, 577–596. https://doi.org/10.1016/j.gca.2018.10.004

Sugiura, N., Fujiya, W., 2014. Correlated accretion ages and ε54Cr of meteorite parent bodies and the evolution of the solar nebula. Meteoritics & Planetary Science 49, 772–787. https://doi.org/https://doi.org/10.1111/maps.12292

Sugiura, N., Ichimura, K., 2010. Mn/Cr relative sensitivity factors for sythetic calcium carbonate measured with a NanoSIMS ion microprobe. Geochemical Journal 44, e11-316. https://doi.org/10.2343/geochemj.1.0089

Sugiura, N., Miyazaki, A., Yanai, K., 2005. Widespread magmatic activities on the angrite parent body at 4562 Ma ago. Earth Planet Sp 57, e13–e16. https://doi.org/10.1186/BF03351858

Telus, M., Alexander, C.M.O., Hauri, E.H., Wang, J., 2019. Calcite and dolomite formation in the CM parent body: Insight from in situ C and O isotope analyses. Geochimica et Cosmochimica Acta 260, 275–291. https://doi.org/10.1016/j.gca.2019.06.012

Tomioka, N., Yamaguchi, A., Ito, M., Uesugi, M., Imae, N., Shirai, N., 2022. Calibrating the shock regime experienced by hydrated asteroid Ryugu. Nature Astronomy.

Tyra, M., Brearley, A., Guan, Y., 2016. Episodic carbonate precipitation in the CM chondrite ALH 84049: An ion microprobe analysis of O and C isotopes. Geochimica et Cosmochimica Acta 175, 195–207. https://doi.org/10.1016/j.gca.2015.10.034

Tyra, M.A., Farquhar, J., Guan, Y., Leshin, L.A., 2012. An oxygen isotope dichotomy in CM2 chondritic carbonates—A SIMS approach. Geochimica et Cosmochimica Acta 77, 383–395. https://doi.org/10.1016/j.gca.2011.10.003

Vacher, L.G., Marrocchi, Y., Villeneuve, J., Verdier-Paoletti, M.J., Gounelle, M., 2018. Collisional and alteration history of the CM parent body. Geochimica et Cosmochimica Acta 239, 213–234. https://doi.org/10.1016/j.gca.2018.08.006

Visser, R., John, T., Whitehouse, M.J., Patzek, M., Bischoff, A., 2020. A short-lived 26Al induced hydrothermal alteration event in the outer solar system: Constraints from Mn/Cr ages of carbonates. Earth and Planetary Science Letters 547, 116440. https://doi.org/10.1016/j.epsl.2020.116440

Warren, P.H., 2011. Stable-isotopic anomalies and the accretionary assemblage of the Earth and Mars: A subordinate role for carbonaceous chondrites. Earth and Planetary Science Letters 311, 93–100. https://doi.org/10.1016/j.epsl.2011.08.047

Yamashita, K., Maruyama, S., Yamakawa, A., Nakamura, E., 2010. 53Mn-53Cr Chronometry of Cb Chondrite: Evidence for Uniform Distribution of 53Mn in the Early Solar System. The Astrophysical Journal 723, 20–24. https://doi.org/10.1088/0004-637X/723/1/20

Yin, Q.-Z., Amelin, Y., Jacobsen, B., 2009. Project Milestones: Testing Consistent Chronologies Between Extinct 53Mn-53Cr and Extant U-Pb Systematics in the Early Solar System. 40th Annual Lunar and Planetary Science Conference 2060.

Young, E.D., 2001. The hydrology of carbonaceous chondrite parent bodies and the evolution of planet progenitors. Philosophical Transactions of the Royal Society of London A: Mathematical, Physical and Engineering Sciences 359, 2095–2110. https://doi.org/10.1098/rsta.2001.0900

Young, E.D., Ash, R.D., England, P., Rumble, D., 1999. Fluid Flow in Chondritic Parent Bodies: Deciphering the Compositions of Planetesimals. Science 286, 1331–1335. https://doi.org/10.1126/science.286.5443.1331

Young, E.D., Zhang, K.K., Schubert, G., 2003. Conditions for pore water convection within carbonaceous chondrite parent bodies – implications for planetesimal size and heat production. Earth and Planetary Science Letters 213, 249–259. https://doi.org/10.1016/S0012-821X(03)00345-5

Zheng, Y.-F., 1995. Oxygen isotope fractionation in magnetites: structural effect and oxygen inheritance. Chemical Geology 121, 309–316. https://doi.org/10.1016/0009-2541(94)00149-3

Zhou, Q., Yin, Q.-Z., Young, E.D., Li, X.-H., Wu, F.-Y., Li, Q.-L., Liu, Y., Tang, G.-Q., 2013. SIMS Pb–Pb and U–Pb age determination of eucrite zircons at < 5 μm scale and the first 50 Ma of the thermal history of Vesta. Geochimica et Cosmochimica Acta 110, 152–175. https://doi.org/10.1016/j.gca.2013.02.016